UNIVERSITY OF CALIFORNIA, SAN DIEGO

Bond-Slip Behavior and Development of Bridge Column Longitudinal Reinforcing Bars in Enlarged Pile Shafts

A dissertation submitted in partial satisfaction of the requirements for the degree

Doctor of Philosophy

in

Structural Engineering

by

Juan Murcia-Delso

Committee in charge:

Professor P. Benson Shing, Chair
Professor Thomas Bewley
Professor Joel P. Conte
Professor Hidenori Murakami
Professor José Restrepo

2013

The dissertation of Juan Murcia-Delso is approved, and it is acceptable in quality and form for publication on microfilm and electronically:

_____

_____

_____

_____

_____

Chair

University of California, San Diego

2013

To my parents, Asun and Juan,

and my sister, Teresa

TABLE OF CONTENTS

SIGNATURE PAGE iii

DEDICATION iv

TABLE OF CONTENTS v

LIST OF ABBREVIATIONS xi

LIST OF SYMBOLS xii

LIST OF FIGURES xxvii

LIST OF TABLES xxxiii

ACKNOWLEDGEMENTS xxxiv

VITA xxxvii

ABSTRACT OF THE DISSERTATION xxxviii

CHAPTER 1

INTRODUCTION 1

1.1 Embedment length of column reinforcement extending into Type II shafts 2

1.2 Research objectives and scope 4

1.3 Outline of the dissertation 4

CHAPTER 2

BOND OF REINFORCEMENT: A LITERATURE REVIEW 9

2.1 Bond of deformed bars 10

2.1.1 Sources of bond resistance and bond-slip behavior 10

2.1.2 Factors affecting bond resistance 14

2.2 Experimental characterization of bond of reinforcement 18

2.2.1 Basic bond-slip tests 18

2.2.2 Effect of confinement on bond strength and radial dilatation 19
2.2.3 Development length and lap splice tests 21
2.2.4 Tests on large-diameter bars 21
2.3 Modeling of bond-slip behavior 22
2.3.1 Rib-scale models 23
2.3.2 Bar-scale models 24
2.3.3 Member-scale models 28

CHAPTER 3

EXPERIMENTAL STUDY ON THE BOND-SLIP BEHAVIOR OF LARGE-DIAMETER BARS IN WELL-CONFINED CONCRETE 43
3.1 Test program, specimen design, and test setup 44
3.2 Instrumentation and loading protocol 47
3.3 Monotonic test results 48
3.4 Cyclic test results 51
3.5 Discussion on factors affecting bond strength 52
3.5.1 Effect of compressive strength of concrete 52
3.5.2 Effect of bar size 53
3.5.3 Effect of pull direction 55
3.5.4 Effect of slip history 55
3.6 Summary and conclusions 56
3.7 Acknowledgement of publication 56

CHAPTER 4

PHENOMENOLOGICAL BOND-SLIP MODEL FOR FINITE ELEMENT ANALYSIS 68
4.1 Bond stress-vs.-slip law for bars in well-confined concrete 69

4.1.1 Monotonic bond stress-slip relation 69
4.1.2 Cyclic law 73
4.1.3 Comparison of analytical and experimental results 78
4.2 Steel-concrete interface model 79
4.3 Three-dimensional modeling of plain concrete 81
4.3.1 Plastic-damage model formulation 81
4.3.2 Validation and calibration of the plastic-damage model 84
4.4 Modeling of steel reinforcement 86
4.5 Finite element analysis verification examples 88
4.6 Summary and conclusions 91

CHAPTER 5

ELASTO-PLASTIC DILATANT INTERFACE MODEL FOR CYCLIC BOND-SLIP BEHAVIOR 107
5.1 Multi-surface plasticity formulation 108
5.1.1 Plastic Mode A: crushing and shearing of concrete between ribs 110
5.1.2 Plastic Mode B: sliding at the concrete-steel surface 114
5.2 Stress update algorithm 117
5.2.1 Return mapping to Yield Surface A 119
5.2.2 Return mapping to Yield Surface B 121
5.2.3 Return mapping to the intersection of Yield Surfaces A and B 122
5.3 Model Calibration and Validation 123
5.4 Verification finite element analyses 125
5.5 Finite element analysis of the effect of concrete cover on bond resistance 129
5.6 Summary and conclusions 131

CHAPTER 6

DEVELOPMENT OF LARGE-DIAMETER BARS IN WELL-CONFINED CONCRETE 147

6.1 Bond-slip of vertical bars in the foundation of a full-scale bridge column tested on a shake table 148

6.2 Pull-push tests on large-diameter bars 151

6.2.1 Test setup and instrumentation 152

6.2.2 Test results 154

6.3 Finite element modeling of pull-push tests 160

6.4 Tension capacity of bars in well-confined concrete 163

6.5 Reliability analysis of the tension capacity of bars anchored in well-confined concrete 168

6.6 Summary and conclusions 173

CHAPTER 7

LARGE-SCALE LABORATORY TESTING OF COLUMN – ENLARGED PILE SHAFT ASSEMBLIES 194

7.1 Description of test specimens 197

7.1.1 Design of specimens 198

7.1.2 Specimen geometry and reinforcement 200

7.2 Construction 202

7.3 Instrumentation 202

7.4 Test setup and loading protocol 204

7.5 Global test results 205

7.5.1 Load-displacement response 205

7.5.2 Test observations for Specimen 1 207

7.5.3 Test Observations for Specimen 2 210

7.6 Strains in steel reinforcement 213

7.6.1 Specimen 1 213

7.6.2 Specimen 2 215

7.7 Summary and conclusions 216

CHAPTER 8

FINITE ELEMENT ANALYSIS OF COLUMN – ENLARGED PILE SHAFT ASSEMBLIES AND NEW DESIGN RECOMMENDATIONS 243

8.1 Finite element modeling of the column-shaft tests 244

8.2 Design recommendations 251

8.2.1 Minimum embedment length of column reinforcement 251

8.2.2 Transverse reinforcement in the shaft 253

8.3 Parametric study to verify the minimum embedment length of column reinforcement in enlarged pile shafts 259

8.3.1 Small-size column-shaft assemblies 261

8.3.2 Large-size column-shaft assemblies 264

8.4 Conclusions 266

CHAPTER 9

SUMMARY AND CONCLUSIONS 284

9.1 Summary 284

9.2 Conclusions 288

9.3 Recommendations for future research 292

APPENDIX A: CONSTRUCTION OF PULL-PUSH TEST SPECIMENS 294

APPENDIX B: CONSTRUCTION OF THE COLUMN-SHAFT ASSEMBLIES 298

APPENDIX C: INSTRUMENTATION PLANS FOR THE COLUMN-SHAFT ASSEMBLIES 311

REFERENCES 329

LIST OF ABBREVIATIONS

AASHTO	American Association of State Highway and Transportation Officials
ACI	American Concrete Institute
ASTM	American Society for Testing and Materials
Cal/OSHA	California Occupational Safety and Health Administration
Caltrans	California Department of Transportation
CIDH	Cast-In-Drilled-Hole
fib	fédération international du béton
	(International Federation for Structural Concrete)
LRFD	Load and Resistance Factor Design
NEES	Network for Earthquake Engineering Simulation
RC	Reinforced Concrete
SDC	Seismic Design Criteria
UCSD	University of California, San Diego

LIST OF SYMBOLS

Chapter 1

$D_{c,\max}$	larger cross-sectional dimension of the column
l_d	required development length for a straight bar in tension

Chapter 2

A_R	projected rib area normal to the bar axis
A_{tr}	transverse reinforcement area
c_b	smaller of the cover of the bar measured from its center and half of the center-to-center spacing of the bars
d_b	bar diameter
f_c'	compressive strength of concrete
n	number of bars being spliced or developed at the plane of splitting
R_r	relative rib area
$s_{R,C}$	center-to-center rib spacing
s_{tr}	spacing of the transverse reinforcement

Chapter 3

A_{tr}	transverse reinforcement area

c_b	smaller of the cover of the bar measured from its center and half of the center-to-center spacing of the bars
CI	confinement index
d_b	bar diameter
f_c'	compressive strength of concrete
f_{cs}	tensile splitting strength of concrete
F	pull-out force
l_e	bonded length of the bar
n	number of bars being spliced or developed at the plane of splitting
s	slip
s_R	clear rib spacing of the bar
s_{tr}	spacing of the transverse reinforcement
τ	bond stress
τ_u	peak bond strength

Chapter 4

c_c	compressive cohesion in the yield surface
c_t	tensile cohesion in the yield surface
C_e	exponential kinematic hardening parameter
C_l	linear kinematic hardening parameter
d	damage parameter

d_b	bar diameter
d_c	damage parameter in compression
d_t	damage parameter in tension
$\hat{d}_b$	damage parameter for the bearing resistance
$\hat{d}_f$	damage parameter for the friction resistance
$\mathbf{E}$	elastic stiffness tensor
$\mathbf{E_0}$	initial elastic stiffness tensor
f_c'	compressive strength of concrete
F	yield function
G	plastic potential
h_R	bar rib height
I_1	first invariant of the stress tensor
J_2	second invariant of the deviatoric stress tensor
$K_{pen,1}$	penalty stiffness coefficient in the normal direction
$K_{pen,3}$	penalty stiffness coefficient in the rotational direction
L_e	length of interface element
s	slip
s_{acc}	cumulative slip
$s_{\max}^{+}$	maximum slip reached in the positive direction
$s_{\max}^{-}$	maximum slip reached in the negative direction in absolute value

s_{peak}	slip at which the peak strength is attained
s_R	clear rib spacing of the bar
u_1	displacement in the normal direction of the interface
u_2	displacement in the longitudinal direction of the interface
u_3	displacement in the rotational direction of the interface
$\tilde{u}_1$	relative displacement in the normal direction of the interface
$\tilde{u}_2$	relative displacement in the longitudinal direction of the interface
$\tilde{u}_3$	relative displacement in the rotational direction of the interface
w_c	weight of stiffness degradation in compression
w_t	weight of stiffness degradation in tension
α	yield surface constant
$\boldsymbol{\alpha}$	backstress tensor
$\boldsymbol{\alpha}'$	deviatoric part of backstress tensor
β	yield surface parameter
γ	yield surface constant
γ_e	exponential kinematic hardening parameter
$\boldsymbol{\varepsilon}$	strain tensor
$\boldsymbol{\varepsilon}^e$	elastic strain tensor
$\boldsymbol{\varepsilon}^p$	plastic strain tensor
$\dot{\varepsilon}_i^p$	i-th principal plastic strain rate

$\tilde{\varepsilon}_c^{\,p}$	equivalent plastic strain in compression
$\tilde{\varepsilon}_t^{\,p}$	equivalent plastic strain in tension
$\hat{\dot{\varepsilon}}^p_{\max}$	maximum principal plastic strain rate
$\hat{\dot{\varepsilon}}^p_{\min}$	minimum principal plastic strain rate
$\dot{\bar{\varepsilon}}^{\,p}$	equivalent plastic strain rate (Von Mises criterion)
ε_s	steel strain
ε_{sh}	strain corresponding to the start of the strain hardening branch
ε_u	ultimate strain of steel
θ	inclination angle of the bond forces with respect to the bar longitudinal axis
$\dot{\lambda}$	plastic multiplier
ρ	bond stress reduction factor
$\boldsymbol{\sigma}$	stress tensor
$\overline{\boldsymbol{\sigma}}$	effective stress tensor
$\boldsymbol{\sigma}'$	deviatoric part of the stress tensor
σ_1	normal stress at the interface
$\hat{\overline{\sigma}}_i$	i-th principal effective stress
$\hat{\sigma}_{\max}$	maximum principal stress
σ_y	yield strength
τ	bond stress
τ_2	longitudinal tangential stress at the interface

τ_3 rotational tangential stress at the interface

τ_b bearing bond resistance

$\tau_{b,\max}$ maximum bearing bond resistance

$\tau_{b,red}$ reduced bearing bond resistance

τ_f friction bond resistance

$\tau_{f,\max}$ maximum friction bond resistance

$\tau_{f,red}$ reduced friction bond resistance

$\tau_{\max}$ maximum bond stress

τ_{red} reduced bond resistance

τ_{res} residual bond stress

τ_{rev} resistance right after slip reversal

τ_u peak bond strength

ψ dilation angle of the concrete

Chapter 5

BE bond effectiveness

c parameter governing the position of the yield surface for Plastic Mode A

$\hat{c}$ cohesion parameter

c_b cover of the bar measured from its center

c_0 initial value of c

CI	confinement index
$\mathbf{d}$	relative displacements at the interface
$\mathbf{d}^e$	elastic relative displacements at the interface
$\mathbf{d}^p$	plastic relative displacements at the interface
$\mathbf{d}_m$	relative displacements at the interface at step m
d_b	bar diameter
d_n	normal relative displacements at the interface
d_t	tangential relative displacements at the interface
$\dot{d}_n^p\big\|_A$	increment of plastic normal displacements caused by Plastic Mode A
$\dot{d}_t^p\big\|_A$	increment of plastic tangential displacements caused by Plastic Mode A
$\dot{d}_t^p\big\|_B$	increment of plastic tangential displacements caused by Plastic Mode B
$\mathbf{D^e}$	elastic stiffness matrix
D_{nn}	normal elastic stiffness coefficient
D_{tt}	tangential elastic stiffness coefficient
E_c	Young modulus of concrete
f_c'	compressive strength of concrete
f_t'	tensile strength of concrete
F	yield function
F_A	yield function for Plastic Mode A
F_B^+	yield function for Plastic Mode B (sliding in the positive direction)

F_B^-	yield function for Plastic Mode B (sliding in the negative direction)
h_R	height of the bar ribs
k_i	constants defining the yield functions and flow rules
K_{tr}	confinement term related to transverse reinforcement
$\mathbf{m}$	plastic flow vector
$\mathbf{m}_m$	plastic flow vector at step m
$\mathbf{m}_{m+1}$	plastic flow vector at step $m+1$
$\mathbf{m}_A$	plastic flow vector for Plastic Mode A
$\mathbf{m}_{B+}$	plastic flow vector for Plastic Mode B (sliding in the positive direction)
$\mathbf{m}_{B-}$	plastic flow vector for Plastic Mode B (sliding in the positive direction)
p^+	plastic tangential displacement associated with Mode A in the positive direction
p^-	plastic tangential displacement associated with Mode A in the negative direction
$\mathbf{q}$	vector of internal variables
$\mathbf{q}_m$	vector of internal variables at step m
$\mathbf{q}_{m+1}$	vector of internal variables at step $m+1$
r	net interface opening caused by Plastic Mode A
s	plastic tangential displacement due to Mode B sliding
s_R	clear bar rib spacing
$u_{\lim}$	horizontal length of the inclined plane

u_{trans}	length of transition zones
α	angle of inclination of the contact surface with respect to the axis of the bar
α_0	maximum inclination of the lateral face of the ribs
$\Delta\mathbf{d}$	displacement increment at step m
$\Delta\mathbf{d}^p$	plastic displacement increment at step m
$\Delta\lambda$	discrete plastic multiplier
θ	constant governing the generalized mid-point rule
$\dot{\lambda}$	plastic multiplier
μ_A	parameter governing the increase of the shear resistance with the normal stress for Plastic Mode A
$\mu_{A,0}$	initial value of μ_A
μ_B	concrete-steel friction coefficient
$\mu^+_{B,eff}$	effective friction coefficient for positive sliding
$\mu^-_{B,eff}$	effective friction coefficient for negative sliding
σ	normal stress at the interface
σ'	normal stress perpendicular to the sliding plane
σ^e	elastic trial normal stress
$\boldsymbol{\sigma}$	vector of stresses at the interface
$\boldsymbol{\sigma}_m$	stress vector at step m
$\boldsymbol{\sigma}_{m+1}$	stress vector at step $m+1$
$\boldsymbol{\sigma}^e$	elastic trial stress vector

$\boldsymbol{\sigma}^{e}_{m+1}$ elastic trial stress vector at step $m+1$

τ tangential stress at the interface

τ' tangential stress parallel to the sliding plane

τ^{e} elastic trial tangential stress

$\tau_{FE,\max}$ bond strength obtained from FE analysis

$\tau_{\max,nac}$ maximum bond resistance with no active confinement

ϕ internal friction angle

Chapter 6

d_b bar diameter

e analytical prediction error

f_c' compressive strength of concrete

f_{cs} tensile splitting strength of concrete

f_y yield strength of steel

f_u tensile strength of steel

F_y expected yield force of the bar

g_y limit-state function for bar yielding capacity

g_{ru} limit-state function for bar reduced ultimate capacity

g_u limit-state function for bar ultimate capacity

$l_{d,AASHTO}$ minimum development length required by AASHTO LRFD

l_e	embedment length
p_F	probability of failure
r	ratio between the actual tensile capacity and the FE prediction
R^2	coefficient of determination
u_5	displacement measured at the positive peak of Cycle 5
u_y	expected displacement at tension yielding
β	reliability index
κ	power constant
λ_e	normalized embedment length (SI units)
$\hat{\lambda}_e$	normalized embedment length (US costumary units)
$\sigma_{\max}$	maximum tensile stress
$\tau_{u,av}$	average bond strength
$\Phi(\cdot)$	cumulative probability function of the standard normal distribution
χ	proportionality constant

Chapter 7

A_l	total cross-sectional area of the longitudinal reinforcement
A_{tr}	cross-sectional area of the transverse reinforcement
c	concrete cover at the top of the shaft
d_b	bar diameter

D_c	column diameter
$D_{c,\max}$	larger cross-sectional dimension of the column
$f_{y,tr}$	yield strength of the transverse reinforcement
f_u	ultimate strength of the longitudinal reinforcement
F_y	ultimate lateral load
F_y'	lateral load at the first yield of the column longitudinal bars
l_d	required development length for a straight bar in tension
l_{db}	basic development length specified in AASHTO LRFD
l_e	embedment length
l_s	splice length required for a contact splice
s	bar spacing in the non-contact splice
$s_{tr,\max}$	maximum spacing of the transverse reinforcement
Δ	lateral displacement of the specimen at the level of the horizontal actuators
Δ_y	equivalent yield displacement
Δ_y'	displacement at the first yield of the column longitudinal bars
ε_y	yield strain of longutdinal reinforcement
μ	system ductility demand

Chapter 8

A_{tr}	cross-sectional area of the transverse reinforcement
c	concrete cover at the top of the shaft
d_b	bar diameter
$d_{b,col}$	bar diameter of column longitudinal reinforcement
$d_{b,sh}$	bar diameter of shaft longitudinal reinforcement
D_c	column diameter
$D_{c,\max}$	larger cross-sectional dimension of the column
D_{ext}	diameter of the inner reinforcing hoops
D_{int}	diameter of the outer reinforcing hoops
D_s	shaft diameter
f	splitting force per unit length
f_c'	compressive strength of concrete
$f_{y,tr}$	yield strength of the transverse reinforcement
l_d	required development length for a straight bar in tension
l_e	embedment length
N_{col}	number of column longitudinal bars
N_{sh}	number of shaft longitudinal bars
p_{ext}	pressure generated by the splitting radial forces of the outer bars
p_{int}	pressure generated by the splitting radial forces of the inner bars

s	bar spacing in the non-contact splice
s_{tr}	spacing of the transverse reinforcement
t_{ext}	tensile force in the external reinforcing hoops
t_{int}	tensile force in the internal reinforcing hoops
u_{cr}	crack opening
ε_s	strain of steel reinforcement
$\varepsilon_{s,\max}$	maximum allowable strain of steel reinforcement
ε_y	yield strain of steel reinforcement
$\rho_{v,shaft}$	volumetric ratio of transverse reinforcement in shaft
σ	radial pressure
τ	bond stress
τ_{col}	bond stress in column longitudinal reinforcement
τ_{sh}	bond stress in shaft longitudinal reinforcement
τ_u	bond strength

Chapter 9

A_{tr}	cross-sectional area of the transverse reinforcement
c	concrete cover at the top of the shaft
$d_{b,col}$	bar diameter of column longitudinal reinforcement
D_c	column diameter

f_c'	compressive strength of concrete
$f_{y,tr}$	yield strength of the transverse reinforcement
l_d	required development length for a straight bar in tension
l_e	embedment length
N_{col}	number of column longitudinal bars
s	bar spacing in the non-contact splice
s_{tr}	spacing of the transverse reinforcement
τ_u	bond strength

LIST OF FIGURES

Figure 1.1: Pull-out of longitudinal reinforcement in bridge columns from foundations during the 1971 San Fernando earthquake (Yashinsky 2001) 8

Figure 1.2: Type I and Type II shafts (Caltrans 2010) 8

Figure 2.1: Sources of bond resistance (ACI 2003)..... 31

Figure 2.2: Cracking pattern due to bond-slip (ACI 2003)..... 31

Figure 2.3: Bond stress vs. slip for different confinement conditions 32

Figure 2.4: Bond failure by splitting of concrete (Choi et al. 2011)..... 32

Figure 2.5: Crushing and shearing of concrete between ribs in a bar pull-out failure..... 33

Figure 2.6: Cyclic bond-slip behavior in pull-out failures (Eligehausen et al. 1983)..... 33

Figure 2.7: Bond-slip relations obtained by Shima et al. (1987b) for bars yielding in tension 34

Figure 2.8: Bond-slip test specimen and setup used by Rehm (1961)..... 34

Figure 2.9: Bond-slip test specimen and setup used by Eligehausen et al. (1983) 35

Figure 2.10: Cyclic bond stress-vs.-slip relations obtained by Eligehausen et al. (1983) 35

Figure 2.11: Bond-slip test specimen with different crack openings used by Gambarova et al. (1989) 36

Figure 2.12: Bond stress-vs.-slip and confining stress-vs.-slip relations for different crack openings obtained by Gambarova et al. (1989) 36

Figure 2.13: Bond stress-vs.-slip and bond stress-vs.-radial displacement relations obtained by Malvar (1992)..... 37

Figure 2.14: Load-vs.-slip and load-vs.- bar strain relations obtained by Lundgren (2000) 37

Figure 2.15: Sketch of typical development and lap splice tests (ACI 2003)..... 37

Figure 2.16: Experimental database from ACI 408 Committee 38

Figure 2.17: Finite element model used by Reinhardt et al. (1984a) to study the bond-slip behavior of bars..... 38

Figure 2.18: Actual vs. idealized concrete-steel interaction (Cox and Herrmann 1998).. 39

Figure 2.19: Analytical bond stress-vs.-slip model proposed by Eligehausen et al. (1983) 39

Figure 2.20: Differential equation of bond-slip and finite difference discretization of a bar (Ciampi et al. 1982) 40

Figure 2.21: Bond-slip element by Lowes et al. (2004) 40
Figure 2.22: Yield surface evolution for the bond-slip model of Cox and Herrmann (1998) 41
Figure 2.23: Yield surfaces for the bond-slip model of Lundgren and Magnusson (2001) 41
Figure 2.24: Surface geometry assumed in the interface element of Serpieri and Alfano (2011) 42
Figure 2.25: Zero-length element proposed by Zhao and Sritharan (2007) 42
Figure 3.1: Test specimen, setup, and instrumentation 59
Figure 3.2: Construction sequence for each series of specimens 60
Figure 3.3: Test setup 61
Figure 3.4: Pull force vs. slip from Test 1 of Series 3 61
Figure 3.5: Average bond stress vs. slip from monotonic load tests 62
Figure 3.6: Pull force vs. slip from Test 1 and Test 2 of Series 4 62
Figure 3.7: Strain in spiral at mid-height of the specimen in Test 1 of Series 3 63
Figure 3.8: Tests on No. 11 bars (Series 1) under monotonic (Test 1 and Test 2) and cyclic load with half cycles (Test 3 and Test 4) 63
Figure 3.9: Tests on No. 11 bars (Series 1) under monotonic (Test 1) and cyclic load with half cycles (Test 5) and full cycles (Test 6) 64
Figure 3.10: Tests on No. 14 bars (Series 2) under monotonic (Test 4) and cyclic load with full cycles (Test 2) and half cycles (Test 3) 64
Figure 3.11: Tests on No. 14 bar (Series 2) under monotonic (Test 4) and cyclic load with single half cycles (Test 5) and double half cycles (Test 6) 65
Figure 3.12: Tests on No. 18 bars (Series 3) under monotonic (Test 1) and cyclic load with full cycles (Test 2 and Test 3) 65
Figure 3.13: Tests on No. 18 bars (Series 3) under monotonic (Test 2) and cyclic load with half cycles (Test 5 and Test 6) 66
Figure 3.14: Tests on No. 14 bars (Series 4) under cyclic load with single full cycles (Test 4) and double full cycles (Test 3) 66
Figure 3.15: Strain in spiral at mid-height of the specimen in Test 3 of Series 3 67
Figure 4.1: Analytical bond stress-slip model 93
Figure 4.2: Analytical and experimental results for monotonic loading 94
Figure 4.3: Analytical and experimental results for cyclic loading 95
Figure 4.4: Analytical and experimental results for tests conducted on No. 8 and 5 bars 96
Figure 4.5: Interface element 96

Figure 4.6: Initial yield function in plane-stress space (Lee and Fenves 1998) 97
Figure 4.7: Uniaxial tension and compression behavior in plastic-damage model 97
Figure 4.8: Tension-compression tests by Reinhardt (1984b) 98
Figure 4.9: Confined compression tests by Hurblut (1985) 98
Figure 4.10: Compression tests by Mander et al. (1989) on RC columns with different transverse reinforcement 99
Figure 4.11: Uniaxial tests on reinforcing steel coupons by Restrepo-Posada et al. (1993) 100
Figure 4.12: FE analysis of bond-slip tests on No. 18 bars 101
Figure 4.13: FE analysis of pull-out tests by Lundgren (2000) 102
Figure 4.14: FE analysis of pull-out tests by Plizzari and Mettelli (2009) 103
Figure 4.15: FE analysis of pull-out tests by Shima et al. (1989b) 104
Figure 4.16: FE model of RC column tested by Lehman and Moehle (2000) 105
Figure 4.17: FE analysis of RC column tested by Lehman and Moehle (2000) 106
Figure 5.1: Interface idealization and plastic deformation modes 134
Figure 5.2: Yield surfaces 135
Figure 5.3: Evolution of the yield surface for Mode A (pull-out) 135
Figure 5.4: (a) Mohr circles for uniaxial compression and tension and Mohr-Coulomb failure surface, and (b) initial yield surface for Mode B and Mohr-Coulomb surface ... 136
Figure 5.5: Evolution of the yield function for Mode B (sliding) 136
Figure 5.6: Evolution of the concrete-steel contact plane 137
Figure 5.7: Possible stress return scenarios for plastic correction 138
Figure 5.8: Stress update algorithm 139
Figure 5.9: Analysis vs. experimental results obtained by Malvar (1992) 140
Figure 5.10: FE model of pull-out tests carried out by Lundgren (2000) 141
Figure 5.11: Analysis vs. monotonic pull-out test results obtained by Lundgren (2000) 141
Figure 5.12: Analysis vs. cyclic pull-out test results obtained by Lundgren (2000) 142
Figure 5.13: Analysis vs. monotonic bond-slip test results 143
Figure 5.14: Analysis vs. cyclic bond-slip test results (Test 3, Series 2) 143
Figure 5.15: Analysis vs. pull-out test results obtained by Plizzari and Mettelli (2009) 144
Figure 5.16: Analysis vs. push-in test results obtained by Choi et al. (2011) 145
Figure 5.17: FE model for parametric study 145
Figure 5.18: Bond strength vs. confinement 146

Figure 6.1: RC column tested at the NEES-UCSD Outdoor Shake Table (Restrepo et al. 2010) 179
Figure 6.2: Bond-slip measurement instrumentation (Restrepo et al. 2010) 179
Figure 6.3: History of strains along the bar anchorage and in the column near the base 180
Figure 6.4: History of bar slip at the column-footing interface 180
Figure 6.5: Bar slip vs. strain at the column-footing interface 181
Figure 6.6: Test specimens and instrumentation (1'=305mm, 1"=25.4 mm) 181
Figure 6.7: Test setup 182
Figure 6.8: Experimental results for Test 1 183
Figure 6.9: Experimental results for Tests 2 and 3 183
Figure 6.10: Bar strain vs. slip at the top of the anchorage in Test 2 184
Figure 6.11: Bar pull-out in Test No. 1 184
Figure 6.12: Bar rupture and damage in concrete cylinder in Test No. 2 185
Figure 6.13: Bar pull-out and damage in concrete cylinder in Test No. 3 186
Figure 6.14: Strain penetration in tests and FE analysis 187
Figure 6.15: Strain in perimeter bars in tests and FE analysis 187
Figure 6.16: Strains in perimeter bars from tests and simple analytical models 188
Figure 6.17: Truss analogy used by McLean and Smith (1997) for non-contact lap splices 188
Figure 6.18: Strains in hoops in Test No. 3 and FE analysis 188
Figure 6.20: Bar stress – bar displacement curves from FE analyses and tests 189
Figure 6.22: Bar axial stress distributions from FE analysis for Test No. 2 190
Figure 6.23: Bar axial stress distributions from FE analysis for Test No. 3 190
Figure 6.25: Bond stress distributions from FE analysis for Test No. 2 191
Figure 6.26: Bond stress distributions from FE analysis for Test No. 3 191
Figure 6.27: Tensile capacity vs. development length 192
Figure 6.28: Tensile capacity vs. normalized development length for $\kappa = 0.5$ 192
Figure 6.29: Tensile capacity vs. normalized development length for $\kappa = 0.75$ 193
Figure 6.30: Tensile capacity vs. normalized development length for $\kappa = 1$ 193
Figure 7.1: Truss analogy proposed by McLean and Smith (1997) 220
Figure 7.2: Bending moment distributions in a real column-shaft and a test specimen . 220
Figure 7.3: Geometry and reinforcement of Specimen 1 221

Figure 7.4: Geometry and reinforcement of Specimen 2 222
Figure 7.5: Test setup 223
Figure 7.6: Loading protocol 224
Figure 7.7: Lateral force vs. drift for Specimens 1 and 2 225
Figure 7.8: Cracks in Specimen 1 at Cycle 4 (1st yield) 226
Figure 7.9: Evolution of damage at the column base in Specimen 1 (north face) 227
Figure 7.10: Damage at the end of the test in the shaft of Specimen 1 228
Figure 7.11: Lateral displacement of Specimen 1 229
Figure 7.12: Curvature envelopes of Specimen 1 229
Figure 7.13: Flexural cracks in Specimen 2 at Cycle 4 (1st yield) 230
Figure 7.14: Splitting cracks at the top of the shaft in Specimen 2 at Cycle 3 230
Figure 7.15: Evolution of damage at the column base in Specimen 2 (north face) 231
Figure 7.16: Evolution of damage at the column base in Specimen 2 (south face) 231
Figure 7.17: Damage in the shaft of Specimen 2 232
Figure 7.18: Displacement of Specimen 2 233
Figure 7.19: Curvature of Specimen 2 233
Figure 7.20: Strains in column longitudinal bars in Specimen 1 (north face) 234
Figure 7.21: Strains in column longitudinal bars in Specimen 1 (south side) 235
Figure 7.22: Strains in shaft longitudinal bars in Specimen 1 236
Figure 7.23: Strains in column hoops in Specimen 1 237
Figure 7.24: Strains in shaft hoops in Specimen 1 237
Figure 7.25: Strains in column longitudinal bars in Specimen 2 (north face) 238
Figure 7.26: Strains in column longitudinal bars in Specimen 2 (south face) 239
Figure 7.27: Strains in shaft longitudinal bars in Specimen 2 240
Figure 7.28: Strains in column hoops in Specimen 2 241
Figure 7.29: Strains in shaft hoops in Specimen 2 242
Figure 8.1: FE model of column-shaft assembly 268
Figure 8.2: Lateral load vs. drift curves for Specimen 1 268
Figure 8.3: Lateral load vs. drift curves for Specimen 2 269
Figure 8.4: Strains in the column longitudinal bar at the north face of Specimen 1 269
Figure 8.5 Strains in the column longitudinal bar at the north face of Specimen 2 270

Figure 8.6: Axial stress variation in the column longitudinal bars at the north face of the specimens 270
Figure 8.7: Bond stresses along the column longitudinal bar at the north face of Specimen 1 271
Figure 8.8: Bond stresses along the column longitudinal bar at the north face of Specimen 2 271
Figure 8.9: Strains in the longitudinal shaft bar at the north face of Specimen 1 272
Figure 8.10: Strains in the longitudinal shaft bar at the north face of Specimen 2 272
Figure 8.11: Strains in the column hoops 273
Figure 8.12: Strains in shaft hoops at the north face of Specimen 1 274
Figure 8.13: Strains in shaft hoops in Specimen 2 275
Figure 8.14: Splitting stress and forces in developed bar 276
Figure 8.15: Cross-section of pile shaft and splitting forces 276
Figure 8.16: ABCD and CDEF free body diagrams 277
Figure 8.17: Splitting crack opening and strain in hoop reinforcement 277
Figure 8.18: Lateral load vs. drift curves for Models 4-6-11-x 278
Figure 8.19: Results for north column longitudinal bar in Models 4-6-11-x at the peak displacement of Cycle 13 278
Figure 8.20: Lateral load vs. drift curves for Models 4-6-14-x 279
Figure 8.21: Results for north column longitudinal bar in Models 4-6-14-x at the peak displacement of Cycle 17 279
Figure 8.22: Strains in shaft hoop in Models 4-6-14-x at the peak displacement of Cycle 17 280
Figure 8.23: Lateral load vs. drift curves for Models 8-10-14-x 280
Figure 8.24: Results for north column longitudinal bar in Models 8-10-14-x at the peak displacement of Cycle 17 281
Figure 8.25: Lateral load vs. drift curve for Model 8-12-14 281
Figure 8.26: Lateral load vs. drift curve for Model 8-12-18 282
Figure 8.27: Results for north column longitudinal bar in Model 8-12-14 at the peak displacement of Cycle 17 282
Figure 8.28: Results for north column longitudinal bar in in Model 8-12-18 at the peak displacement of Cycle 17 283

LIST OF TABLES

Table 3.1: Test matrix and specimen properties 58
Table 3.2: Geometric properties of the bars 58
Table 4.1: Bond-slip model parameters 92
Table 4.2: Plastic-damage model calibration 92
Table 5.1: Bar and concrete properties for model validation 133
Table 5.2: Fixed model parameters 133
Table 5.3: Relation between confinement and bond strength 133
Table 6.1: Ground motions in RC column test (Carrea 2010) 175
Table 6.2: Specimen properties and test results 175
Table 6.3: Location of strain gages 176
Table 6.4: pull-push tests loading protocol 176
Table 6.5: Parametric study variables and results 177
Table 6.6: Loading protocol for parametric analysis 178
Table 6.7: Reliability analysis results for $l_e = l_{d,AASHTO}$ and f'_c =24.8 MPa (3.6 ksi) 178
Table 6.8: Reliability analysis results for $l_e = l_{d,AASHTO}$ and f'_c =34.5 MPa (5 ksi) 178
Table 7.1: Compressive strength of concrete on the day of test 219
Table 7.2: Yield and ultimate tensile strengths of longitudinal reinforcement 219
Table 8.1: FE models of column-shaft assemblies for parametric study 267

ACKNOWLEDGEMENTS

The research presented in this dissertation was conducted under the supervision of Professor Benson Shing. The core of this research was related to the project “Required Embedment Length of Column Rebar Cage into Type II Shafts,” supported by the California Department of Transportation (Caltrans).

I would like to express my deepest gratitude and appreciation to my advisor, Professor Benson Shing. His expertise, encouragement, and wise guidance have been a great support during my doctoral studies at UCSD. I am very thankful to him for providing me the opportunity to develop my research in a very stimulating topic, and for showing me the way and challenging me to become a better researcher. I have very much enjoyed working with and learning from him.

I would like to thank my PhD Committee members, Professor Thomas Bewley, Professor Joel P. Conte, Professor Hidenori Murakami, and Professor José Restrepo for their inspiring courses, their interest in my research work, and their useful suggestions for my dissertation.

I would like to express my gratitude to “Fundació La Caixa” and “Fundación Caja Madrid” for the graduate fellowships that supported the first four years of my doctoral studies. I am also grateful for the financial support from Caltrans for my last year of studies and for the laboratory work.

The experiments presented in this dissertation were conducted in the Powell Structural Engineering Laboratories at UCSD. I would like to express my gratitude to the laboratory staff for their effort and technical support. Special thanks to Dr. Chris Latham,

Mr. Paul Greco, Mr. Noah Aldrich, Mr. Darren McKay, and Mr. Bob Peters for their help.

I would like to acknowledge the contributions of Professor Andreas Stavridis and Ms. Yujia Liu to the laboratory studies. Professor Andreas Stavridis participated as a post-doctoral researcher at UCSD in the design and preparation of the basic bond-slip tests presented in Chapter 3, and the development length tests presented in Chapter 6. I am grateful for his precious support and advice. Ms. Yujia Liu contributed to the preparation of the column-pile shaft assembly tests presented in Chapter 7 of this dissertation. I am thankful for her valuable help in the design, construction, and instrumentation of the specimens.

I would like to thank Mr. Vassilis Papadopoulos for his valuable contributions in the validation of the constitutive model for concrete that has been used in the analytical studies presented in this dissertation.

Chapter 6 of this dissertation includes an analysis of experimental data on the bond-slip behavior of bars obtained from a full-scale bridge RC column tested by Professor José Restrepo and his coworkers on the NEES-UCSD Shake Table. I am very grateful to Professor Restrepo, Dr. Matt Schoettler, and Mr. Gabriele Guerrini for generously sharing with me the experimental data and pictures from their test.

I would like to add to the acknowledgement lists other colleagues and friends who I have had the pleasure to work with, and who have helped me in one way or another: Professors Hussein Okail, Ioannis Koutromanos, and André Barbosa; Drs. Flavio Mosele, Ming-Chen Hsu, and Giovanni de Francesco; and Mr./Ms. Alexandra Kottari, Marios Mavros, Rodrigo Astroza, and Kyung-Tae Kim.

I would like to thank my family and friends for their encouragements. I want to thank my parents and my sister for their tireless and unconditional support. I fondly dedicate this dissertation to them. Finally, I would like to express my immense gratitude and admiration to my wife, Anna. Your generosity and courage made this journey possible. Your support and patience helped me all the way.

Part of Chapter 3 is a reprint of the material that will appear in a paper, titled "Bond strength and cyclic bond deterioration of large-diameter bars in well-confined concrete" to be published in the ACI Structural Journal in 2013. The author of this dissertation was the first and primary author of the paper.

VITA

2005 *Ingeniero de Caminos, Canales y Puertos* (BS/MS in Civil Engineering), Technical University of Catalonia, Spain.

2008 Master of Science in Structural Analysis of Monuments and Historical Constructions, University of Minho, Portugal, and Technical University of Catalonia, Spain.

2013 Doctor of Philosophy in Structural Engineering, University of California, San Diego, USA.

ABSTRACT OF THE DISSERTATION

Bond-Slip Behavior and Development of Bridge Column Longitudinal Reinforcing Bars in Enlarged Pile Shafts

by

Juan Murcia-Delso

Doctor of Philosophy in Structural Engineering

University of California, San Diego, 2013

Professor P. Benson Shing, Chair

Enlarged (Type II) pile shaft foundations are used frequently in reinforced concrete bridges because of the convenience in construction and efficiency in post-earthquake inspection and repair. According to the specifications of the California Department of Transportation (Caltrans), the diameter of a Type II shaft should be at least 610 mm (2 ft) larger than that of the column. Hence, the column reinforcement extended into the pile shaft can be perceived as forming a non-contact splice with the pile

shaft reinforcement. Because of the lack of data, the seismic design specifications of Caltrans on the embedment length of column reinforcement in Type II shafts are very conservative for large-diameter columns, which could complicate the construction work and entail high construction costs.

This dissertation presents an experimental and analytical investigation to characterize the bond between concrete and reinforcing steel when a reinforced concrete member is subjected to severe cyclic loading, and determine the minimum embedment length required for column longitudinal reinforcement extended into a Type II shaft. Experiments were carried out to investigate the bond strength and cyclic bond deterioration of large-diameter bars (No. 11, 14, and 18) commonly used in large-diameter bridge columns and piles. The experimental results have been used to develop, calibrate, and validate a phenomenological bond-slip model for bars embedded in well-confined concrete. The model successfully reproduces bond deterioration caused by cyclic bar-slip reversals and tensile yielding of the bar, and has been implemented in an interface element in a finite element program. A physics-based dilatant interface model formulated with a multi-surface plasticity concept has also been developed and implemented in the finite element program to simulate bond-slip under a broad range of confinement situations.

With the phenomenological bond-slip model, nonlinear finite element analysis has been conducted to extrapolate results of development length tests conducted on large-diameter bars, and assess the reliability of the development lengths required in the AASHTO LRFD Bridge Design Specifications. Finally, two large-scale tests on column-pile shaft assemblies were conducted. The tests were combined with finite element

analysis to evaluate the conservatism of the current Caltrans specifications, and provide new design recommendations that can significantly reduce the embedment length required for column reinforcement, while ensuring an appropriate performance of the column-pile shaft connections under severe seismic loads.

CHAPTER 1

INTRODUCTION

The performance of reinforced concrete (RC) structures depends on the composite action of the concrete and reinforcing steel, which relies on the bond between the two materials. When RC structures are subjected to earthquake loads, they may experience severe bond stress demands in regions where the reinforcement is anchored, e.g., in the foundation of a bridge column. Inadequate embedment lengths in these regions can lead to bond failures causing structural collapse like those observed in bridge columns during the 1971 San Fernando earthquake (Yashinsky 2001), which had longitudinal reinforcement pulled out from the foundation, as shown in Figure 1.1. After this earthquake, the development length for large-diameter bars, which are frequently used in large bridge columns and piles, was increased and more confinement steel was provided in bridge footings and columns (Yashinsky 2001).

Despite the fact that extensive research has been carried out over the last few decades on the bond strength and bond-slip behavior of reinforcing bars, there was little data on the bond strength and required development length for large-diameter bars (No.11 [36-mm] and larger). The development length specifications in ACI 318-08 (ACI

2008) and AASHTO LRFD Bridge Design Specifications (AASHTO 2010) are largely based on experimental data obtained from No. 11 and smaller bars, and they do not allow lap-splicing of bars larger than No. 11. Moreover, no data were available for the cyclic bond deterioration for large-diameter bars. Most of the experimental data on the cyclic bond-slip behavior of bars were obtained from the study of Eligehausen et al. (1983) for No. 8 (25-mm) bars. New experimental data on the bond strength, cyclic bond deterioration, and development length of large-diameter bars could help to improve the design of RC bridges.

While the bond-slip behavior of reinforcement has a strong influence in the behavior of reinforced concrete structures, this aspect has been generally overlooked in the finite element analysis of RC structures. Reliable bond-slip models are needed to properly capture crack spacing, and the stiffness and deformation capability of RC members. These models can also be used in fundamental studies to interpret and extrapolate experimental results to determine the required development and lap splice lengths for reinforcing bars. To better understand the performance of RC structures during earthquakes and improve their seismic design, accurate and efficient models for the cyclic bond-slip behavior of reinforcing bars need to be developed.

1.1 Embedment length of column reinforcement extending into Type II shafts

Pile shaft foundations are used frequently in RC bridge columns because of the convenience in construction. Two types of pile shafts are typically used in California: pile shafts that have the same diameter as the column (Type I), and pile shafts with an enlarged section (at least 0.61 m [2 ft] larger) with respect to the column diameter (Type

II), as shown in Figure 1.2. For columns on Type I shafts, plastic hinges will develop in the shafts underneath the ground surface when subjected to severe seismic loads (e.g., see Budek et al. 2000, Chai 2002, Chai and Hutchinson 2002). Type II shafts are capacity protected elements and their damage inspection after an earthquake will be easier because plastic hinging will occur at the column base. Besides the structural benefits, Type II shafts also provide more flexibility for the alignment of bridge columns. However, because of the different diameters of the column and the shaft, it is not possible to have a continuous reinforcing cage for the column and the shaft, and the column longitudinal reinforcement extended into the shaft is terminated at a certain distance forming a non-contact lap splice with the longitudinal shaft reinforcement.

The minimum seismic design requirements to meet the performance goals for *Ordinary* bridges in California are established in Caltrans Seismic Design Criteria (Caltrans 2010). Section 8.2.4 of Caltrans Seismic Design Criteria requires that column longitudinal reinforcement be extended into Type II shafts in a staggered manner with the minimum embedment lengths of $D_{c,\max} + l_d$ and $D_{c,\max} + 2l_d$, respectively, where $D_{c,\max}$ is the larger cross-sectional dimension of the column and l_d is the required development length for a straight bar in tension. This requirement was found to be conservative based on a finite element analysis study by Chang and Dameron (2009). However, there was no experimental data on the cyclic bond-slip behavior of large diameter bars to calibrate the finite element model and to evaluate how conservative this requirement was.

1.2 Research objectives and scope

The main objective of this dissertation was to determine the minimum embedment length required for column reinforcement extended into Type II shafts and develop improved design recommendations for the embedment length and the transverse reinforcement required in bar anchorage zones of these pile shafts. Furthermore, this research also evaluated the reliability of current AASHTO LRFD specifications (AASHTO 2010) on the development length for large-diameter bars when they are subjected to severe cyclic tension and compression up to the ultimate tensile capacity of the bars. To this end, basic experimental data on the cyclic bond-slip behavior of large-diameter reinforcing (No. 11, 14 [43-mm], and 18 [57-mm]) bars were obtained and development length tests were conducted on these bars embedded in cylindrical concrete specimens. Two bond-slip models have been developed and implemented in the finite element analysis program ABAQUS (Simulia 2010). One is a phenomenological model that accounts for cyclic bond deterioration and the radial stress introduced by bond-slip in a semi-empirical manner. The second is a physics-based model formulated with the plasticity theory. The study included detailed nonlinear finite element modeling as well as large-scale testing of column-shaft assemblies to validate the finite element models and proposed design recommendations.

1.3 Outline of the dissertation

The first part of the dissertation, Chapters 2 through 5, focuses on the fundamental study of the bond-slip behavior of reinforcing bars. It includes a literature

review, an experimental study on the basic bond-slip behavior of large-diameter bars, and the development and validation of computational models to simulate the bond-slip behavior of bars in finite element analysis. The second part of the dissertation, Chapters 6 through 8, presents studies conducted with computational models and large-scale tests on the development length of large-diameter bars, and the minimum embedment length of column longitudinal reinforcement in Type II shafts.

Chapter 2 presents a review of the fundamental aspects of bond of reinforcement reported in the literature, and some of the most relevant experimental and analytical studies in this area.

Chapter 3 presents the experimental study conducted on the bond-slip behavior of large-diameter bars embedded in well-confined concrete. Monotonic pull-out and cyclic pull-pull tests were conducted on No. 11, 14, and 18 bars to study their bond strength and bond stress-vs.-slip relations. The specimens, test setup, and experimental results are presented. Based on these results and on studies carried out by others, the effect of the bar diameter, concrete strength, pull direction and loading history on the bond strength are investigated.

Chapter 4 presents a new model to simulate the cyclic bond-slip behavior of reinforcing bars for finite element analysis of RC members. A phenomenological law to predict the cyclic bond stress-vs.-slip relation of bars embedded in well-confined concrete is presented. This law has been calibrated with the experimental data presented in Chapter 3, and implemented in an interface element in the finite element analysis program ABAQUS. Finite element analyses of laboratory tests are provided to validate the bond-slip model.

In Chapter 5, a new physics-based interface model formulated with the plasticity theory is presented to simulate the cyclic bond-slip behavior of deformed bars with an accurate account of the radial dilatation generated by bond-slip. This model is more general than the phenomenological model presented in Chapter 4 in that it is applicable to a broader range of concrete confinement situations. The formulation, numerical implementation scheme, and calibration of the model are presented. This model has also been implemented in ABAQUS. Finite element verification analyses are provided.

Chapter 6 presents the results of experimental and computational studies on the development of large-diameter bars in well-confined concrete. These studies included pull-push tests conducted to evaluate the development length required in the AAHSTO LRFD Bridge Design Specifications (AASHTO 2010) for large-diameter bars embedded in well-confined concrete. The test results have been interpreted with the help of finite element analysis incorporating the phenomenological bond-slip model presented in Chapter 4. A parametric study has been carried out with finite element models, and, based on these results, an analytical equation has been derived to determine the tensile capacity of a bar for given embedment length, and concrete and steel strengths. Based on this equation, a Monte Carlo simulation has been conducted to assess the reliability of current AASHTO development length specifications in developing the yield and ultimate capacity of a bar.

Chapter 7 presents two large-scale tests conducted on RC bridge column - enlarged pile shaft assemblies with quasi-static cyclic lateral loading. These tests were intended to identify the minimum embedment length required for column longitudinal reinforcement extending into Type II shafts, and to validate nonlinear finite element

models including the bond-slip behavior. The specimen design, test setup, and experimental results are presented.

Chapter 8 presents a computational study on the required embedment length for the column reinforcement extending into Type II shafts. Finite element analysis with the phenomenological bond-slip model has been conducted on the large-scale column-shaft specimens presented in Chapter 7 to further understand the bond-slip behavior of the longitudinal column bars in the anchorage zone. Based on the experimental and analytical results, new design recommendations are proposed for the embedment length required for column reinforcement and the quantity of transverse steel required in the bar anchorage zone of a shaft. A parametric study using finite element models is also presented to validate the design recommendations for different column-shaft geometries and bar sizes and quantities.

Chapter 9 presents the summary and conclusions of this research. Recommendations for future research are also presented.

Figure 1.1: Pull-out of longitudinal reinforcement in bridge columns from foundations during the 1971 San Fernando earthquake (Yashinsky 2001)

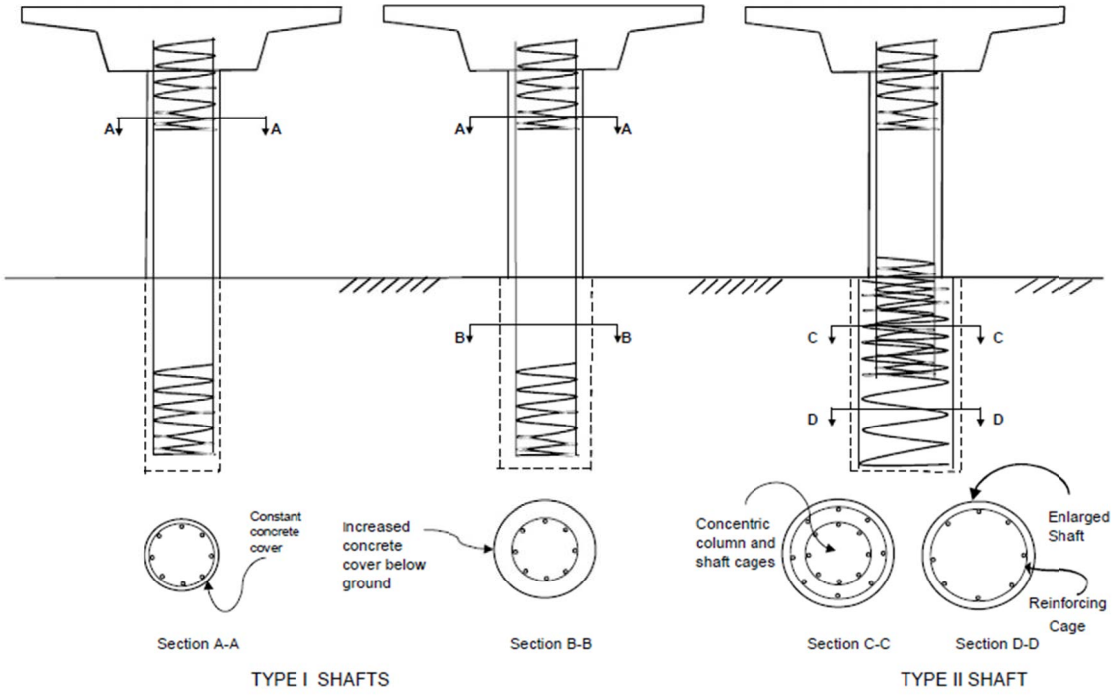

Figure 1.2: Type I and Type II shafts (Caltrans 2010)

CHAPTER 2

BOND OF REINFORCEMENT: A LITERATURE REVIEW

The stress transfer capacity between concrete and a reinforcing bar is generally referred to as the bond of reinforcement. It is an essential mechanism that engages the composite action of concrete and steel in reinforced concrete (RC) construction. The study of bond between concrete and a reinforcing bar has attracted the attention of many researchers. According to Abrams (1913), tests to study the bond between concrete and iron bars were conducted as early as 1876 (only nine years after Joseph Monier obtained his first patent on reinforced concrete) by Thaddeus Hyatt. Bond of deformed steel bars, used in modern RC construction, has been extensively studied over the last few decades, and comprehensive monographic reports have been published by the International Federation for Structural Concrete (fib 2000) and the American Concrete Institute (ACI 2003).

In this chapter, the fundamental mechanisms governing the bond behavior of deformed bas as reported in different studies are first discussed, and relevant experimental studies of the bond strength and bond-slip behavior of deformed bars are summarized. Special attention is given to studies focused on the cyclic deterioration of

the bond resistance and on the bond characteristics of large-diameter bars because they are particularly relevant to the research presented in this dissertation. Finally, the different approaches that have been proposed to model the bond-slip behavior of deformed bars are summarized.

2.1 Bond of deformed bars

In deformed bars, the term bond refers not only to the chemical adhesion between the two materials, but also to the resistance provided by friction forces and the wedging action of the bar deformations (or ribs). The bond behavior of deformed bars has been well characterized by the work of a large number of researchers, which has led to a certain agreement on its fundamental mechanisms, as documented in fib (2000) and ACI (2003). The description of the bond behavior presented here is based on the findings described in these two reports. This description is limited to deformed bars. No reference to plain bars, which correspond to old concrete construction practice, is made here.

2.1.1 Sources of bond resistance and bond-slip behavior

The bond force between a deformed bar and the surrounding concrete can be attributed to the resisting mechanisms shown in Figure 2.1: (a) chemical adhesion between the steel and the concrete, (b) friction forces acting at the interface, and (c) bearing forces of the bar ribs acting against the concrete. The nature and magnitude of the bond force depends on the relative displacement, or slip, between the concrete and the bar. Some could argue that there is no such phenomenon as bar slip based on the fact that most of the relative displacement of a bar is due to inelastic phenomena (cracking,

crushing, and shearing) that take place in the concrete surrounding the bar, not at the interface. However, in this dissertation, as in most studies, slip is idealized as the lumped sum of the relative displacement at the interface and that due to the abovementioned inelastic deformations.

At low bond stress demands, bond is mostly due to chemical adhesion, and no slip occurs between the bar and the concrete. As the chemical adhesion is overcome by increased demand, the bar starts to slip with respect to the concrete, which mobilizes friction forces at the bar surface due to its roughness and bearing forces at the ribs caused by the wedging action against the concrete. The pressure that the ribs exert onto the concrete creates micro-cracks, commonly referred to as Goto cracks (Goto 1971), starting at the tip of the ribs and propagating transversely away from the bar, as shown in Figure 2.2. The opening of these micro-cracks allows further slippage of the bar with respect to the concrete. As slip occurs, the wedging action of the ribs tends to introduce a radial expansion at the interface, which activates the passive confinement in the concrete. Radial expansion produces a hoop expansion in the concrete, which causes splitting cracks to develop at the surface in contact with the bar and propagate radially, as shown in Figure 2.2. This hoop expansion is restrained by the undamaged outer concrete ring as well as the confining reinforcement if any. For low confinement conditions, splitting cracks propagate radially through the concrete cover and the bond fails abruptly, as shown in Figure 2.3. This type of failure is referred to as splitting failure. Figure 2.4 shows a splitting failure obtained during a pull-out test by Choi et al. (2011).

With sufficient cover and confining reinforcement, the activation of the confinement introduces large radial stresses at the contact between the concrete and the

steel, which increase the bond resistance. In this case, further slip is achieved by crushing the concrete in front of the ribs. The accumulation of crushed particles in front of the ribs contributes to the expansion of the interface and increases the radial component of the bearing forces. At this stage, the increase of the hoop stresses can still result in a splitting failure if the cover and the confining reinforcement are not sufficient. When the concrete is well confined, splitting failure is precluded and higher bond strengths can be achieved, as shown in Figure 2.3. In this case, the bond fails due to loss of the interlocking action caused by crushing and shearing of the concrete keys between the ribs. Finally, the bar is pulled out from the concrete, and only a residual frictional resistance remains. This type of failure is referred to as pull-out failure. Figure 2.5 shows a bar that was pulled out from the concrete during a test presented in Chapter 3, in which crushed particles between the ribs are visible.

The bond-slip mechanism for bars with pull-out failures under cyclic loading has been theorized by Eligehausen et al. (1983). A comparable explanation for splitting-dominated failure is not available (ACI 2012). Figure 2.6 shows the damage mechanisms and bond-slip behavior under cyclic loading as presented by Eligehausen et al. (1983). In Figure 2.6a, it is assumed that the slip is reversed before horizontal shear cracks develop. After unloading (along path AF in the figure), the gap between the right side of the ribs and the adjacent concrete, caused by concrete crushing on the left side of the ribs, remains open with a width equal to the residual slip at point F. Only a small fraction of the slip is recovered by the elastic unloading of the concrete. When the slip is reversed (along path GH), some frictional resistance is built up. At H, the ribs are in contact again with the concrete (but a gap has opened on the left side of the ribs). Because of a resumed

contact with the concrete, a sharp increase in stiffness occurs (along path HI). With increasing load, the old inclined cracks close, allowing the transfer of compressive stresses across them with no noticeable reduction in stiffness (with the monotonic loading curve recovered at this point). Inclined cracks perpendicular to the old ones appear as the stress increases in this direction. At point I, a gap equal to the distance between points F and I has opened. When reversing the slip, the path IKL is similar to AFH, described previously. However, the bond resistance starts to increase again at L, when the ribs start to press broken pieces of concrete against the previous bearing face. With further movement, the transverse cracks previously closed are opened and the cracks previously opened are closed. At M, the ribs and the concrete are in full contact and the monotonic loading curve is recovered.

If the slip reversal takes place after horizontal shear cracks have initiated, a different behavior is obtained as shown in Figure 2.6b. When loading in the opposite direction (along path HI), the ribs press against the concrete in between whose resistance has been lowered by the shear cracks. Therefore, the bond resistance is lowered compared to the monotonic curve. When reversing the slip again (along path IKLMN), the resistance is further lowered compared to that at point I because of the additional shearing damage in the concrete.

When a large slip is imposed during the first cycle, almost all the concrete between the ribs can be sheared off and the behavior will be like the one shown in Figure 2.6c. When moving the bar back (along path GH), the frictional resistance is higher than that for the previous cases, in which the slip in the first cycle is smaller, because the concrete surface along the shear crack is rougher. When reloading in the opposite

direction, the peak resistance (point I) is lowered. When reversing the slip again, the frictional resistance is lowered because the surface has been smoothened (path KL).

2.1.2 Factors affecting bond resistance

Bond between reinforcement and concrete depends on many factors that involve not only the characteristics of the contact area but also aspects related to the boundary conditions. ACI (2003) classifies these factors into three groups: concrete properties, bar properties, and structural properties. Concrete properties that have an important influence on bond are the compressive and tensile strengths. Bar properties that have such influence include, but are not limited to, the bar size, the rib geometry, and the yield strength of the bar. Among the structural properties, the most relevant are the cover and spacing of bars, the transverse reinforcement, and the bar casting position. The influence of these factors is summarized in the following paragraphs. A more exhaustive list of factors and a detailed explanation of their effects are provided in ACI (2003).

Bond resistance is related to the compressive and tensile strengths of concrete because it depends on the bearing resistance of the concrete in front of the ribs, the shearing resistance of the concrete keys between the ribs, and the tensile resistance of the concrete subjected to splitting stresses (fib 2000). Experimental studies have shown a significant increase of the bond strength with the increase of the compressive strength of concrete, f_c'. A number of studies, e.g., Eligehausen et al. (1983), have suggested that the bond strength can be assumed to be proportional to $f_c'^{1/2}$. This relation has been adopted in bond-strength equations (ACI 2003) and in development-length equations specified in design codes such as ACI 318-08 (ACI 2008) and AASHTO LRFD Bridge

Design Specifications (AASHTO 2010). However, there are other studies that have indicated that the bond strength is proportional to f_c' (Rehm 1961) or $f_c'^{1/3}$ (Zsutty 1985). Based on a large number of lap-splice tests, Zuo and Darwin (2000) have concluded that for splices not confined by transverse reinforcement, the average bond strength is proportional to $f_c'^{1/4}$, and the additional bond strength attributed to the presence of transverse reinforcement is proportional to $f_c'^{3/4}$. Based on these observations, the relation between the compressive strength of concrete and the bond strength seems to depend on the level of the confinement, which could explain the different conclusions obtained in different studies. ACI (2003) states that $f_c'^{1/2}$ may not accurately represent the effect of the concrete strength on the bond strength because the effect of other parameters has been generally overlooked. In conclusion, even though the resisting mechanisms of bond are known to be related to the concrete strength, a general theory to relate the compressive and tensile strength of concrete with the bond strength is not available.

Regarding the effect of bar size on the bond resistance, it is generally accepted that smaller bars have an advantage with respect to larger bars (ACI 2003). Several researchers, e.g., Eligehausen et al. (1983), have reported a reduction of the bond strength with increasing bar size. As a result, the ACI 318-08 (ACI 2008) and AASHTO LRFD (AASHTO 2010) provisions for the development length imply that the bond strength is larger for smaller bars. However, Ichinose et al. (2004) have provided experimental evidence that the influence of the bar size on the bond strength depends on the level of confinement. In their tests, the bond strength decreased with increasing bar size for low

levels of confinement and splitting failures, but this effect was negligible for specimens with high confinement and pull-out failures.

As explained earlier, the bond resistance of deformed bars depends to a large extent on the wedging action of the ribs. Therefore, the geometry of the ribs can be regarded as an important parameter affecting bond strength. Some studies have shown that the rib pattern has a strong influence on the bond strength, but others have shown that this influence is very small (ACI 2003). Current ASTM specifications for reinforcing bars, e.g., ASTM A 706 (ASTM 2009), have requirements on the height and spacing of the ribs, which are based on the test results obtained by Clark (1946, 1950) for different deformation patterns. In Clark's studies, the bond performance was found to improve with a higher relative rib area (R_r), which is defined as the ratio of the projected rib area normal to the bar axis (A_R) to the bar perimeter times the center-to-center rib spacing ($s_{R,C}$), i.e.,

$$R_r = \frac{A_R}{\pi d_b s_{R,C}} \tag{2.1}$$

in which d_b is the bar diameter. Typical values of R_r for bars used in the US are between 0.057 and 0.087 (Choi et al. 1990). Based on the results of an experimental investigation, Darwin and Graham (1993) have concluded that under conditions of relatively low confinement, in which bond is governed by the splitting of concrete, the bond strength is independent of the rib pattern, but the bond strength increases with the relative rib area when additional confinement is provided by transverse reinforcement or larger concrete covers. In addition, they have concluded that the bond strength is a function of the

relative rib area when sufficient confinement is present, regardless of the specific rib height or rib spacing.

The bond resistance is also affected by the strain in the reinforcing bar. This influence is small as long as the steel remains in the elastic range (fib 2000). Experimental studies by Viwathanatepa et al. (1979) and Shima et al. (1987b) have shown that the bond resistance can be considerably reduced after a reinforcing bar yields in tension. In the pull-out tests carried out by Shima et al. (1987b), the bond stress-vs.-slip relations were estimated at different locations along the embedment length of a bar being pulled out from a concrete block. As shown in Figure 2.7, their results have indicated that the bond resistance dropped rapidly to 25% of the peak stress once a bar yielded regardless of the amount of bar slip.

The concrete cover and bar spacing are important parameters that affect the bond resistance and bond failure mode. With the increase of the cover and spacing, the failure mode changes from concrete splitting to bar pull-out, and the bond strength increases. Additional confinement can be provided by transverse reinforcement. The confining effect of concrete and transverse steel is accounted for in design equations on the development length for reinforcing bars. For example, the development length required in ACI 318-08 (ACI 2008) is inversely proportional to a confinement index defined as $\left(c_b + 40A_{tr} / s_{tr} n\right)/ d_b$, in which c_b is the smaller of the cover of the bar measured from its center and half of the center-to-center spacing of the bars, s_{tr} is the spacing of the transverse reinforcement, A_{tr} is the transverse reinforcement area within distance s_{tr}, and n is the number of bars being spliced or developed at the plane of splitting. According to

ACI 318-08, when $(c_b + 40A_{tr}/sn)/d_b$ is less than 2.5, a splitting failure is likely, and for values above 2.5, a pull-out failure is expected.

Finally, the position of the bar with respect to the concrete casting direction affects the bond performance. Horizontal bars located near the top face of the concrete member have lower bond strengths than horizontal bars lower in the member. The higher the location of the bar is, the more is the settlement and accumulation of bleed water underneath the bar (ACI 2003). This effect is taken into account in the ACI 318-08 provisions on the development length of bars. Similarly, bond performances are better in vertically cast bars when they are loaded upward than when they are loaded downward because of the different qualities of the concrete against which the ribs push against (fib 2000).

2.2 Experimental characterization of bond of reinforcement

2.2.1 Basic bond-slip tests

Pull-out tests of bars with short embedment lengths (typically equal to or less than five times the bar diameter) are commonly used to study the bond strength and bond stress-vs.-slip relations. The test specimens and setups used in different studies are all very similar to those shown in Figure 2.8, proposed by Rehm (1961). With this type of setups, the concrete is placed in compression when the bar is pulled, which does not represent the actual stress field in concrete in a real structure for most situations. However, this is good enough for the assessment of the local bond behavior of a bar. In these tests, the bonded area of the bar is located away from the surface on which the

compressive force is applied to reduce an arching effect that may unrealistically increase the bond strength.

Many experimental investigations have been carried out to obtain the bond strength and bond stress-vs.-slip relations of bars subjected to monotonically increasing slip using pull-out tests. However, few studies have focused on the cyclic bond-slip behavior of bars. The study by Eligehausen et al. (1983) has been the only major effort that has provided most of our understanding of the cyclic bond-slip behavior of reinforcing bars. Their experimental investigation focused on the bond deterioration of deformed bars under fully reversed cyclic loading with confinement conditions similar to those in beam-column joints. A typical specimen and the test setup are shown in Figure 2.9. A total of 125 pull-out tests were carried out to study the influence of different parameters, such as the loading history, the level of confinement, and the bar size. Most of the tests were carried out with 25-mm (1-in.)-diameter bars, and some tests were done with 32-mm (1.25-in.) bars. The bond stress-vs.-slip relations obtained from some of these tests are shown in Figure 2.10.

2.2.2 Effect of confinement on bond strength and radial dilatation

A few researchers have investigated experimentally the interaction between the tangential (bond) stress and displacement (slip) of a bar embedded in concrete with the normal (confining) stress and displacement (radial dilatation). These researchers carried out pull-out tests with short embedment lengths and employed special setups to control and/or monitor the confining stresses and radial dilatation. These studies have provided

very valuable data to understand the effect of confinement on the bond-slip behavior of bars.

Gambarova et al. (1989, 1996) carried out pull-out tests of bars in pre-splitted concrete specimens subjected to external confinement, as shown in Figure 2.11. Most of the specimens were tested with a constant splitting crack width. The bond stress-vs.-slip and confining stress-vs.-slip relations were obtained for different values of crack opening. With increasing crack width, both the bond strength and stiffness decreased, as shown in Figure 2.12. Gambarova et al. (1996) conducted a second set of tests on specimens that were subjected to a constant confining stress. The results of these tests show that the bond strength varied almost linearly with the confining stress.

Malvar (1992) carried out a set of pull-out tests of bars in pre-splitted concrete cylinders subjected to a constant confining stress. Relations between the bond stress, the slip, and the radial displacement were obtained for different levels of confining stress, as shown in Figure 2.13. Bond strength increased significantly with increasing confining stress, but this effect was less pronounced as the confinement level increased. With increasing slip, radial dilatation increased up to a value dependent on the confining stress (the higher the confinement, the lower the radial dilatation), and then decreased due to the smoothening of the interface.

Lundgren (2000) carried out monotonic pull-out and cyclic pull-pull tests of bars in concrete cylinders confined by a thin steel tube. Relations between the hoop strains in the tube, the applied load, and the slip were obtained, as shown in Figure 2.14.

2.2.3 Development length and lap splice tests

Beam specimens, like those presented in Figure 2.15, have been used to study the required development and lap splice lengths for reinforcing bars. A database of results from this type of tests is maintained by the ACI 408 Committee (ACI 2003). Based on this database, several equations have been proposed to determine the development and lap-splice strengths. The equations developed by Orangun et al. (1975, 1977) have been used to establish the design specifications in ACI 318-08 (ACI 2008). More recently, new design equations have been recommended by the ACI Committee 408 (ACI 2003) based on the work of Zuo and Darwin (2000).

2.2.4 Tests on large-diameter bars

Despite the extensive experimental work on the bond of reinforcement, data on the bond strength and bond-slip behavior of large-diameter bars is scarce. As shown in Figure 2.16, there are very few test results available in the ACI 408 Committee database (ACI 2003) for bars larger than No. 11 (36-mm). For this reason, the development length requirements in ACI 318-08 (ACI 2008) and AASHTO LRFD Bridge Design Specifications (AASHTO 2010) are largely based on experimental data obtained from No. 11 and smaller bars, and they do not allow lap-splicing of bars larger than No. 11.

Recently, pull-out and lap-splice tests were conducted on large-diameter bars (Ichinose et al. 2004, Plizzari and Mettelli 2009, and Steuck et al. 2009). Ichinose et al. (2004) carried out such tests on bars up to 52-mm (2-in.) in diameter. In their pull-out and lap-splice tests conducted on specimens with no stirrups, bond failures were governed by concrete splitting and the bond strength decreased significantly with the increase of the

bar size. Even though lap splices in specimens confined by stirrups also failed by the splitting of concrete, the effect of the bar size was not so significant. However, in the pull-out tests conducted on specimens confined by stirrups, bond failures were caused by the localized crushing of concrete in front of the bar ribs and the effect of the bar size on the bond strength was not noticeable. Plizzari and Mettelli (2009) carried out pull-out tests on 40-mm (1.6-in.) and 50-mm (2-in.) diameter bars under low confinement conditions. Bond failures in all these tests were caused by the splitting of concrete, and the resulting bond strengths were significantly lower than those obtained for smaller bars tested by the same researchers. Steuck et al. (2009) carried out pull-out tests on No.10 (32-mm), 14 (43-mm), and 18 (57-mm) bars embedded in well-confined high-strength grout. All specimens failed by the pull-out of the bars and no significant variation in the bond strengths was observed for the different bar sizes. All the tests on large-diameter bars mentioned in these studies were carried out under monotonically increasing slip. No information has been reported on the cyclic bond-slip behavior of large-diameter bars.

2.3 Modeling of bond-slip behavior

Modeling of the bond-slip behavior of reinforcement is needed to properly capture crack spacing, and the stiffness and deformation capability of RC members. It can also be used to study the anchorage of bars, and determine minimum development lengths. Cox and Herrmann (1998) have classified bond-slip models into three categories depending on their scale: rib scale, bar scale, or member scale. In *rib-scale* models, the interaction between the deformed bar and the concrete is accounted for by explicitly modeling in a detailed manner the concrete and the steel bar including the ribs. In *bar-*

scale models, the concrete-steel interaction is represented by a law that relates the stresses and relative displacements at their interface. In *member-scale* models, the effect of bond-slip is accounted for with rotational springs or special structural element formulations. The literature review presented in this section is organized based on this classification.

2.3.1 *Rib-scale* models

Several researchers, e.g. Reinhardt et al. (1984a), Maekawa et al. (2003), Daoud et al. (2012), have used *rib-scale* finite element models to study the interaction between the deformed bars. In these models, both the concrete and the bar including the ribs were represented with continuum elements, e.g., see Figure 2.17. The explicit modeling of the ribs is what ultimately provides the interaction between the reinforcement and concrete. These models require a detailed definition of the bar geometry and the use of appropriate constitutive laws for steel and concrete. Some studies have included modeling features like the contact conditions (Reinhardt et al. 1984a, Maekawa et al. 2003), the steel-concrete transition zone (Maekawa et al. 2003), or the internal structure of concrete consisting of cement matrix and aggregate (Daoud et al. 2012).

Detailed models like these can be used to investigate the basic characteristics of bond of reinforcement, but are not deemed suitable for the analysis of RC structures because they are computationally very intensive. Furthermore, they may not necessarily yield more reliable results because of the uncertainties related to the bar surface deformation, friction, and adhesion, and the various simplifying assumptions used in the

constitutive models for concrete, which may not allow a precise simulation of the localized failure mechanism.

2.3.2 *Bar-scale* models

Bar-scale models idealize the interaction between the reinforcement and the concrete, as shown in Figure 2.18. The forces and deformations at the steel-concrete interface are lumped into an average stress and relative displacement. This modeling strategy is appropriate for studying the effect of bond-slip on the cracking pattern in structural members or the required development and splicing lengths for reinforcing bars. The idealized interface has no ribs, and the relative displacements are assumed to occur between the bar surface and a layer of concrete not subjected to any of the inelastic phenomena induced by the local action of the ribs: crushing, shearing, and transverse cracking. The term bar slip is usually considered as the relative tangential displacement defined under these terms. The forces acting between the periodic cell between two consecutive ribs (adhesion and friction forces at the steel surface, and bearing forces at the rib) are homogenized as a tangential (bond) stress and a normal stress at this idealized interface. Coupling between the tangential and normal components of stress and displacements is expected due to the wedging action of the ribs.

When studying the interaction between the reinforcement and the concrete, most of the interest is focused on the bond stress and the slip of a bar. For this reason, a significant number of models have been proposed to relate the bond stress and the slip, overlooking the interaction between the normal and tangential directions. The bond stress-vs.-slip relations provided by these models are only valid for specific levels of

confinement and failure modes. More advanced models have been proposed to account for the coupling between the tangential and normal stresses and displacements by incorporating shear dilatation of the interface. These models have the capability of predicting different failure modes and providing the appropriate bond stress-vs.-slip relations for different levels of confinement. Examples of these two types of models are described below.

Bond stress-vs.-slip models

Most of the models proposed for the bond stress-vs.-slip relations are limited to relatively well-confined conditions with the pullout failure of the bar. Typically, they are phenomenological models, in which the bond stress is defined as a nonlinear function of the monotonically increasing slip. The resulting function is scaled to the bond strength, which is related to the compressive strength of concrete empirically. The first model of this type was proposed by Rehm (1961), while the most widely used is that proposed by Eligehausen et al. (1983), which is shown in Figure 2.19, based on extensive experimental data obtained from No. 8 bars. Some models of this type have factors that modify the bond stress to account for the axial strain in the reinforcement (Shima et al. 1989a, Fernandez Ruiz et al. 2007, Lowes et al. 2004), or to account for the confining pressure (Lowes et al. 2004).

Some of these models can also predict the bond stress-slip relation under severe cyclic slip demands. In Eligehausen et al.'s model, the monotonic bond stress-slip relation is reduced at each slip reversal using a damage parameter that depends on the energy dissipated by bond-slip. In addition, unloading and reloading rules are defined. Other models have been proposed based on similar concepts but with different

improvements. The main variation in these models is the way the monotonic envelope is scaled to account for cyclic bond deterioration. The scaling factor proposed by Lowes et al. (2004) depends on the maximum slip and the number of cycles. Pochanart and Harmon (1989) and Yankelevski et al. (1992) have proposed to scale the bearing and friction contributions to the total bond resistance independently based on the maximum slip and the number of load cycles.

The local bond stress-vs.-slip relation can be viewed as a constitutive model for the bond behavior of reinforcing bars. Combining such a model with material models for steel and concrete, and applying the necessary equilibrium and kinematic conditions, one can derive a governing differential equation for the bond-slip behavior of a bar embedded in concrete. Closed-form solutions have been found for simple bond stress-vs.-slip relations (Raynor 2000), but, in general, numerical methods are required to solve such problems. Ciampi et al. (1982) have solved the differential equation based on the bond-slip law proposed by Eligehausen et al. (1983) using a finite difference scheme to study the behavior of an anchored bar that is being pulled and pushed at one of its ends (see Figure 2.20). Filippou et al. (1983) have proposed a weighted residual method to study the same problem using different shape functions to approximate the displacement and stress fields in the bar. Monti et al. (1997) have found it to be more advantageous to approximate the bond and bar stress fields, and have proposed a flexibility-based finite element formulation to solve this problem. Other researchers have opted to incorporate local bond-slip laws in interface elements to connect steel and concrete elements in general-purpose finite element programs. Lowes (2004) has formulated a four-node zero-thickness bond-slip element to be used for two-dimensional finite element modeling of

reinforced concrete structures (see Figure 2.21). The model is defined by a normalized bond stress-vs.-slip relation and a relationship between the maximum bond strength and the concrete confining pressure, the concrete damage state, and the steel strain state in the vicinity of the concrete-steel interface. A nonlocal modeling technique has been used to relate the bond strength to the steel strain and concrete damage attained in the surrounding elements. Santos and Henriques (2012) have implemented the bond stress-vs.-slip law proposed in Model Code 2010 (fib 2012) in an orthotropic four-node plane stress element to model the steel-concrete interface using the commercial finite element program DIANA.

Dilatant interface formulations

In these models, the wedging action between the ribs of a bar and the concrete can be captured in terms of the shear dilatation of the interface. Dilatant interface formulations have been proposed to model the bond-slip behavior of deformed bars by Herrmann and Cox (1994), Cox and Herrmann (1998, 1999), Lundgren and Magnusson (2001), and Serpieri and Alfano (2011).

Herrmann and Cox (1994) and Cox and Herrmann (1998) have used an elasto-plastic formulation with a non-associative flow rule to control shear dilatation. The evolution of the yield surface and the flow rule is shown in Figure 2.22. It is based on the experimental data obtained by Malvar (1992). The model requires the calibration of a few physical properties and shows acceptable accuracy as compared to experimental results corresponding to different levels of confinement obtained from different studies. Tests with monotonically increasing slip and pull-out failures have been used to validate the

model (Cox and Herrmann 1999). In Herrmann and Cox (1994), an extension of this model was proposed for cyclic loading using ad-hoc reloading rules

A similar plasticity model has been proposed by Lundgren and Magnusson (2001) for monotonic loading. In this model, a Mohr-Coulomb yield criterion with a non-associated flow rule is used to represent the frictional behavior at the interface, and a second yield surface with associated plasticity is used as a cap for pull-out failure, as shown in Figure 2.23. Lundgren (2005) has extended the model to account for cyclic behavior using ad-hoc reloading rules. The model has been successful in reproducing experimental results from a limited number of monotonic and cyclic tests.

The formulation proposed by Serperi and Alfano (2011) represents the periodic geometry of the steel-concrete interface by three planes with different inclinations, as shown in Figure 2.24. The interaction within each of these surfaces is governed by a damage-friction interface formulation modeling adhesion and friction. The dilatation and wedging mechanism are obtained as a result of the prescribed surface geometry. The model is capable of qualitatively reproducing the bond stress-vs.-slip behaviors under monotonic and cyclic loading. However, the concrete crushing mechanism that dominates the pull-out failure of a bar is not simulated. The model has shown reasonably good agreement with results from a monotonic pull-out test. No attempt has been made to validate the model with experimental data from cyclic tests.

2.3.3 *Member-scale* models

Several researchers have proposed special beam-column elements or used simple macro-models that inherently account for the bond-slip behavior without the explicit

definition of steel-concrete interfaces. This type of models is useful in the analysis of large structures.

Monti and Spacone (2000) have proposed a force-based fiber-section beam-column element that accounts for slip between the longitudinal reinforcement and the concrete. In this element, a bar model with bond-slip proposed by Monti et al. (1997) is introduced into the force-based fiber-section element developed by Spacone et al. (1996). The beam section is assumed to remain plane, but the steel fiber strains are computed as the sum of two contributions: the bar strain and anchorage slip. A similar model has been proposed by Ayoub (2006) based on a two-field mixed formulation with independent approximations of forces and displacements.

Simple macro models have been proposed to simulate the end rotation of RC beams and columns due to the slip of the reinforcement anchored in connecting members. In these models, bars are assumed to be well anchored and bar slip is entirely due to strain penetration in the anchorage zone. Sritharan et al. (2000) have proposed the use of a set of springs in finite element analysis to represent the opening of a joint due to bar slip. Tension springs are used to represent bar elongation due to strain penetration in the anchorage zone and compression springs are used to represent the contact between concrete surfaces. Based on experimental data, Zhao and Sritharan (2007) have proposed a law to relate the bar stress and bar slip at the end of the anchorage in a footing-column or beam-column connection. This law has been used as a constitutive relation for the steel fibers in a zero-length fiber-section element to simulate the end rotation of an RC column represented by a fiber-section beam-column element, as shown in Figure 2.25. Berry and

Eberhard (2007) have followed the same modeling strategy, but they have obtained the bar stress-vs.-slip law analytically based on a simple bond stress-vs.-slip relation.

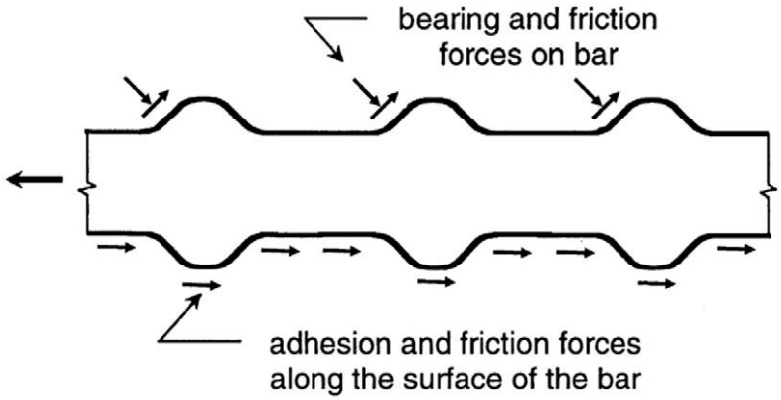

Figure 2.1: Sources of bond resistance (ACI 2003)

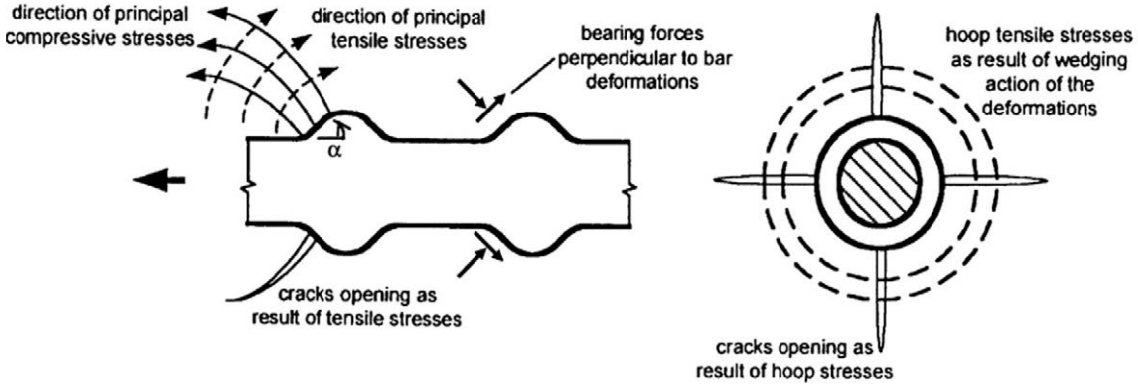

Figure 2.2: Cracking pattern due to bond-slip (ACI 2003)

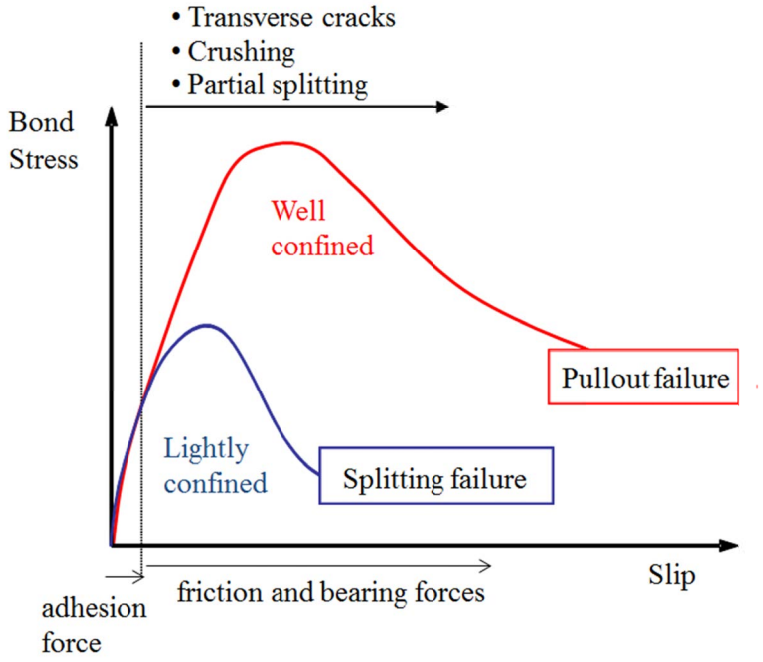

Figure 2.3: Bond stress vs. slip for different confinement conditions

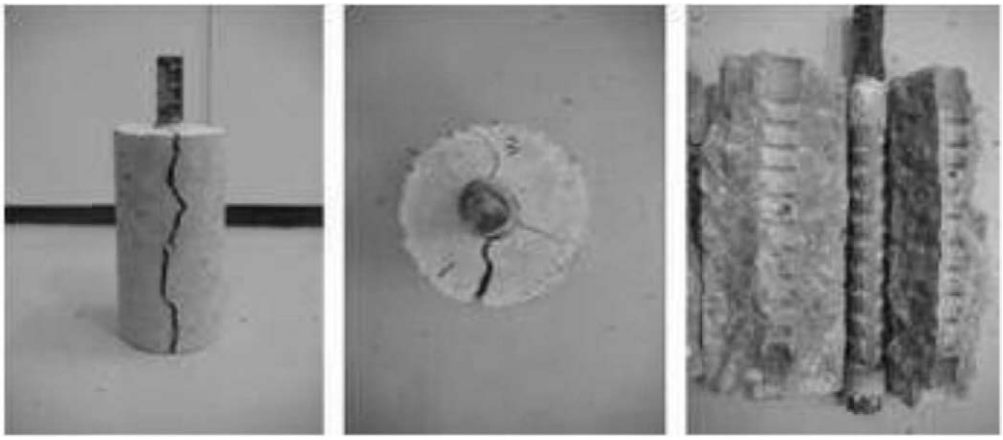

Figure 2.4: Bond failure by splitting of concrete (Choi et al. 2011)

Figure 2.5: Crushing and shearing of concrete between ribs in a bar pull-out failure

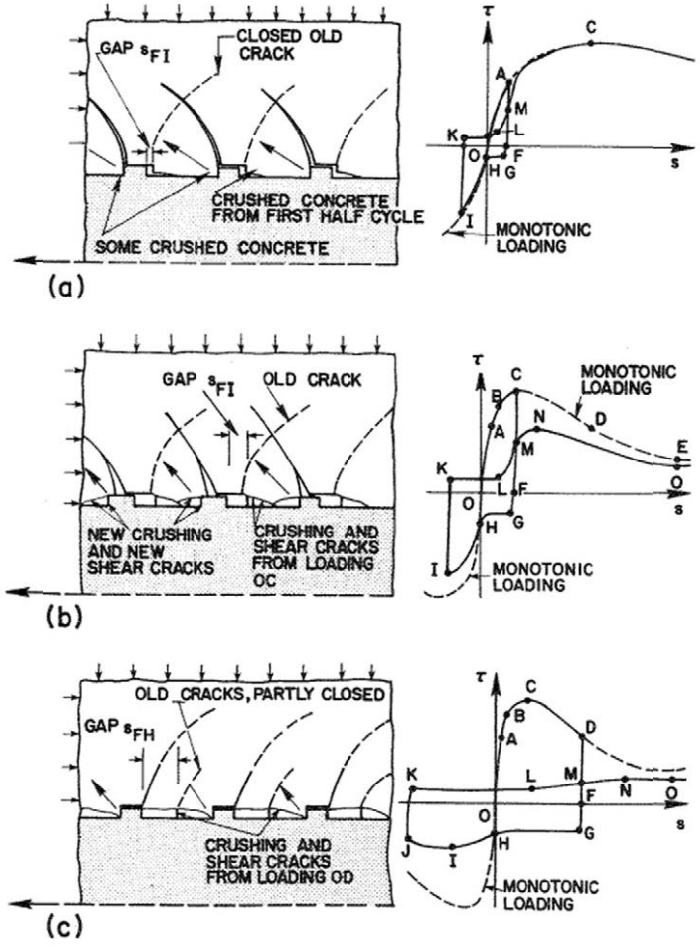

Figure 2.6: Cyclic bond-slip behavior in pull-out failures (Eligehausen et al. 1983)

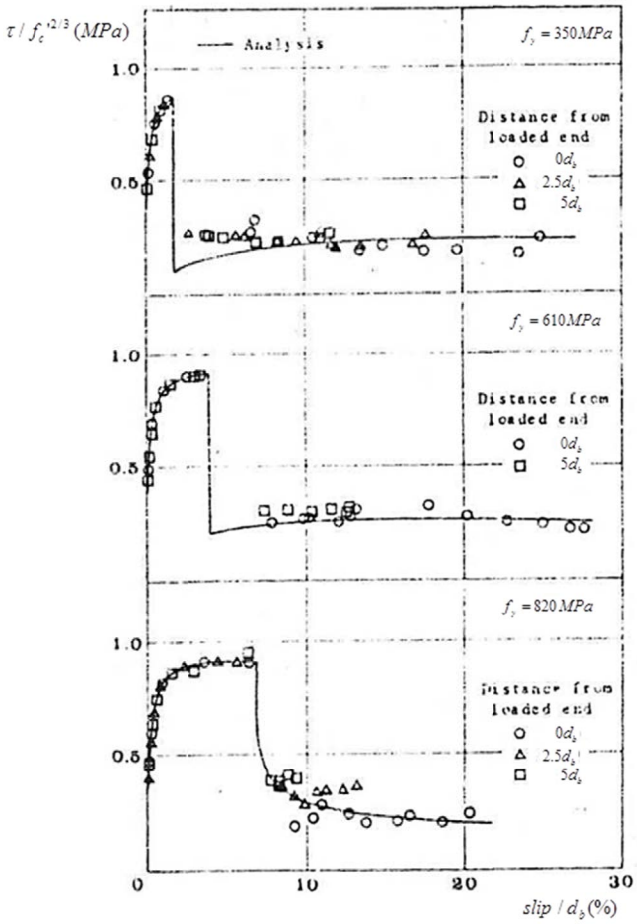

Figure 2.7: Bond-slip relations obtained by Shima et al. (1987b) for bars yielding in tension

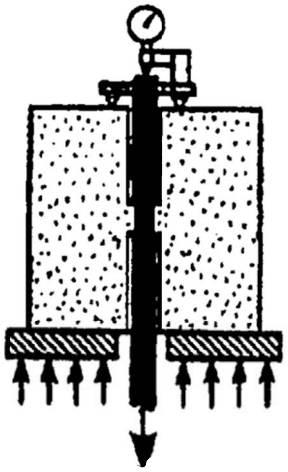

Figure 2.8: Bond-slip test specimen and setup used by Rehm (1961)

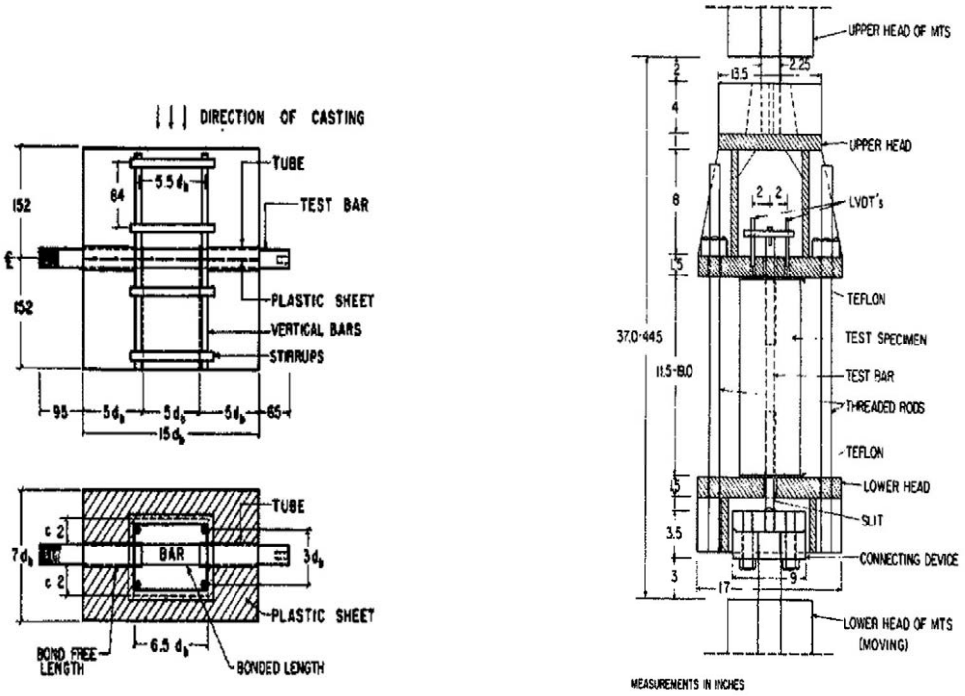

(a) Specimen (b) Setup

Figure 2.9: Bond-slip test specimen and setup used by Eligehausen et al. (1983)

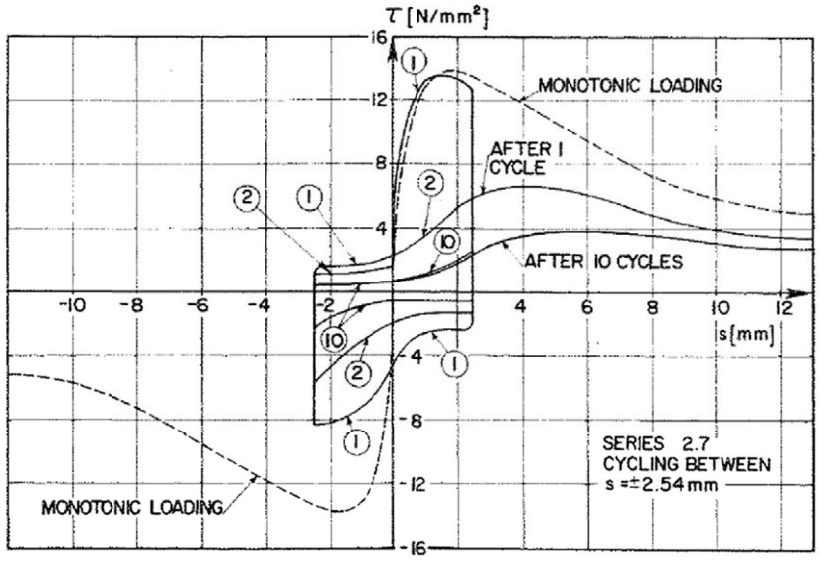

Figure 2.10: Cyclic bond stress-vs.-slip relations obtained by Eligehausen et al. (1983)

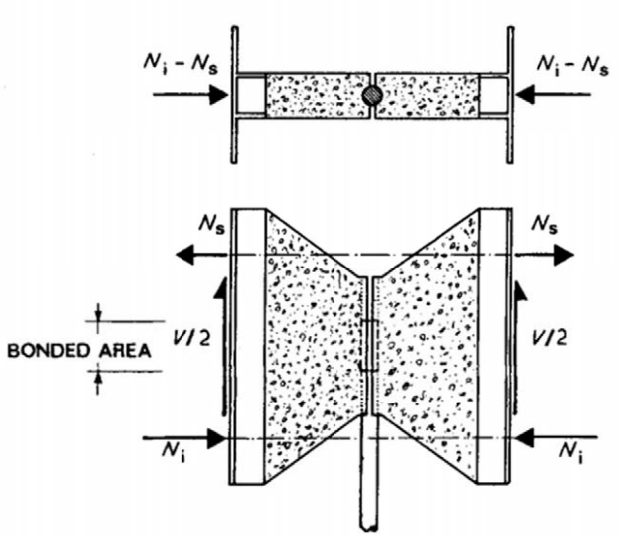

Figure 2.11: Bond-slip test specimen with different crack openings used by Gambarova et al. (1989)

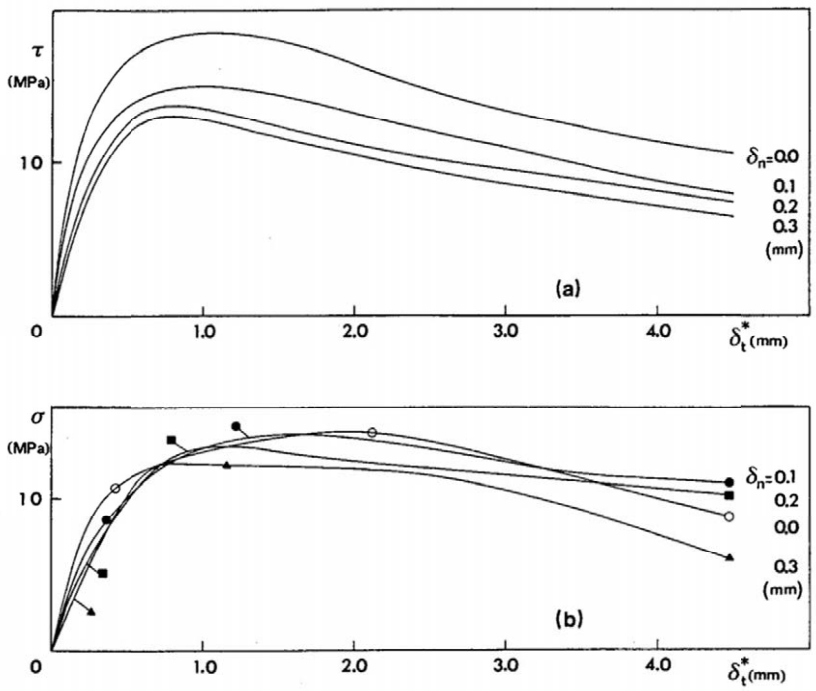

Figure 2.12: Bond stress-vs.-slip and confining stress-vs.-slip relations for different crack openings obtained by Gambarova et al. (1989)

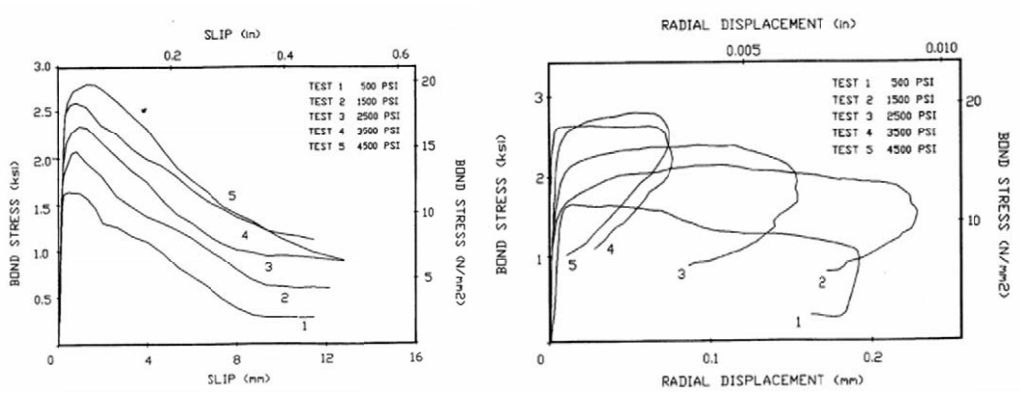

Figure 2.13: Bond stress-vs.-slip and bond stress-vs.-radial displacement relations obtained by Malvar (1992)

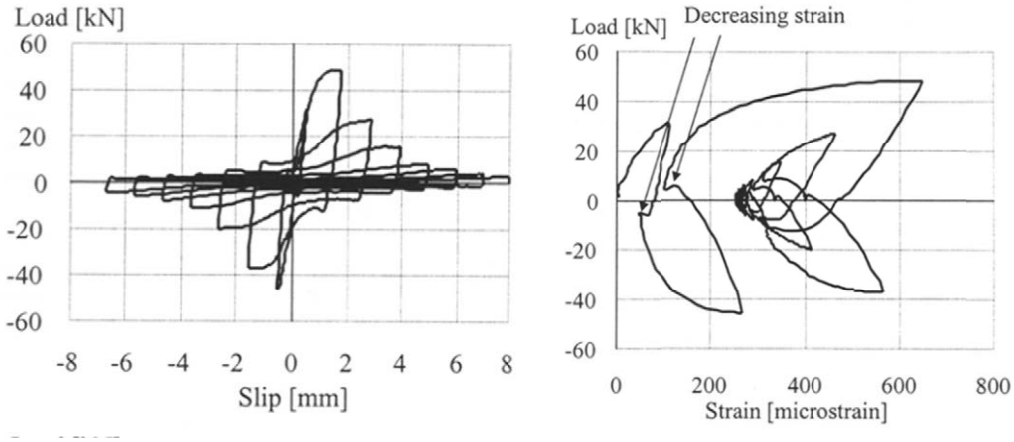

Figure 2.14: Load-vs.-slip and load-vs.- bar strain relations obtained by Lundgren (2000)

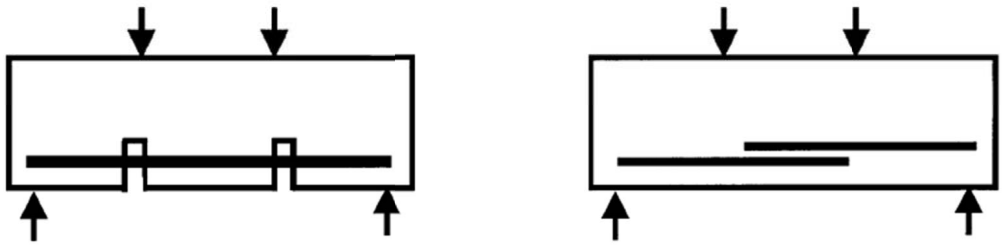

(a) Development tests (b) Lap splice tests

Figure 2.15: Sketch of typical development and lap splice tests (ACI 2003)

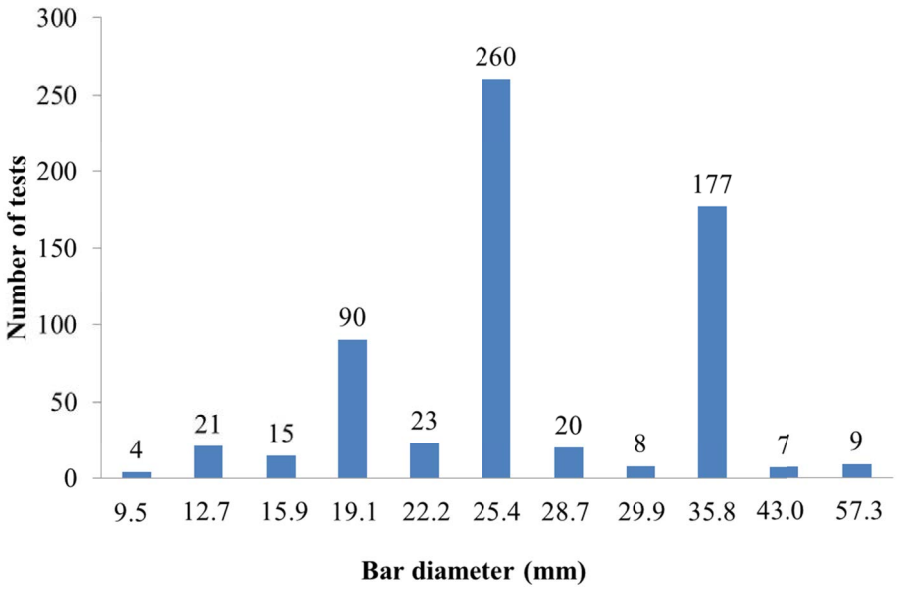

Figure 2.16: Experimental database from ACI 408 Committee

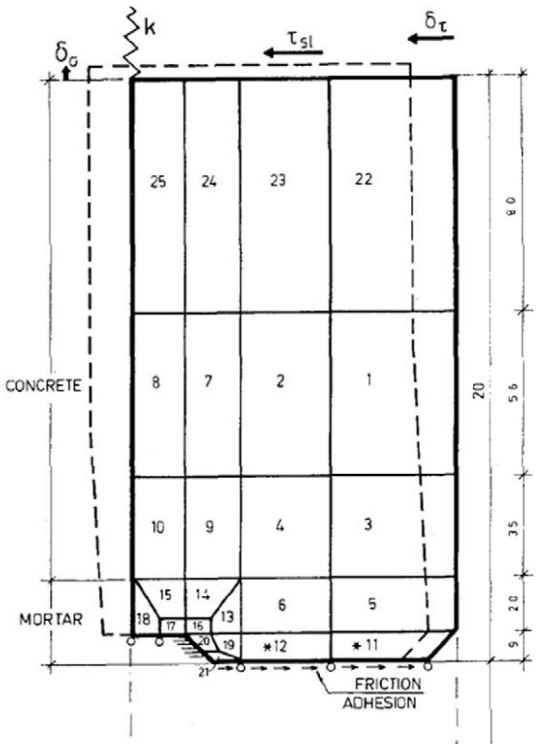

Figure 2.17: Finite element model used by Reinhardt et al. (1984a) to study the bond-slip behavior of bars

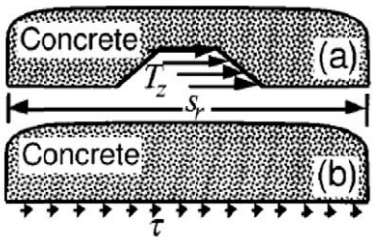

(a) actual vs. idealized force transfer

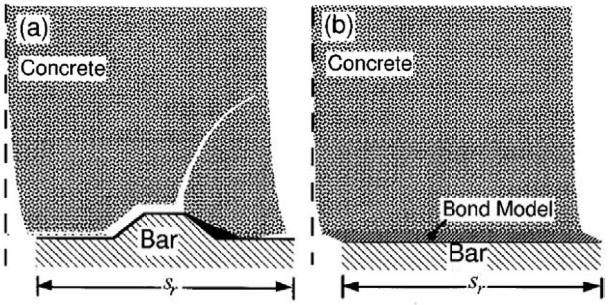

(b) actual vs. idealized deformations

Figure 2.18: Actual vs. idealized concrete-steel interaction (Cox and Herrmann 1998)

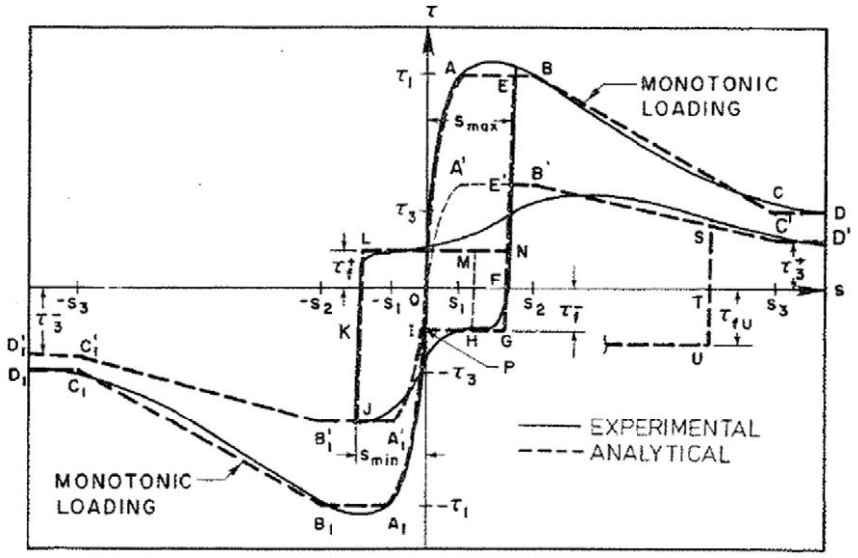

Figure 2.19: Analytical bond stress-vs.-slip model proposed by Eligehausen et al. (1983)

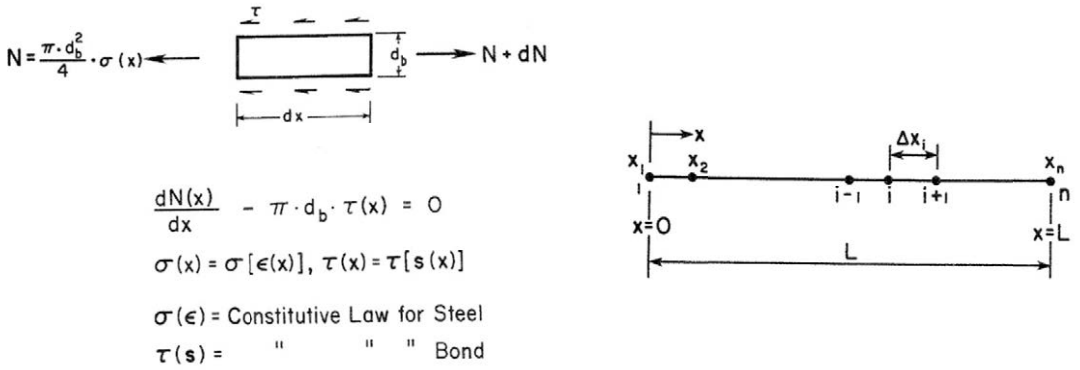

Figure 2.20: Differential equation of bond-slip and finite difference discretization of a bar (Ciampi et al. 1982)

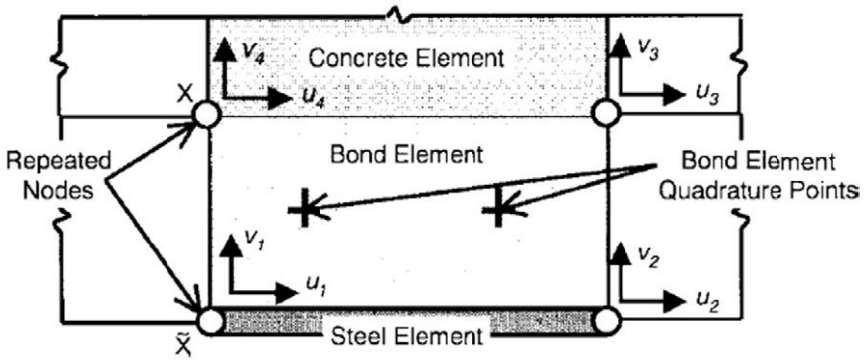

Figure 2.21: Bond-slip element by Lowes et al. (2004)

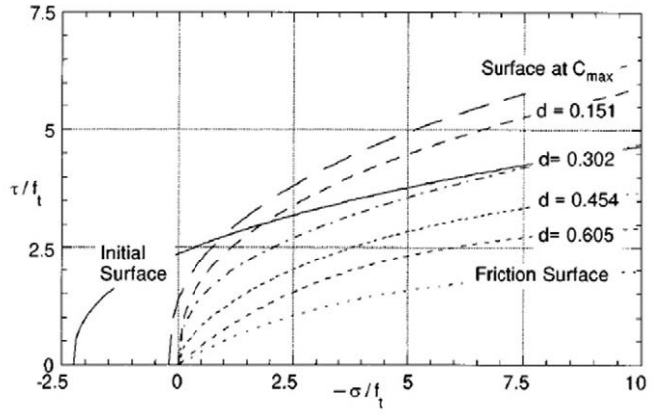

Figure 2.22: Yield surface evolution for the bond-slip model of Cox and Herrmann (1998)

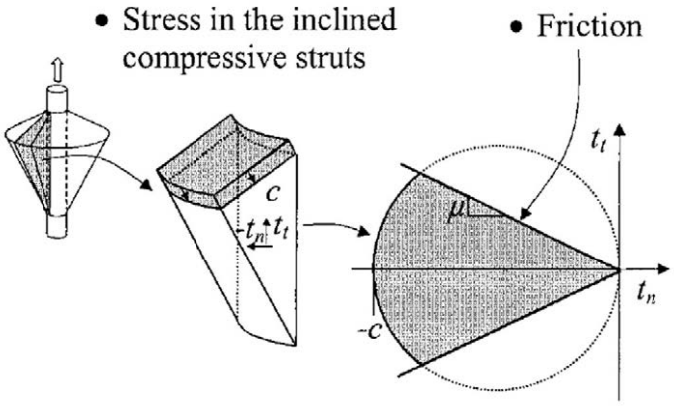

Figure 2.23: Yield surfaces for the bond-slip model of Lundgren and Magnusson (2001)

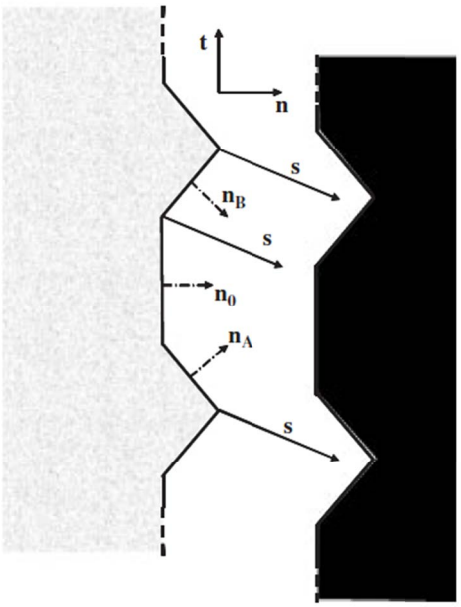

Figure 2.24: Surface geometry assumed in the interface element of Serpieri and Alfano (2011)

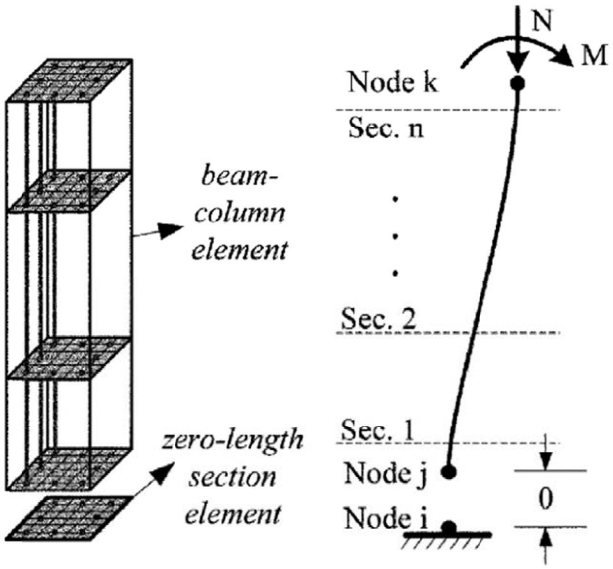

Figure 2.25: Zero-length element proposed by Zhao and Sritharan (2007)

CHAPTER 3

EXPERIMENTAL STUDY ON THE BOND-SLIP BEHAVIOR OF LARGE-DIAMETER BARS IN WELL-CONFINED CONCRETE

This chapter presents an experimental study on the bond strength and cyclic bond deterioration of large-diameter reinforcing bars embedded in well-confined concrete. For large RC components, such as large bridge columns and piles, the use of reinforcing bars with diameters greater than 25-mm (No. 8) is common. However data on the bond strength and bond-slip behavior of large-diameter bars is scarce. Because of the lack of experimental data, the development length requirements in ACI 318-08 (ACI 2008) and AASHTO LRFD Bridge Design Specifications (AASHTO 2010) are largely based on experimental data obtained from No. 11 (36-mm) and smaller bars, and do not allow lap-splicing of bars larger than No. 11.

Recently, pull-out and lap-splice tests were conducted on large-diameter bars by Ichinose et al. (2004), Plizzari and Mettelli (2009), and Steuck et al. (2009), as discussed in Chapter 2. However, all these tests were carried out under monotonically increasing

slip. No data has been reported on the cyclic bond-slip behavior of large-diameter bars. It has not been certain that the data obtained for the cyclic bond-slip behavior of No. 8 bars by Eligehausen et al. (1983) is applicable to larger bars. As mentioned in Chapter 2, studies have shown that the bar size may have an effect on the bond characteristics (ACI 2003).

This chapter presents the monotonic pull-out and cyclic pull-pull tests that were conducted on No. 11, 14, and 18 (36, 43, and 57-mm) bars to obtain the bond strength and cyclic bond stress-slip relation of these bars. The confinement level considered in the tests is representative of that for vertical reinforcing bars extending from a bridge column into an enlarged pile shaft, whose diameter is normally 610 mm (2 ft) larger than that of the column according to the design specifications of the California Department of Transportation (Caltrans). Similar confinement conditions can be found for reinforcing bars anchored in other type of foundations. Based on this study and on studies carried out by others, the effect of the bar diameter, concrete strength, pull direction (for a vertically cast bar), and loading history on the bond strength are investigated.

3.1 Test program, specimen design, and test setup

Four series of pull-out tests were conducted on large-diameter reinforcing bars embedded in well-confined concrete. Three of them were conducted to study the respective bond-slip behavior of No. 11, 14, and 18 bars under different loading histories, and the fourth was conducted to study the influence of the compressive strength of concrete on the bond strength. A total of 22 specimens were tested, of which 8 were subjected to a monotonically increasing slip and 14 to cyclic loading. The specimen

properties, type of loading, and the bond strengths obtained are summarized in Table 3.1. These tests were conducted to identify the fundamental bond stress-vs.-slip relation of a bar. In all the tests, bond failure was governed by the pull-out of the bars from the concrete.

The design and test setup for a typical specimen are shown in Figure 3.1. Each specimen consisted of a reinforcing bar embedded in a 914-mm (3-ft) diameter concrete cylinder that had a height of 15 times the nominal bar diameter, d_b. The bar was bonded only in the mid-height region of the concrete cylinder over a length of $5d_b$, and PVC tubes were used to create unbonded regions of $5d_b$ in length on each end of the bonded zone to minimize any local disturbance to the bond stress due to the loading setup. This short embedment length was intended to provide a fairly uniform bond stress distribution and to prevent the yielding of the steel so that the fundamental bond stress-vs.-slip relation could be obtained.

Bars with a specified yield strength of 414 MPa (60 ksi) were used. The No. 11, 14, and 18 bars had relative rib areas (ratio of the projected rib area normal to the bar axis to the bar surface area between the ribs) ranging from 0.068 to 0.095. The geometric properties of the bars are summarized in Table 3.2. Each end of a bar had a T-headed anchor, which provided a reaction for the application of the pulling force during a test.

The diameter of the cylinder and the quantity of the spiral reinforcement were selected to mimic the concrete cover and confinement level for the vertical reinforcing bars extending from a bridge column into an enlarged pile shaft designed according to the Caltrans Bridge Design Specifications (Caltrans 2008) and the AASHTO LRFD Bridge

Design Specifications (AASHTO 2010). The concrete cylinder was confined with No. 4 (13-mm) spiral reinforcement with a pitch of 61 mm (2.4 in.) on center and an outer diameter of 813 mm (32 in.). This resulted in a confinement volumetric ratio of 1%.

Two concrete mixes with different compressive strengths were used. Series 1 through 3 tests had a concrete with a targeted compressive strength of 34.5MPa (5 ksi), maximum aggregate size of 9.5 mm (3/8 in.), water-to-cement ratio of 0.45, and specified slump of 178 mm (7 in.). Series 4 had a concrete with a targeted compressive strength of 55 MPa (8 ksi), maximum aggregate size of 12.7 mm (0.5 in.), water-to-cement ratio of 0.32, and slump of 203 mm (8 in.). The aggregate size and high slump used in these two mixes represent what is typically used for CIDH (Cast-In-Drilled-Hole) piles. All specimens in each series were fabricated with the construction sequence shown in Figure 3.2. They were cast together in an upright position. The test numbering in Table 3.1 reflects the order in which the specimens were tested. The tests started on the day when the concrete strength was close to the targeted value. Setting up a test, testing, and dismantling took one to two days per specimen. The compressive and tensile splitting strengths of the concrete on the first and last days of testing for each test series are shown in Table 3.1.

The test setup is shown in Figure 3.1b. This setup was designed to allow the bar to be pulled upward or downward using center-hole hydraulic jacks that were positioned one at each end of the bar. The bar was pulled out from the concrete cylinder when one of the hydraulic jacks pushed against the adjacent anchor head while the other jack was de-pressurized to allow the opposite end of the bar to move freely. To reverse the pull direction, the jack initially pushing against the anchor head was de-pressurized before the

other jack started to push against the anchor head at the opposite end. This was a self-reacting system; thus, the concrete was subjected to compression when the bar was being pulled out.

3.2 Instrumentation and loading protocol

A load cell was placed between a hydraulic jack and the adjacent bearing head to measure the pull-out force during the test. Two strain gages were attached on two opposite sides of the bar right outside the bonded region at each end to measure the bar deformation, as shown in Figure 3.1a. In Series 3, four strain gages were also attached on two opposite sides of the spiral at two elevations to monitor the spiral strain that could be introduced by the dilatation of the concrete during bar slip. Bar slip was measured with two linear potentiometers mounted at each end on the opposite sides of the bar, as shown in Figure 3.1b. Each pair of potentiometers measured the displacement of the attachment point on the bar with respect to the bearing head. A picture of one of the specimens and the test setup is shown in Figure 3.3.

For all but one specimens that were tested with a monotonically increasing slip, the bar was pulled upward. Several load histories were used for the cyclic tests, with variables including the increment size of the slip amplitude in each loading cycle, the number of cycles per amplitude, and the type of cyclic reversals. Two types of cyclic reversals were considered: (a) full cycles with the same slip amplitudes in both directions for each cycle; and (b) half cycles with slips mainly in one direction and slightly passing the origin in the other. In most of the tests, only a single cycle was applied for each slip amplitude. However, in two tests, each amplitude had two cycles. The type of loading

protocol used for each specimen is given in Table 3.1.

3.3 Monotonic test results

The local bond stress (τ) - slip (s) relations have been obtained as the average bond stress vs. the average of the slips at the two ends of the bonded zone. The average bond stress was calculated by dividing the pull-out force, *F*, by the nominal contact area between the bar and the concrete as shown in the following equation.

$$\tau = \frac{F}{\pi d_b l_e} \tag{3.1}$$

where l_e is the bonded length of the bar.

The slip at each end was calculated as the average of the slips measured by the pair of linear potentiometers. At the loaded end, the bar elongation between the attachment point of the linear potentiometers and the end of the bonded zone was subtracted from the potentiometer reading to get the actual slip. The bar elongation was calculated from strain gage readings. Figure 3.4 shows the pull force vs. the slips at the loaded and unloaded ends, and the average slip for one of the monotonic tests. Based on the small differences observed in slip at the two ends, the average relations obtained from the tests can be assumed a good approximation of the local bond stress-slip relations.

The bond stress-slip relations obtained from monotonic pull-out tests in Series 1 to 3, which had concrete strengths around 34.5 MPa (5 ksi), are plotted in Figure 3.5. For comparison, the curve obtained by Eligehausen et al. (1983) for a No. 8 (25-mm) bar and 30-MPa (4.35-ksi) concrete is also included in Figure 3.5. All the bond stress-slip curves show similar patterns. The slip at the peak strength was around 1.8 mm (0.07 in.) for the

No. 8 bar, and around 3.0 mm (0.12 in.) for the No. 11, 14, and 18 bars. With increasing slip, the bond resistance dropped and tended to stabilize at a residual value that was approximately 20-30% of the peak resistance. Eligehausen et al. (1983) pointed out that a practically constant residual resistance was achieved when the value of the slip was approximately equal to the clear rib spacing of the bar, s_R. This can be explained by the total damage of the concrete between the ribs. Beyond this point, the resistance to slip was provided solely by friction. Figure 3.5 and the s_R values given in Table 3.2 confirm this observation for the large-diameter bars. However, the transition between the peak and the residual resistance seems to be more gradual for large-diameter bars as compared to the No. 8 bars tested by Eligehausen et al. (1983).

The bond strengths, τ_u, obtained from the tests are summarized in Table 3.1. The results from Series 1 to 3 show that τ_u slightly increases with the bar diameter from 15.2 MPa (2.2 ksi) for No. 11 bars to an average of 17.6 MPa (2.55 ksi) for No. 18 bars. The tests conducted by Eligehausen et al. (1983) for No. 8 bars obtained an average bond strength of 13.8 MPa (2.0 ksi), but a direct comparison cannot be established because a concrete with a lower compressive strength and a lower degree of confinement was used by them. As Figure 3.5 shows, the bond strength obtained for a No. 11 bar that was pulled downward (Test 2 from Series 1) was 20% lower than that for a bar pulled upward (Test 1 from Series 1). The initial stiffness was also reduced and the peak strength was reached at a slip of 4.6 mm (0.18 in.).

Results from Series 4 tests on No. 14 bars with 55-MPa (8-ksi) concrete have shown a 45% increase of the average bond strength as compared to that obtained from

Series 2, which had the same bar size but 34.5-MPa (5-ksi) concrete. Owing to the high bond strengths developed in Series 4, the bars subjected to a monotonically increasing load (Tests 1 and 2) yielded at the pulled end. As shown in Figure 3.6, the difference in slip at the loaded and unloaded ends was very large once the bar yielded at the loaded end because of the plastic penetration of the bar strain. The slip and bond stress distribution cannot be considered uniform and the bond stress-slip curves cannot be obtained from the test data. In addition, studies have shown that bond resistance could be reduced in regions where a bar yielded. Hence, the bond strength for a bar without yielding would be higher than the average strength calculated from the results of this series of tests. However, this influence does not appear to be significant because the ratio of the average bond strength obtained from these two bars to that from the cyclic tests (Test 3 and 4 of Series 4), in which the bars did not yield, is comparable to the corresponding strength ratios obtained for the other series.

The strain gages placed in the confining spirals registered small tensile strains (with the maximum being $2 \cdot 10^{-5}$), as shown in Figure 3.7. The tension in the spirals indicates that the concrete expanded slightly in the lateral direction as the bar was being pulled out. This can be explained in part by the dilatation caused by the wedging action of the bar ribs when the bar slipped. Another cause is the Poisson effect induced by the vertical compressive force exerted on the concrete cylinder as the bar was pulled. Figure 3.7 also shows the estimated strain due to the Poisson effect. The small strain readings indicate that the dilatation effect of bar slip on the transverse reinforcement is negligible. This is expected because a very good confinement is already provided by the large concrete cover.

3.4 Cyclic test results

The bond stress-slip relations for the cyclic tests are presented and compared to the monotonic test results in Figure 3.8 through Figure 3.14. The hysteretic response in all the tests shows a consistent behavior. Upon the reversal of the slip direction, a small resistance immediately developed in the other direction. This resistance started to increase when the slip approached the previously attained maximum slip. After this point, the resistance followed a curve similar in shape to the monotonic bond stress-slip curve. However, the stress level of this new curve is lower than that indicated by the original monotonic bond stress-slip curve due to bond deterioration induced by cyclic slip reversals. In addition, the absolute value of the slip at which the peak stress developed increased as the cumulative slip increased.

The maximum bond resistance obtained from a cyclic test is between 75 and 95% of that obtained from a monotonic load test, as shown in Table 3.1. The residual bond resistance diminishes to almost zero after severe cyclic slip reversals, as shown in Figure 3.8 through Figure 3.14. Moreover, the results presented in Figure 3.9 and Figure 3.10 indicate that full cycles induced a more severe deterioration of the bond resistance than half cycles given the same slip amplitude in one direction. Likewise, Figure 3.11 and Figure 3.14 show that a second cycle between the same levels of slip produced an additional reduction of the bond stress. Overall, the observed hysteretic bond stress-slip relation for large diameter bars is similar to that obtained by Eligehausen et al. (1983) for No. 8 bars.

Figure 3.15 shows the tensile strain registered in the confining spirals during one

of the cyclic tests, and the estimated contribution of the Poisson effect to this strain. The magnitude of strain is small and is comparable to that obtained for monotonic loading.

3.5 Discussion on factors affecting bond strength

The tests presented here have provided useful information on the influence of the compressive strength of concrete, bar size, pull direction (for a vertically cast bar), and slip history on the bond strength. A review of previous findings related to these effects has been presented in Chapter 2. The observations made here and by others are compared, and these effects are further analyzed and quantified in this section with additional data available in the literature.

3.5.1 Effect of compressive strength of concrete

The tests presented in this chapter have shown that the compressive strength of concrete, f_c' , has an important effect on the bond strength. These tests have shown that the bond strength was increased by about 45% when 55-MPa (8-ksi) concrete was used instead of 34.5-MPa (5-ksi) concrete. This implies that the bond strength is more or less proportional to $f_c'^{3/4}$, although it is possible that this effect could be slightly under-estimated here because, as mentioned in Section 3.3, the bond strength calculated for the 8-ksi (55-MPa) concrete could be influenced by the yielding of the bars. In any case, this effect is stronger than what has been reported by Eligehausen et al. (1983) and what is assumed in codes, which suggests that bond strength is proportional to $f_c'^{1/2}$.

As mentioned in Chapter 2, the relation between the compressive strength of concrete and the bond strength can be influenced by the level of the confinement, based on the analysis done by Zuo and Darwin (2000) of splice test results. The level of confinement in the tests presented here is stronger than that in Eligehausen et al. (1983). Therefore, it can be expected that the influence of the compressive strength of concrete on the bond strength would be higher here. This difference can be explained by the nature of the failure mechanisms obtained for different levels of confinement. For low levels of confinement, bond failure is due to the splitting of the concrete surrounding the bar, which is governed by the tensile strength of concrete, which can be assumed to vary with $f_c'^{1/2}$ (ACI 2003). For high levels of confinement, bond failure is due to pull-out of the bar associated to the crushing of the concrete in front of the ribs, and therefore it is strongly related to f_c' .

3.5.2 Effect of bar size

The test results show a slight increase of the bond strength with increasing bar size. The bond strength for No. 14 bars is approximately 7% higher than that for No. 11 bars, and that for No. 18 is about 8% higher than that for No. 14. However, ACI (2008) and AASHTO (2010) provisions for the development length imply that the bond strength is reduced with increasing bar size. As mentioned in Chapter 2, Ichinose et al. (2004) have shown that the influence of the bar size on the bond strength depends on the level of confinement. To interpret and compare results from different tests with different confinement levels, a factor used in ACI 318-08 (ACI 2008) to calculate the required development length of deformed bars in tension is used as a confinement index. This

index, which is denoted as *CI* here, is expressed as $(c_b + 40A_{tr}/s_{tr}n)/d_b$, in which c_b is the distance of the center of a bar to the nearest concrete surface, s_{tr} is the spacing of the transverse reinforcement, A_{tr} is the transverse reinforcement area within distance s_{tr}, and n is the number of bars being spliced or developed at the plane of splitting. According to ACI 318-08, when *CI* is less than 2.5, splitting failure is likely, and for values above 2.5, pull-out failure is expected. Some studies have shown that when the confinement level was low enough that bond failure was governed by concrete splitting, the bond strength would increase significantly with the decrease of the bar size (Ichinose et al. 2004, Plizzari and Mettelli 2009). The value of *CI* considered in these studies ranges from 2 to 5. For pull-out tests with *CI* between 5 and 16 (Ichinose et al. 2004, Steuck et al. 2009), splitting failure was prohibited and the effect of the bar size was negligible. The tests reported in this chapter had *CI* between 11 and 17. A small increase in the bond strength with the bar size observed here is consistent with the observation made by Ichinose et al. (2004).

An explanation for the aforementioned observations is that larger bars have larger ribs, which induce a more severe dilatation effect and, thereby, a larger concrete splitting stress as a bar slips. With little or no confinement, this would result in an earlier splitting failure. With high confinement, not only splitting failure would be prohibited but the dilatation effect induced by the wedging action of the ribs would induce a higher passive confinement pressure. An increase of the confining pressure would result in a higher bond stress, based on results as shown by other studies, e.g., Malvar (1991). Nevertheless, in the studies of Eligehausen et al. (1983) and Viwathanatepa et al. (1979),

even though the specimens were well confined and bond failed by pull-out of the bars, there was a slight increase of the bond strength for smaller bars. It should be noted that the specimens used by Eligehausen et al. (1983) and Viwinathapea et al. (1979) had *CI* between 3 and 13, and 9 and 14, respectively. They are on average lower than that considered in the present study and the study of Steuck et al. (2009), which had *CI* between 9 and 16.

3.5.3 Effect of pull direction

The influence of the pull direction on the bond strength was examined in the tests of No. 11 bars, which have shown a lower bond strength and bond stiffness when a bar was pulled downward instead of upward (see Table 3.1 and Figure 3.5). This is related to the different quality of the concrete above and beneath the ribs for bars casted vertically, as mentioned in Chapter 2.

3.5.4 Effect of slip history

The experimental results presented here have confirmed the observation made by Eligehausen et al. (1983) that the peak bond strength was reduced when a prior load cycle went beyond 70 to 80% of the peak of the monotonic bond stress-slip curve, indicating the deterioration of the concrete surrounding the bar. In addition, these tests have also shown that the decay of the bond resistance depends on the characteristics of the load cycles (slip in one direction or fully-reversed), the accumulated slip, and the number of cycles. A law to calculate the bond stress as a function of the slip and of the slip history is presented in Chapter 4.

3.6 Summary and conclusions

The bond strength and bond-slip behavior of large-diameter bars embedded in well-confined concrete have been examined. Monotonic pull-out tests and cyclic pull-pull tests were conducted on No. 11 (36-mm), 14 (43-mm), and 18 (57-mm) bars. All the specimens failed by pull-out of the bar from the concrete. The large-diameter bars exhibited a bond stress-slip relation similar to that of No. 8 (25-mm) and smaller bars, including the bond deterioration behavior under monotonic and cyclic loads. These tests have also shown that the bond strength tends to increase slightly with increasing bar size, and that the compressive strength of concrete has a notable effect on the bond strength. The bond strength observed here is proportional to $f_c'^{3/4}$. Results from this and other studies have indicated that the influence of the concrete strength and bar size on the bond strength depends on the level of confinement in the concrete specimen. However, data on this is limited, and a systematic and comprehensive investigation of the effects of the bar size and concrete strength on the bond strength under a wide range of confinement levels is needed to further confirm this observation and arrive at more general guidelines. Finally, for a bar positioned vertically during casting, the bond strength is smaller when the bar is pulled down than when it is pulled up. This observation is consistent with other studies.

3.7 Acknowledgement of publication

Part of this chapter is a reprint of the material that will appear in a paper, titled “Bond strength and cyclic bond deterioration of large-diameter bars in well-confined

concrete” to be published in the ACI Structural Journal in 2013. The author of this dissertation was the first and primary author of this paper.

Table 3.1: Test matrix and specimen properties

Series no.	Test no.	Bar Size	Concrete compressive strength f_c' MPa (ksi)	Tensile splitting strength f_{cs} MPa (ksi)	Loading history	Peak bond strength τ_u MPa (ksi)
1	1	No. 11	33.8–36.5 (4.9-5.3)	3.1 (0.45)	Monotonic up	15.2 (2.2)
	2				Monotonic down	12.4 (1.8)
	3				Half cycles	13.8 (2.0)
	4				Half cycles	14.5 (2.1)
	5				Half cycles	11.7 (1.7)
	6				Full cycles	12.4 (1.8)
2	1	No. 14	33.8–37.2 (4.9-5.4)	2.8 (0.40)	Monotonic up	19.3 (2.8)[1]
	2				Half cycles	15.2 (2.2)
	3				Full cycles	15.2 (2.2)
	4				Monotonic up	16.5 (2.4)
	5				Half cycles	15.2 (2.2)
	6				Double half cycles	15.2 (2.2)
3	1	No. 18	34.5–40.7 (5.0-5.9)	3.1-3.5 (0.45-0.50)	Monotonic up	17.2 (2.5)
	2				Full cycles	13.1 (1.9)
	3				Full cycles	13.8 (2.0)
	4				Monotonic up	17.9 (2.6)
	5				Half cycles	14.5 (2.1)
	6				Half cycles	15.2 (2.2)
4	1	No. 14	54.5–56.5 (7.9-8.2)	3.8 (0.55)	Monotonic up	24.1 (3.5)
	2				Monotonic up	22.8 (3.3)
	3				Double full cycles	19.3 (2.8)
	4				Full cycles	20.0 (2.9)

[1]Sealing in a PVC tube failed during construction resulting in a little concrete accumulated at the end of the tube and, thereby, an increase of the bonded length. Since the actual embedment length is unknown, the bond strength has been calculated with the specified embedment length of $5d_b$.

Table 3.2: Geometric properties of the bars

Bar Size No.	d_b mm (in.)	Rib area ratio	Clear rib spacing mm (in.)
11	36 (1.41)	0.070	19.1 (0.75)
14	43 (1.69)	0.068	24.9 (0.98)
18	57 (2.26)	0.095	24.4 (0.96)

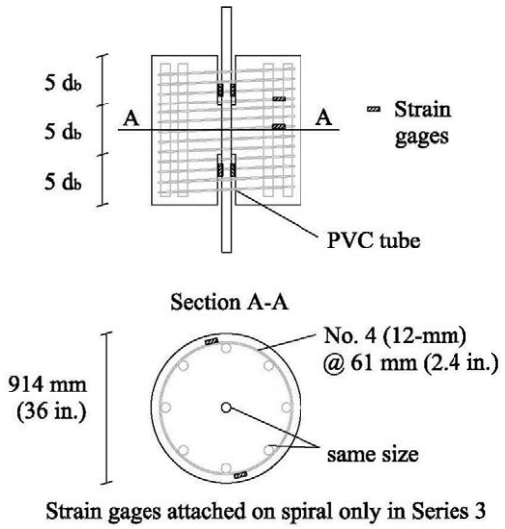

(a) Typical test specimen and strain gage locations

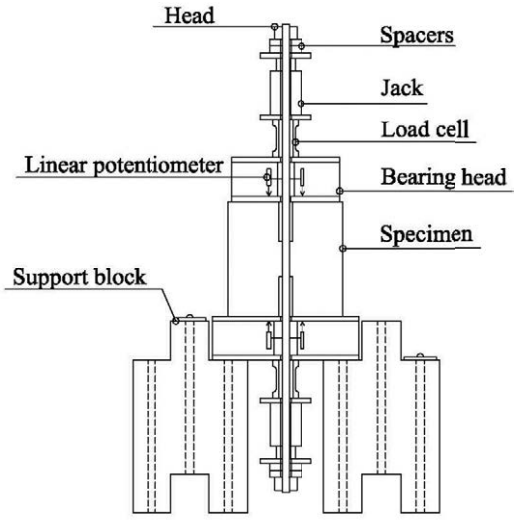

(b) Test setup and linear potentiometer locations

Figure 3.1: Test specimen, setup, and instrumentation

(a) Placing strain gages on test bars

(b) Assembling steel cages and placing strain gages on spiral

(c) Centering test bar, and placing PVC tubes and form

(d) Concrete pour

Figure 3.2: Construction sequence for each series of specimens

Figure 3.3: Test setup

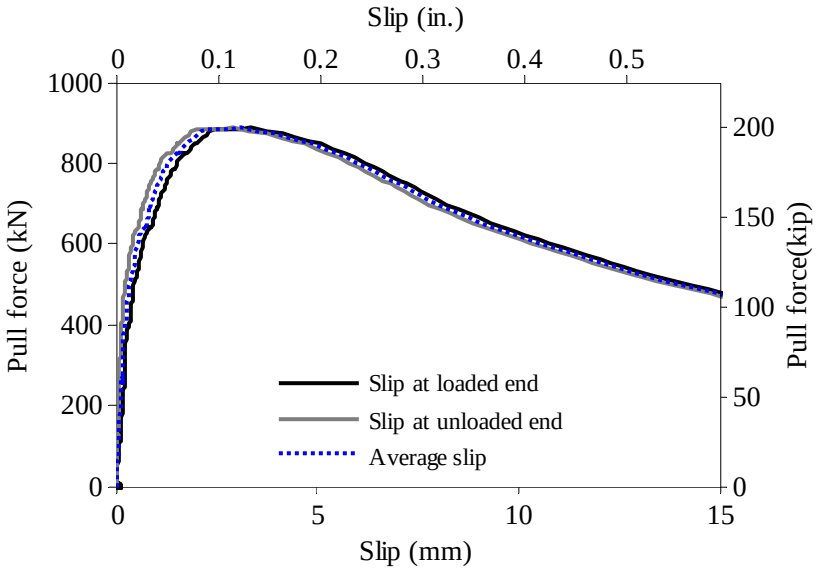

Figure 3.4: Pull force vs. slip from Test 1 of Series 3

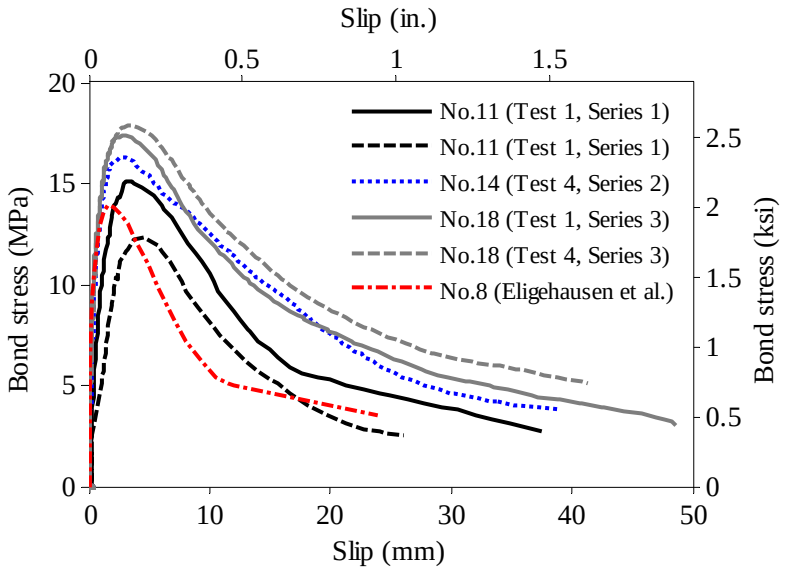

Figure 3.5: Average bond stress vs. slip from monotonic load tests

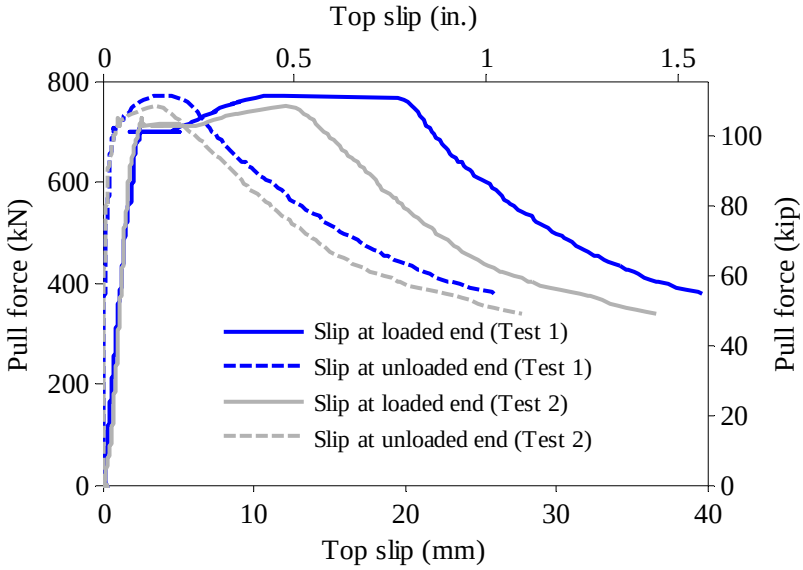

Figure 3.6: Pull force vs. slip from Test 1 and Test 2 of Series 4

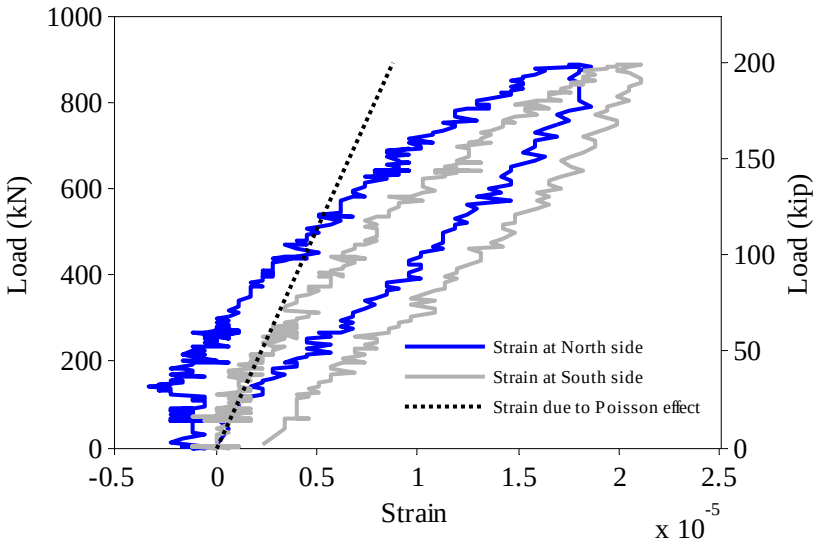

Figure 3.7: Strain in spiral at mid-height of the specimen in Test 1 of Series 3

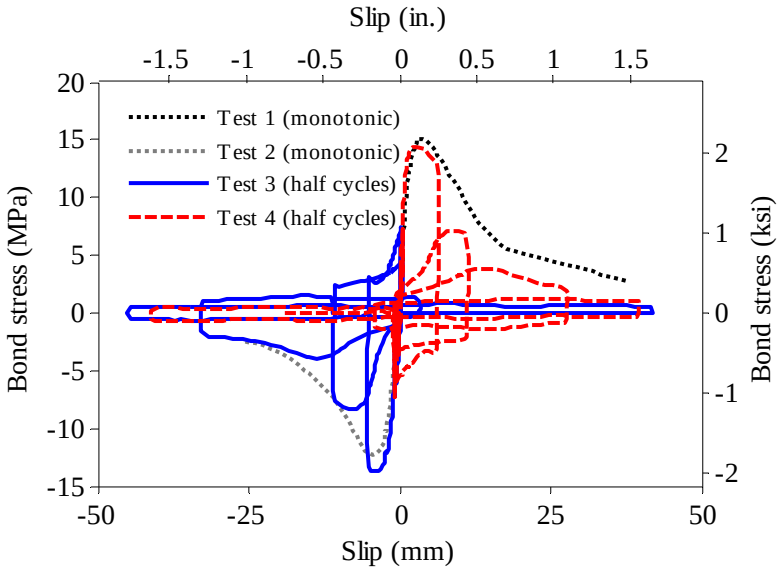

Figure 3.8: Tests on No. 11 bars (Series 1) under monotonic (Test 1 and Test 2) and cyclic load with half cycles (Test 3 and Test 4)

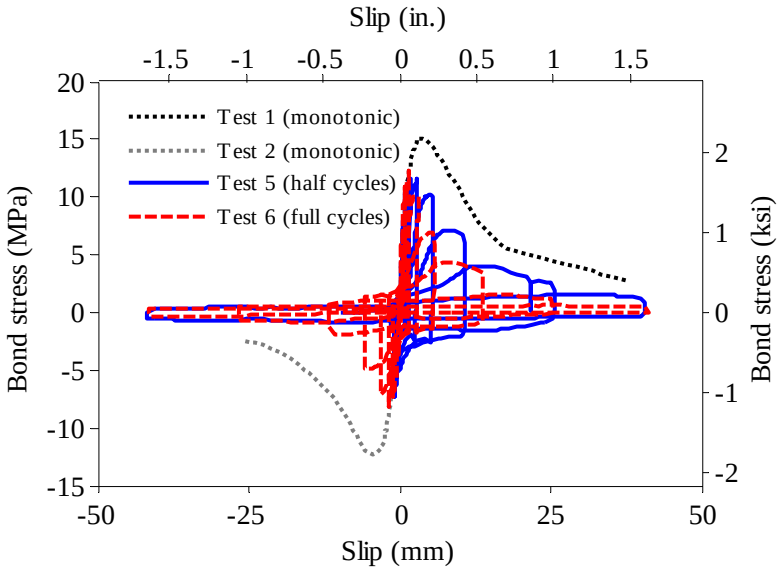

Figure 3.9: Tests on No. 11 bars (Series 1) under monotonic (Test 1) and cyclic load with half cycles (Test 5) and full cycles (Test 6)

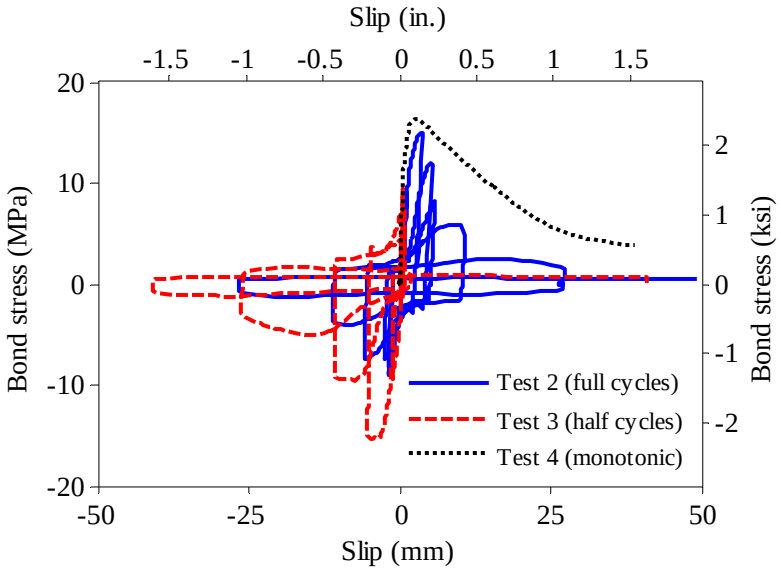

Figure 3.10: Tests on No. 14 bars (Series 2) under monotonic (Test 4) and cyclic load with full cycles (Test 2) and half cycles (Test 3)

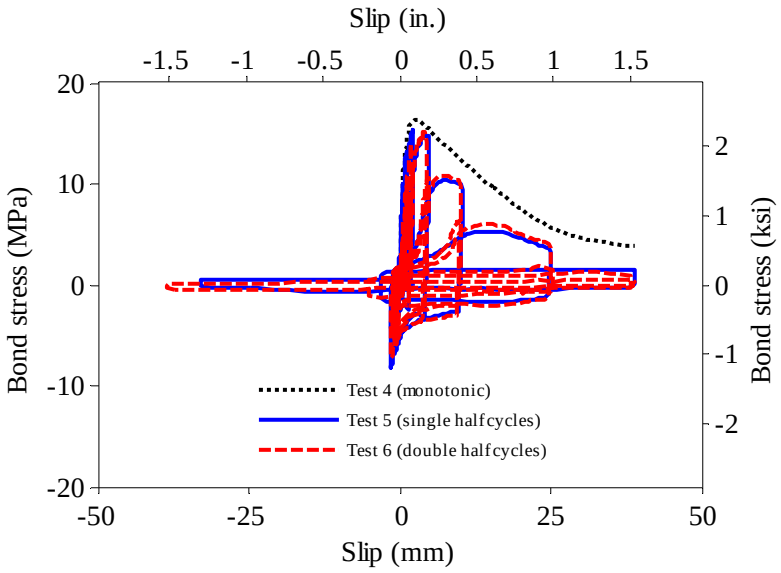

Figure 3.11: Tests on No. 14 bar (Series 2) under monotonic (Test 4) and cyclic load with single half cycles (Test 5) and double half cycles (Test 6)

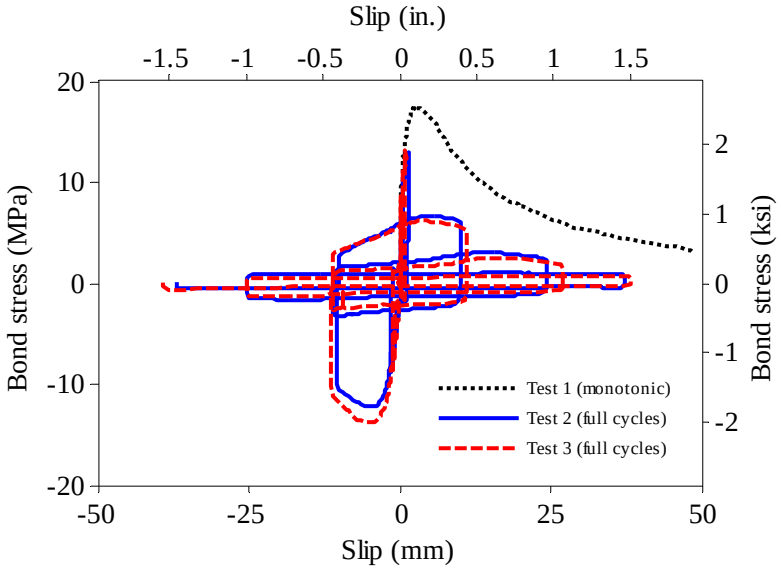

Figure 3.12: Tests on No. 18 bars (Series 3) under monotonic (Test 1) and cyclic load with full cycles (Test 2 and Test 3)

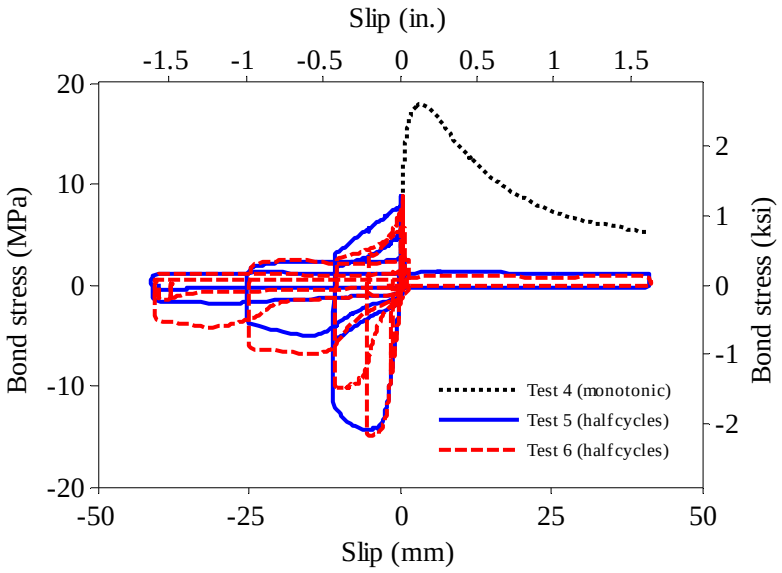

Figure 3.13: Tests on No. 18 bars (Series 3) under monotonic (Test 2) and cyclic load with half cycles (Test 5 and Test 6)

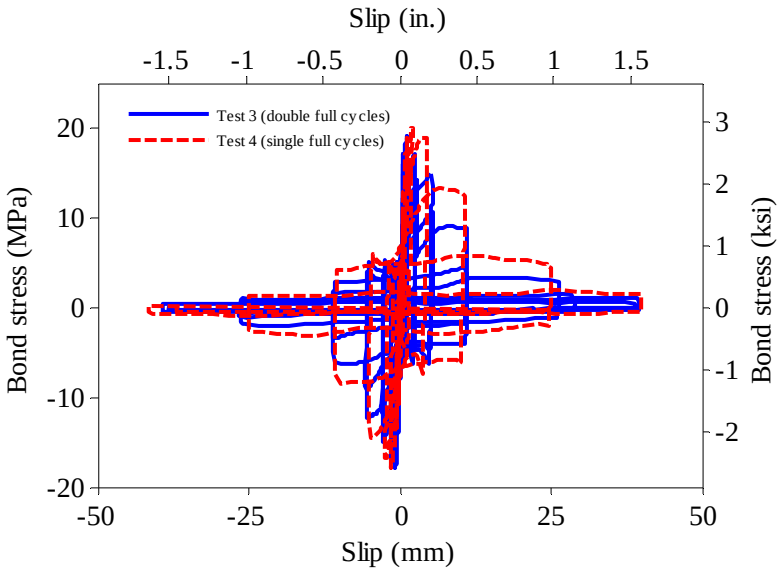

Figure 3.14: Tests on No. 14 bars (Series 4) under cyclic load with single full cycles (Test 4) and double full cycles (Test 3)

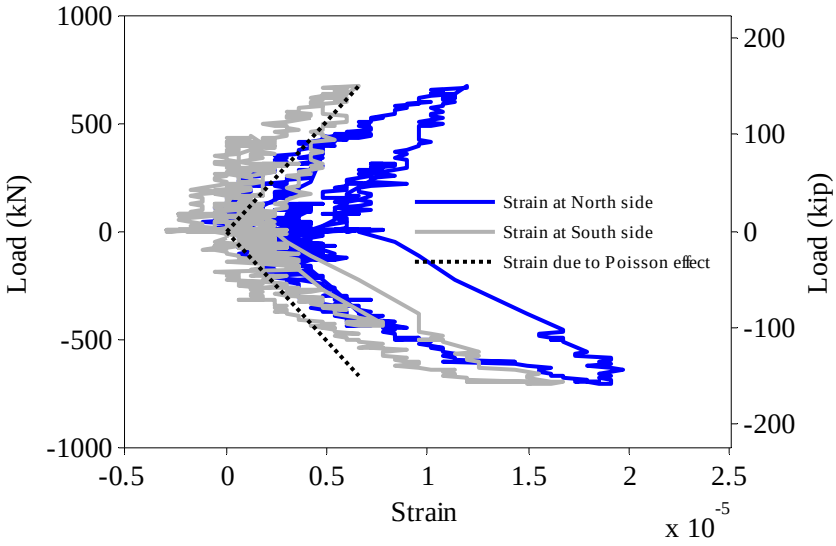

Figure 3.15: Strain in spiral at mid-height of the specimen in Test 3 of Series 3

CHAPTER 4

PHENOMENOLOGICAL BOND-SLIP MODEL FOR FINITE ELEMENT ANALYSIS

In this chapter, a new model to simulate the bond-slip behavior of bars in the finite element analysis of reinforced concrete (RC) members is presented. A phenomenological law to predict the bond stress-slip relation of bars embedded in well-confined concrete is proposed. This law has been calibrated with the bond-slip data presented in Chapter 3, and has been taken as the constitutive relation in an interface element implemented in the commercial finite element (FE) program ABAQUS (Simulia 2010). The constitutive models available in ABAQUS to model concrete and steel have been calibrated and validated for the FE analysis of RC members. The chapter is concluded with the use of laboratory experiments to validate the bond-slip model. These experiments include different types of pull-out tests and a test on an RC column subjected to cyclic lateral loading.

4.1 Bond stress-vs.-slip law for bars in well-confined concrete

A phenomenological bond stress-vs.-slip law for bars embedded in well-confined concrete has been developed based on the experimental data presented in Chapter 3 and on concepts originally proposed by Eligehausen et al. (1983) and further extended by others (Pochanart and Harmon 1989, Yankelevsky et al. 1992, and Lowes et al. 2004). However, it is distinct from previous models in that it requires the calibration of only three parameters to be applied to bars of different sizes and concrete of different strengths. The model presented here is an enhancement of that presented in Murcia-Delso et al. (2013).

In this model, the relation between the bond stress and slip for monotonic loading is described by a set of polynomial functions. For cyclic loading, a similar relation is used but the bond strength is reduced at each slip reversal using two damage parameters, whose values are based on the slip history, to account for cyclic bond deterioration. In addition, cyclic unloading and loading rules similar to those proposed by Eligehausen et al. (1983) are adopted to describe bond resistance right after slip reversal. The model is described in detail in the following sections.

4.1.1 Monotonic bond stress-slip relation

The monotonic bond stress (τ) - slip (s) relation assumed in this model is shown in Figure 4.1a. It is defined piecewise by five polynomial functions, as shown in Equation 4.1, in terms of three governing parameters: the peak bond strength (τ_u), the slip at

which the peak strength is attained (s_{peak}), and the clear spacing between the ribs (s_R). These functions are given below.

$$\tau(s)=\begin{cases} 4\dfrac{\tau_{\max}}{s_{peak}}s & 0\le s<0.1s_{peak} \\ \tau_{\max}\left[1-0.6\left(\dfrac{s-s_{peak}}{0.9s_{peak}}\right)^4\right] & 0.1s_{peak}\le s<s_{peak} \\ \tau_{\max} & s_{peak}\le s<1.1s_{peak} \\ \tau_{\max}-(\tau_{\max}-\tau_{res})-0.75\dfrac{s-1.1s_{peak}}{s_R-1.1s_{peak}} & 1.1s_{peak}\le s<s_R \\ \tau_{res} & s\ge s_R \end{cases} \tag{4.1}$$

in which $\tau_{\max}$ and τ_{res} are the maximum and residual bond stress of the monotonic curve, respectively. For a bar that has not yielded, $\tau_{\max}=\tau_u$ and $\tau_{res}=0.25\tau_u$. Until reaching 40% of the maximum stress, $\tau_{\max}$, (point A in Figure 4.1a) the bond stress increases linearly with the slip. The nonlinear hardening behavior is represented by a fourth-order polynomial (A-B), followed by a plateau at $\tau_{\max}$ (B-C). The bond strength decay is described by a linear descending branch (C-D). When the slip equals the clear rib spacing, s_R, of the bar (point D) a residual bond stress is reached and this value remains constant for larger slip values.

The use of the proposed law requires the determination of the three governing parameters. The value of s_R is a known geometric property of the bar, and it is usually between 40 to 60% of the bar diameter. As discussed in Chapter 3, τ_u depends on many factors and no theoretical formulas are available to accurately estimate its value. The same situation applies to s_{peak}. Therefore, these values have to be determined

experimentally for each case if possible. For the No. 11, 14, and 18 (36, 43, and 57-mm) bars and concrete strengths considered in this study, experimental data is provided in Table 4.1.

When no experimental data is available, the following approximations, based on data obtained in this study and by others, can be used to determine τ_u and s_{peak}. The bond strength can be assumed to be 16.5 MPa (2.4 ksi) for 34.5 MPa (5-ksi) concrete regardless of the bar size. This is based on the average τ_u value obtained from Test Series 1 to 3, as shown in Table 4.1. The slight increase of the bond strength with the increase of the bar size observed in these tests can be ignored in view of the lack of a comprehensive study with a broad range of bar sizes to examine this influence. For concrete strengths other than 34.5 MPa (5 ksi), τ_u can be scaled accordingly with the assumption that it is proportional to $f_c'^{3/4}$. As shown in Table 4.1, s_{peak} for the No. 11, 14, and 18 bars is about 1.7 times that for No. 8 (25-mm) bars (Eligehausen et al. 1983) and three times that for No.5 (16-mm) bars (Lundgren 2000). This seems to indicate a scale effect with respect to the bar size, but these values could also be influenced by other factors such as the confinement, concrete properties, and loading conditions. In addition, some studies (Eligehausen et al. 1983, Pochanart and Harmon 1989) have indicated that that s_{peak} also depends on the relative rib area. Owing to the lack of more conclusive data, it is recommended that speak be taken to be 7% of the bar diameter, which is the average of the experimentally obtained s_{peak} values, as presented in Table 4.1, normalized by the bar respective bar diameters.

The experimental results presented here and those obtained by Lundgren (2000) have shown that the bond strength and the bond stiffness are reduced when a vertically cast bar is pulled downward. Based on this data, the monotonic bond stress-slip relation for a vertically cast bar pulled downward is described by Equation 4.2. Note that for a bar pulled downward, the slip and bond stress have a negative sign here.

$$\tau(s) = \begin{cases} -2.3\dfrac{\tau_{\max}}{s_{peak}}|s| & -0.15s_{peak} \le s < 0 \\ -\tau_{\max}\left[0.85 - 0.505\left(\dfrac{|s| - 1.5s_{peak}}{1.35s_{peak}}\right)^4\right] & -1.5s_{peak} \le s < -0.15s_{peak} \\ -0.85\tau_{\max} & -1.6s_{peak} \le s < -1.5s_{peak} \\ -0.85\tau_{\max} + (0.85\tau_{\max} - \tau_{res})\dfrac{|s| - 1.6s_{peak}}{s_R - 1.6s_{peak}} & -s_R \le s < -1.6s_{peak} \\ -\tau_{res} & s < -s_R \end{cases} \quad (4.2)$$

As mentioned in Chapter 2, the bond resistance can be considerably reduced after a reinforcing bar yields in tension. This behavior could not be observed in this study although the bars yielded in two of the monotonically loaded specimens. The reason is that in these two cases, the concrete had a compressive strength of 55 MPa (8 ksi), and there were no other specimens tested monotonically that had the same concrete strength but no bar yielding. In addition, in these specimens, yielding occurred at the loaded end of the bar while the other end remained unstrained. As a result, yielding might have occurred only in the upper portion of the bonded region and the total bond force was probably only slightly affected by this. As discussed in Chapter 2, in pull-out tests carried out by Shima et al. (1987b) on bars with long embedment length, the bond resistance dropped to approximately 25% of the peak bond strength at bar yielding, and it continued to decrease gradually as the inelastic deformation of the bar increased. To account for this

effect in the model, $\tau_{\max}$ and τ_{res} are defined as a function of the steel strain, ε_s, as shown in Equation 4.3. Once the bar yields, the peak of the monotonic envelope will decrease linearly until it reaches 25% of the bond strength, τ_u, at a bar strain corresponding to the start of the strain hardening branch, ε_{sh}, which can be assumed to be 1%. For larger bar strains, both the peak and the residual resistances decrease linearly to zero when the bar strain reaches the ultimate strain of steel, ε_u, which can be assumed to be 15%.

$$\tau_{\max}(\varepsilon_s) = \begin{cases} \tau_u & \varepsilon_s \le \varepsilon_y \\ \tau_u \left(1 - 0.75 \dfrac{\varepsilon_s - \varepsilon_y}{\varepsilon_{sh} - \varepsilon_y}\right) & \varepsilon_y < \varepsilon_s \le \varepsilon_{sh} \\ 0.25\tau_u \dfrac{\varepsilon_u - \varepsilon}{\varepsilon_u - \varepsilon_{sh}} & \varepsilon_s > \varepsilon_{sh} \end{cases} \tag{4.3a}$$

$$\tau_{res}(\varepsilon_s) = \begin{cases} 0.25\tau_u & \varepsilon_s \le \varepsilon_{sh} \\ 0.25\tau_u \dfrac{\varepsilon_u - \varepsilon}{\varepsilon_u - \varepsilon_{sh}} & \varepsilon_s > \varepsilon_{sh} \end{cases} \tag{4.3b}$$

4.1.2 Cyclic law

The extension of the bond stress-slip law to cyclic loading is based on the experimental evidence presented in this study and the bond-slip mechanism hypothesized by Eligehausen et al. (1983). It is assumed that at a large slip, part of the concrete in contact with the ribs on the bearing side is crushed and a gap has been created on the other side of the ribs. This gap needs to be closed before the bearing resistance in the opposite direction can be activated. Hence, the initial bond resistance developed upon slip

reversal after a large slip can be attributed solely to friction. Once contact is resumed on the bearing side of the rib, the bond resistance increases. However, this resistance is lower than that under a monotonic load for the same level of slip due to the deterioration of the concrete around the ribs. The analytical law for cyclic loading is plotted in Figure 4.1b.

In most phenomenological models, bond deterioration under cyclic slip reversals is simulated by scaling the monotonic bond stress-slip relation, and the scale factors are updated upon each slip reversal. Some of these models adopt a single damage parameter that is a function of the energy dissipated by bond-slip (Eligehausen et al. 1983) or of the slip history (Lowes et al. 2004) to determine a scale factor. Some models (Pochanart and Harmon 1989, Yankelevsky et al. 1992, and Lowes et al. 2004) distinguish the bearing and friction resistances. Pochanart and Harmon (1989) and Yankelevsky et al. (1992) scale independently these two contributions. The latter approach has been adopted here based on the experimental evidence that the reduction of the peak strength is in general more rapid than that of the residual strength. The peak strength in a monotonic bond stress-slip curve is mainly contributed by the bearing resistance, while the residual strength is entirely due to friction. Friction deterioration is caused by the smoothening of the interface between the steel and concrete, and, therefore, can be assumed to be dependent on the total cumulative slip. The deterioration of the bearing resistance is caused by the crushing and/or shearing of the concrete between the ribs. Therefore, it can be assumed to be dependent only on the maximum slips attained in the two loading directions. For sliding between previously attained levels of slip, there will be no bearing contact between the concrete and the ribs, and, therefore, no further crushing and

shearing of concrete could occur. These mechanisms are consistent with the cyclic behavior observed in the tests presented in Chapter 3. Fully-reversed cycles are more damaging than half cycles because the maximum slip excursion and the total slip accumulated are larger, causing more deterioration in both the bearing and the friction resistances. Double cycles between the same slip levels induce slightly more damage than single cycles because the second cycle causes a further reduction of the friction resistance.

Based on the reasoning presented above, the monotonic bond stress-slip relation in this model is separated into a bearing component and a friction component as shown in Figure 4.1a. From the origin to the end of the plateau at the peak of the curve (point C), the bearing resistance, τ_b, is assumed to be 75% of the total bond resistance, and the remaining 25% is assumed to be contributed by the friction resistance, τ_f. After the peak, τ_b is assumed to decay linearly to zero when the slip is equal to s_R, i.e., when the concrete between the ribs has been completely crushed or sheared off. The friction resistance, τ_f, is assumed to remain constant as slip continues to increase after the peak. The maximum bearing and friction resistances are therefore $\tau_{b,\max} = 0.75\tau_{\max}$ and $\tau_{f,\max} = 0.25\tau_{\max}$, respectively. To model the cyclic bond deterioration, the following damage law is used.

$$\begin{aligned} \tau_{red} &= \tau_{b,red} + \tau_{f,red} \\ \tau_{b,red} &= \left(1 - \hat{d}_b\right) \cdot \tau_b \\ \tau_{f,red} &= \left(1 - \hat{d}_f\right) \cdot \tau_f \end{aligned} \tag{4.4}$$

in which τ_{red} is the reduced bond resistance, $\tau_{b,red}$ is the reduced bearing resistance, $\tau_{f,red}$ is the reduced friction resistance, $\hat{d}_b$ is the damage parameter for the bearing resistance, and $\hat{d}_f$ is the damage parameter for the friction resistance. The bond stress-slip relation is updated using Equation 4.4 when the load is reversed. The damage laws have been calibrated using the experimental data from Test Series 1, 2 and 3. Data from Series 4 was not used because of the lack of a reliable experimental monotonic bond stress-slip relation to allow a direct comparison with the cyclic behavior.

The damage parameter affecting the bearing resistance, $\hat{d}_b$, is defined as a function of the maximum slip.

$$\hat{d}_b(\bar{s}_{\max}) = 1 - 1.2e^{-2.7\left(\frac{\bar{s}_{\max}}{s_R}\right)^{0.8}} \geq 0 \tag{4.5a}$$

where

$$\bar{s}_{\max} = 0.75\max\left(s^+_{\max}, s^-_{\max}\right) + 0.25\left(s^+_{\max} + s^-_{\max}\right) \tag{4.5b}$$

in which $s^+_{\max}$ and $s^-_{\max}$ are the maximum slips reached in the positive and negative directions in absolute value. Since full cycles produce more damage than half cycles, the maximum slip considered here is a weighted average of the absolute maximum slip reached in any of the two directions and the sum of the maximum slips in the two directions. As mentioned previously, cyclic deterioration starts to become apparent after the maximum bond stress in a previous cycle has reached 70 to 80% of the peak bond strength developed under a monotonic load. This is represented in the above damage index as follows. Based on Equation 4.5a, $\hat{d}_b$ starts to increase only when $\frac{\bar{s}_{\max}}{s_R} > 0.034$.

For monotonic loading, the bond stress is equal to 70% of the peak bond strength when $s = 0.034 s_R$ according to Equation 4.1, assuming that $s_{peak} = 0.07 d_b$ and $s_R = 0.5 d_b$.

The friction resistance decreases progressively as a result of the smoothening of the bond interface, which depends on the total cumulative slip. However, more severe deterioration has been observed in the residual bond strength as the maximum slip increases in a subsequent cycle. Therefore, the damage parameter for the friction resistance, $\hat{d}_f$, is assumed to be a function of both the absolute maximum slip attained in each loading direction and the cumulative slip, s_{acc}.

$$\hat{d}_f(s_{acc}, s^+_{\max}, s^-_{\max}) = \frac{\min\left(s^+_{\max} + s^-_{\max}, s_R\right)}{s_R}\left(1 - e^{-0.45\left(\frac{s_{acc}}{s_R}\right)^{0.75}}\right) \tag{4.6}$$

To avoid an overestimation of damage that could otherwise be caused by a large number of small cycles, s_{acc} is considered zero before the slip displacement has exceeded the slip at the peal stress, s_{peak}, for the first time. This is a reasonable assumption if one agrees that friction should play a minor role at the beginning when bearing is significant.

Right after each slip reversal, unloading and reloading in the other stress direction follows the initial stiffness of the monotonic curve until the friction resistance in the opposite direction is reached. If the maximum slip ever achieved exceeds the slip at the peak resistance, s_{peak}, the resistance τ_{rev} right after slip reversal is equal to the reduced friction, $\tau_{f,red}$, given in Equation 4.4. Otherwise, it is a fraction of the reduced friction as shown in Equation 4.7, which is a modification of that suggested by Eligehausen et al. (1983).

$$\tau_{rev} = k_{rev}\tau_{f,red} \tag{4.7a}$$

where

$$k_{rev} = \frac{\max(s^{+}_{\max}, s^{+}_{\max})}{s_{peak}} \leq 1 \tag{4.7b}$$

4.1.3 Comparison of analytical and experimental results

The ability of the analytical model to reproduce the bond stress-slip relations obtained from the experiments presented in Chapter 3 and by others has been evaluated. The experimental and analytical results for two monotonic load tests from Chapter 3, and for No. 8 (25-mm) bars tested by Eligehausen et al. (1983) are presented in Figure 4.2. Two sets of analytical curves have been generated. The first set is based on the values of τ_u and s_{peak} directly obtained from the monotonic tests while the second set is based on the values estimated with the recommendations provided in Section 4.1.1. The values of τ_u and s_{peak} for both sets of curves are presented in Table 4.1. The results in Figure 4.2 show that once the values of τ_u and s_{peak} have been determined with experimental data, the ascending and descending branches are well represented by the proposed polynomial functions. The curves based on the estimated values also provide a satisfactory match given the simplicity of the rules used to derive these values.

The cyclic bond stress-slip relations have been reproduced analytically using the parameters calibrated with the monotonic tests. The analytical and experimental results for selected tests in Series 1, 3, and 4 are compared in Figure 4.3. The model accurately reproduces the cyclic bond stress-slip relations, including the bond strength decay.

Experiments by Eligehausen et al. (1983) and Lundgren (2000), which had smaller bars, more cycles per amplitude level, and cycles with finer amplitude increments, are also well reproduced by the analytical model, as shown in Figure 4.4.

4.2 Steel-concrete interface model

An interface model is used to simulate the interaction between steel and concrete in two-dimensional and three-dimensional finite element analysis of reinforced concrete members. This model is based on the bond stress-vs.-slip law presented in Section 4.1. The relative displacement at the concrete-steel interface has three components: one normal, $\tilde{u}_1$, and two tangential components, $\tilde{u}_2$ and $\tilde{u}_3$, as shown in Figure 4.5. Likewise, the stress transfer at the interface is decomposed into one normal, σ_1, and two shear components, τ_2 and τ_3. The constitutive relations at the concrete and steel interface are presented in Equations 4.8 through 4.10.

In Equation 4.8, the bond stress-vs.-slip law proposed in Section 4.1 is used to define the relation between the tangential relative displacement and shear stress in the longitudinal direction of the bar, i.e., between $\tilde{u}_2$ and τ_2. However, to introduce the capability of modeling bond resistance in low confinement situations and splitting failure, a bond stress reduction factor, ρ, has been introduced.

$$\tau_2 = \rho(\tilde{u}_1) \cdot \tau(\tilde{u}_2, \varepsilon_s) \tag{4.8a}$$

The reduction factor ρ depends on the normal opening of the interface, $\tilde{u}_1$, with respect to the bar rib height, h_R, as follows.

$$\rho(\tilde{u}_1) = \begin{cases} 1 & \tilde{u}_1 \le 0.5h_R \\ 2(1-\tilde{u}_1/h_R) & 0.5h_R < \tilde{u}_1 \le h_R \\ 0 & \tilde{u}_1 > h_R \end{cases} \quad (4.8b)$$

For well-confined situations, the opening of the interface is minimal and ρ is equal to one. If the interface opening is larger than the rib height, i.e., the confining action is lost due to concrete splitting, the bond resistance disappears. A smooth transition is assumed between these two situations.

As shown in Equation 4.9, the normal stress is defined as a fraction of the bond stress to account for the inclined direction of the bond forces with respect to the longitudinal direction of the bar. This inclination is defined by angle θ. A similar approach was used in the bond-slip model proposed by Lowes et al. (2004). In addition, a penalty factor governed by a stiffness parameter, $K_{pen,1}$, and active only in compression has been added to the normal stress to avoid interpenetration of the steel and concrete.

$$\sigma_1 = |\tau_2| \tan\theta + K_{pen,1} \min(\tilde{u}_1, 0) \quad (4.9)$$

For three-dimensional models, the rotation of the bar around its longitudinal axis is restrained using a penalty stiffness parameter, $K_{pen,3}$, as presented in Equation 4.10.

$$\tau_3 = K_{pen,3}\tilde{u}_3 \quad (4.10)$$

The steel-concrete model has been implemented in a user-defined element subroutine in ABAQUS (Simulia 2010). The element has linear shape functions and two integration points located at the ends of the element (see Figure 4.5). The force per unit length of the interface is obtained by multiplying the interface stresses by the tributary perimeter of the bar that the interface element represents. Finally, the axial strain of the

bar required in the constitutive equations is calculated from the displacements parallel to the bar axis of the nodes connected to the bar (nodes A and B in Figure 4.5) and the length of the element, L_e, as

$$\varepsilon_s = \frac{u_{2B} - u_{2A}}{L_e} \tag{4.11}$$

4.3 Three-dimensional modeling of plain concrete

In the finite element analyses presented in this dissertation, plain concrete has been modeled with continuum elements and a plastic-damage constitutive model available in ABAQUS (Simulia 2000). Plastic-damage models are attractive to simulate the behavior of concrete because they combine the capabilities of plasticity and continuum damage models to account for plastic deformations and stiffness degradation, respectively. The model available in ABAQUS, called concrete damaged plasticity, is based on the formulations proposed by Lubliner et al. (1989) and Lee and Fenves (1998). In this section, the theory of the plastic-damage model available in ABAQUS is briefly reviewed, and the model is validated and calibrated by experimental data.

4.3.1 Plastic-damage model formulation

Following the classical theory of plasticity, the strain tensor is decomposed into an elastic part and a plastic part, and the stress tensor is obtained as the double contraction of the elastic stiffness tensor and the elastic strain tensor.

$$\boldsymbol{\varepsilon} = \boldsymbol{\varepsilon}^e + \boldsymbol{\varepsilon}^p \tag{4.12a}$$

$$\boldsymbol{\sigma} = \mathbf{E} : \boldsymbol{\varepsilon}^{e} = \mathbf{E} : \left(\boldsymbol{\varepsilon} - \boldsymbol{\varepsilon}^{p} \right) \tag{4.12b}$$

To account for stiffness degradation, the elastic stiffness tensor is related to the initial stiffness tensor as

$$\mathbf{E} = (1 - d)\mathbf{E_0} \tag{4.12c}$$

where d is a scalar parameter that controls the stiffness degradation. In damage theory, d represents the ratio of the (undamaged) effective load-carrying area to the overall section area. The effective stress in the undamaged area is defined as

$$\overline{\boldsymbol{\sigma}} = \mathbf{E}_0 : \boldsymbol{\varepsilon}^{e} = \mathbf{E}_0 : \left(\boldsymbol{\varepsilon} - \boldsymbol{\varepsilon}^{p} \right) \tag{4.12d}$$

The yield surface of the damaged plasticity model is based on that proposed by Lubliner et al. (1989) with the modifications proposed by Lee and Fenves (1998) to account for the different behavior in tension and compression. The initial shape of the yield surface in the principal stress plane for a plane stress situation is plotted in Figure 4.6. The yield function is defined in terms of the invariants I_1 and J_2 as

$$F = \frac{1}{1-\alpha}\left[\alpha I_1 + \sqrt{3J_2} + \beta(\tilde{\varepsilon}_c^{\,p}, \tilde{\varepsilon}_t^{\,p}) < \hat{\sigma}_{\max} > - \gamma < -\hat{\sigma}_{\max} > \right] - c_c(\tilde{\varepsilon}_c^{\,p}) \tag{4.13}$$

in which $< \cdot >$ is the Macaulay bracket, $\hat{\sigma}_{\max}$ is the maximum principal stress, α and γ are constants, and β and c_c are parameters that depend on two history variables, $\tilde{\varepsilon}_c^{\,p}$ and $\tilde{\varepsilon}_t^{\,p}$, representing the equivalent plastic strains in compression and tension, respectively. These variables are later on defined in Equation 4.15.

A non-associated plastic potential, G, is assumed and the plastic strain rate is defined as $\dot{\boldsymbol{\varepsilon}}^p = \dot{\lambda}\dfrac{\partial G}{d\boldsymbol{\sigma}}$, where $\dot{\lambda}$ is the plastic multiplier. The plastic potential is defined in Equation 4.14 using the Drucker-Prager criterion.

$$G = \sqrt{3J_2} + \frac{I_1}{3}\tan\psi \tag{4.14}$$

where ψ is the dilation angle of the concrete.

The history variables $\tilde{\varepsilon}_c^{\,p}$ and $\tilde{\varepsilon}_t^{\,p}$ are related to the plastic flow as follows

$$\dot{\tilde{\varepsilon}}_t^{\,p} = r\left(\hat{\bar{\boldsymbol{\sigma}}}\right)\dot{\hat{\varepsilon}}_{\max}^{p} \tag{4.15a}$$

$$\dot{\tilde{\varepsilon}}_c^{\,p} = \left(1 - r\left(\hat{\bar{\boldsymbol{\sigma}}}\right)\right)\dot{\hat{\varepsilon}}_{\min}^{p} \tag{4.15b}$$

in which $\dot{\hat{\varepsilon}}_{\max}^{p}$ and $\dot{\hat{\varepsilon}}_{\min}^{p}$ are obtained from the principal plastic strains rates ($\dot{\varepsilon}_1^p$, $\dot{\varepsilon}_2^p$, $\dot{\varepsilon}_3^p$) as $\dot{\hat{\varepsilon}}_{\max}^{p} = \dot{\varepsilon}_1^p$ and $\dot{\hat{\varepsilon}}_{\min}^{p} = \dot{\varepsilon}_3^p$ in which $\dot{\varepsilon}_1^p \geq \dot{\varepsilon}_2^p \geq \dot{\varepsilon}_3^p$, and

$$r\left(\hat{\bar{\boldsymbol{\sigma}}}\right) = \begin{cases} 0 & \text{if } \hat{\bar{\boldsymbol{\sigma}}} = 0 \\ \dfrac{\sum_{i=1}^{3}\left\langle \hat{\bar{\sigma}}_i \right\rangle}{\sum_{i=1}^{3}\left|\hat{\bar{\sigma}}_i\right|} & \text{otherwise} \end{cases} \tag{4.15c}$$

where $\hat{\bar{\sigma}}_i$ are the principal effective stresses.

The parameter β is defined as

$$\beta = \frac{c_c(\tilde{\varepsilon}_c^{\,p})}{c_t(\tilde{\varepsilon}_c^{\,p})}(1-\alpha) - (1+\alpha) \tag{4.16}$$

where the functions $c_t\left(\tilde{\varepsilon}_t^{\,p}\right)$ and $c_c\left(\tilde{\varepsilon}_c^{\,p}\right)$ represent the tensile and compressive cohesion in the yield surface, and are calibrated from the uniaxial compression and tension test data.

The damage parameter d is a function of both the damage parameter in tension, $d_t = d_t\left(\tilde{\varepsilon}_t^{\,p}\right)$, and the damage parameter in compression, $d_c = d_c\left(\tilde{\varepsilon}_c^{\,p}\right)$, as follows:

$$(1-d) = (1-s_t d_c)(1-s_c d_t) \tag{4.17a}$$

where

$$s_t = 1 - w_t r\left(\hat{\bar{\boldsymbol{\sigma}}}\right) \tag{4.17b}$$

$$s_c = 1 - w_c\left(1 - r\left(\hat{\bar{\boldsymbol{\sigma}}}\right)\right) \tag{4.17c}$$

In Equation 4.17, w_t and w_c are constants that control stiffness degradation in tension and compression, respectively. The functions $d_t = d_t\left(\tilde{\varepsilon}_t^{\,p}\right)$ and $d_c = d_c\left(\tilde{\varepsilon}_c^{\,p}\right)$ are calibrated from cyclic uniaxial tension and compression tests, respectively. The uniaxial tension and compression stress-strain curves for this model are shown in Figure 4.7.

4.3.2 Validation and calibration of the plastic-damage model

Lee and Fenves (1998) validated the model for monotonic uniaxial and biaxial compression and tension loading. The model available in ABAQUS (Simulia 2010) has been calibrated and further validated here for cyclic compression-tension behavior and compression under lateral confinement. The values selected here for some key model parameters that are believed to be independent of the concrete strength are presented in Table 4.2. These values have been kept constant for all the analyses presented in this dissertation. Together with these parameters, the calibration of the model in ABAQUS demands the uniaxial compressive stress-strain and tensile stress-crack opening curves.

Given the value of the compressive strength of concrete, the uniaxial compressive stress-strain curves have been defined based on the model proposed by Karthik and Mander (2011) for unconfined concrete. In tension, the tensile strength is assumed to decay linearly with the opening of the crack.

The cyclic tension-compression tests carried out by Reinhardt (1984b) are sufficiently well reproduced by the model, as shown in Figure 4.8. Stiffness degradation in tension allows the plastic-damage model to simulate the closing and opening of a crack. However, for large inelastic strains, complete closure of the crack would require very large stiffness degradation (with the value of the damage parameter very close to one), which will lead to numerical problems. Hence, the model is not capable of simulating the complete closure of a crack. This can be observed in Figure 4.8 for the larger amplitude displacement cycles. To circumvent this problem, contact conditions can be used to represent cracks in a discrete manner in ABAQUS.

The parameters affecting the yield surface have been calibrated to match experimental results obtained by Hurblut (1985) and Mander et al. (1989) to capture the behavior of confined concrete in compression. As shown in Figure 4.9, the model is capable of reproducing the effect of the lateral confining stress on the compressive strength and lateral expansion of concrete observed in the tests of Hurblut (1985). However, the increase of ductility due to increasing confining pressure is not captured by the model. This has also been observed when attempting to replicate the experimental results obtained by Mander et al. (1989) on concrete cylinders that had different amount of confining steel. For the model to match the experimental results, the decaying slope of the input uniaxial compression curve has to be modified a priori based on the level of

confining steel, as shown in Figure 4.10a. For this purpose, the post-peak slope of the uniaxial compressive stress-strain law proposed by Karthik and Mander (2011) for unconfined concrete is modified to match that proposed by the same authors for confined concrete. With this modification, the model is capable of reproducing sufficiently well both the increase of strength and ductility observed in Mander et al. (1989), as shown in Figure 4.10b.

In conclusion, the plastic-damage model available in ABAQUS is able to capture most of the relevant features in the behavior of concrete in compression, i.e., the degradation of strength due to concrete crushing, the plastic lateral expansion, and the increase of resistance due to confining action, and the behavior in tension, i.e., the softening due to crack opening, and the closing and opening of cracks. Ad hoc remedies have been taken to overcome the observed limitations of the constitutive law.

4.4 Modeling of steel reinforcement

A rate-independent elasto-plasticity model with kinematic hardening available in ABAQUS (Simulia 2010) has been used to simulate the behavior of steel reinforcement. This model uses the Von Mises yield condition with an associated plastic flow. Hence, the yield function and plastic potential are defined by the same function.

$$F(\boldsymbol{\sigma},\boldsymbol{\alpha}) = \sqrt{\frac{3}{2}\left(\boldsymbol{\sigma}'-\boldsymbol{\alpha}'\right):\left(\boldsymbol{\sigma}'-\boldsymbol{\alpha}'\right)} - \sigma_y \tag{4.18}$$

in which $\boldsymbol{\sigma}'$ and $\boldsymbol{\alpha}'$ are the deviatoric part of the stress tensor, $\boldsymbol{\sigma}$, and backstress tensor, $\boldsymbol{\alpha}$, respectively, and σ_y is the yield strength. The backstress tensor controls the translation of the yield surface in the stress space due to kinematic hardening. Two types

of kinematic hardening functions are available in ABAQUS: linear and exponential. The evolution of $\boldsymbol{\alpha}$ for linear kinematic hardening is defined as

$$\dot{\boldsymbol{\alpha}} = C_l \dot{\bar{\varepsilon}}^p \frac{1}{\sigma_y} \left(\boldsymbol{\sigma}' - \boldsymbol{\alpha}' \right) \tag{4.19}$$

in which C_l is the linear hardening parameter and $\dot{\bar{\varepsilon}}^p$ is the equivalent plastic strain rate, defined as $\dot{\bar{\varepsilon}}^p = \sqrt{\frac{3}{2} \dot{\boldsymbol{\varepsilon}}^{\mathbf{p}} : \dot{\boldsymbol{\varepsilon}}^{\mathbf{p}}}$. This model requires the calibration of two parameters: σ_y and C_l. For exponential kinematic hardening, the hardening rate drops exponentially and the evolution of $\boldsymbol{\alpha}$ is defined as

$$\dot{\boldsymbol{\alpha}} = C_e \dot{\bar{\varepsilon}}^p \frac{1}{\sigma_y} \left(\boldsymbol{\sigma}' - \boldsymbol{\alpha}' \right) - \gamma_e \boldsymbol{\alpha} \dot{\bar{\varepsilon}}^p \tag{4.20}$$

in which C_e and γ_e are the exponential kinematic hardening parameters. Hence, this model requires the calibration of three parameters: σ_y, C_e, and γ_e.

The ability of the steel model with linear and exponential kinematic hardening to simulate the monotonic and cyclic axial stress-vs.-strain relations obtained experimentally for reinforcing bar coupons by Restrepo-Posada et al. (1993) is shown in Figure 4.11. The exponential hardening law approximates better the strain hardening behavior of steel, limiting the axial stress to the ultimate strength of steel, as shown in Figure 4.11a. There is no stress limit in the linear kinematic hardening law. However, none of the models can capture the yield plateau and the strength decay and bar rupture. As shown in in Figure 4.11b, the model approximates sufficiently well the cyclic hysteresis with either kinematic hardening law.

Reinforcing bars are modeled using truss or beam elements with the elasto-plastic constitutive model presented above. For cases where bending of the reinforcement is negligible, truss elements are used; otherwise, beam elements are used. For truss elements, the exponential kinematic hardening law has been used because it provides a better approximation of the strain-stress relations. For beam elements, the exponential hardening law is not available. In this case, the linear kinematic hardening law has been employed.

4.5 Finite element analysis verification examples

Finite element (FE) modeling of reinforced concrete members employing the phenomenological bond-slip model proposed in this chapter and the concrete and steel models available in ABAQUS (Simulia 2010) has been validated by experimental data. These data, obtained from Chapter 3 and from the literature, correspond to different types of pull-out tests and a test on a RC column subjected to cyclic lateral loading. For the pull-out tests, the reinforcing bars are modeled with truss elements, and in the RC column the vertical bars are modeled with beam elements. The inclination angle of the bond force, θ , is assumed to be 60 degrees unless indicated otherwise. While it is commonly assumed that the resultant of the bond resistance has a 45-degree angle with respect to the bar longitudinal axis (Cairns and Jones 1996), Tepfers and Olsson (1992) have observed from pull-out tests that this angle varies between 35 and 65 degrees, depending on the rib geometry and the intensity of the bond force. The use of a 60-degree angle is justified based on the examples described below.

Two of the basic bond-slip tests presented in Chapter 3 have been replicated with

FE models. As shown in Figure 4.12a, only one fourth of the specimen is modeled taking advantage of the axial symmetry of the specimen. As shown in Figure 4.12b and Figure 4.12c, the force-vs.-displacement relations measured during a monotonic and a cyclic test are well reproduced in FE analysis.

To evaluate the capability of the model to simulate the radial dilatation caused by the wedging action of the ribs, bond-slip tests carried out by Lundgren (2000) and Plizzari and Mettelli (2009) have been modeled. Figure 4.13 plots the comparison between the FE model and experimental results for the pull-out tests conducted by Lundgren (2000) on bars embedded in concrete cylinders confined by a steel casing. The FE analysis results show good correlation with experimental results not only for the force-displacement relations, but also for the strains measured in the steel casing when the inclination angle of the bond forces, θ , is taken as 45 degrees. If θ is equal to 60 degrees, the force-displacement relations do not vary, but the steel strains increase significantly. As shown in Figure 4.14a, the FE analysis is also able to reproduce the splitting failure of a large-diameter bar in a poorly confined specimen tested by Plizzari and Mettelli (2009) when θ is equal to 60 degrees. The splitting crack caused by the expansion of the steel-concrete interface can be observed from the maximum principal strain in the concrete, as shown in Figure 4.14b. However, if θ is taken as 45 degrees, a higher bond strength is obtained and bond fails by the pull-out of the bar from the concrete. In conclusion, the model is capable of reproducing the radial dilatation of the concrete-steel interface in an approximate manner. Based on these results and on the range of values provided in the literature, it is recommended that θ be equal to 60 degrees. This is a conservative assumption because it increases the chances of

reproducing a splitting failure.

The results obtained by Shima et al. (1989b) on a bar with long embedment length subjected to pull action have also been well replicated by the FE model. Figure 4.15 compares the FE analysis and experimental results in terms of the force-displacement relations at the loaded end of the bar, and the bar strain distribution along the embedment length. The small differences observed are related to the absence of plateau in the steel model, which characterizes the post-yield stiffness. These results show that the model is successful in predicting the bond stress distributions in long bars, including bond decay due to bar yielding.

Finally, the FE model shown in Figure 4.16 has been created to replicate the test by Lehman and Moehle (2000) on an RC column subjected to quasi-static lateral loading. In this model, the vertical bars are modeled with beam elements. The column and the footing are meshed independently and a contact condition has been imposed at their interface (see Figure 4.16b). This is a simple way in ABAQUS to introduce a discrete crack in the model at a location where large cracking is expected, and overcome the limitation of the concrete model to simulate the opening and closing of cracks, as discussed in Section 4.3.2. The results presented in Figure 4.17a show that the model is successful in predicting the lateral load capacity and force-displacement envelope. The hysteretic behavior is fairly well captured, even though the reloading branches are stiffer in the model. This difference is caused by the early closing of the cracks in the concrete model. The load decay observed at the end of the test was caused by the buckling and fracture of vertical bars at the base of the column, where a plastic hinge had formed. The model predicts the formation of the plastic hinge at the column base, but bar buckling and

fracture are not captured. Hence, the load drop observed in the test is not captured by the model. Figure 4.17b shows that the FE model provides a good prediction of the strain penetration along the development length inside the footing, which proves that bond-slip of these bars is well represented. However, the steel strains at the column-footing interface are overestimated. These differences are considered acceptable knowing that a small difference in bar stress can produce a large variation in strain in the post-yield range, and that the post-yield curve is approximated by a straight line in the model.

4.6 Summary and conclusions

A new phenomenological bond stress-vs.-slip model has been proposed in this chapter. This model requires the calibration of only three parameters and can be applied to any bar size and concrete strength. The model successfully reproduces the monotonic and cyclic bond-slip behavior of the large-diameter bars tested in this study, as well as that of smaller bars tested by others. Implemented in an interface element in ABAQUS, it has shown good accuracy in simulating the bond-slip behavior of bars in well-confined concrete members. Also, through a simple representation of the wedging action of the ribs, it can capture splitting failures and bond decay due to the lack of confinement in an approximate manner.

Table 4.1: Bond-slip model parameters

Test	τ_u MPa (ksi)		s_{peak} mm (in.)		s_R mm (in.)
	from tests	estimated	from tests	estimated	
Series 1	15.2 (2.20)	16.5 (2.40)	3.0 (0.12)	2.5 (0.10)	19.1 (0.75)
Series 2	16.2 (2.35)	16.5 (2.40)	2.8 (0.11)	3.0 (0.12)	24.9 (0.98)
Series 3	17.6 (2.55)	16.5 (2.40)	3.0 (0.12)	4.0 (0.16)	24.4 (0.96)
Series 4	23.8 (3.45)	23.4 (3.40)	- [1]	3.0 (0.12)	24.9 (0.98)
Eligehausen et al.	13.9 (2.00)	14.8 (2.15)	1.8 (0.07)	1.8 (0.07)	10.2 (0.40)
Lundgren	20.0 (2.90)	17.2 (2.50)	1.0 (0.04)	1.1 (0.04)	7.6 (0.30) [2]

[1] Monotonic bond stress-slip curve not available
[2] Value estimated

Table 4.2: Plastic-damage model calibration

Parameter	Description	Calibration
α	Controls biaxial compression strength	0.12
ψ	Dilation angle	20º
γ	Controls shape of the yield surface	1.91
w_c	Compression recovery factor	0
w_t	Tension recovery factor	1

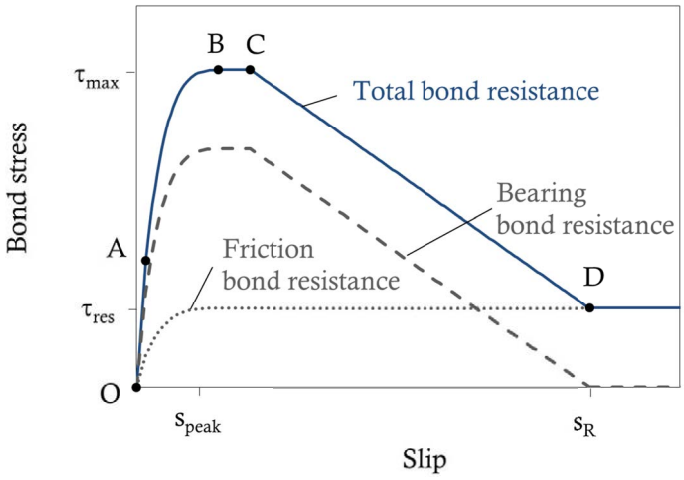

(a) monotonic response

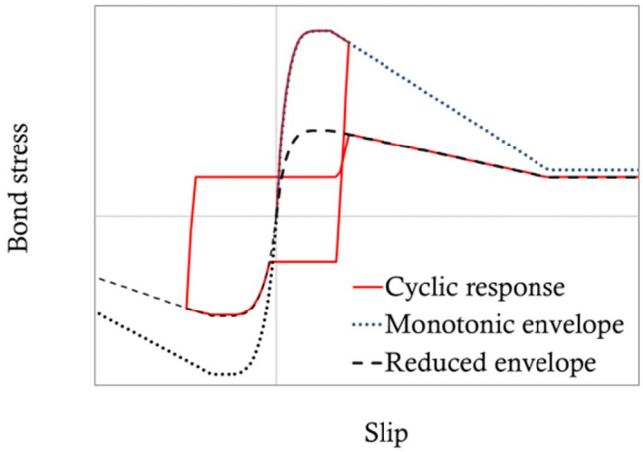

(b) cyclic response

Figure 4.1: Analytical bond stress-slip model

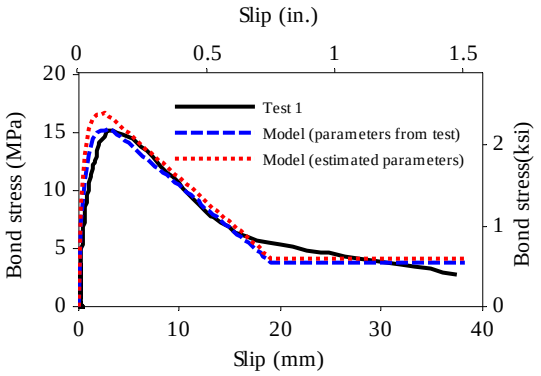

(a) No. 11, Series 1

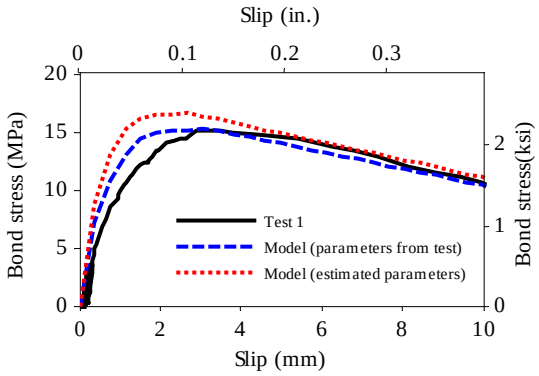

(b) Enlargement of (a) near origin

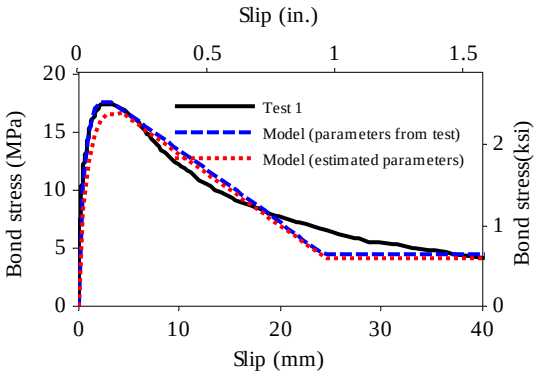

(c) No. 18, Series 3

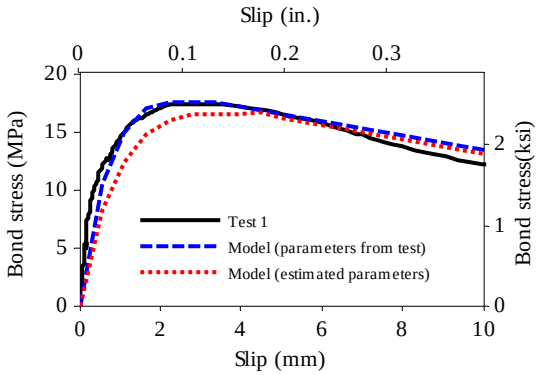

(d) Enlargement of (c) near origin

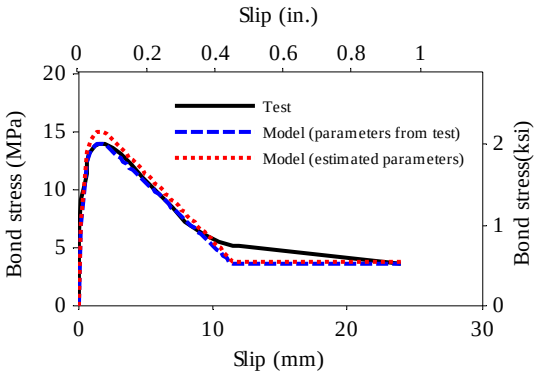

(e) No. 8, Eligehausen et al.

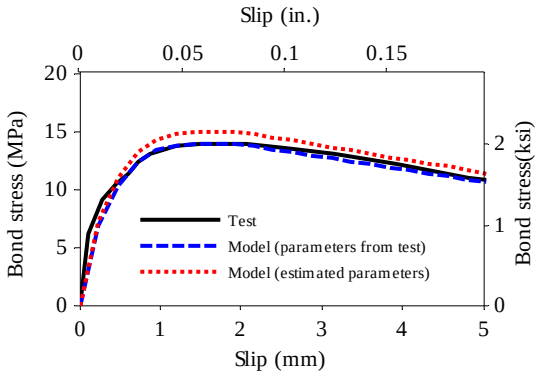

(f) Enlargement of (e) near origin

Figure 4.2: Analytical and experimental results for monotonic loading

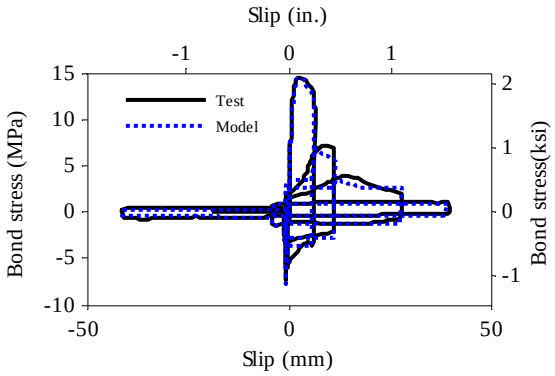

(a) Test 4, Series 1

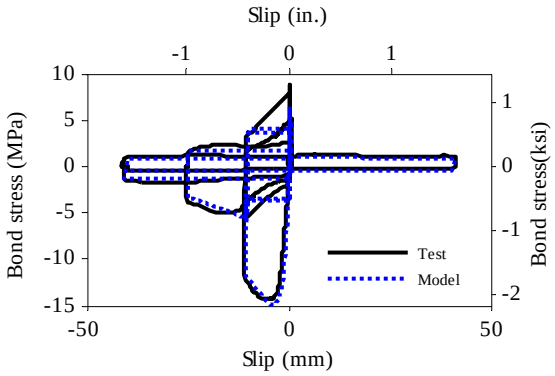

(b) Test 5, Series 3

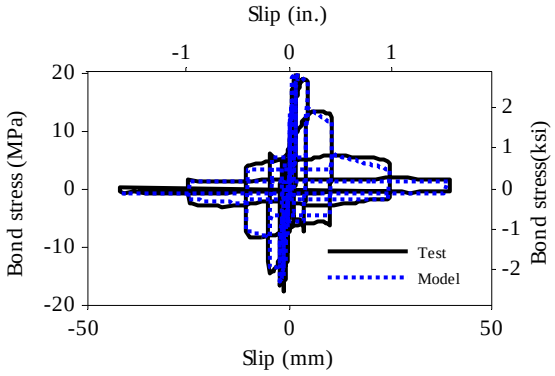

(c) Test 4, Series 4

Figure 4.3: Analytical and experimental results for cyclic loading

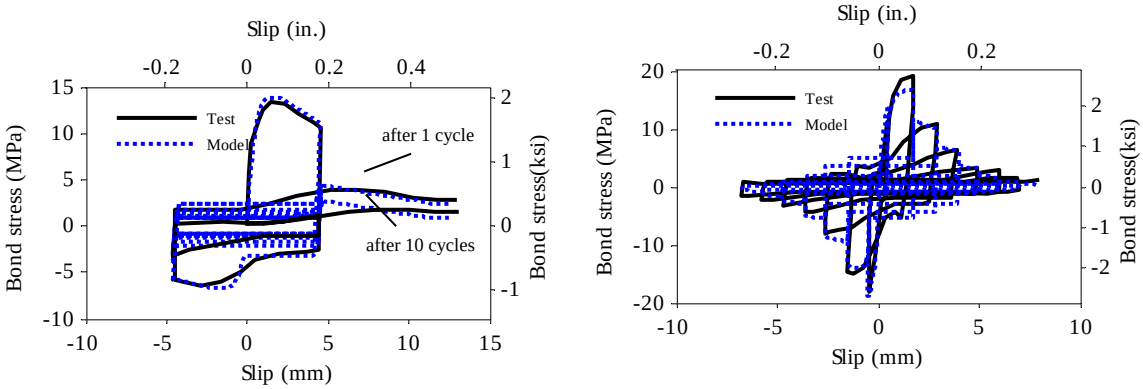

(a) No. 8 bar tested by Eligehausen et al. (b) No. 5 bar tested by Lundgren

Figure 4.4: Analytical and experimental results for tests conducted on No. 8 and 5 bars

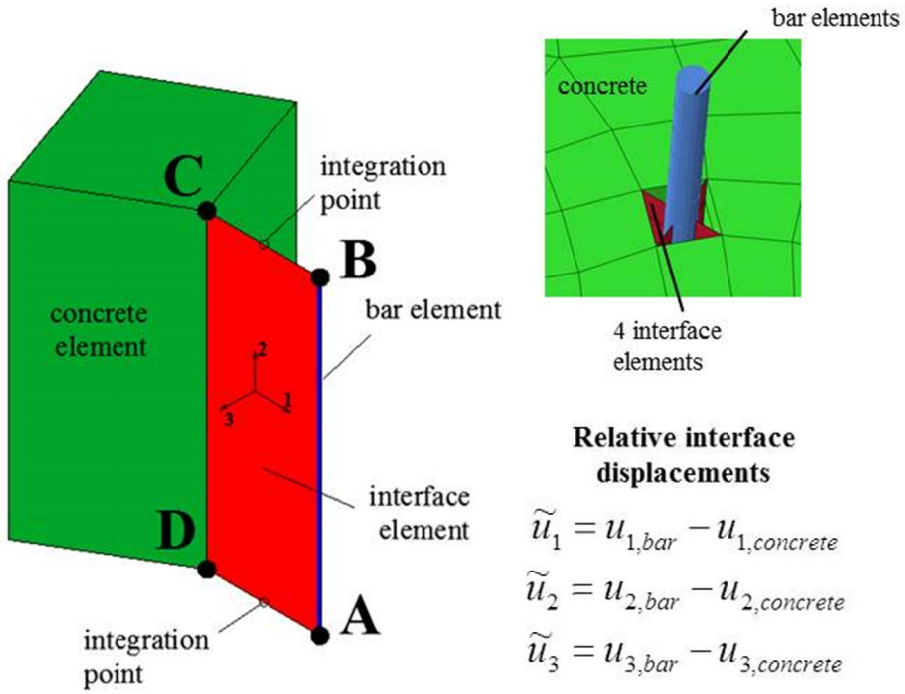

Figure 4.5: Interface element

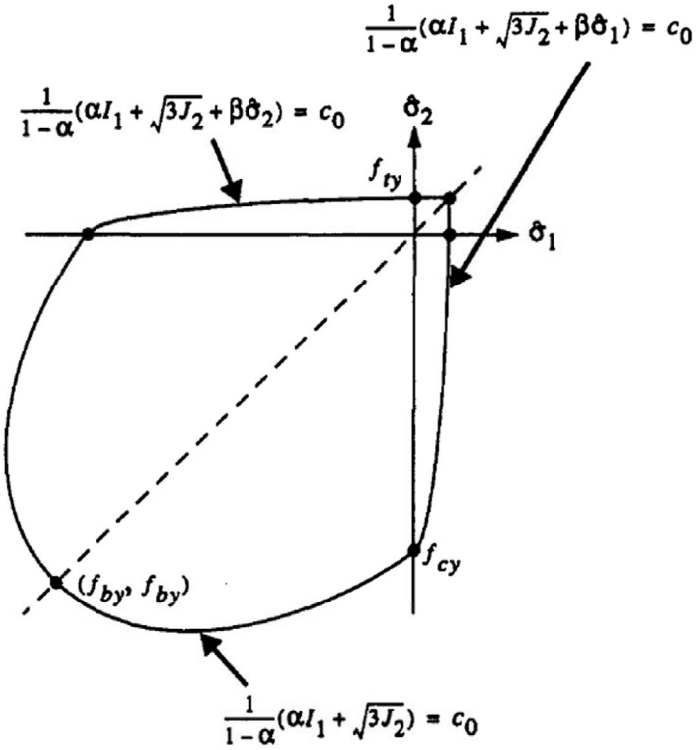

Figure 4.6: Initial yield function in plane-stress space (Lee and Fenves 1998)

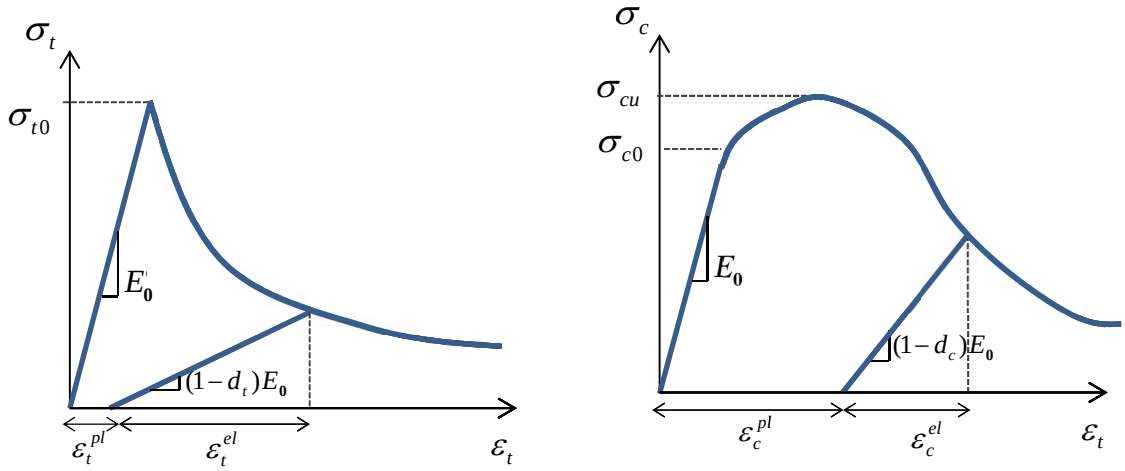

(a) uniaxial tension (b) uniaxial compression

Figure 4.7: Uniaxial tension and compression behavior in plastic-damage model

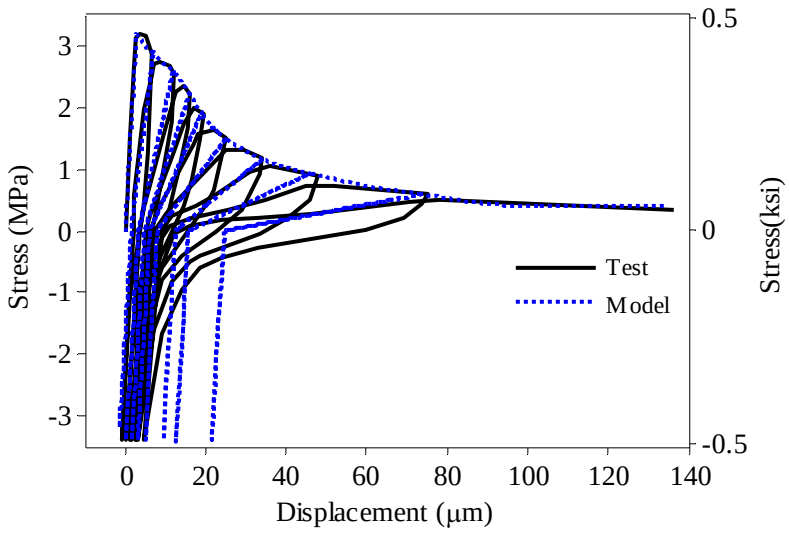

Figure 4.8: Tension-compression tests by Reinhardt (1984b)

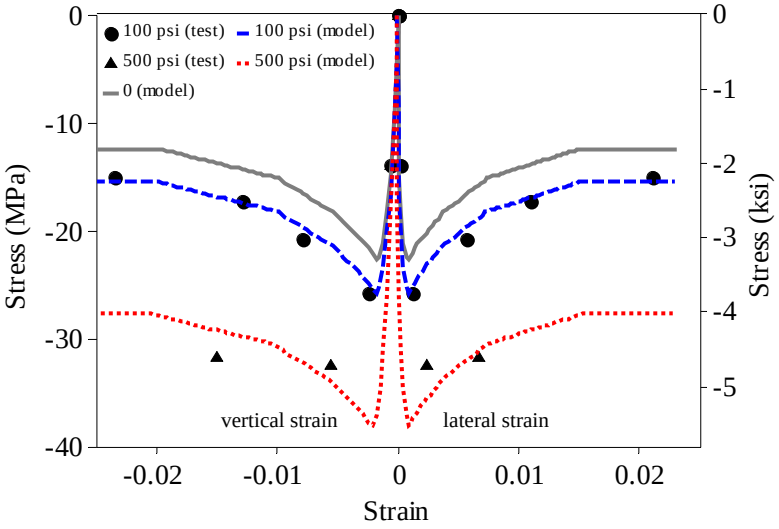

Figure 4.9: Confined compression tests by Hurblut (1985)

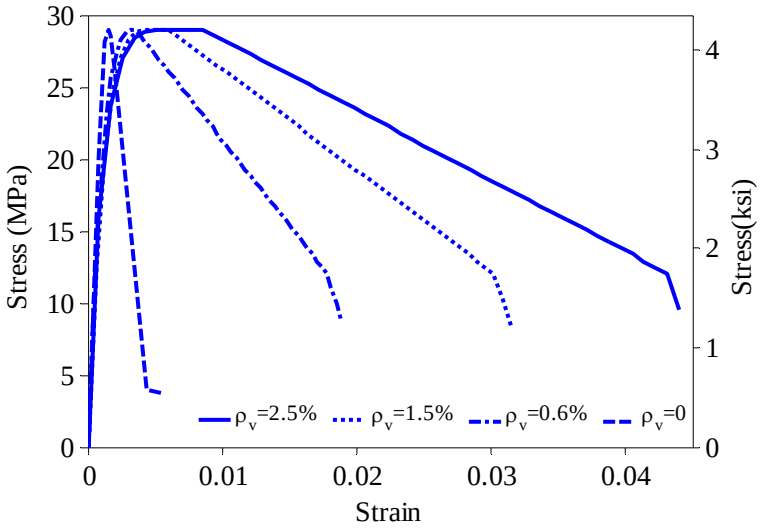

(a) Uniaxial compression curve input in concrete model

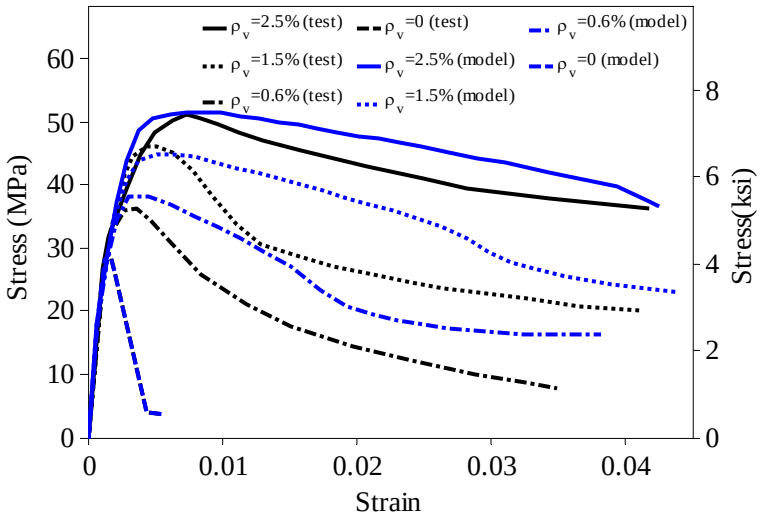

(b) Comparison between model and experimental results

Figure 4.10: Compression tests by Mander et al. (1989) on RC columns with different transverse reinforcement

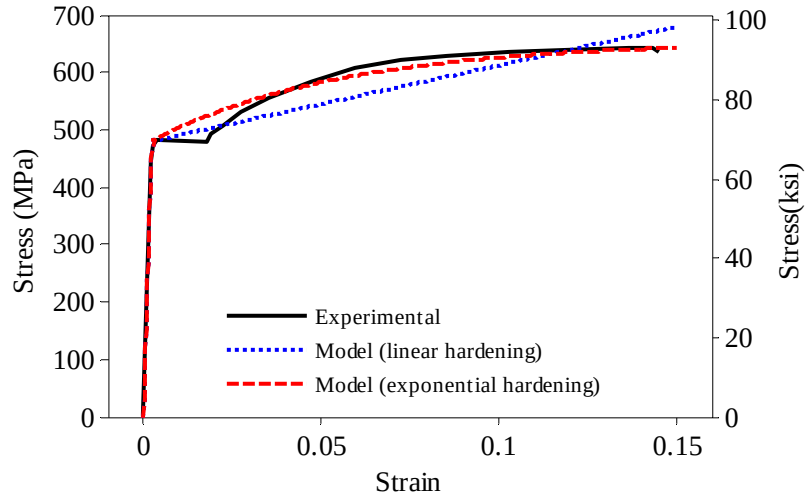

(a) Monotonic loading

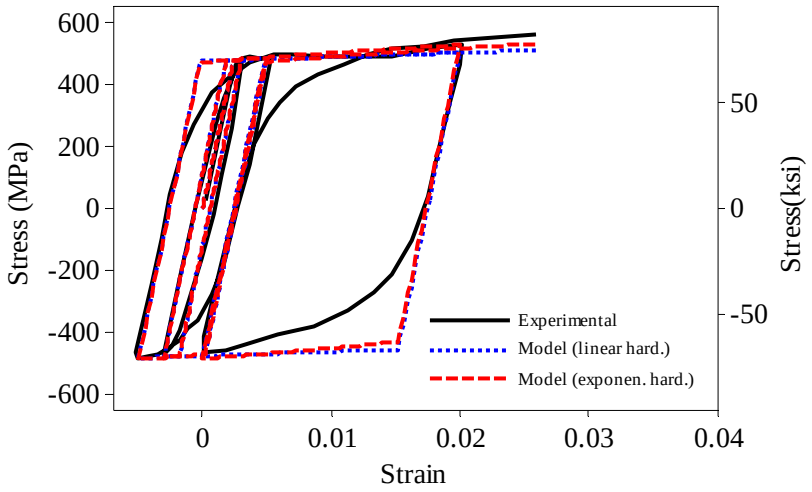

(b) cyclic loading

Figure 4.11: Uniaxial tests on reinforcing steel coupons by Restrepo-Posada et al. (1993)

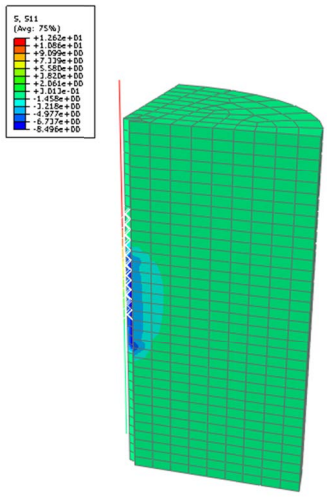

(a) FE model of test specimen

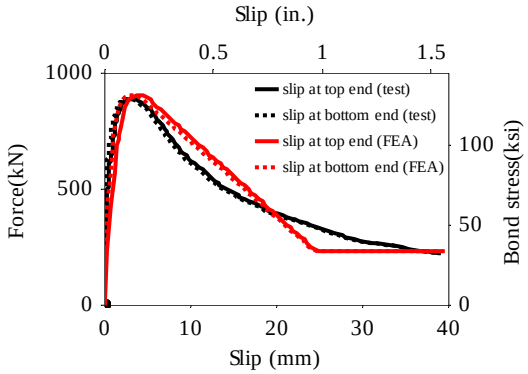

(b) Force vs. displacement for monotonic test (Test 1)

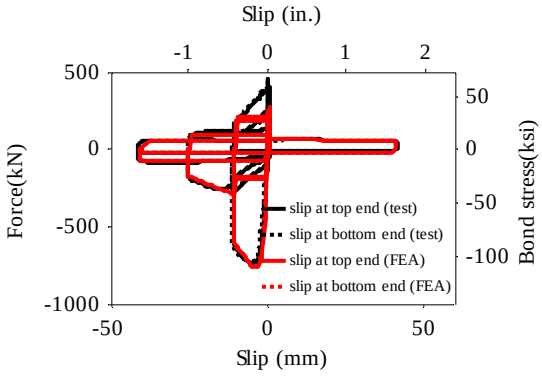

(c) Force vs. displacement for cyclic test (Test 5)

Figure 4.12: FE analysis of bond-slip tests on No. 18 bars

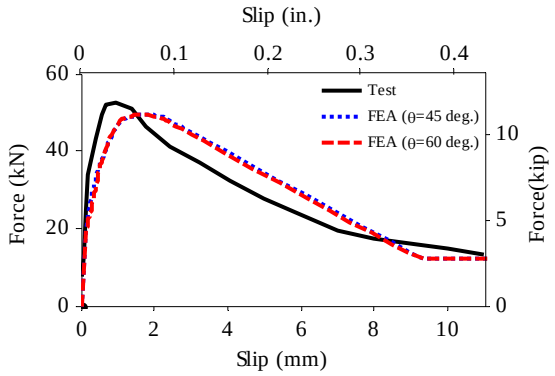

(a) Force-slip relations in monotonic test

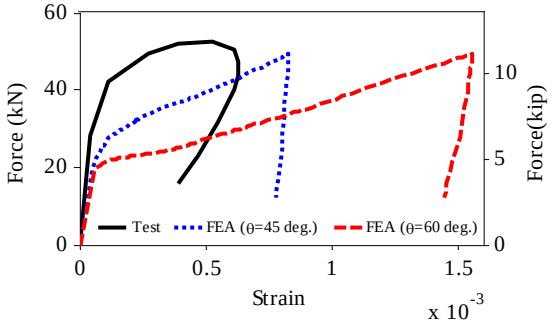

(b) Strain in steel casing during monotonic test

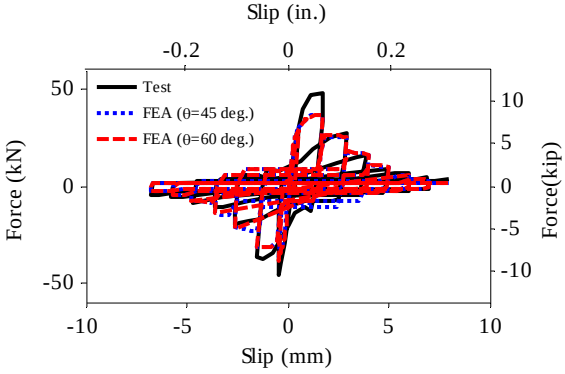

(c) Force-slip relations in cyclic test

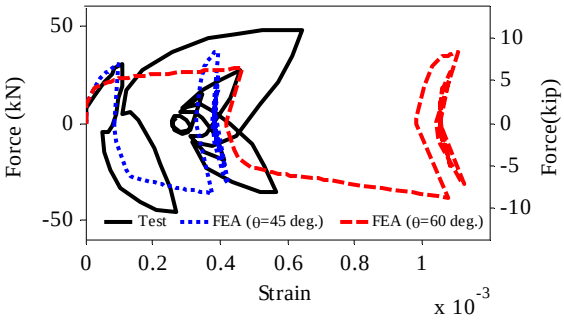

(d) Strain in steel casing during cyclic test

Figure 4.13: FE analysis of pull-out tests by Lundgren (2000)

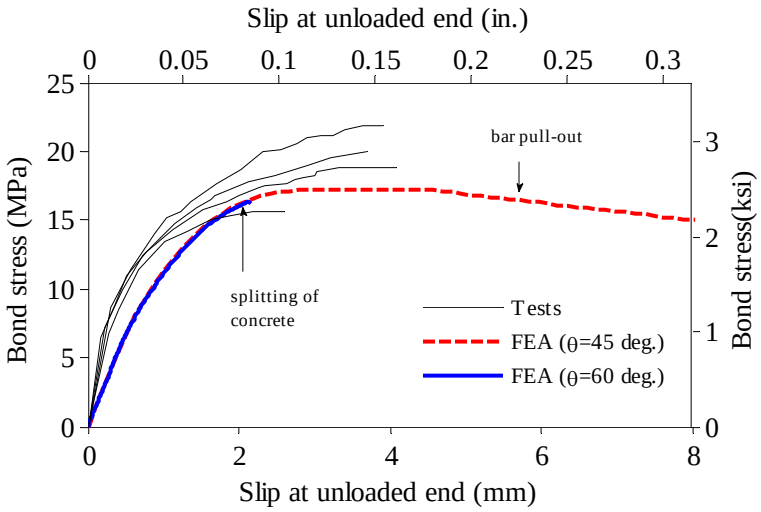

(a) Bond stress vs. slip at unloaded end

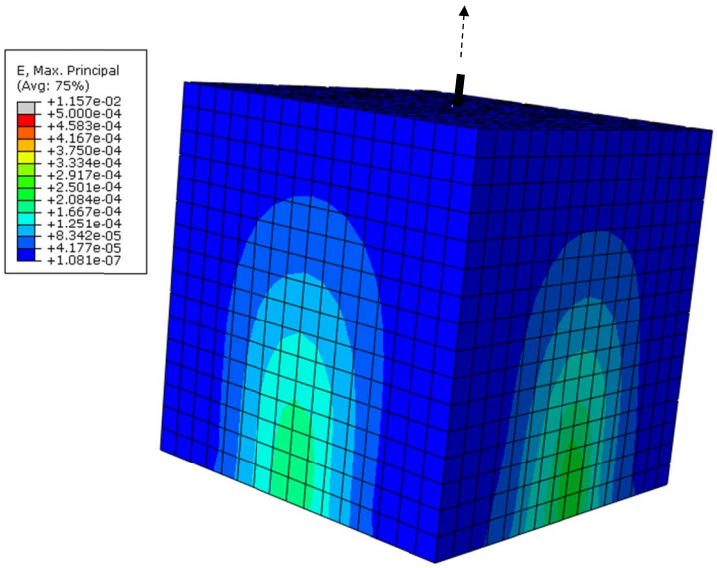

(b) Maximum principal strains in concrete from FE model at 2-mm slip (θ = 60 degrees)

Figure 4.14: FE analysis of pull-out tests by Plizzari and Mettelli (2009)

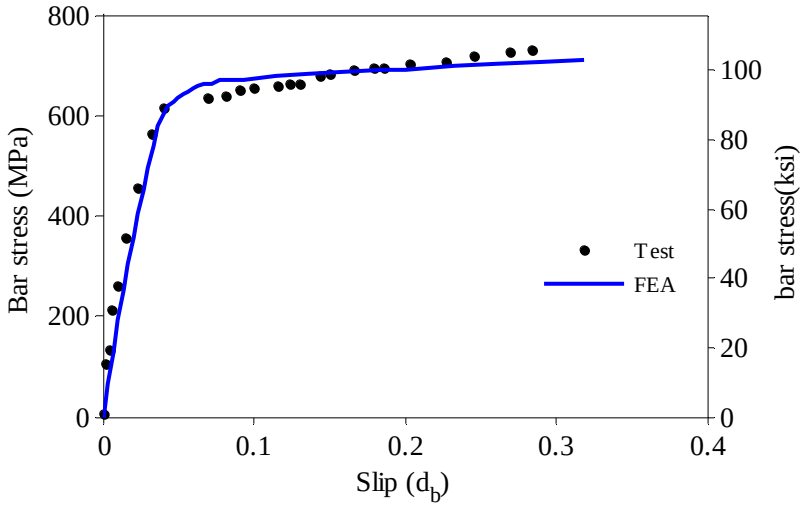

(a) Bar stress vs. displacement at loaded end

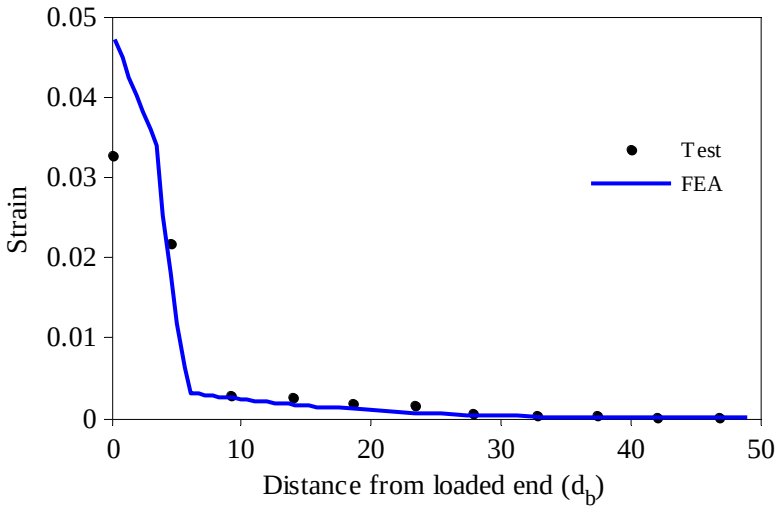

(b) Strain distribution at slip=0.225d_b

Figure 4.15: FE analysis of pull-out tests by Shima et al. (1989b)

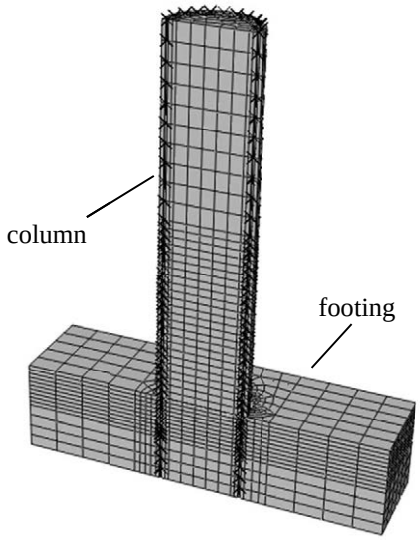

(a) Global view of the FE model

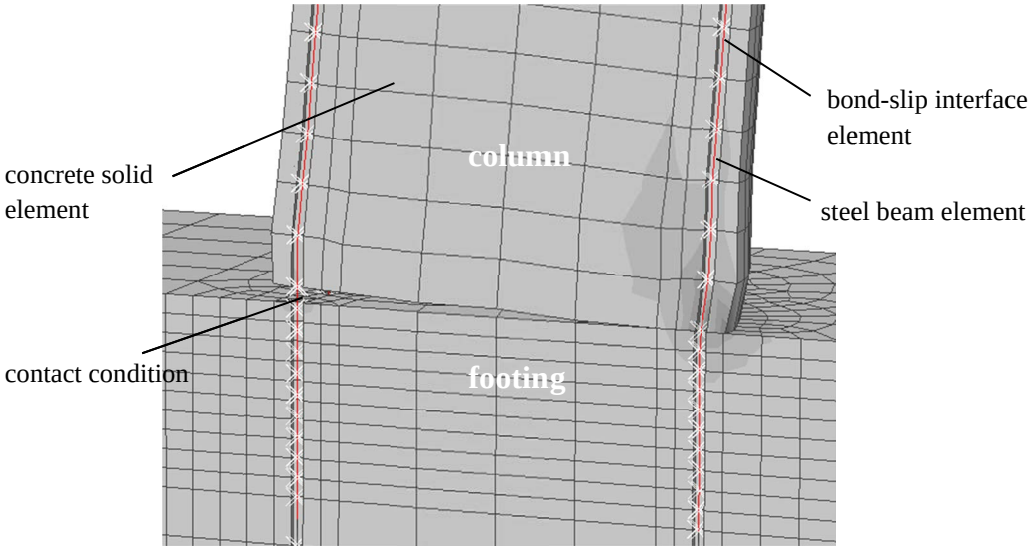

(b) Close-view of the deformed shape of the column-footing interface

Figure 4.16: FE model of RC column tested by Lehman and Moehle (2000)

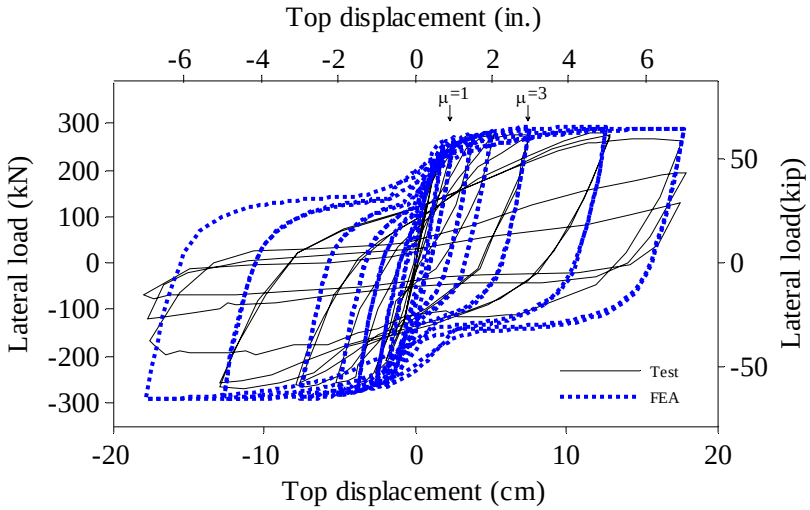

(a) Lateral load vs. top displacement

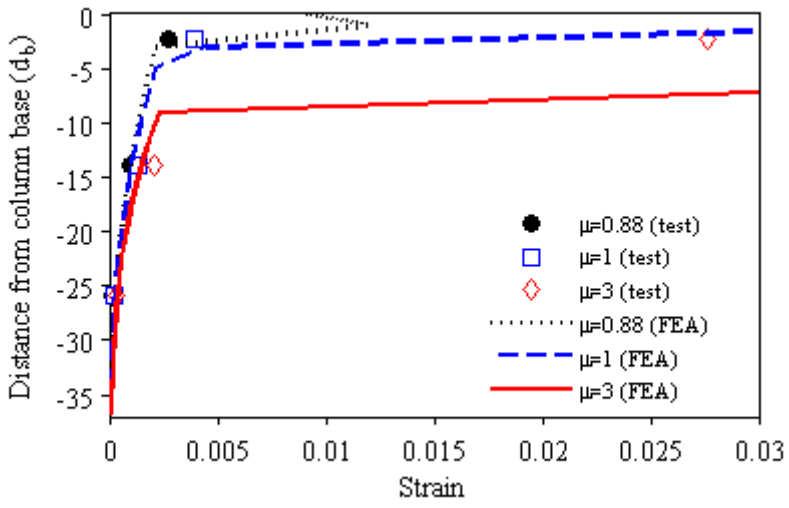

(b) Strain penetration of vertical reinforcement into footing

Figure 4.17: FE analysis of RC column tested by Lehman and Moehle (2000)

CHAPTER 5

ELASTO-PLASTIC DILATANT INTERFACE MODEL FOR CYCLIC BOND-SLIP BEHAVIOR

Elasto-plastic dilatant interface formulations have been used by many researchers to model the fracture behavior of quasi-brittle materials, e.g., see Lofti and Shing (1994), Carol et al. (1997), Puntel et al. (2006), and Koutromanos and Shing (2012). In these formulations, mixed-mode fracture is governed by a failure surface defined in a stress space with its coordinates corresponding to the normal and shear stresses on the interface; and shear sliding and shear dilatation due to the wedging action of joint asperities can be modeled with a plastic flow rule. Shear dilatation can also be directly treated as a reversible geometric phenomenon under slip reversals. This modeling approach is also attractive for simulating the interaction between a reinforcing bar and the surrounding concrete, which is dominated by the wedging action of the bar ribs against the surrounding concrete. However, bar ribs have a different scale and higher strength and stiffness than the asperities in cracks and joints in quasi-brittle materials. Bar slip involves a number of mechanisms including the sliding between the concrete and steel surfaces, the crushing and shearing of the concrete between the ribs, and the opening of

transverse cracks at the top of the ribs. To account for these mechanisms, dedicated dilatant interface formulations are needed. To date, only a few such models have been proposed. These include the work of Herrmann and Cox (1994), Cox and Herrmann (1998, 1999), Lundgren and Magnusson (2001), Lundgren (2005), and Serperi and Alfano (2011), as discussed in Chapter 2.

A new elasto-plastic dilatant interface model is presented in this chapter to simulate the cyclic bond-slip behavior of deformed bars. This model adopts a theoretical formulation that closely reflects the physics of the problem and can be applied to a broader range of confinement situations than the phenomenological bond-slip model presented in Chapter 4. The model is intended to overcome some limitations in the above-mentioned models of this kind, which include the lack of a unified formulation for monotonic and cyclic behaviors, or the inability to simulate both splitting and pull-out failures in an accurate manner. A multi-surface plasticity formulation is used here to model the two major inelastic deformation mechanisms in bond-slip, namely, the crushing and shearing of the concrete between the bar ribs, and the sliding between the concrete and bar surfaces. These two mechanisms are represented by different yield surfaces and plastic flow rules. The flow rules account for the shear dilatation of the interface to simulate the wedging action of the ribs.

5.1 Multi-surface plasticity formulation

The interaction between a reinforcing bar and the surrounding concrete is modeled using an interface element, as shown in Figure 5.1a. The relation between the

relative displacements, $\mathbf{d} = \{d_n \quad d_t\}^T$, and stresses, $\boldsymbol{\sigma} = \{\sigma \quad \tau\}^T$, at the interface is governed by an elasto-plastic formulation. Accordingly, the relative interface displacements are decomposed into an elastic and a plastic component, i.e., $\mathbf{d} = \mathbf{d}^e + \mathbf{d}^p$. The stress is linearly related to the elastic interface displacements.

$$\boldsymbol{\sigma} = \mathbf{D}^{\mathbf{e}}\mathbf{d}^{\mathbf{e}} \tag{5.1}$$

in which $\mathbf{D}^{\mathbf{e}}$ is a diagonal elastic stiffness matrix.

$$\mathbf{D}^{\mathbf{e}} = \begin{bmatrix} D_{nn} & 0 \\ 0 & D_{tt} \end{bmatrix} \tag{5.2}$$

The yield condition is a function of the stress vector, $\boldsymbol{\sigma}$, and a set of internal variables, collected in a vector $\mathbf{q}$.

$$F(\boldsymbol{\sigma}, \mathbf{q}) = 0 \tag{5.3}$$

A non-associative flow rule is defined to determine the rate of plastic displacement:

$$\dot{\mathbf{d}}^{\mathbf{p}} = \dot{\lambda}\mathbf{m} \tag{5.4}$$

in which $\dot{\lambda}$ is a plastic multiplier, and $\mathbf{m}$ is a vector that defines the direction of the plastic flow. Plastic flow complies with the Kuhn-Tucker conditions, which are $F \le 0$, $\dot{\lambda} \ge 0$, and $F\dot{\lambda} = 0$, and the consistency condition, $\lambda\dot{F} = 0$. A generalization of these conditions for multi-surface plasticity can be found in Simo and Hughes (1998). For n yield functions, there are n plastic multipliers $\dot{\lambda}_i$ that satisfy the following conditions for $i = 1, \ldots, n$.

$$F_i(\boldsymbol{\sigma}, \mathbf{q}) = 0, \quad \dot{\lambda}_i \ge 0, \quad F_i\dot{\lambda}_i = 0 \tag{5.5}$$

$$\lambda_i\dot{F}_i(\boldsymbol{\sigma}, \mathbf{q}) = 0 \tag{5.6}$$

Here, three yield functions are considered. One represents the crushing and shearing of the concrete between bar ribs leading to a pull-out of the bar, which is called Plastic Mode A, as shown in Figure 5.1b. The other two govern the initiation of sliding at the concrete-steel interface, which is called Plastic Mode B, as shown in Figure 5.1c. Bond failure in Mode B corresponds to a situation of low confinement related to the development of radial splitting cracks in the surrounding concrete. The corresponding yield surfaces are shown in Figure 5.2. The yield condition $F_A = 0$ governs Mode A, while $F_B^+ = 0$ governs Mode B when sliding is in the positive direction, and $F_B^- = 0$ is for sliding in the negative direction. These yield functions and their corresponding flow rules are described in the following sections.

5.1.1 Plastic Mode A: crushing and shearing of concrete between ribs

The resisting mechanism associated to Mode A is the interlocking action of the concrete with the ribs. The resistance provided by the interlocking action is lowered as the concrete between ribs is crushed and sheared off as shown in Figure 5.1b. Based on the analysis of experimental data from pull-out tests in which bond failed by crushing and shearing of the concrete between ribs, Cox and Herrmann (1998) have concluded that the bond resistance increases with the normal confining stress, but that the relation between the bond resistance and the confinement stress is not exactly linear. Based on their observation, the following yield function is proposed for Mode A failure. It is expressed in a dimensionless form by normalizing the stress quantities by the compressive strength of concrete , f_c'.

$$F_A = \left| \frac{\tau}{f_c'} \right|^{k_1} - \left(\frac{c}{f_c'} \right)^{k_1} + \mu_A \frac{\sigma}{f_c'} \tag{5.7}$$

in which the parameter c governs the position of the yield surface, and the parameter μ_A and the index k_1 govern the increase of the shear resistance with the normal stress. The resulting yield surface $F_A = 0$ is shown in Figure 5.3. The deterioration of the bond resistance due to the shearing and crushing of the concrete between ribs is controlled by the decrease of the values of c and μ_A as a function of the plastic deformation, which causes the yield surface to shift and shrink, as shown in Figure 5.3. The following softening rules are defined to control the evolution of c and μ_A.

$$c = c_0 < 1 - \frac{p^+ + p^-}{s_R} > \tag{5.8a}$$

$$\mu_A = \mu_{A,0} e^{-k_2 \frac{p^+ + p^-}{s_R}} \tag{5.8b}$$

where c_0 is the initial value of c, $\mu_{A,0}$ is the initial value of μ_A, s_R is the clear rib spacing, k_2 is a constant controlling the decrease of the value of μ_A, and p^+ and p^- are the plastic tangential displacements (slips) associated with Mode A in the positive and negative direction, respectively. These two variables are initially zero, and their evolution is related to the increment of plastic tangential displacements caused by Mode A, $\dot{d}_t^{\,p}\big|_A$, as follows.

$$\dot{p}^+ = < \dot{d}_t^{\,p}\big|_A > \tag{5.9a}$$

$$\dot{p}^- = < -\dot{d}_t^{\,p}\big|_A > \tag{5.9b}$$

As shown in Equation 5.8a, c is assumed to decay linearly to zero when the total bar slip caused by Mode A, $p^+ + p^-$, is equal to the clear rib spacing, s_R, representing the condition that all the concrete between ribs has been damaged by crushing and shearing. At this stage, only the frictional resistance remains. As shown in Equation 5.8b, μ_A is assumed to decay exponentially to zero as the total plastic slip increases to represent the smoothening of the interface.

The parameters in the yield function are calibrated by assuming that under a low confinement stress, the crushing and shearing failure of concrete is governed by a Mohr-Coulomb condition with a cohesion parameter, $\hat{c}$, and an internal friction angle, ϕ. These two parameters can be expressed in terms of the concrete compressive strength, f_c', and tensile strength, f_t', as follows.

$$\hat{c} = 0.5\sqrt{f_c' f_t'} \tag{5.10a}$$

$$\phi = \sin^{-1}\left(\frac{f_c' - f_t'}{f_c' + f_t'}\right) \tag{5.10b}$$

Equation 5.10 can be obtained from the failure conditions for uniaxial compression and tension, as shown in Figure 5.4a. Setting the initial yield surface for Mode A tangent to the Coulomb failure surface at $\sigma = 0$, as shown in Figure 5.4b, c_0 and $\mu_{A,0}$ can be determined as

$$c_0 = 0.5\sqrt{f_c' f_t'} \tag{5.11a}$$

$$\mu_{A,0} = 0.5^{k_1} k_1 \left(f_c' - f_t'\right) f_c'^{-0.5k_1} f_t'^{(0.5k_1 - 1)} \tag{5.11b}$$

Malvar (1992) has observed in his pull-out tests that bar slip will initially induce a radial expansion of the surrounding concrete, which is then followed by compaction as the concrete between the ribs is severely damaged. To account for this behavior, the following plastic flow vector $\mathbf{m}_A$ is proposed.

$$\mathrm{m}_A = \begin{Bmatrix} k_3 \left\langle 1 - \frac{\langle -\sigma \rangle}{f_c'} \right\rangle e^{-k_4 \frac{p^+ + p^-}{h_R}} - k_5 \frac{\langle -\sigma \rangle}{f_c'} \frac{\langle r \rangle}{h_R} \\ 1 \cdot sign(\tau) \end{Bmatrix} \tag{5.12}$$

in which k_3, k_4, and k_5 are constants, h_R is the height of the ribs, and r represents the net interface opening caused by this plastic mode. Initially, r is zero, and its evolution depends on the increment of the plastic normal displacement caused by Mode A, $\dot{d}_n^p\big|_A$, as follows.

$$\dot{r} = \dot{d}_n^p\big|_A \tag{5.13}$$

In Equation 5.12, the first element in the vector represents the dilatation caused by the dislocation of the crushed concrete particles. This term diminishes linearly with the magnitude of the confining stress σ (normalized by the compressive strength of concrete), and exponentially with the bar slip (normalized by the rib height) caused by this plastic mode. The second element in the vector controls the compaction caused by the gradual smoothening of the interface due to bar slip. The rate of smoothening increases linearly with the magnitude of the confining stress (normalized by the compressive strength of concrete) and the net opening of the interface r (normalized by the rib height) caused by the dislocation of the crushed particles.

5.1.2 Plastic Mode B: sliding at the concrete-steel surface

Plastic Mode B will dominate when the concrete around a bar has low confinement so that bond failure will be governed by radial splitting cracks in the surrounding concrete rather than the crushing and shearing of the concrete between the ribs. In this case, bond resistance between the concrete and steel is assumed to be governed by a Mohr-Coulomb law with no cohesion and a constant friction coefficient μ_B for the contact surface. Due to the existence of the bar ribs, contact between the concrete and steel can take place on the inclined surface of the ribs, as shown on Figure 5.1c, or on a plane parallel to the bar axis between the bar ribs. The Coulomb law for sliding along a plane is expressed as

$$F_B = |\tau'| + \mu_B \sigma' = 0 \tag{5.14}$$

in which σ' and τ' are the normal and shear stresses perpendicular and parallel to the sliding plane. Based on equilibrium conditions, Equation 5.14 can be expressed in terms of the normal and shear stresses, σ and τ, perpendicular and parallel to the axis of the bar.

$$F_B = |\tau \cos\alpha + \sigma \sin\alpha| + \mu_B (\sigma \cos\alpha - \tau \sin\alpha) = 0 \tag{5.15}$$

in which α is the angle of inclination of the contact surface with respect to the axis of the bar. This angle is defined positive for the surface on the left side of the rib and negative for the surface on the right. By rearranging Equation 5.15, one can obtain two yield conditions. For the sliding of the concrete towards right, which is defined as positive sliding, one has the following yield condition.

$$F_B^+ = \tau + \mu_{B,eff}^+ \sigma = 0 \tag{5.16a}$$

where $\mu^{+}_{B,eff}$ is the effective friction coefficient for positive sliding, which depends on the coefficient of friction μ_B of the contact surface and the angle α as follows.

$$\mu^{+}_{B,eff} = \frac{\mu_B \cos\alpha + \sin\alpha}{\cos\alpha - \mu_B \sin\alpha} \tag{5.16b}$$

Equation 5.16b requires that $\cos\alpha > 0$ and $\tan\alpha < 1/\mu_B$.The yield condition for negative sliding (concrete slides towards the left) can be expressed as

$$F^{-}_{B} = -\tau + \mu^{-}_{B,eff}\sigma = 0 \tag{5.17a}$$

where $\mu^{-}_{B,eff}$ is the effective friction coefficient for negative sliding, which depends on μ_B and α as follows.

$$\mu^{-}_{B,eff} = \frac{\mu_B \cos\alpha - \sin\alpha}{\cos\alpha + \mu_B \sin\alpha} \tag{5.17b}$$

Equation 5.17b requires that $\cos\alpha > 0$ and $\tan\alpha > -1/\mu_B$. The above yield surfaces for sliding are two straight lines as shown in Figure 5.5. These lines rotate with respect to the origin of the $\sigma - \tau$ plane as α changes.

The value of α is defined by a smooth function that depends on the geometry of the bar surface. The initial shape of this function is shown in Figure 5.6a. This function is defined by the rib height, h_R, the maximum inclination of the lateral face of the ribs, α_0, and, the horizontal length of the inclined plane, $u_{\lim}$. The function provides smooth transitions between sliding on the left and right ribs, and the lateral (inclined) face and top (horizontal) face of the ribs. In these transition zones, the inclination angle varies linearly with the horizontal distance. The length of these transition zones are equal to u_{trans}, as shown in Figure 5.6a. It is assumed that $u_{trans} = 0.05u_{\lim}$ and

$u_{\lim} = h_R / \left(0.9\tan\alpha_0 - 0.05\ln\left|\cos\alpha_0\right| / \alpha_0\right)$ to ensure that this geometry results in the correct rib height.

When the pull-out mechanism (Mode A) is activated, the shape of the contact surface is modified to reflect concrete damage. A gap develops between the concrete and the ribs due to concrete crushing. As a result, the transition zone between the left and right inclined planes is expanded as shown Figure 5.6b. The length of the horizontal expansion is equal to the sum of the total bar slip caused by Mode A, p^+ and p^-. The contact geometry shown in Figure 5.6 can be expressed as

$$\alpha(s) = \begin{cases} 0 & s + p^+ \le -u_{\lim} \\ \alpha_0 \dfrac{s - u_{\lim} + p^+}{u_{trans}} & -u_{\lim} < s + p^+ \le -u_{\lim} + u_{trans} \\ -\alpha_0 & -u_{\lim} + u_{trans} < s + p^+ \le -u_{trans} \\ \alpha_0 \dfrac{s + p^+}{u_{trans}} & -u_{trans} < s + p^+ \le 0 \\ 0 & -p^+ < s \le p^- \\ \alpha_0 \dfrac{s - p^-}{u_{trans}} & 0 < s - p^- \le u_{trans} \\ \alpha_0 & u_{trans} < s - p^- \le u_{\lim} - u_{trans} \\ \alpha_0 \dfrac{u_{\lim} - s + p^-}{u_{trans}} & u_{\lim} - u_{trans} < s - p^- \le u_{\lim} \\ 0 & s - p^- > u_{\lim} \end{cases} \tag{5.18}$$

in which s is the plastic tangential displacement due to Mode B sliding. This variable is initially zero, and its value depends on the increment of the plastic tangential displacement caused by Mode B, $\dot{d}_t^{\,p}\Big|_B$, as

$$\dot{s} = \dot{d}_t^{\,p}\Big|_B \tag{5.19}$$

For Mode B, the only plastic displacement is the sliding on the contact plane defined by the inclination angle α , which can be zero or non-zero depending on the position of contact. Hence, the plastic flow vector $\mathbf{m}_B$ for F_B^+ has the following expression:

$$\mathbf{m}_{B+} = \begin{Bmatrix} \tan\alpha \\ 1 \end{Bmatrix} \tag{5.20}$$

and for F_B^- , it is

$$\mathbf{m}_{B-} = -\begin{Bmatrix} \tan\alpha \\ 1 \end{Bmatrix} \tag{5.21}$$

However, if the elastic trial stress, $\boldsymbol{\sigma}^e$, in the stress update algorithm is such that $\sigma^e > 0$ and $\frac{\tau^e}{D_{tt}}\tan\alpha < \frac{\sigma^e}{D_{nn}}$, the return to the yield surface will not be possible with the flow rules defined in Equations 5.20 and 5.21. To assure a correct stress return to the apex of the yield surface and ensure the continuity of the plastic flow in the stress space, the plastic flow vector assumes the following form.

$$\mathbf{m}_B = \sqrt{\frac{1+\tan^2\alpha}{\left(\sigma^e/D_{nn}\right)^2 + \left(\tau^e/D_{tt}\right)^2}} \begin{Bmatrix} \sigma^e/D_{nn} \\ \tau^e/D_{tt} \end{Bmatrix} \tag{5.22}$$

5.2 Stress update algorithm

The elasto-plastic formulation has been implemented numerically for a displacement-driven situation. Given the stress vector, $\boldsymbol{\sigma}_m$, internal variables,

$\mathbf{q}_m = \left\{ p_m^+ \quad p_m^- \quad r_m \quad c_m \quad \mu_{A,m} \quad s_m \right\}^T$, the displacement vector, $\mathbf{d}_m$, and the displacement increment, $\Delta\mathbf{d}$, at step m, the stresses, $\boldsymbol{\sigma}_{m+1}$, and internal variables, $\mathbf{q}_{m+1}$, at step $m+1$ are to be calculated. To this end, an elastic predictor - plastic corrector algorithm is used. Hence, the stress update is a two-step procedure defined by Equation 5.23.

$$\boldsymbol{\sigma}^e_{m+1} = \boldsymbol{\sigma}_m + \mathbf{D}^e \Delta\mathbf{d} \tag{5.23a}$$

$$\boldsymbol{\sigma}_{m+1} = \boldsymbol{\sigma}^e_{m+1} - \mathbf{D}^e \Delta\mathbf{d}^p \tag{5.23b}$$

The first equation represents the elastic predictor and the second is the plastic corrector. The increment of the plastic strains, $\Delta\mathbf{d}^p$, is obtained with the generalized mid-point rule (Ortiz and Popov 1985), which results in the following equation.

$$\boldsymbol{\sigma}_{m+1} = \boldsymbol{\sigma}^e_{m+1} - \Delta\lambda \mathbf{D}^e \left[(1-\theta)\mathbf{m}_m + \theta \mathbf{m}_{m+1} \right] \tag{5.24}$$

in which $0 \le \theta \le 1$. The internal variables are also updated with the generalized mid-point rule.

$$\mathbf{q}_{m+1} = \mathbf{q}_m + \Delta\lambda \left[(1-\theta) \left(\frac{\partial \mathbf{q}}{\partial \mathbf{d}^p} \right)_m + \theta \left(\frac{\partial \mathbf{q}}{\partial \mathbf{d}^p} \right)_{m+1} \right] \left[(1-\theta)\mathbf{m}_m + \theta \mathbf{m}_{m+1} \right] \tag{5.25}$$

Hence, the elastic predictor-plastic corrector method results in a nonlinear problem defined by $F(\boldsymbol{\sigma}_{m+1}, \mathbf{q}_{m+1}) = 0$ and Equations 5.24 and 5.25, which has to be solved iteratively to find $\Delta\lambda$. The exact forms of Equations 5.24 and 5.25 depend on the specific yield surface and flow rule used for the plastic correction. The plastic correction is to bring the stress state from the elastic prediction back to the yield surface. Figure 5.7 shows three possible return scenarios for $\tau > 0$: (a) return to the yield surface corresponding to Mode A ($F_A = 0$), (b) return to the yield surface corresponding to

Mode B ($F_B^+ = 0$), and (c) return to the intersection of the above two yield surfaces ($F_A = 0$ and $F_B^+ = 0$). Similar return possibilities exist for $\tau < 0$.

The stress-update algorithm developed in this study adopts a simple return-mapping strategy to determine the stress return to an appropriate yield surface. This algorithm is shown in Figure 5.8. In essence, an admissible stress solution should satisfy both conditions that $F_A \le 0$ and $F_B^{\pm} \le 0$, and it should be represented by one of the three cases shown in Figure 5.7 if plastic deformation occurs in any step m. The stress return to one of the yield surfaces is valid if it is also admissible with respect to the other yield condition. If no valid stress return is found or the stress returns to Mode A and Mode B yield surfaces are both admissible solutions, the stress is returned to the intersection of these two yield surfaces. As a result, the scheme is objective in that the solution will not depend on which yield condition is checked first. The equations corresponding to each of the possible three stress returns are provided in the following sections.

5.2.1 Return mapping to Yield Surface A

To have the stress state returned to the yield surface corresponding to Mode A, the plastic correction based on the mid-point rule is expressed as:

$$\sigma_{m+1} = \sigma_{m+1}^e - \Delta\lambda D_{nn}\left[(1-\theta)m_{A,1}(\sigma_m, \tau_m, \mathbf{q}_m) + \theta m_{A,1}(\sigma_{m+1}, \tau_{m+1}, \mathbf{q}_{m+1})\right] \qquad (5.26a)$$

$$\tau_{m+1} = \tau_{m+1}^e - \Delta\lambda D_{tt} sign(\tau) \qquad (5.26b)$$

in which the internal variables, $\mathbf{q}_{m+1}$, are updated as follows:

$$p_{m+1}^+ = p_m^+ + \left\langle \Delta\lambda \cdot sign(\tau) \right\rangle \qquad (5.27a)$$

$$p_{m+1}^{-} = p_m^{-} + \left\langle -\Delta\lambda \cdot sign(\tau) \right\rangle \tag{5.27b}$$

$$r_{m+1} = r_m + \Delta\lambda\left[(1-\theta)m_{A,1}(\sigma_m, \tau_m, \mathbf{q}_m) + \theta m_{A,1}(\sigma_{m+1}, \tau_{m+1}, \mathbf{q}_{m+1})\right] \tag{5.27c}$$

$$c_{m+1} = c_m - \Delta\lambda \frac{c_0}{s_R} \geq 0 \tag{5.27d}$$

$$\mu_{A,m+1} = \mu_{A,0} e^{-k_2 \frac{p_{m+1}^{+} + p_{m+1}^{-}}{s_R}} \tag{5.27e}$$

$$s_{m+1} = s_m \tag{5.27f}$$

The value of $\Delta\lambda$ is to be evaluated iteratively until the condition that $F_A(\boldsymbol{\sigma}_{m+1}, \mathbf{q}_{m+1}) = 0$ and Equations 5.26 and 5.27 are all satisfied. For this purpose, an iterative bracketing strategy has been followed. The solution for $\Delta\lambda$ is bracketed with a lower bound and an upper bound $\Delta\lambda$ that satisfy that $F_A > 0$ and $F_A < 0$, respectively. This bracket is updated following the bisection method until the condition that $F_A(\boldsymbol{\sigma}_{m+1}, \mathbf{q}_{m+1}) = 0$ is satisfied with a pre-defined tolerance.

In the iterative bracketing scheme, given a value of $\Delta\lambda$, the values of $\boldsymbol{\sigma}_{\mathbf{m+1}}$ and $\mathbf{q}_{\mathbf{m+1}}$ are updated with Equations 5.26 and 5.27. Since Equations 5.26a and 5.27c are nonlinear and implicit with respect to σ_{m+1} and r_{m+1}, they need to be solved iteratively to obtain values of σ_{m+1} and r_{m+1}. The iterative solution is carried out with Equation 5.28 by updating the values of $\sigma_{m+1,k}$ and $r_{m+1,k}$ until convergence is reached. Initially, $\sigma_{m+1,0} = \sigma_m$ and $r_{m+1,0} = r_m$.

$$\sigma_{m+1,k+1} = \sigma_{m+1}^{e} - \Delta\lambda D_{nn}\left[(1-\theta)m_{A,1}(\sigma_m, \tau_m, \mathbf{q}_m) + \theta m_{A,1}(\sigma_{m+1,k}, \tau_{m+1}, \mathbf{q}_{m+1,k})\right] \tag{5.28a}$$

$$r_{m+1,k+1} = r_{m+1} - \Delta\lambda\left[(1-\theta)m_{A,1}(\sigma_m, \tau_m, \mathbf{q}_m) + \theta m_{A,1}(\sigma_{m+1,k}, \tau_{m+1}, \mathbf{q}_{m+1,k})\right] \tag{5.28b}$$

5.2.2 Return mapping to Yield Surface B

The same strategy as above can be used to return the stress state to the yield surface corresponding to Mode B. In this case, the stresses and internal variables are updated as follows.

$$\sigma_{m+1} = \sigma^e_{m+1} - \Delta\lambda D_{nn}\left[(1-\theta)m_{B,1}(\mathbf{q}_m) + \theta m_{B,1}(\mathbf{q}_{m+1})\right] \tag{5.29a}$$

$$\tau_{m+1} = \tau^e_{m+1} - \Delta\lambda D_{tt} \text{ (for } F_B^+\text{)} \tag{5.29b}$$

$$\tau_{m+1} = \tau^e_{m+1} + \Delta\lambda D_{tt} \text{ (for } F_B^-\text{)} \tag{5.29c}$$

$$p^+_{m+1} = p^+_m \quad p^-_{m+1} = p^-_m \quad r_{m+1} = r_m \quad c_{m+1} = c_m \quad \mu_{A,m+1} = \mu_{A,m} \tag{5.30a}$$

$$s_{m+1} = s_m + \Delta\lambda \text{ (for } F_B^+\text{)} \tag{5.30b}$$

$$s_{m+1} = s_m - \Delta\lambda \text{ (for } F_B^-\text{)} \tag{5.30c}$$

The nonlinear problem defined by $F_B(\boldsymbol{\sigma}_{m+1}, \mathbf{q}_{m+1}) = 0$ and Equations 5.29 and 5.30 is solved to determine the value of $\Delta\lambda$ by employing the bisection bracketing method.

However, if $\sigma^e_{m+1} > 0$ and $\frac{\tau^e_{m+1}}{D_{tt}}\tan\alpha_m < \frac{\sigma^e_{m+1}}{D_{nn}}$, a different flow rule needs to be used as mentioned in Section 5.1.2, and Equations 5.29 and 5.30 will not be used. In this case, the stress state is returned to the apex of the yield surface, and since the final stress for this situation is known, the plastic flow vector is $\Delta\lambda\mathbf{m}_\mathbf{s} = \begin{Bmatrix} \sigma^e_{m+1}/D_{nn} \\ \tau^e_{m+1}/D_{tt} \end{Bmatrix}$. The updated stress and internal variables become

$$\sigma_{m+1} = 0 \tag{5.31a}$$

$$\tau_{m+1} = 0 \tag{5.31b}$$

$$p^{+}_{m+1} = p^{+}_{m} \quad p^{-}_{m+1} = p^{-}_{m} \quad r_{m+1} = r_m \quad c_{m+1} = c_m \quad \mu_{A,m+1} = \mu_{A,m} \tag{5.32a}$$

$$s_{m+1} = s_m + \frac{\tau^{e}_{m+1}}{D_{11}} \tag{5.32b}$$

5.2.3 Return mapping to the intersection of Yield Surfaces A and B

The stress return to the intersection of the yield surfaces corresponding to Modes A and B requires a special treatment. For this case, the plastic correction is considered as a linear combination of the corrections obtained with the flow rules for Mode A and Mode B, respectively. Hence, the stresses and internal variables are updated as follows.

$$\begin{aligned}\sigma_{m+1} = \quad & \sigma^{e}_{m+1} - \Delta\lambda_1 D_{nn}\left[(1-\theta)m_{A,1}(\sigma_m, \tau_m, \mathbf{q}_m) + \theta m_{A,1}(\sigma_{m+1}, \tau_{m+1}, \mathbf{q}_{m+1})\right] \\ & - \Delta\lambda_2 D_{nn}\left[(1-\theta)m_{B,1}(\mathbf{q}_m) + \theta m_{B,1}(\mathbf{q}_{m+1})\right]\end{aligned} \tag{5.33a}$$

$$\tau_{m+1} = \tau^{e}_{m+1} - \Delta\lambda_1 D_{tt} - \Delta\lambda_2 D_{tt} \text{ (for } F^{+}_{B}) \tag{5.33b}$$

$$\tau_{m+1} = \tau^{e}_{m+1} - \Delta\lambda_1 D_{tt} + \Delta\lambda_2 D_{tt} \text{ (for } F^{-}_{B}) \tag{5.33c}$$

$$p^{+}_{m+1} = p^{+}_{m} + \left\langle \Delta\lambda_1 sign(\tau) \right\rangle \tag{5.34a}$$

$$p^{-}_{m+1} = p^{-}_{m} + \left\langle -\Delta\lambda_1 sign(\tau) \right\rangle \tag{5.34b}$$

$$r_{m+1} = r_m + \Delta\lambda_1\left[(1-\theta)m_{A,1}(\sigma_m, \tau_m, \mathbf{q}_m) + \theta m_{A,1}(\sigma_{m+1}, \tau_{m+1}, \mathbf{q}_{m+1})\right] \tag{5.34c}$$

$$c_{m+1} = c_m - \Delta\lambda_1 \frac{c_0}{s_R} \geq 0 \tag{5.34d}$$

$$\mu_{A,m+1} = \mu_{A,0} e^{-k_2 \frac{p^{+}_{m+1} + p^{-}_{m+1}}{s_R}} \tag{5.34e}$$

$$s_{m+1} = s_m + \Delta\lambda_2 \text{ (for } F^{+}_{B}) \tag{5.34f}$$

$$s_{m+1} = s_m - \Delta\lambda_2 \ \text{(for } F_B^- \text{)} \tag{5.34g}$$

Equations 5.33a and 5.34c need to be solved iteratively with the form shown in Equation 5.35.

$$\begin{aligned}\sigma_{m+1,k+1} = \quad & \sigma^e_{m+1} - \Delta\lambda_1 D_{nn}\left[(1-\theta)m_{A,1}(\sigma_m, \tau_m, \mathbf{q}_m) + \theta m_{A,1}(\sigma_{m+1,k}, \tau_{m+1}, \mathbf{q}_{m+1,k})\right] \\ & - \Delta\lambda_2 D_{nn}\left[(1-\theta)m_{B,1}(\mathbf{q}_m) + \theta m_{B,1}(\mathbf{q}_{m+1,k})\right]\end{aligned} \tag{5.35a}$$

$$r_{m+1,k+1} = r_{m+1} - \Delta\lambda_1\left[(1-\theta)m_{A,1}(\sigma_m, \tau_m, \mathbf{q}_m) + \theta m_{A,1}(\sigma_{m+1,k}, \tau_{m+1}, \mathbf{q}_{m+1,k})\right] \tag{5.35b}$$

An algorithm has been developed to solve the nonlinear problem defined by the two yield conditions, $F_A(\boldsymbol{\sigma}_{m+1}, \mathbf{q}_{m+1}) = 0$ and $F_B(\boldsymbol{\sigma}_{m+1}, \mathbf{q}_{m+1}) = 0$, and Equations 5.33 and 5.34. The algorithm consists of two nested loops that employ the bisection bracketing method to solve for $\Delta\lambda_1$ and $\Delta\lambda_2$. In the internal loop, $\Delta\lambda_1$ is kept constant, and the value of $\Delta\lambda_2$ that satisfies $F_B(\boldsymbol{\sigma}_{m+1}, \mathbf{q}_{m+1}) = 0$ is determined with the bracketing method. In the external loop, with the value of $\Delta\lambda_2$ determined in the internal loop, a value for $\Delta\lambda_1$ is bracketed with the aim to satisfy $F_A(\boldsymbol{\sigma}_{m+1}, \mathbf{q}_{m+1}) = 0$. The process is repeated until convergence is reached.

5.3 Model Calibration and Validation

Several of the parameters defining the model can be determined based on the geometry of the bar and the mechanical properties of the concrete. The rest of the parameters, which define the yield conditions and flow rules, have been calibrated with experimental results obtained by Malvar (1992). These experiments provide unique data to characterize the relations between the tangential and normal stresses and relative

displacements at the concrete-steel interface. They consist of data from pull-out tests on No. 6 (19-mm [0.75 in.] diameter) bars embedded in pre-splitted concrete cylinders subjected to a constant radial stress. During the tests, the average bond stress, the slip, and the radial displacement were measured. Five different levels of confinement were used, ranging between 3.45 MPa (500 psi) and 31.03 MPa (4500 psi). In all the cases, bond failed by the pull-out of the bar, and crushed concrete between the ribs was observed.

The experimental results have been replicated with the interface model presented in this chapter. In these analyses, the bar slip has been increased monotonically while keeping the radial stress constant. The values of the model parameters related to the bar geometry and concrete strength have been determined from the information reported in Malvar (1992) and are presented in Table 5.1. The values of the parameters related to the yield surface and flow rule are presented in Table 5.2. It has been verified that the values of μ_s and α satisfy the conditions for Equations 5.16b and 5.17b to be valid. The values of the parameters in Table 5.2 are fixed regardless of the bar and concrete characteristics. In addition, the constants of the elastic stiffness matrix need to be defined. The elastic tangential stiffness is taken as $D_{tt} = 0.04\frac{E_c}{d_b}$, as proposed by Cox and Herrmann (1998) to match the initial stiffness of the bond stress-vs.-slip curves from different experiments. The elastic normal stiffness is a penalty parameter assumed to be $D_{nn} = \frac{E_c}{d_b}$. This value is large enough to ensure that the elastic normal deformation is small compared to the plastic normal deformations. The Young modulus of concrete is calculated based on ACI

318-08 (ACI 2008) as $E_c = 4{,}730\sqrt{f_c'}$ in MPa ($E_c = 57{,}000\sqrt{f_c'}$ in psi). Finally, θ is taken to be 0.5 for the stress update algorithm, resulting in a mid-point rule.

The interface model successfully reproduces the bond resistance and dilatation obtained for different levels of confinement by Malvar (1992). The experimental and analytical results for the tests with confining stresses of 3.45 MPa (500 psi), 17.24 MPa (2500 psi), and 31.03 MPa (4500 psi) are compared in terms of the bond stress vs. the slip, and the bond stress vs. the radial displacement in Figure 5.9. In all cases, Plastic Mode B (sliding) is first activated, but as the Mode-B yield surface rotates in the $\sigma - \tau$ plane, the yield surface corresponding to Mode A is activated. Plastic Mode A involves the crushing and shearing of the concrete between the ribs, and the resulting bond deterioration is represented by the shrinking of the yield surface. An additional case with a lower confining pressure of $\sigma = 1.72$ MPa (250 psi) has been analyzed to illustrate the capability of the model to simulate a bond failure caused by pure sliding. In this case, Plastic Mode A is never activated and the plastic displacement is solely due to sliding on the concrete-steel surface. As shown in Figure 5.9a, the bond strength is lower and the failure is more brittle than for the cases where Plastic Mode A occurs. Also, the dilatation is higher and its maximum value is equal to the rib height (0.81 mm [0.032 in.]).

5.4 Verification finite element analyses

The model presented in this chapter has been implemented as the constitutive law of a user-defined interface element in ABAQUS for finite element (FE) analysis. Several examples are provided herein to validate the ability of this model to predict the bond-slip

behavior of bars under different loading scenarios and confinement conditions, as observed in different experiments. The fixed model parameters presented in Table 5.2 have been used in all analyses. The bar and concrete properties have been adjusted in each example based on the information reported for these experiments. These values are presented in Table 5.1.

The pull-out tests carried out by Lundgren on bars embedded in concrete cylinders confined in a steel casing have been reproduced with FE analyses using the proposed bond-slip model. The FE model of a test specimen is presented in Figure 5.10. Continuum elements are used to model the steel bar so that the the change of the diameter of the bar under elastic and plastic tensile deformation can be captured. The cross section of the bar is idealized as an octagon with an area equal to that of the circular section. The steel nodes located at the vertices of the octagon are connected to the concrete nodes through the bond-slip interface elements. The FE model reproduces the bond stress-vs.-slip response of the bar under monotonic loading well, as shown in Figure 5.11a. The bond strength is underestimated by 22%, but the model well predicts the slip at the peak and the decay of the bond resistance. The tangential hoop strain in the steel casing during the test is fairly well captured but overestimated, as shown in Figure 5.11b. The FE model is also capable of replicating the cyclic bond stress-vs.-slip relations in another test, including the decay in the bond resistance, and the unloading and reloading branches, as shown in Figure 5.12a. However, the cyclic hysteresis for the hoop strain in the steel casing cannot be matched, as shown in Figure 5.12b. This is mainly attributed to the inability of the concrete model to close the radial splitting cracks that have formed in

the concrete cylinder, which is related to a limitation of the constitutive model as discussed in Chapter 4.

FE analyses of some of the bond-slip tests on large-diameter bars presented in Chapter 3 have also been performed. Figure 5.13 plots the analytical and experimental results obtained in two monotonic tests conducted on specimens with different concrete strengths. Figure 5.13a presents the average bond stress-vs.-slip relation obtained for a No. 14 bar embedded in a concrete with a compressive strength of 34.5 MPa (5 ksi). Figure 5.13b presents the pull force-vs.-displacement curve for a No. 14 bar embedded in a concrete with a compressive strength of 55 MPa (8 ksi). As mentioned in Chapter 3, the bond stress-slip relation is not provided for this test because the bar yielded, and as a consequence, the assumptions made to calculate this relation are not valid. The FE results provide a good correlation with the test results. In both cases, the model overestimates the average bond strength by 10%, but it is successful in predicting the increase of the average bond strength by 48% from one test to the other due to the increase of the concrete strength by 60%. As shown in Figure 5.14, the FE model also provides a good representation of the cyclic bond-slip behavior of a No. 14 bar embedded in a concrete with a compressive strength of 34.5 MPa (5 ksi).

Pull-out tests carried out by Plizzari and Mettelli (2009) on 40-mm (1.57-in.) bars embedded in 400-mm (15.7-in.) concrete cubes with an average compressive strength of 37.6 MPa (5.45 ksi) and no transverse reinforcement have been analyzed to validate the capability of the proposed model to predict splitting failures. The five specimens tested by Plizzari and Mettelli (2009) failed in a sudden manner due to the splitting of the concrete, and the bond strengths varied between 10 MPa (1.45 ksi) and 22 MPa (3.2 ksi).

The FE model is capable of predicting the sudden splitting failure, and provides a fairly good representation of the average bond-slip behavior observed in these tests, as shown in Figure 5.15a. The post-peak response cannot be captured in the model due to convergence problems. Figure 5.15b plots the principal plastic strains at the peak load, and shows bands of large plastic strains that correspond to the formation of splitting cracks.

The bond strength and splitting failure obtained by Choi et al. (2011) by pushing a No. 7 (22.2-mm) bar embedded in a concrete cylinder with a 100-mm (3.94-in.) diameter are also well replicated with the FE model, as shown in Figure 5.16. The bond strength and sudden drop in the bond resistance are well predicted. In this case, the entire post-peak response is obtained. A residual bond resistance is obtained because the concrete in the model can still provide some confinement despite the occurrence of splitting cracks. This is caused by the tensile residual resistance assumed for concrete to overcome convergence problems.

These examples have shown the capability of the model to predict several aspects of the bond-slip behavior of deformed bars, namely, the variation of the bond strength with the concrete strengths and the level of confinement, the deterioration of bond under monotonic and cyclic loading, and different failure modes. Given the generality of the model and the simple calibration procedure, the performance of the model is more than satisfactory.

5.5 Finite element analysis of the effect of concrete cover on bond resistance

Finite element analyses employing the dilatant bond-slip model have been used here to study the effect of concrete cover on the bond strength and failure mode of single bars pulled out from concrete cylinders. Pull-out specimens similar to those presented in Chapter 3 have been modeled, as shown in Figure 5.17. The analysis has been restricted to No. 14 bars and a concrete compressive strength equal to 34.5 MPa (5 ksi). No transverse reinforcement is considered. The same model input parameters as for the bond-slip tests have been assumed. The clear concrete cover for the bar used in these analyses varies between one and ten times the bar diameter, as presented in Table 5.3. In absence of transverse reinforcement, the value of $\frac{c_b}{d_b}$, in which c_b is the concrete cover measured from the center of the bar, is equal to the confinement index, *CI*. This is the name given in Chapter 3 to the confinement term $\frac{c_b + K_{tr}}{d_b}$ used to calculate the minimum development length required by ACI 318-08 (ACI 2008). As the confinement term increases, the development length required by the code decreases.

The bond strength and failure modes obtained in these analyses are presented in Table 5.3, and the bond stress-vs.-slip relations are plotted in Figure 5.18a. For *CI* equal to or lower than 3.5, vertical splitting cracks develop over the entire concrete cover and bond fails in a relative brittle way. For *CI* higher than 3.5, the decay of bond resistance is more gentle. These observations are consistent with the Commentary of ACI 318-08 (ACI 2008), which indicates that when the confinement term $\frac{c_b + K_{tr}}{d_b}$ is lower than 2.5,

splitting failures are likely to occur, and pull-out failures are expected for values above 2.5. The analysis results have also shown that the bond strength increases with *CI*. However, for *CI* values higher than 5.5, no further increase of bond strength is obtained by increasing the concrete cover. This saturation of the bond strength with the passive confinement is also considered in ACI 318-08 (ACI 2008), but it is presumed to occur at a lower confinement level by limiting the maximum value of $\frac{c_b + K_{tr}}{d_b}$ to 2.5.

For a pull-out failure, the relation between the bond resistance and the normal stresses can be obtained from the yield function presented in Equation 5.7 as

$$\tau = f_c' \left[\left(\frac{c}{f_c'} \right)^{k_1} + \mu_p \frac{\sigma}{f_c'} \right]^{1/k_1} \tag{5.36}$$

When no active confinement is provided, the normal stress cannot be higher than f_c'. This can be explained as follows. When $\sigma = f_c'$, shear dilatation becomes zero according to Equation 5.12, and no further increase in confinement pressure can be introduced. Hence, the maximum bond resistance with no active confinement is estimated as

$$\tau_{\max,nac} = f_c' \left[\left(\frac{c_0}{f_c'} \right)^{k_1} + \mu_{p,0} \right]^{1/k_1} \tag{5.37}$$

This value is compared to the bond strengths, $\tau_{FE,\max}$, obtained from the finite element analyses for different concrete covers to evaluate the effectiveness of the cover in increasing the bond resistance. For this purpose, the following ratio has been defined.

$$\text{Bond effectiveness } (BE) = \frac{\tau_{FE,\max}}{\tau_{\max,nac}} \tag{5.38}$$

The *BE* values obtained from the analyses are presented in Table 5.3, and Figure 5.18b presents the relation between *CI* and *BE*. Despite the splitting failure, bond effectiveness reaches 78% for *CI* = 3.5. A bond effectiveness of 95% is achieved at *CI* = 5.5, and remains practically constant for larger values of *CI*. *BE* = 100% is never achieved because the values of c and μ_A drop a little due to bond deterioration before the estimated maximum bond resistance can be achieved.

5.6 Summary and conclusions

The formulation, implementation, and validation of a new elasto-plastic dilatant interface model for cyclic bond-slip analysis have been presented in this chapter. The model is based on a multi-surface plasticity formulation with a non-associative flow rule that captures the shear dilatation of the interface due to bar slip. The plasticity constitutive equations are integrated numerically using an elastic prediction - plastic correction algorithm with a generalized mid-point rule. The model has been implemented in an interface element in ABAQUS for nonlinear finite element analysis. The model is easy to calibrate and is capable of reproducing the bond-slip behavior of bars under a wide range of confinement situations, and both pull-out and splitting failures. Finite element analyses of pull-out tests from different studies have been carried out to validate these capabilities. The interface model proposed in this chapter has been used in a limited study on the influence of the concrete cover on the bond resistance. In the future, similar analyses can be performed to have a more extensive study of the effect of the concrete

cover, bar spacing, and transverse reinforcement on the bond strength and bond-slip behavior of bars.

Table 5.1: Bar and concrete properties for model validation

	Malvar (1992)	Lundgren (2000)	UCSD bond-slip tests	Plizzari (2009)	Choi (2011)
d_b *(mm)*	19	16	43	40	22.2
h_R *(mm)*	0.81	0.8 [1]	2.3	2 [1]	1.25
s_R *(mm)*	9.8	8 [2]	24.9	20 [2]	12.2
f_c' *(MPa)*	39.3	36	34.5 / 55.0	37.6	30.0
f_t' *(MPa)*	4.8	3. [3]	2.9 / 3.8	5.5	3.0 [3]

[1]: information not available, estimated as 5% of the bar diameter
[2]: information not available, estimated as 50% of the bar diameter
[3]: information not available, estimated as 10% of the compressive strength of concrete (25.4 mm = 1 in., 1 MPa = 0.145 ksi)

Table 5.2: Fixed model parameters

k_1	2.5
k_2	2.4
k_3	0.05
k_4	1.0
k_5	2.5
μ_B	0.2
α_0	62º

Table 5.3: Relation between confinement and bond strength

Clear cover, d_b	Confinement index, *CI*	Failure mode	Bond Strength, MPa (ksi)	Bond effectiveness, *BE*
1	1.5	splitting	7.9 (1.15)	0.41
2	2.5	splitting	11.4 (1.66)	0.59
3	3.5	splitting	15.1 (2.19)	0.78
4	4.5	pull-out	17.6 (2.56)	0.91
5	5.5	pull-out	18.4 (2.66)	0.95
7.5	8	pull-out	18.6 (2.69)	0.96
10	10.5	pull-out	18.6 (2.69)	0.96
15	15.5	pull-out	18.6 (2.70)	0.96

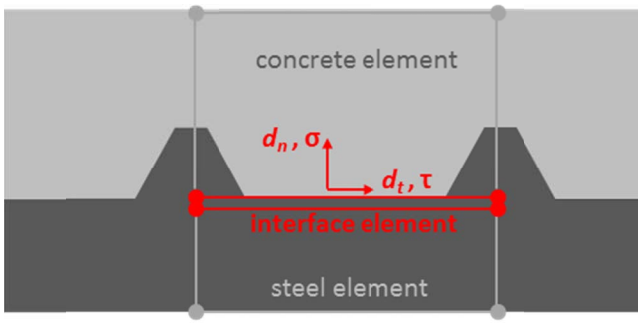

(a) Interface element

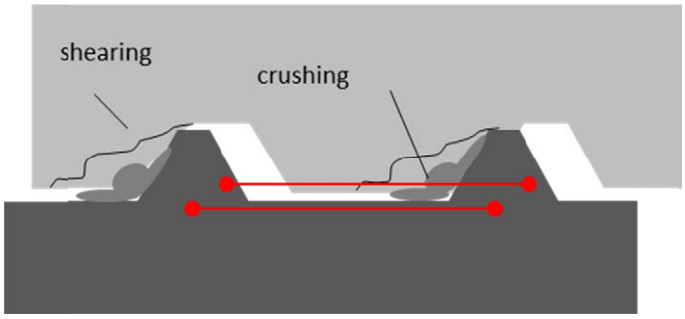

(b) Plastic Mode A : crushing and shearing (pull-out)

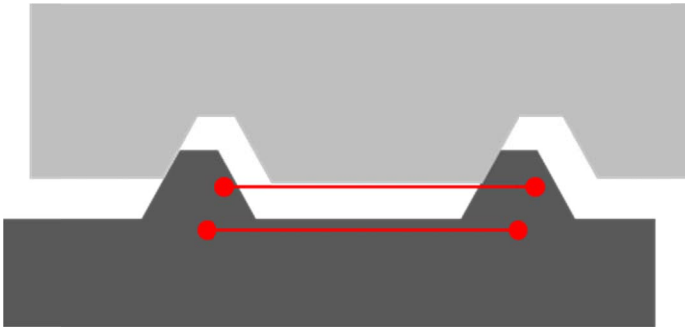

(c) Plastic Mode B: sliding

Figure 5.1: Interface idealization and plastic deformation modes

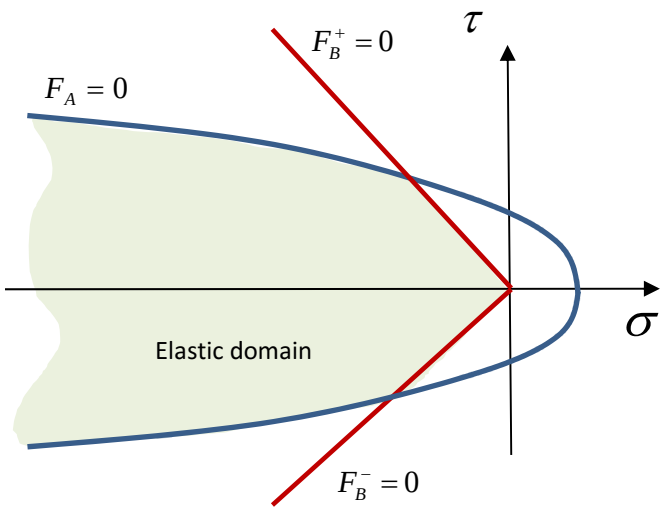

Figure 5.2: Yield surfaces

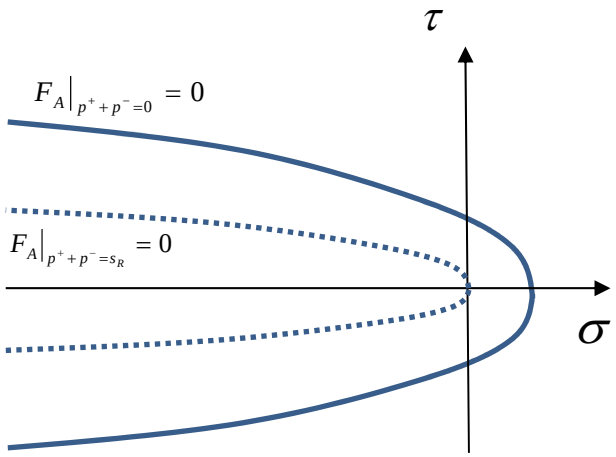

Figure 5.3: Evolution of the yield surface for Mode A (pull-out)

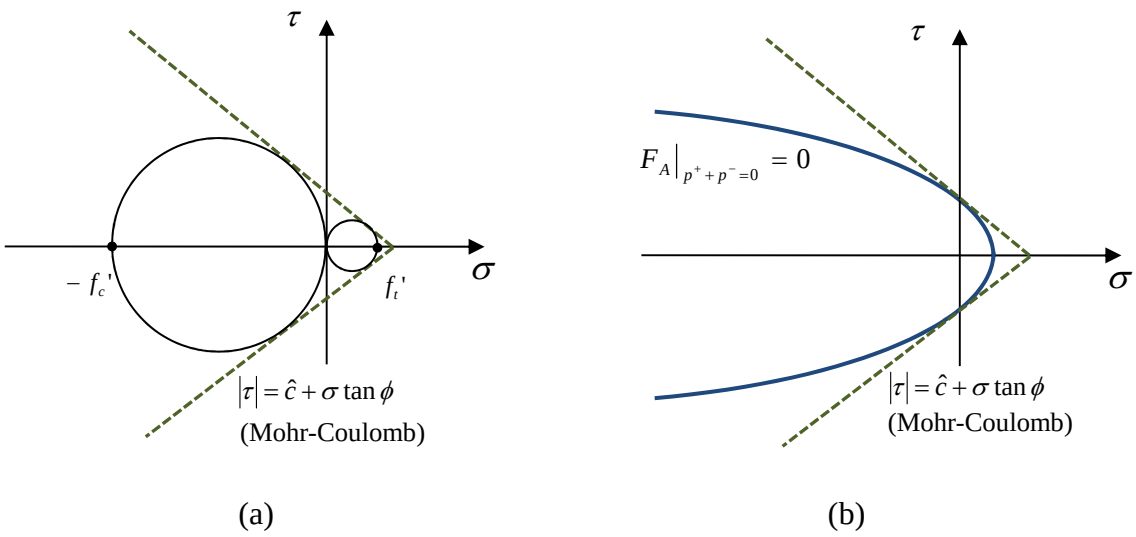

Figure 5.4: (a) Mohr circles for uniaxial compression and tension and Mohr-Coulomb failure surface, and (b) initial yield surface for Mode B and Mohr-Coulomb surface

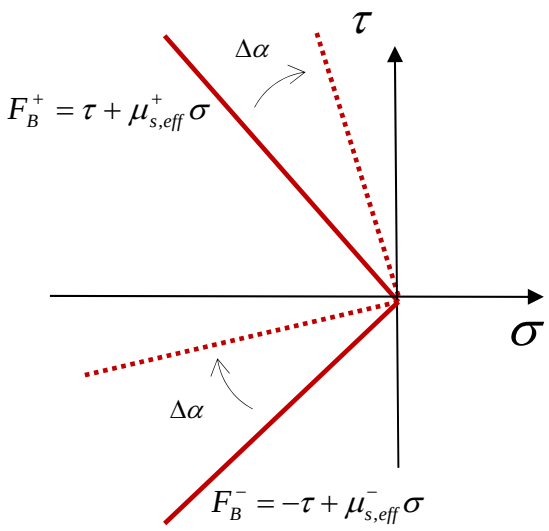

Figure 5.5: Evolution of the yield function for Mode B (sliding)

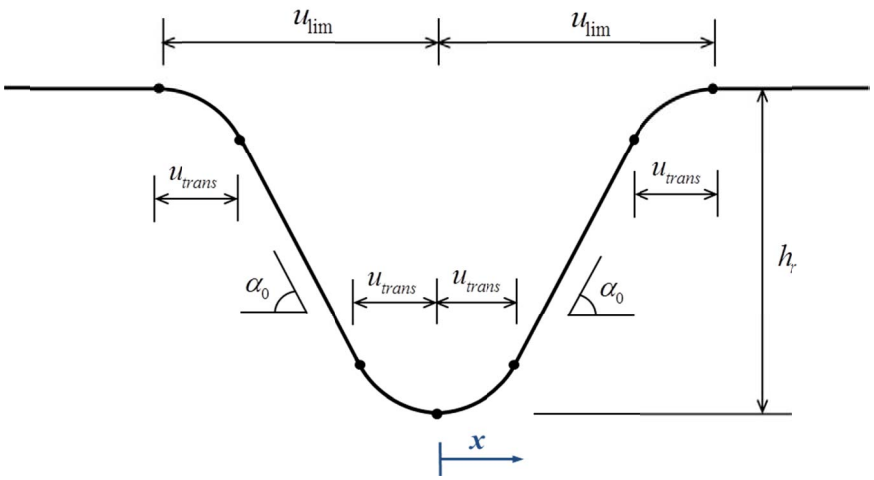

(a) Initial, $p^+ = p^- = 0$

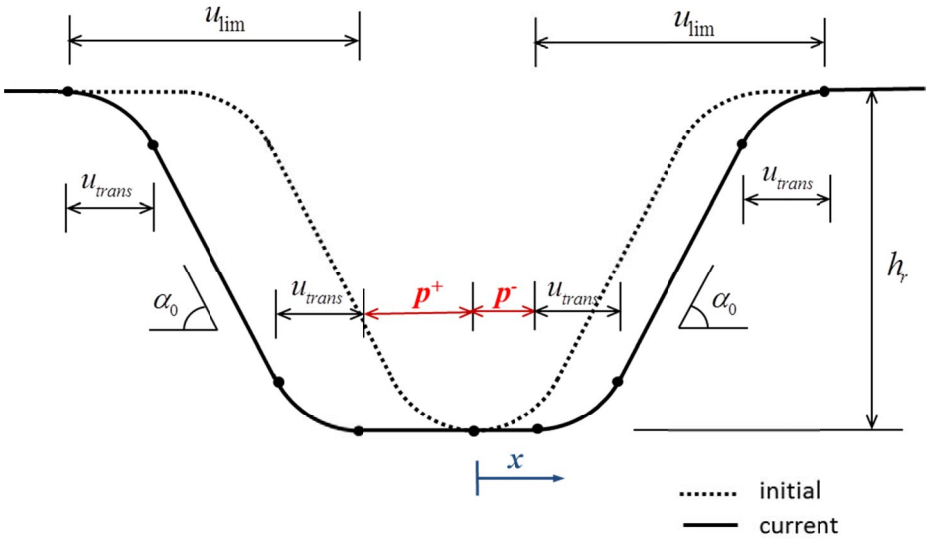

(b) With $p^+ > 0$ and $p^- > 0$

Figure 5.6: Evolution of the concrete-steel contact plane

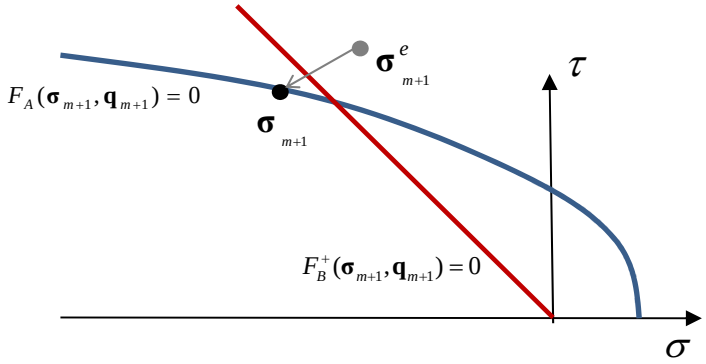

(a) Return-mapping to Surface A

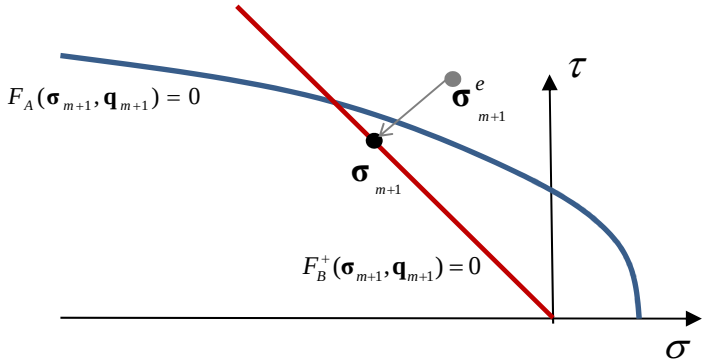

(b) Return-mapping to Surface B

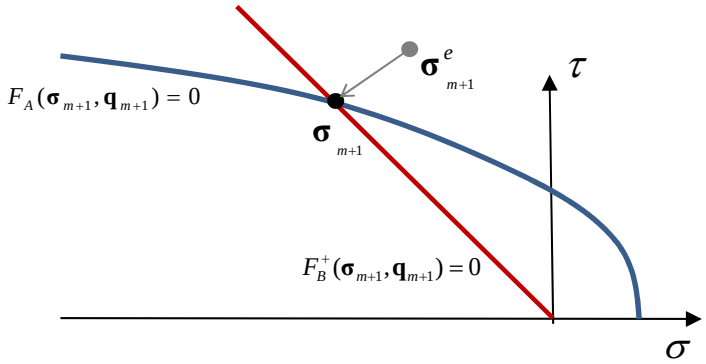

(c) Return-mapping to intersection of two surfaces

Figure 5.7: Possible stress return scenarios for plastic correction

1. Elastic prediction: $\boldsymbol{\sigma}^{e}_{m+1} = \boldsymbol{\sigma}_{m} + \mathbf{D}^{e} \cdot \Delta\mathbf{d}$

2. IF $F_A\left(\boldsymbol{\sigma}^{e}_{m+1}, \mathbf{q}_m\right) \le 0$ and $F_B^{\pm}\left(\boldsymbol{\sigma}^{e}_{m+1}, \mathbf{q}_m\right) \le 0$, THEN elastic step:

$\boldsymbol{\sigma}_{m+1} = \boldsymbol{\sigma}^{e}_{m+1}$, $\mathbf{q}_{m+1} = \mathbf{q}_m$

3. ELSE, plastic correction:

$Flag = -1$ (1: valid plastic correction, -1: plastic correction not valid)

3a. IF $F_A\left(\boldsymbol{\sigma}^{e}_{m+1}, \mathbf{q}_m\right) > 0$, THEN return to Yield Surface A:

Return to $\boldsymbol{\sigma}^{tr,A}_{m+1}, \mathbf{q}^{tr,A}_{m+1}$ such that $F_A\left(\boldsymbol{\sigma}^{tr,A}_{m+1}, \mathbf{q}^{tr,A}_{m+1}\right) = 0$

IF $F_B^{\pm}\left(\boldsymbol{\sigma}^{tr,A}_{m+1}, \mathbf{q}^{tr,A}_{m+1}\right) \le 0$, THEN

$\boldsymbol{\sigma}^{tr}_{m+1} = \boldsymbol{\sigma}^{tr,A}_{m+1}$, $\mathbf{q}^{tr}_{m+1} = \mathbf{q}^{tr,A}_{m+1}$, $Flag = -Flag$

ELSE, plastic correction is not valid

3b. IF $F_B^{\pm}\left(\boldsymbol{\sigma}^{e}_{m+1}, \mathbf{q}_m\right) > 0$, THEN return to Yield Surface B:

Return to $\boldsymbol{\sigma}^{tr,B}_{m+1}, \mathbf{q}^{tr,B}_{m+1}$ such that $F_B^{\pm}\left(\boldsymbol{\sigma}^{tr,B}_{m+1}, \mathbf{q}^{tr,B}_{m+1}\right) = 0$

IF $F_A\left(\boldsymbol{\sigma}^{tr,B}_{m+1}, \mathbf{q}^{tr,B}_{m+1}\right) \le 0$, THEN

$\boldsymbol{\sigma}^{tr}_{m+1} = \boldsymbol{\sigma}^{tr,B}_{m+1}$, $\mathbf{q}^{tr}_{m+1} = \mathbf{q}^{tr,B}_{m+1}$, $Flag = -Flag$

ELSE, plastic correction is not valid

3c. IF $Flag = 1$, THEN plastic correction in 3a or 3b is valid:

$\boldsymbol{\sigma}_{m+1} = \boldsymbol{\sigma}^{tr}_{m+1}$ $\mathbf{q}_{m+1} = \mathbf{q}^{tr}_{m+1}$

ELSE, return to intersection of Yield Surfaces A and B:

Return to $\boldsymbol{\sigma}_{m+1}, \mathbf{q}_{m+1}$ such that $F_A\left(\boldsymbol{\sigma}_{m+1}, \mathbf{q}_{m+1}\right) = 0$ and $F_B^{\pm}\left(\boldsymbol{\sigma}_{m+1}, \mathbf{q}_{m+1}\right) = 0$

Figure 5.8: Stress update algorithm

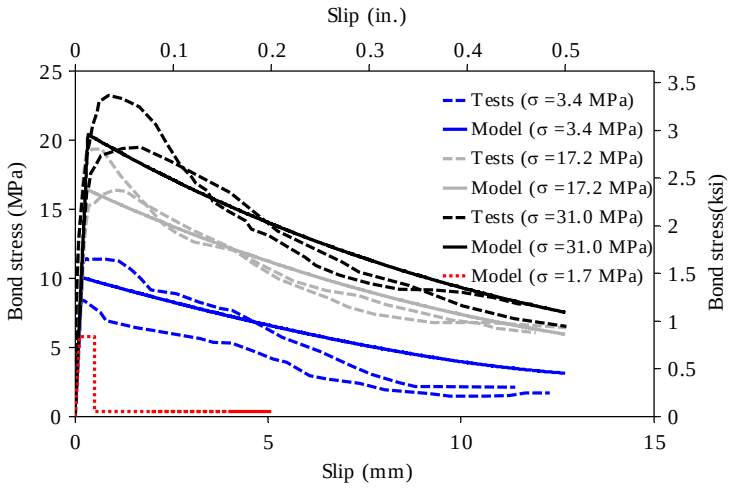

(a) bond stress vs. slip

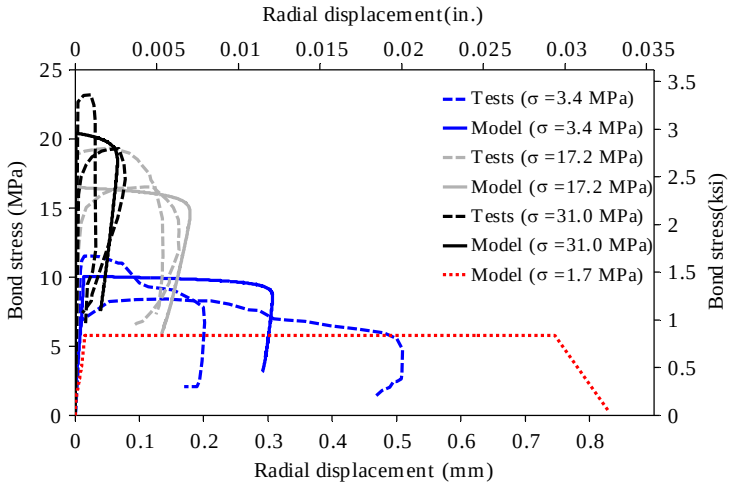

(b) bond stress vs. radial displacement

Figure 5.9: Analysis vs. experimental results obtained by Malvar (1992)

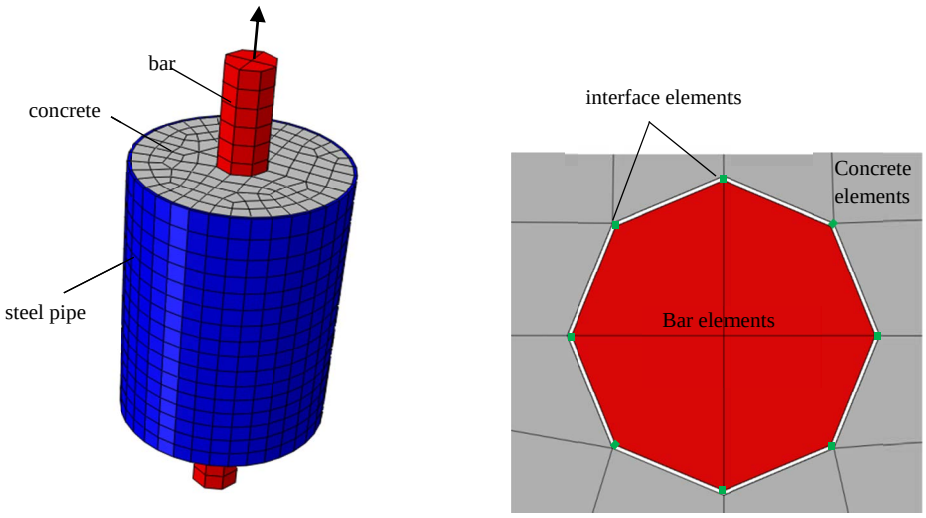

Figure 5.10: FE model of pull-out tests carried out by Lundgren (2000)

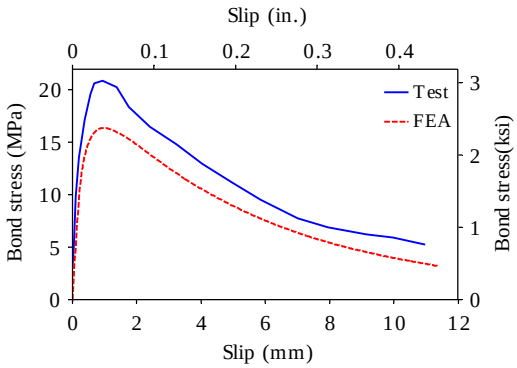

(a) average bond stress vs. slip

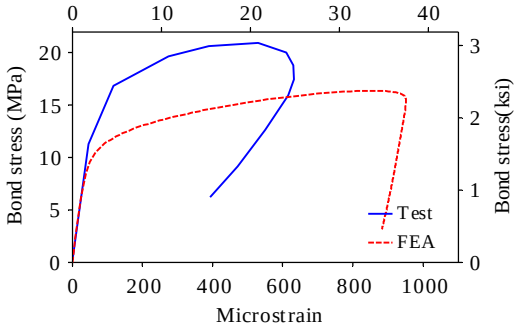

(b) average bond stress vs. hoop strain in the steel casing

Figure 5.11: Analysis vs. monotonic pull-out test results obtained by Lundgren (2000)

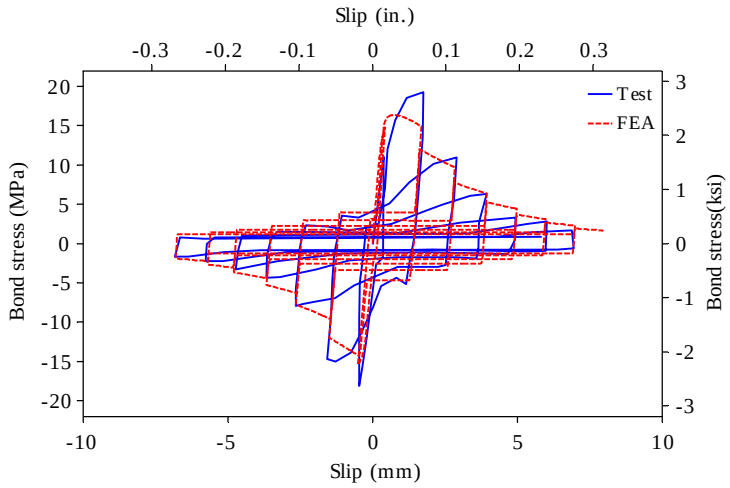

(a) average bond stress vs. slip

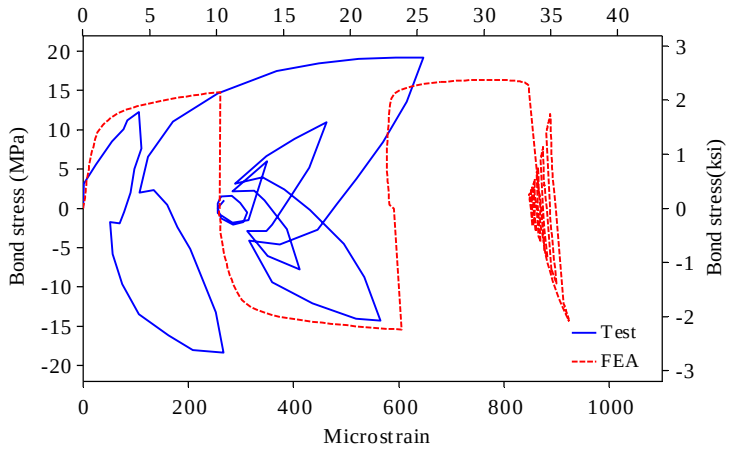

(b) average bond stress vs. hoop strain in the steel casing

Figure 5.12: Analysis vs. cyclic pull-out test results obtained by Lundgren (2000)

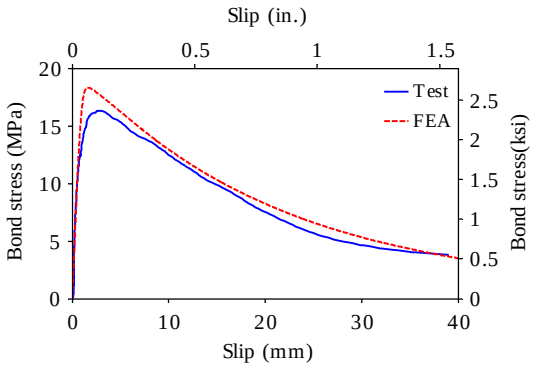

(a) average bond stress vs. slip in Test 4, Series 2

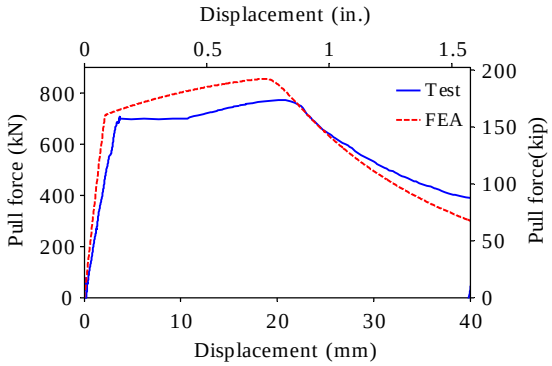

(b) pull force vs. slip in Test 1, Series 4

Figure 5.13: Analysis vs. monotonic bond-slip test results

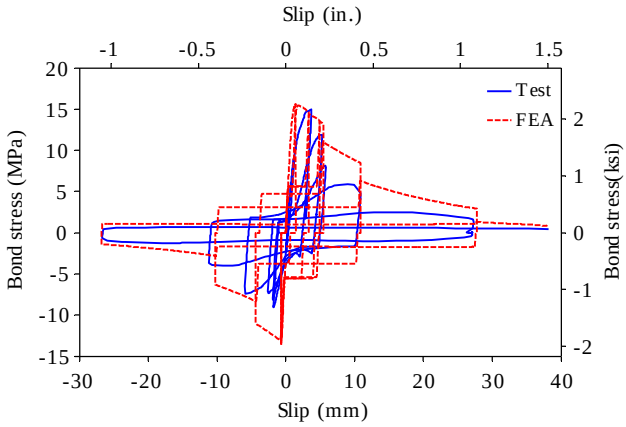

Figure 5.14: Analysis vs. cyclic bond-slip test results (Test 3, Series 2)

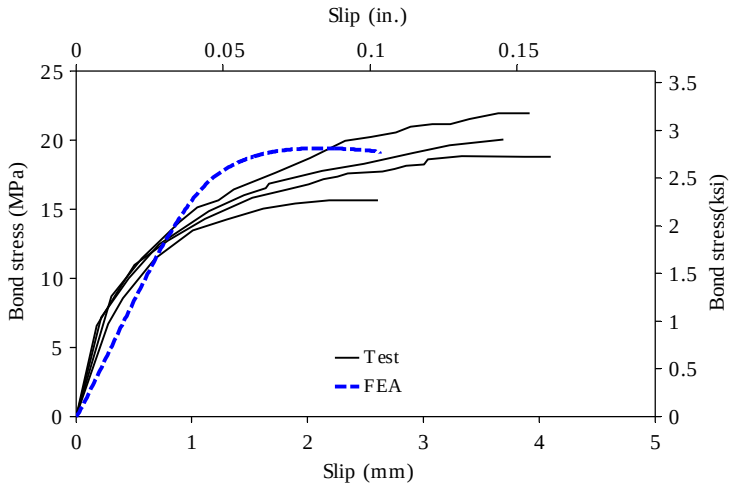

(a) average bond stress vs. slip

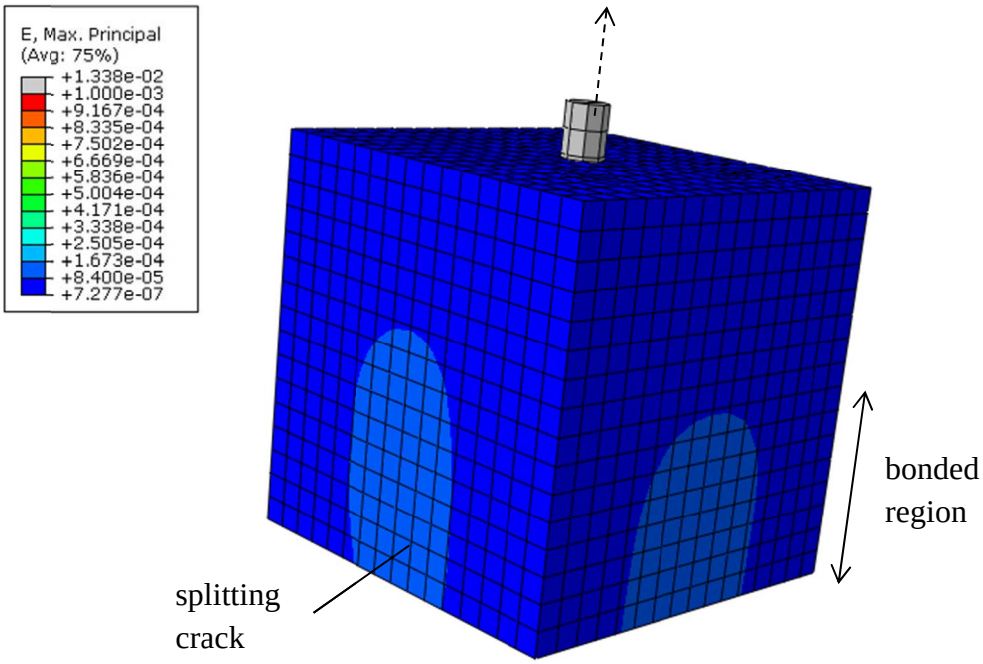

(b) maximum principal plastic strains at peak load

Figure 5.15: Analysis vs. pull-out test results obtained by Plizzari and Mettelli (2009)

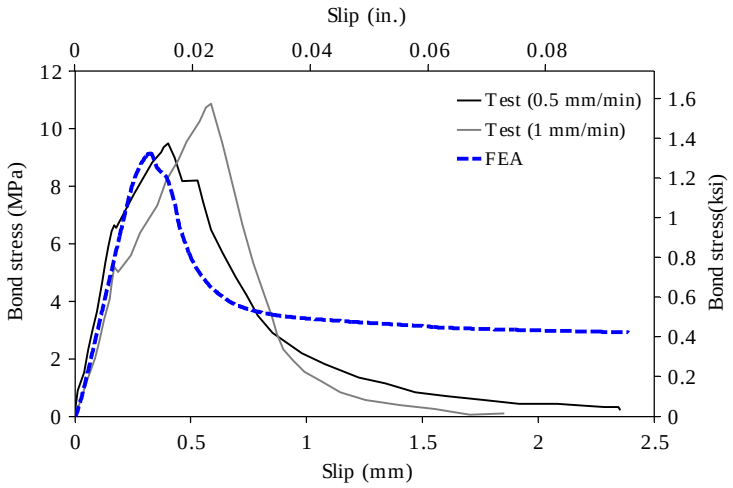

Figure 5.16: Analysis vs. push-in test results obtained by Choi et al. (2011)

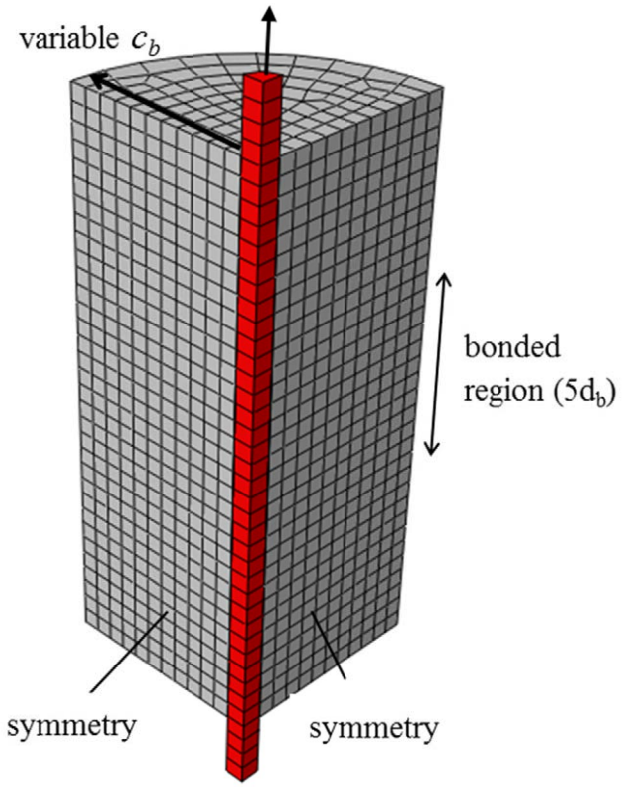

Figure 5.17: FE model for parametric study

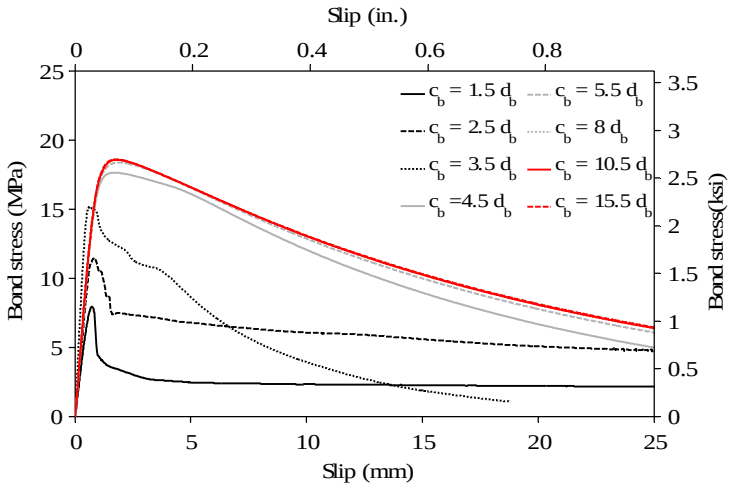

(a) Bond stress vs. slip relations

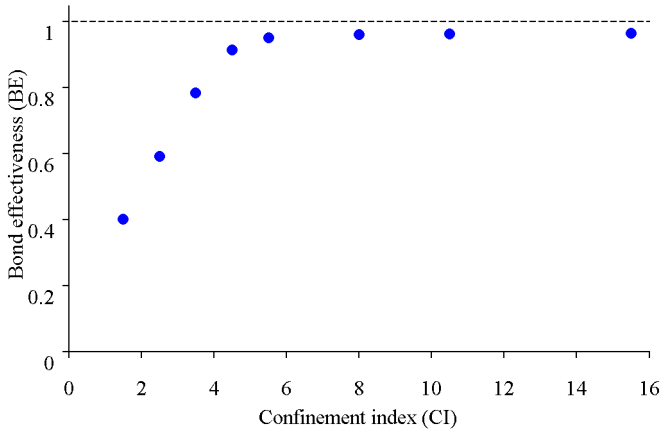

(b) Bond effectiveness vs. confinement index

Figure 5.18: Bond strength vs. confinement

CHAPTER 6

DEVELOPMENT OF LARGE-DIAMETER BARS IN WELL-CONFINED CONCRETE

The development of large-diameter reinforcing bars embedded in well-confined concrete subjected to severe cyclic loading, e.g., caused by an earthquake, is studied in this chapter. To characterize the demands on a bar anchorage during an earthquake, data obtained from a full-scale bridge column tested by Restrepo et al. (2010) on the NEES-UCSD Outdoor Shake Table was first analyzed. Quasi-static pull-push tests were conducted on individual No. 14 (43-mm) and 18 (57-mm) bars embedded in well-confined concrete cylinders in the Powell Structural Engineering Laboratories of UCSD to evaluate the adequacy of the tension development requirements stipulated in the AASHTO LRFD Bridge Design Specifications (AASHTO 2010) to sustain severe cyclic loading. These tests were also to validate a finite element (FE) model developed to simulate this type of tests using the bond-slip law presented in Chapter 4. Further FE analyses have been carried out in a parametric study to investigate how the tension capacity of bars anchored in well-confined concrete varies with the embedment length, the bar size, and the strengths of steel and concrete. Finally, a reliability analysis has been

conducted to determine the reliability level of the AASHTO specifications on the development of large-diameter bars in well-confined concrete with uncertainties in material properties and construction quality.

6.1 Bond-slip of vertical bars in the foundation of a full-scale bridge column tested on a shake table

In 2010, a full-scale model of a circular RC bridge column was tested on the NEES-UCSD Outdoor Shake Table by Restrepo et al. (2010). The test specimen, shown in Figure 6.1, was designed according to current design standards in California and was subjected to ten ground motions of increasing intensity till the column was in a near-collapse condition. The earthquake records listed in Table 6.1 were used to shake the specimen in its East-West direction. The objective of this test was to monitor the evolution of the dynamic nonlinear response of a hinging column to determine the adequacy of current design criteria and predictive analysis methods (Carrea 2010). The specimen had a diameter of 1219 mm (4 ft) and a clear height of 7315 mm (6 ft), resulting in an aspect ratio (H/L) of 6. It was on a 1219-mm (4-ft) tall footing that was post-tensioned to the shake table. A mass of 2322 kN (522 kips) was built on top of the column to generate the inertia force. This mass also subjected the column to a vertical stress that was 7.5% of the specified compressive strength of concrete.

During the test, the slip of key longitudinal column bars was monitored at the column-footing interface, and axial strains in these bars were measured along their development length inside the footing. The data gathered provide very valuable information to characterize the bond demands along the development length of column

longitudinal bars during an earthquake. In this section, only these data are analyzed. Details about the design of the specimen, test setup, instrumentation, loading protocol, and response of the column to the shaking are provided in Carrea (2010).

The longitudinal column reinforcement consisted of 18 No. 11 (35-mm) bars, resulting in a reinforcement ratio of 1.55%. The longitudinal bars were anchored in the footing with a development length equal to $32d_b$. The column reinforcement was Grade 60 complying with ASTM A 706 standards. Normal strength concrete with a specified compressive strength of 29.6 MPa (4 ksi) was used for both the column and the footing. The actual compressive strength of the concrete on the day of the test were 41 MPa (5.9 ksi) in the column and 42.0 MPa (6.1 ksi) in the footing. The vertical steel had a yield strength of 519 MPa (75.2 ksi) and ultimate tensile strength of 707 MPa (102.4 ksi).

To study the bond-slip of the vertical reinforcement, bar slip at the top of the footing was monitored and strain gages were placed at two different heights along the development length for two selected bars which were expected to be subjected to most severe stresses. One was a bar on the east side and the other on the west side of the specimen. Steel brackets with braces were attached to these bars using three screws, as shown in Figure 6.2a, at one inch below the footing surface. Two steel targets were welded to each brace to be able to measure the bar vertical displacement by subtracting the possible rotation of the steel piece attached to be bar. No concrete was poured on top of the measuring device so that the metal piece could move freely, as shown in Figure 6.2b. The displacement transducers measuring the slip were attached to a rigid support bolted to the footing at a sufficient distance of the column, as shown in Figure 6.2b. Strain gage readings were obtained for these same bars inside the column at different

heights and inside the footing at $6.5d_b$ and $15d_b$ below the column-footing interface. The slip and strains of the east bar are presented here.

The strain of the east bar at $2d_b$ above the column-footing interface and at $6.5d_b$ and $15d_b$ below this interface are plotted in Figure 6.3. The bar remained elastic during Earthquakes 1 and 2 as identified in Table 6.1. The bar yielded in tension at the base of the column during Earthquake 3 (this ground motion was estimated to represent the design event for this column). As shown in Figure 6.3, yielding penetrated to the level of the first strain gage inside the footing, i.e., to a depth of $6.5d_b$. Large compressive strains also developed after tensile yielding due to plastic compression. The strain gage located at $15d_b$ below the footing surface did not record bar yielding, but experienced a peak strain equal to 92% of the yield strain during Earthquake 7. No strain data beyond Earthquake 7 was obtained from any of these strain gages.

The slip of the east bar at the top of the anchorage is plotted in Figure 6.4. Only the results for the first four ground motions are plotted. The slip measurements beyond the fourth ground motion are considered unreliable based on sudden jumps observed in these measurements. These jumps could indicate that the attachment of the metal piece to the vertical bar was loosened due to the plastic contraction of the bar. Very small slip was measured during the first two earthquakes while the bar remained elastic. The maximum slips were 0.8mm (0.033 in.) upward and 0.5 mm (0.019 in.) downward. During the third earthquake, the bar slip increased significantly due to the yielding of the bar in tension. This increase in slip was caused by the penetration of the plastic strain inside the anchorage. During this ground motion, the maximum upward slip was 4.2 mm (0.167

in.), and at the end of the shaking, there was a residual upward displacement of 1.2 mm (0.046 in.). In the negative direction, the maximum slip recorded was 0.7 mm (0.027 in.). In Earthquake 4, the slip displacement varied between 0.7 mm (0.027 in.) and 2.7 mm (0.105 in.). The experimental data show that the slip of the bar in the positive direction increased gradually with the intensity of the earthquake, while the net slip in the negative direction remained small.

The relation between the slip of the bar at the top of the anchorage and the strain of the bar at $2d_b$ above the column-footing interface is plotted in Figure 6.5 for the first four earthquakes. This relation is linear for the first two earthquakes, in which the bar remained elastic. There is a clear change in the strain-slip relation once the bar yielded during Earthquake 3. A bilinear hysteretic behavior is observed in that earthquake. As the bar experienced plastic strain in tension, the strain-slip slope becomes larger than the initial one. This same slope is observed when the bar strain was reduced as a result of plastic compression. However, during unloading and elastic reloading, the initial slope was recovered. This is observed for example during Earthquake 4.

6.2 Pull-push tests on large-diameter bars

Three pull-push tests were carried out on No. 14 (43-mm) and 18 (57-mm) vertical bars with long embedment lengths to investigate the tension development strength, and strain penetration to, thereby, deduce the progressive bond deterioration along these bars under repeated cyclic tension and compression. These tests were to check whether the development length requirements stipulated in the AASHTO LRFD

Bridge Design Specifications (AASHTO 2010) are adequate or not when these bars are subjected to severe cyclic tension and compression up to the ultimate tensile strengths of the bars. Two tests, one for each bar size, were conducted with development lengths complying to the AASHTO specifications. An additional test was conducted on a No. 18 bar with a shorter embedment length.

6.2.1 Test setup and instrumentation

The geometries, reinforcing details, and instrumentation of the test specimens are shown in Figure 6.6. The same types of reinforcing bars, concrete mix design, and confinement level used in the basic bond-slip tests presented in Chapter 3 were employed. Tests No. 1 and 2 were conducted on a No. 14 bar and a No. 18 bar, respectively, with an embedment length, l_e, equal to the tension development length required by the AASHTO LRFD Bridge Design Specifications (AASHTO 2010). The development lengths were determined based on the targeted concrete compressive strength of 34.5 MPa (5 ksi). The basic tension development length was multiplied by a compound reduction factor equal to 0.6 accounting for sufficient bar spacing and clear concrete cover, and sufficient transverse reinforcement. Test No. 3 was done on a No. 18 bar with an embedment length equal to 60% the development length required by the AASHTO specifications. This length was determined to be sufficient to yield the bar and sustain a small amount of strain hardening based on a FE analysis, which will be presented with more details in Section 6.3. Specimens 2 and 3 were tested when the compressive strength of the concrete reached 34.5 MPa (5 ksi). For Specimen 1, the compressive strength of concrete was only 29.3 MPa (4.25 ksi) on the day of the test at

an age of 24 days. The characteristics of each specimen and test results are summarized in Table 6.2. The yield strength (f_y) and tensile strength (f_u) of the bars were obtained from material tests on bar specimens.

All the specimens were cast with the bar in an upright position. However, Specimen 1 was later rotated and anchored to a strong wall to be tested horizontally. The bar was pulled from and pushed into the concrete using a servo-controlled hydraulic actuator attached to a reaction block, which was anchored to the strong floor. This test setup is shown in Figure 6.7a. The test setup was changed for Specimens 2 and 3, as shown in Figure 6.7b. These specimens were cast and tested in an upright position. In this setup, the actuator was attached to a steel reaction frame secured to the footing of the specimens. In both test setups, the reaction of the pull-push force was not transferred to the concrete surrounding the bar so that the bar and the concrete were simultaneously in tension or compression, which closely represented a bar developed in a real structure.

The instrumentation of these specimens is presented in Figure 6.6. Strain gages were attached to the bar at different heights to obtain the longitudinal strain distribution along the embedded length during the test. In Specimens 1 and 2, strain gages were also placed in two perimeter bars to monitor the transfer of the tensile force from the pulled bar to these bars. In Specimen 3, strain gages were attached to the transverse reinforcement at two locations to monitor the hoops strains introduced by bar slip. The exact location of the strain gages for each of the specimens is given in Table 6.3. In addition, the displacement of the bar at the loaded end was monitored during the test. Since the top concrete surface was expected to be damaged during the test, this displacement was measured relative to a point 150 mm (6 in.) below the top of the

concrete cylinder. For this purpose, two displacement transducers were secured to the two opposite sides of the concrete cylinder at this height. The other end of each transducer was attached to a horizontal metal rod welded to a collar, which was secured to the bar at a position right above the concrete surface. This metal piece was similar to that used in the shake-table test as presented in Section 6.1. Pictures of the setup to measure bar slip are shown Figure 6.7c and Figure 6.7d. Pictures of specimen construction are provided in Appendix A.

The tests were intended to replicate severe tension and compression demands at the anchorage of longitudinal column bars during an earthquake, like those presented in Section 6.1. The bars were subjected to increasingly demanding tension in pull-push cycles, with two cycles per amplitude level, in displacement control. Even though plastic compression would be expected, based on the results presented in Section 6.1, the compressive force in these tests was limited to 50% of the expected yield strength of the bar, which was 469 MPa (68 ksi), to avoid bar buckling. The loading protocol is presented in Table 6.4. For the initial cycles, the amplitude in tension was set as a fraction of the expected yield strength. After the bar had reached 75% of its expected yield strength, the amplitude was specified in terms of the displacement level. Failure of the specimen occurred either by the fracture of the bar or by the pull-out of the bar from the concrete.

6.2.2 Test results

The results of Tests No. 1 through 3 are presented in terms of the bar stress vs. the displacement of the bar at the top of the anchorage in Figure 6.8 and Figure 6.9. Also,

Figure 6.10 provides the bar strain vs. displacement at the top of the anchorage for Test No. 2. The bilinear relation observed in Figure 6.10 is very similar to that shown in Figure 6.5 for a column vertical bar embedded during the shake-table test. The only difference is that in the pull-push tests there was no plastic loading in compression.

In Test No.1, the No. 14 bar yielded in tension and sustained significant inelastic deformation before it was pulled out from the concrete cylinder. As shown in Figure 6.8b, the stiffness in tension and compression were very similar before the bar yielded in tension at a displacement of 1 mm (0.04 in.). After yielding, the displacement at the loaded end increased with little increase in the pull force. The maximum pull force was reached at a displacement of 76 mm (3.0 in.). Under this load, the bar was subjected to 98% of the tensile strength of the bar, which was obtained from material tests. After this point, the load dropped with increasing displacement due to the failure of the anchorage. The load tended to stabilize a residual resistance that was one third of the peak load when the displacement reached 140 mm (5.5 in.). This residual resistance corresponds to the residual friction bond strength of the bar observed in the basic bond-slip tests in Chapter 3. At this point, the test was stopped. As the bar was being pulled out from the cylinder, pulverized concrete remained attached to the bar between the ribs, as shown in Figure 6.11. Furthermore, a cone-shaped concrete piece, approximately 50-mm (2-in.) deep and 125-mm (5 in.) in maximum diameter was detached from the top of the concrete cylinder as shown in Figure 6.11a.

In Test No. 2, the No. 18 bar yielded and reached its ultimate strength, then necked and fractured. The bar yielded in tension at a displacement of 1.5 mm (0.06 in), which is higher than that for the No. 14 bar. The tensile strength of the bar was reached at

a displacement of 60 mm (2.35 in.). After this, the load dropped, which was not caused by the failure of the anchorage, but due to the bar necking. The bar fractured at a location right below the surface of the concrete cylinder when the displacement was 93 mm (3.66 in.). Even though there was no anchorage failure, widely-open splitting cracks were visible at the top surface of the concrete cylinder, as shown in Figure 6.12. These cracks radiated from the bar to the outer surface of the concrete cylinder and extended vertically 125 mm (5 in.) down from the top surface (see Figure 6.12a). In addition, a circumferential horizontal crack was observed at this depth. Post-test inspection of the specimen revealed that this horizontal crack was an extension of a 200-mm (8-in.) deep cone-shaped crack. Figure 6.12c shows the shape of the crack surface after the upper concrete piece was removed. The use of a larger bar with larger ribs generates larger splitting forces in the concrete. This explains the more severe damage induced on the concrete specimen in Test No. 2. Results from these two tests indicate that the AASHTO LRFD Bridge Design Specifications (AASHTO 2010) for the development length of these bars are appropriate. The bars were able to yield and sustain significant hardening, and even reached bar fracture in Test No. 2.

Even though the bar in Test No. 3 had an embedment length significantly shorter than the development length required by the AASHTO specifications, it was able to yield and experience a small amount of strain hardening before the bond failed. The response before the bar yielded in tension was very similar to that of Test No. 2. However, the bar yielded in tension at a displacement of 1.9 mm (0.075 in), which is 25% larger than that in Test No. 2. This reduction in stiffness is caused by the shorter embedment length in Test No. 3. The maximum pull force was reached at a displacement of 5.9 mm (0.23 in.)

when the bar stress was 10% higher than its actual yield strength with a tensile strain of 1.7% at the pulled end. There was extensive bond failure, which resulted in larger displacements in compression as compared to Test No. 2, and a steady reduction of the load capacity in tension until the bar was completely pulled out from the concrete cylinder. Pictures of the specimen at the end of the test are shown in Figure 6.13. Pulverized concrete was observed between the ribs of the bar as it was being pulled out from the concrete cylinder. A crack pattern similar to that in Test No. 2 was observed in the upper portion of the concrete specimen, with widely-opened splitting cracks and a large concrete cone detached from the top of the specimen.

The strains measured in the loaded bars provide useful information to understand the bond deterioration along the embedment length. The strains at different locations along the length and at different stages of the tests are plotted in Figure 6.14. The displacement at the loaded end of a bar right above the anchorage zone is due to the strain penetration inside the embedment zone. When the anchorage failed in Tests No. 1 and 3, the displacement was mainly contributed by the rigid body displacement of the bar. Results obtained from the tests indicate that there was a significant penetration of plastic strain inside the embedment zone. As explained in Chapter 4, bond resistance will drop significantly at a location where the bar has yielded, which will exacerbate the plastic strain penetration as the bar undergoes strain hardening. For Test No. 1, plastic strains were measured up to a depth of $18\,d_b$ at a slip of 75mm (3 in.), prior to the anchorage failure, as shown in Figure 6.14a. With a total embedment length of $26\,d_b$, this means that the lowest $8\,d_b$ of the embedment length was sufficient to develop yield stress in the bar.

In Test No. 2, the maximum plastic strain penetration was at least $11 d_{b,}$ or 44% of the total embedment length. Despite this significant plastic penetration, the bar was able to reach its tensile strength and fracture. In Test No. 3, the maximum plastic strain penetration was at least $3.5 d_{b,}$ or 30% of the total embedment length, before the anchorage failed. This means that the lowest $10.5 d_b$ of the embedment length were sufficient to develop the yield force.

The strains measured in the perimeter bars provide further information to understand the damage observed in the test specimens and the transfer of the tensile force in the pulled bar to the surrounding concrete and reinforcing bars. The strains measured at two different heights of a perimeter bar at different stages of Tests No. 1 and 2 are plotted in Figure 6.15. These results show that the tensile strains in these bars increased with the depth. This was caused by the gradual transfer of the tensile force from the central bar. These strains were much larger in Test No. 2 than in Test No. 1, as shown in Figure 6.15. To understand this difference, the strains measured in these bars close to the end of the tests are compared with the strain distributions calculated with two simple analytical models in Figure 6.16. In both models, the bond stress on the bar being pulled out is assumed uniform. The first model assumes that the concrete is uncracked and that both the concrete and the perimeter bars remain linearly elastic. The tension force from the pulled bar is transferred to the concrete and perimeter bars, which experience the same axial strain at a given cross section. For this model, the modulus of elasticity of the concrete is estimated with the ACI 318-08 (ACI 2008) formula. In the second model, the tension force from the pulled bar is transferred to the perimeter bars through a truss

mechanism as proposed by McLean and Smith (1997) and others. The force transfer mechanism in this model is shown in Figure 6.17. The struts in Figure 6.17 are assumed to have a 45-degree inclination. As shown in Figure 6.16a, the strain in the perimeter bar in Test No. 1 shows a better match with the first model. According to this model, the concrete would be subjected to a maximum vertical tensile stress of 1.2 MPa (0.18 ksi), which is half of the tensile strength of 2.5 MPa (0.36 ksi) obtained from split-cylinder tests. This is in agreement with the fact that no cracks perpendicular to the bars were observed in the concrete cylinder. In Test No. 2, horizontal cracks were actually observed at different heights along the concrete cylinder. For this reason, the first model, which assumes that the concrete behaves elastically, underestimates significantly the strains of the perimeter bars, as shown in Figure 6.16b. The truss analogy matches well the strain reading in the upper gage, but overestimates the strain in the lower gage. This can be explained by the fact that the bond stress and thereby the strut force along the splice length is not uniform. Overall, the results from these two tests indicate that the truss analogy might not necessarily represent well the tensile force transfer in a non-contact lap splice.

The strains measured in the spiral reinforcement in Test No. 3 indicate that significant hoops strains were induced by bar slip. As shown in Figure 6.18, the tensile strains in the spiral reached 10^{-3} and $4 \cdot 10^{-4}$ at depths of $1.8\,d_b$ and $7.1\,d_b$, respectively, when the slip of the bar was 10 mm (0.4 in.). At a slip of 25 mm (1 in.), the strains dropped significantly probably because the steady smoothening action of bar slip had reduced the roughness created at the contact between the bar and the concrete at the beginning of the slip.

6.3 Finite element modeling of pull-push tests

FE analyses have been conducted to simulate the pull-push tests presented in Section 6.2. The purpose of these analyses is to validate the bond-slip constitutive law presented in Chapter 4 and gain more insight to the bond-slip behavior in the pull-push tests. For these analyses, three-dimensional models presenting one quarter of a test specimen have been employed by taking advantage of the axial symmetry of the specimens. Figure 6.19 shows the FE model for Test No.3. The constitutive models for the concrete, steel, and bond-slip behavior used here are the same as those presented in Chapter 4. The concrete and steel models are calibrated to the material strengths obtained from the material samples of the respective specimens, while the bond-slip model is calibrated according to the method recommended in Chapter 4.

Results from the FE analyses for Tests No. 1, 2, and 3 are presented in Figure 6.20 in terms of the bar stress-vs.-displacement relations at the loaded end of the bar. Not only the experimental relations are well replicated by the model, but the failure modes are also captured. For Test No. 1, the pull-out of the bar is well predicted by the model. For Test No. 2, the model shows that the bar reaches its tensile strength as it happened during the test. However, the load degradation due to bar necking and bar fracture is not captured by the FE model because the steel model cannot represent these features. For Test No. 3, the early pull-out of the bar after yielding and the cyclic deterioration of the anchorage capacity are well replicated.

The match between the FE analysis and experimental results in terms of the distributions of the tensile strain in the bar along the embedment zone at different stages

of the tests is reasonably good, as shown in Figure 6.14. The analysis results complement the discrete data points obtained from the tests and provide a better estimation of the plastic penetration in the bars. Based on these results, the extents of the plastic strain penetration developed in Tests No. 1, 2, and 3 at the peak loads are $15\,d_b$, $13\,d_b$, and $4\,d_b$, respectively. For Test No. 2, in which the tensile strength of the steel was reached, the extent of plastic strain penetration represents 52% of the total embedment length.

The bar axial stress distributions along the embedment zone of the loaded bars obtained from the FE analysis are plotted in Figure 6.21 through Figure 6.23. The bond stress distributions are calculated from the gradient of the axial stress distributions, and are plotted in Figure 6.24 through Figure 6.26. Tests No. 1 and 2, in which the bars had the embedment lengths satisfying the AASHTO LRFD Bride Design Specifications (AASHTO 2010), the bond stress distributions are highly nonlinear. The maximum bond stress develops near but not exactly at the top of the embedment zone while the bar behaves elastically. Once the bar yields in tension, the plastic strain penetrates inside the embedment zone and the peak bond stress moves downward. The maximum bond stresses plotted in Figure 6.24 through Figure 6.26 are smaller than the peak strengths obtained from the basic bond-slip tests. The reason is that the bar yields in tension before the slip that corresponds to the peak bond strength is reached. The yielding of the bar introduces lateral contraction, which weakens the bond capacity. In compression, the maximum bond stress is also smaller than the expected peak value due to the limited downward slip of the bar and the bond deterioration introduced by the large upward slip. Figure 6.24b and Figure 6.25b show that the same compressive force is developed

differently in the first and last cycle due to the bond deterioration at the top of the embedment length.

The bond stress distributions for Test No.3, as plotted in Figure 6.26, are more uniform than for the previous cases. This stems from the fact that the slip of the bar becomes more uniform once it starts to be pulled out from the concrete. Towards the end of the test, the bond resistance is very low due to the complete loss of the bearing resistance and the deterioration of the frictional resistance. Despite this severe deterioration, the bar is still able to develop 50% of the yield strength in compression at this stage (see Figure 6.26b) primarily due to the bearing of the tip of bar with the concrete at the bottom of the anchorage. The model is also successful in reproducing the dilatation caused by bar slip in a satisfactory way. As shown in Figure 6.18, the strains in the transverse reinforcement in Test No. 3 from FE analysis match the experimental measurements relatively well. However, the reduction of the dilatation effect observed experimentally for very large slips is not well captured due to the inability of the concrete model to close splitting cracks, as pointed out in Chapter 4. The FE model can also reproduce the strain variation along the perimeter bars in Test No.1, as shown in Figure 6.15a. These strains were very small because the concrete was capable of carrying the tensile force developed by the pulled force. However, as shown in Figure 6.15b, the model underestimates the strains in the perimeter bars in Test No. 2 because it overestimates the tensile capacity of the concrete and, therefore, it does not capture the horizontal cracking of the concrete cylinder.

6.4 Tension capacity of bars in well-confined concrete

FE analysis has been conducted to investigate the influence of the embedment length, bar size, compressive strength of concrete, and yield strength of steel on the tension or pull capacity of a reinforcing bar embedded in well-confined concrete, and to identify the minimum embedment lengths required to develop the yield and tensile strengths of a bar. For this purpose, a total of 120 pull-push tests have been simulated with FE models. The models have the same concrete cylinder dimensions and confining reinforcement as the test specimens presented in Section 6.2. This study is focused on No. 11, 14, and 18 bars. For each bar size, ten different embedment lengths, namely, lengths equal to 4, 8, 12, 16, 20, 24, 28, 32, 36, and 40 times the bar diameter, have been considered. Three different compressive strengths of concrete have been considered: 24.1 MPa (3.5 ksi), 34.5 MPa (5 ksi), and 48.3 MPa (7 ksi). The tensile strength of concrete has been assumed to be equal to 10% of the compressive strength. The bond strength has been determined based on the compressive strength of concrete, f_c', using the empirical relation that the bond strength is proportional to $f_c'^{3/4}$, as proposed in Chapter 4. Steel bars with yield strengths of 469 MPa (68 ksi) and 586 MPa (85 ksi) have been considered. The tensile strength of steel has been assumed to be equal to 1.4 times the yield strength. The embedment length, bar size, and the concrete and steel strengths for each of the analyses are presented in Table 6.5.

The loading protocol used in the parametric analyses is presented in Table 6.6. This protocol is slightly different from that used in the tests. Since the bars are not expected to yield in tension in all the analyses, the positive (pull) amplitude of each cycle

is prescribed as a fraction of the displacement at which the bar of the same size yielded in the actual test specimen that had the development length complying to the AASHTO specifications. The amplitude in compression is defined in terms of the expected yield strength of the bar as in the tests, but for the later cycles, the compressive stress imposed exceeds the yield stress to have a more demanding situation. This is also more consistent with the compression demands obtained for the column longitudinal bars in the shake-table test, as presented in Section 6.1.

Results of the analyses are presented in Table 6.5 in terms of the ratio of the maximum tensile stress developed at the pulled end of the bar, σ_{max}, to the yield strength of the steel, f_y. These results show that the yielding of a bar can be achieved for an embedment length as short as 8 to 12 times the bar diameter, and the tensile strength of the steel can be developed for an embedment length that is 20 to 32 times the bar diameter, depending on the compressive strength of the concrete and the yield strength of the bar. Figure 6.27 shows that for a given embedment length, normalized by the bar diameter, there is a large scatter in the tensile capacities obtained in different analyses. As expected, increasing the steel strength and decreasing the concrete strength decreases the σ_{max} / f_y ratio. The bar size has a very small influence in the tensile stress capacity developed by the bar.

The relation between the tension capacity of a bar embedded in concrete and the embedment length, bar size, compressive strength of concrete, and yield strength of steel can be established as follows. For a bar of diameter d_b subjected to a tensile force at the free end, the following equilibrium condition holds when a pull-out failure occurs.

$$\sigma_{\max} \frac{\pi d_b^{\,2}}{4} = \tau_{u,av} \pi d_b l_e \tag{6.1}$$

in which $\sigma_{\max}$ is the maximum tensile stress developed in the bar, and $\tau_{u,av}$ is the average bond strength along the embedment length, l_e. Dividing both sides of Equation 6.1 by the yield strength of steel and rearranging the terms, one has

$$\frac{\sigma_{\max}}{f_y} = \frac{4\tau_{u,av} l_e}{f_y d_b} \tag{6.2}$$

Assuming that the bond strength is proportional to a power of the compressive strength of the concrete, one can rewrite Equation 6.2 as

$$\frac{\sigma_{\max}}{f_y} = \chi \frac{f_c'^{\kappa} l_e}{f_y d_b} = \chi \lambda_e \tag{6.3}$$

in which χ is a proportionality constant and λ_e is defined as:

$$\lambda_e = l_e \frac{f_c'^{\kappa}}{f_y d_b} \tag{6.4}$$

Note that neither χ nor λ_e is dimensionless and that the value of χ may vary with the embedment length and, thereby, λ_e. The latter is due to the fact the bond stress distribution along the embedment zone may change as the embedment length changes, which will affect the average bond strength $\tau_{u,av}$. Therefore, Equation 6.3 can be more generally expressed as

$$\frac{\sigma_{\max}}{f_y} = f\left(\lambda_e\right) \tag{6.5}$$

To characterize the above relation, the values of $\sigma_{\max} / f_y$ obtained from the FE analyses are plotted against λ_e that assumes different values of κ. Most design codes assume that the average bond strength is proportional to $f_c'^{1/2}$, while the local bond strength assumed in the FE models is proportional to $f_c'^{3/4}$. Figure 6.28 through Figure 6.30 show the plots of $\sigma_{\max} / f_y$ vs. λ_e for values of κ equal to 0.5, 0.75, and 1, respectively. It can been seen for all three cases that a tri-linear relation ending with a horizontal line provides a good correlation with the numerical results. The horizontal line corresponds to the tensile strength of the bars, which is assumed to be 1.4 times the yield strength in the analyses. The expressions for the other two lines that provide a best fit of the data are determined with the least-squares method. The goodness of fit is measured by the coefficient of determination, R^2, which is calculated for the lines obtained for the different values of κ. The R^2 values are shown in Figure 6.28 through Figure 6.30. It can be seen that κ equal to 0.75 results in the values of R^2 closest to one, which indicates the best correlation between the numerical data and the tri-linear curve. This can be largely attributed to the fact that the local bond strength assumed in FE models is proportional to $f_c'^{3/4}$. Based on the findings in Chapter 3 and the fact that this investigation focuses on the development length required for well-confined cases, the trilinear relation that has κ equal to 0.75 has been chosen to be most appropriate. This relation is expressed as follows:

$$\frac{\sigma_{\max}}{f_y} = \begin{cases} 3.25\lambda_e & \lambda_e \le 0.375 \\ (0.45\lambda_e + 1.05) \le 1.4 & \lambda_e > 0.375 \end{cases} \tag{6.6a}$$

where

$$\lambda_e = l_e \frac{f_c'^{0.75}}{f_y d_b} \tag{6.6b}$$

in which f_c' and f_y are in MPa. With US customary units, this relation becomes

$$\frac{\sigma_{\max}}{f_y} = \begin{cases} 2.0\hat{\lambda}_e & \hat{\lambda}_e \le 0.61 \\ (0.275\hat{\lambda}_e + 1.05225) \le 1.4 & \hat{\lambda}_e > 0.61 \end{cases} \tag{6.7a}$$

where

$$\hat{\lambda}_e = l_e \frac{f_c'^{0.75}}{f_y d_b} \tag{6.7b}$$

in which f_c' and f_y are in ksi.

Based on Equation 6.6, the minimum values of λ_e required to develop the yield and tensile strengths of a bar are 0.31 and 0.78, respectively. These lead to the conclusion that for a reinforcing bar with an expected yield strength of 469 MPa (68 ksi) and embedded in 34.5-MPa (5-ksi) concrete, the minimum embedment lengths required to develop the yield and tensile strengths are $10.3\,d_b$ and $25.8\,d_b$, respectively. Equation 6.6 also reveals that the tension capacity of a bar is linearly proportional to the embedment length up to a bar stress that is slightly beyond the yield point. This observation is consistent with the provisions in Article 12.2.5 of ACI 318-08 (ACI 2008) and Article 5.11.2.2.2 of the AASHTO LRFD Bridge Design Specifications (AASHTO 2010) that the development length can be reduced in proportion to the ratio of the required bar stress to the yield strength of the bar. However, the embedment length has to be increased significantly more to develop tensile forces beyond yield. This is shown by the fact that the ratio of the minimum embedment length required to develop the tensile strength of a

bar to that required to develop the yield strength is 2.5, while the tensile strength is only 1.4 times the yield strength.

6.5 Reliability analysis of the tension capacity of bars anchored in well-confined concrete

The minimum embedment length required to develop the yield and ultimate capacities of a bar can be determined with Equation 6.6 based on the actual strengths of the concrete and steel. However, to establish a design recommendation, one needs to ensure that an acceptable margin of safety can be achieved with uncertainties related to the material properties, the geometry of the structure, the analytical models, etc. For this purpose, a reliability analysis has been carried out to (a) assess the level of safety of the AASHTO LRFD Bridge Design Specifications (AASHTO 2010) in developing the yield and ultimate tensile strengths of large-diameter bars in well-confined concrete; and (b) determine the minimum embedment length required for column longitudinal bars to develop their ultimate tensile capacity with an acceptable reliability level. To this end, a reliability analysis has been conducted. The reliability analysis is based on Equation 6.6, and the best estimates of the probability distributions for the compressive strength of concrete, the yield strength of steel, the embedment length, and the analytical prediction error. This analysis has been limited to No.11, 14, and 18 Grade 60 bars, and concrete with specified strengths of 24.8 MPa (3.6 ksi) and 34.5 MPa (5 ksi) because these are typical specified material properties used in California for bridge columns and piles.

The probability distributions of the material properties have been obtained from the literature. The yield strength of steel is assumed to be normally distributed with a

mean equal to 1.145 times the specified value and a coefficient of variation of 0.05, as reported by Nowak and Szerszen (2003). The compressive strength of concrete is also assumed to be normally distributed based on the study carried out by Unanwa and Mahan (2012) on concrete properties of recently constructed highway bridges in California. For a 24.8-MPa (3.6-ksi) concrete, the mean is equal to 1.45 times the specified strength, and the coefficient of variation is 0.19. For a 34.5 MPa (5 ksi) concrete, the mean is equal to 1.33 times the specified strength, and the coefficient of variation is 0.13. To account for construction errors, the actual embedment length is also defined as a normally distributed random variable with a mean equal to the specified length and a standard deviation equal to 16 mm (0.61 in.), as suggested by Darwin et al. (1998). The uncertainty related to the use of Equation 6.6 and the FE results to predict the actual tensile capacity of the bar also needs to be considered. To account for the uncertainty of Equation 6.6, the error, e, in predicting $\sigma_{\max} / f_y$ obtained from FE analysis is defined as a random variable with a normal distribution. Based on the statistics of this error, the mean and standard deviation of e are 0.0 and 0.05, respectively. In addition, the ratio between the actual tensile capacity and the FE prediction, r, is defined as a normally distributed random variable. Due to the lack of sufficient experimental data, the mean is taken as 1 and the dispersion is determined based on engineering judgment. Assuming that there is a 90% probability that the error between the actual capacity and that predicted by FE model is equal to or less than 10% (the error made by the FE model for the three pull-push tests is less than 3%), the standard deviation of r becomes 0.06. All random variables are statistically independent. The ratio of the ultimate to the yield strength of steel has been assumed to

be a deterministic parameter. The limit-state functions for the bar yielding capacity, g_y, and bar ultimate strength, g_u, are defined in Equations 6.8 and 6.9, respectively. These functions are based on Equation 6.6, and are defined in terms of the abovementioned random variables and one deterministic variable, d_b.

$$g_y = \begin{cases} r\left(3.25 l_e \dfrac{f_c'^{3/4}}{f_y d_b} + e\right) - 1.0 & l_e \dfrac{f_c'^{3/4}}{f_y d_b} \le 0.375 \\ r\left(0.45 l_e \dfrac{f_c'^{3/4}}{f_y d_b} + 1.05 + e\right) - 1.0 & l_e \dfrac{f_c'^{3/4}}{f_y d_b} > 0.375 \end{cases} \tag{6.8}$$

$$g_u = \begin{cases} r\left(3.25 l_e \dfrac{f_c'^{3/4}}{f_y d_b} + e\right) - 1.4 & l_e \dfrac{f_c'^{3/4}}{f_y d_b} \le 0.375 \\ r\left(0.45 l_e \dfrac{f_c'^{3/4}}{f_y d_b} + 1.05 + e\right) - 1.4 & l_e \dfrac{f_c'^{3/4}}{f_y d_b} > 0.375 \end{cases} \tag{6.9}$$

The probabilities of failure, p_F, in reaching these two limit states have been calculated through Monte Carlo simulation with the program CALREL (Liu et al. 1989). The probability of failure is related to the reliability index, β, through the definition that $p_F = \Phi(-\beta)$, in which Φ is the cumulative probability function of the standard normal distribution. Higher reliability indices imply higher safety levels.

The reliability of the AASHTO specifications in developing the yield and tensile strengths have been studied with the limit-state functions presented in Equations 6.8 and 6.9. The development lengths required by AASHTO specifications for No.11, 14, and 18 Grade 60 bars and a specified compressive strength of concrete equal to 24.8 MPa (3.6 ksi) are $26 d_b$, $31 d_b$, and $30 d_b$, respectively, for the best confined scenario. For a specified compressive strength of concrete equal to 34.5 MPa (5 ksi), these lengths are $22 d_b$, $26 d_b$,

and $25d_b$, respectively. The specified embedment lengths have been used as the median of l_e.

Results of the Monte Carlo simulations for the limit-states corresponding to the yield and ultimate strengths of the bar for f_c' = 24.8 MPa (3.6 ksi) and f_c' = 34.5 MPa (5 ksi) are presented in Table 6.7 and Table 6.8, respectively. The probabilities of not reaching bar yielding for these bars are between $3 \cdot 10^{-6}$ and $3.5 \cdot 10^{-5}$. Darwin et al. (1998) have suggested that the reliability index β to prevent bond failure should be around 3.5. This is equivalent to a probability of bond failure of no more than $2 \cdot 10^{-4}$, which is one fifth of that accepted for the failure of beams in bending and that of columns in combined bending and compression under typical loading conditions. Hence, the development length requirements in AASHTO specifications for well-confined situations are clearly adequate in terms of developing the yield strength of a bar. The probabilities of not reaching the ultimate strength of the bar are much higher, between 24 and 47%. However, these bars are not expected to reach such high stresses under typical loading conditions.

For RC members designed to behave in a ductile manner in flexure during an earthquake, the longitudinal reinforcement is expected to yield and enter the strain hardening regime. The failure limit state for flexure is defined in Caltrans Seismic Design Criteria (Caltrans 2010) as either the concrete reaching its ultimate compressive strain or the steel reaching a reduced ultimate tensile strain, which is thirty-three percent less than the expected ultimate tensile strain. The tensile stress corresponding to the reduced ultimate strain is around 1.35 times the actual yield strength of the reinforcing bars, based

on the tensile tests conducted in this study on large-diameter bars. This can be considered as the minimum strength that needs to be developed in longitudinal reinforcing bars in a hinging column. Hence, a third limit-state, g_{ru}, as presented below, is defined for a bar to develop its reduced ultimate capacity.

$$g_{ru} = \begin{cases} r\left(3.25 l_e \dfrac{f_c'^{3/4}}{f_y d_b} + e\right) - 1.35 & l_e \dfrac{f_c'^{3/4}}{f_y d_b} \le 0.375 \\ r\left(0.45 l_e \dfrac{f_c'^{3/4}}{f_y d_b} + 1.05 + e\right) - 1.35 & l_e \dfrac{f_c'^{3/4}}{f_y d_b} > 0.375 \end{cases} \tag{6.10}$$

Monte Carlo simulations have been performed to study the reliability of the AASHTO specifications in developing the reduced ultimate strength of a bar for f_c' = 24.8 MPa (3.6 ksi) and f_c' = 34.5 MPa (5 ksi). As shown in Table 6.7 and Table 6.8, the probabilities of not reaching the reduced ultimate capacity vary between 12 and 30%. If one adopts a target reliability index of $\beta = 1.75$ ($p_F = 4\%$) as suggested by Ellingwood et al. (1980) for earthquake loads, these development lengths are not sufficient.

Reliability analysis has been conducted to solve an inverse problem: given a target level of reliability, the minimum embedment lengths required to develop the yield and reduced ultimate tensile strengths of a bar is to be determined. For the yield strength, the desired reliability index is $\beta = 3.5$ as suggested by Darwin et al. (1998) for typical loading conditions. For the reduced ultimate strength, the target reliability index used here is $\beta = 1.75$, as suggested by Ellingwood et al. (1980) for earthquake loads. Monte Carlo simulations have been performed for different embedment lengths until the target value of β has been achieved. The results have shown that embedment lengths of $21\,d_b$

and $17\,d_b$ satisfy the minimum reliability level of $\beta = 3.5$ for a bar to reach its yield strength when the specified compressive strengths of concrete are 24.8 MPa (3.6 ksi) and 34.5 MPa (5 ksi), respectively. To develop the reduced ultimate tensile strength of a bar with a reliability level of $\beta = 1.75$, the embedment length has to be increased to $38\,d_b$ and $31\,d_b$ when the specified compressive strengths of concrete are 24.8 MPa (3.6 ksi) and 34.5 MPa (5 ksi), respectively.

6.6 Summary and conclusions

The development of large-diameter bars typically used in bridge columns and piles in California has been studied in this chapter. Experiments on large-diameter bars with long embedment length have confirmed that the development length requirements in AASHTO LRFD Bridge Design Specifications (AASHTO 2010) are appropriate for large-diameter bars in well-confined concrete, such as that in a bridge foundation. Tests on bars with this development length were not only able to yield, but also sustained significant inelastic strain up to or very close to the ultimate strength of the steel. A formula to calculate the tensile capacity of a bar given the embedment length, and actual concrete and steel strengths has been proposed in this chapter based on a parametric study with FE analysis. Reliability analyses based on this formula have shown that the AASHTO LRFD specifications for large-diameter bars in well-confined concrete ensure the yielding of a bar with an acceptable level of safety. However, these analyses have also indicated that if one wants to preclude bond failures in longitudinal reinforcement

before reaching the flexural failure limit state in a hinging column with an appropriate reliability level, then the development lengths need to be increased.

The experimental and FE analysis results presented in this chapter have also provided very useful information to characterize the bond-slip behavior in the anchorage zone of a bar subjected to earthquake loading. These results have shown that the slip and inelastic strain penetration can be very significant even for a bar that is well anchored. The FE analysis results have also shown that the bond stress distributions are highly nonlinear along the anchorage length.

Table 6.1: Ground motions in RC column test (Carrea 2010)

Reference	Earthquake	Station	Motion scale factor
Earthquake 1	1989 Loma Prieta	Agnew State Hospital-090	1.0
Earthquake 2	1989 Loma Prieta	Corralitos-090	1.0
Earthquake 3	1989 Loma Prieta	Los Gatos-000	1.0
Earthquake 4	1989 Loma Prieta	Corralitos-090	1.0
Earthquake 5	1995 Kobe	Takatori-000	-0.8
Earthquake 6	1989 Loma Prieta	Los Gatos-000	1.0
Earthquake 7	1995 Kobe	Takatori-000	-1.2
Earthquake 8	1995 Kobe	Takatori-000	1.2
Earthquakes 9 and 10	1995 Kobe	Takatori-000	1.2

Table 6.2: Specimen properties and test results

	Specimen properties						Test results			
Test No.	Bar size mm (in.)	l_e (d_b)	f_c' MPa (ksi)	f_{cs} MPa (ksi)	f_y MPa (ksi)	f_u MPa (ksi)	Slip at bar yield mm (in.)	Bar peak stress MPa (ksi)	Slip at peak stress mm (in.)	Failure mode
1	43 (1.41)	26	29.3 (4.25)	2.5 (0.36)	450 (65)	630 (91.5)	1 (0.04)	616 (89)	76 (3.0)	Bar pullout after yielding
2	57 (1.69)	25	35.9 (5.2)	3.0 (0.44)	470 (68)	655 (95)	1.5 (0.06)	655 (95)	60 (2.35)	Bar fracture
3	57 (2.25)	14	34.5 (5.0)	2.8 (0.40)	470 (68)	655 (95)	1.9 (0.075)	513 (74)	5.9 (0.23)	Bar pullout after yielding

Table 6.3: Location of strain gages

	Specimen 1		Specimen 2		Specimen 3	
	Central bar	North and south perimeter bars	Central bar	North and south perimeter bars	Central bar	North and south of spiral
Distance from concrete surface, mm (in.)	25 (1) -203 (-8) -508 (-20) -812 (-32)	-203 (-8) -508 (-20)	25 (1) -203 (-8) -406 (-16) -610 (-24) -914 (-36) -1219 (-48)	-508 (-20) -914 (-36)	25 (1) -203 (-8) -406 (-16) -610 (-24)	-102 (-4) -508 (-20)

Note: positive distances indicates that the strain gage is located above the concrete surface, i.e., outside the anchorage.

Table 6.4: pull-push tests loading protocol

Specimen 1			Specimens 2 and 3		
Cycle No.	+ peak	- peak	Cycle No.	+ peak	- peak
1,2	$0.25\,F_y$	$0.25\,F_y$	1,2	$0.25\,F_y$	$0.25\,F_y$
3,4	$0.50\,F_y$	$0.50\,F_y$	3,4	$0.50\,F_y$	$0.50\,F_y$
5,6	$0.75\,F_y$	$0.50\,F_y$	5,6	$0.75\,F_y$	$0.50\,F_y$
7,8	$2\,u_5$	$0.50\,F_y$	7,8	$2\,u_5$	$0.50\,F_y$
9,10	$4\,u_5$	$0.50\,F_y$	9,10	$4\,u_5$	$0.50\,F_y$
11,12	$8\,u_5$	$0.50\,F_y$	11,12	$8\,u_5$	$0.50\,F_y$
13,14	$12\,u_5$	$0.50\,F_y$	13,14	$12\,u_5$	$0.50\,F_y$
15,16	$20\,u_5$	$0.50\,F_y$	15,16	$16\,u_5$	$0.50\,F_y$
17,18	$32\,u_5$	$0.50\,F_y$	17,18	$20\,u_5$	$0.50\,F_y$
19	Load to failure		19,20	$32\,u_5$	$0.50\,F_y$
			21	Load to failure	

F_y: expected yield force of the bar

u_5: displacement measured at the positive peak of Cycle 5

Table 6.5: Parametric study variables and results

Model parameters			Analysis results, σ_{max} / f_y		
l_e (d_b)	f_c' MPa (ksi)	f_y MPa (ksi)	No. 11	No. 14	No. 18
4	34.5 (5)	469 (68)	0.35	0.31	0.33
8			0.79	0.82	0.71
12			1.18	1.23	1.02
16			1.26	1.27	1.28
20			1.31	1.33	1.33
24			1.38	1.38	1.38
28			1.40	1.40	1.40
32			1.40	1.40	1.40
36			1.40	1.40	1.40
40			1.40	1.40	1.40
4	48.3 (7)	469 (68)	0.47	0.44	0.46
8			1.07	1.13	0.98
12			1.29	1.29	1.29
16			1.34	1.34	1.36
20			1.39	1.39	1.39
24			1.40	1.40	1.39
28			1.40	1.40	1.40
32			1.40	1.40	1.40
36			1.40	1.40	1.40
40			1.40	1.40	1.40
4	23.1 (3.5)	469 (68)	0.29	0.23	0.29
8			0.59	0.54	0.63
12			0.97	1.02	0.93
16			1.22	1.25	1.26
20			1.31	1.25	1.26
24			1.32	1.32	1.31
28			1.36	1.37	1.37
32			1.38	1.39	1.37
36			1.38	1.40	1.39
40			1.40	1.40	1.40
4	34.5 (5)	586 (85)	0.28	0.25	0.26
8			0.63	0.65	0.56
12			1.04	1.04	0.80
16			1.26	1.28	1.14
20			1.28	1.29	1.29
24			1.31	1.34	1.32
28			1.38	1.38	1.37
32			1.39	1.39	1.40
36			1.40	1.40	1.40
40			1.40	1.40	1.40

Table 6.6: Loading protocol for parametric analysis

Cycle No.	+ peak	- peak
1	$0.25u_y$	$0.25F_y$
2	$0.50u_y$	$0.50F_y$
3	$0.75u_y$	$0.75F_y$
4,5	u_y	$1.0F_y$
6,7	$2u_y$	$1.0F_y$
8,9	$4u_y$	$1.0F_y$
10,11	$8u_y$	$1.1F_y$
12,13	$12u_y$	$1.1F_y$
14,15	$16u_y$	$1.1F_y$
16,17	$20u_y$	$1.2F_y$
18,19	$32u_y$	$1.2F_y$
20	$50u_y$	

F_y: expected yield force of the bar

u_y: expected displacement at tension yielding for $l_e=l_{d,AASHTO}$

Table 6.7: Reliability analysis results for $l_e = l_{d,AASHTO}$ and f'_c=24.8 MPa (3.6 ksi)

Bar size	Probability of not yielding the bar	Probability of not reaching the ultimate strength of the bar	Probability of not reaching the reduced ultimate strength of the bar
No.11	$3.5 \cdot 10^{-5}$	0.47	0.30
No.14	$7 \cdot 10^{-6}$	0.26	0.14
No.18	$8 \cdot 10^{-6}$	0.29	0.16

Table 6.8: Reliability analysis results for $l_e = l_{d,AASHTO}$ and f'_c=34.5 MPa (5 ksi)

Bar size	Probability of not yielding the bar	Probability of not reaching the ultimate strength of the bar	Probability of not reaching the reduced ultimate strength of the bar
No.11	$1.9 \cdot 10^{-5}$	0.44	0.27
No.14	$3 \cdot 10^{-6}$	0.24	0.12
No.18	$4 \cdot 10^{-6}$	0.28	0.14

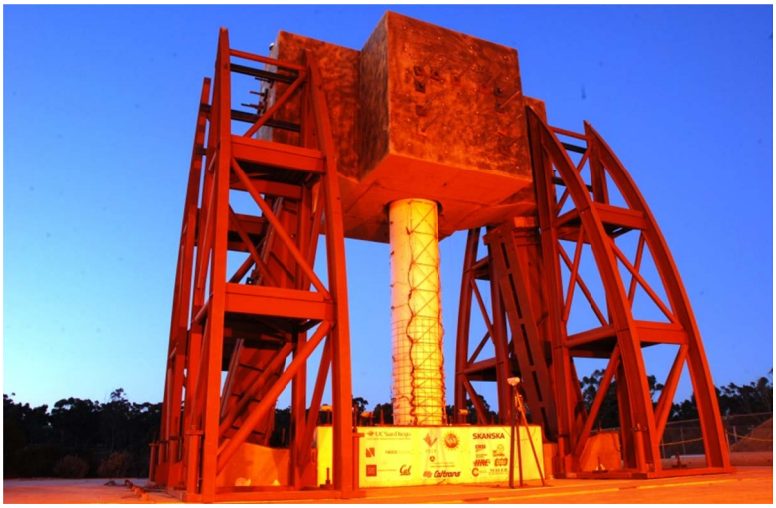

Figure 6.1: RC column tested at the NEES-UCSD Outdoor Shake Table (Restrepo et al. 2010)

(a) steel pieces attached to column bars

(b) displacement transducers using the steel piece at the column-footing interface as reference

Figure 6.2: Bond-slip measurement instrumentation (Restrepo et al. 2010)

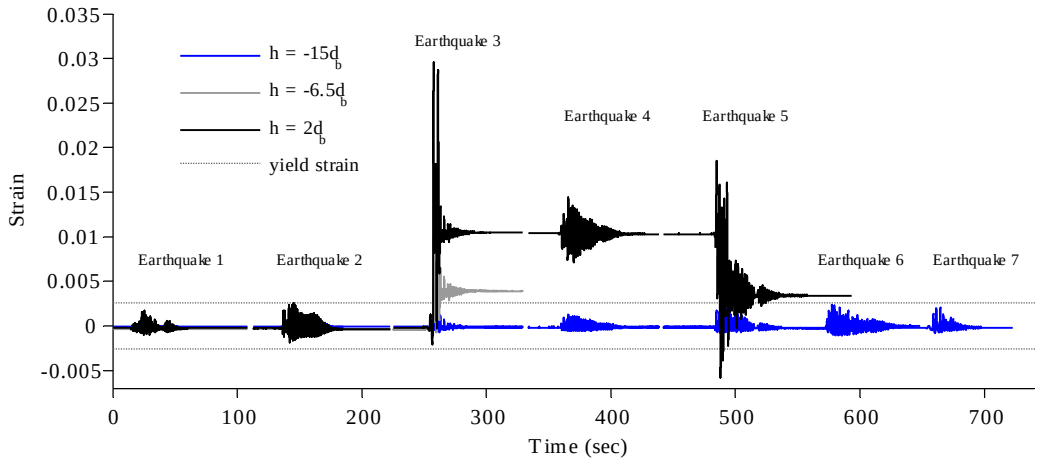

Figure 6.3: History of strains along the bar anchorage and in the column near the base

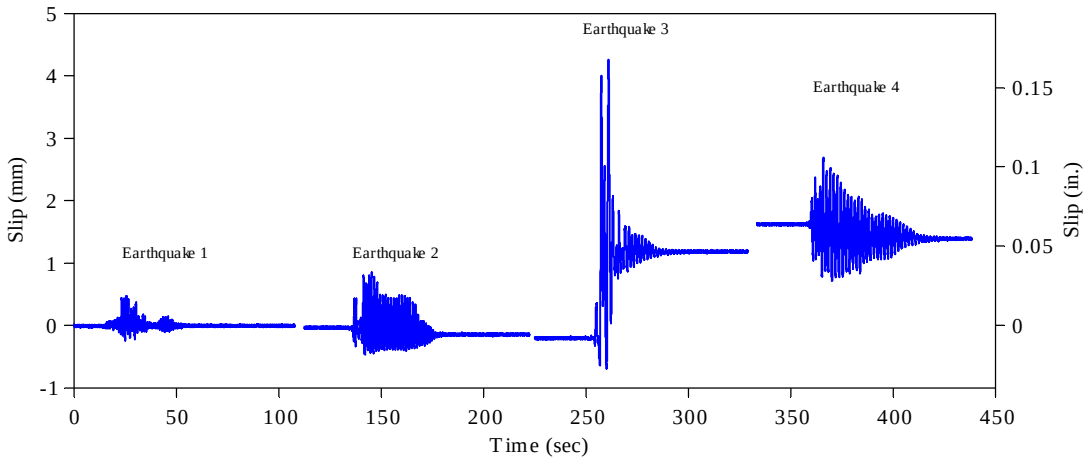

Figure 6.4: History of bar slip at the column-footing interface

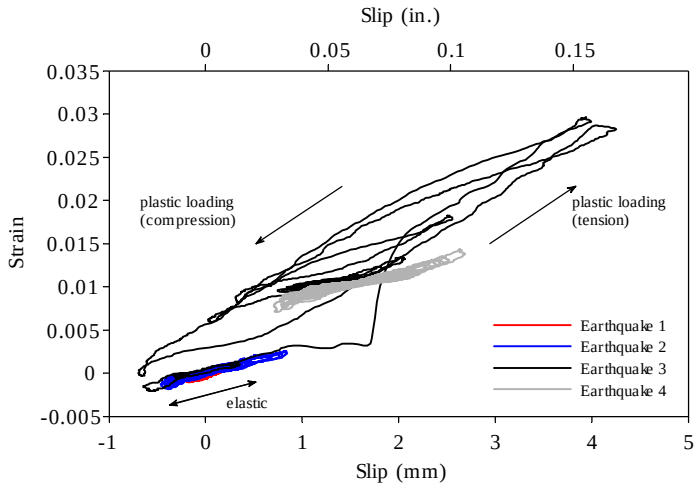

Figure 6.5: Bar slip vs. strain at the column-footing interface

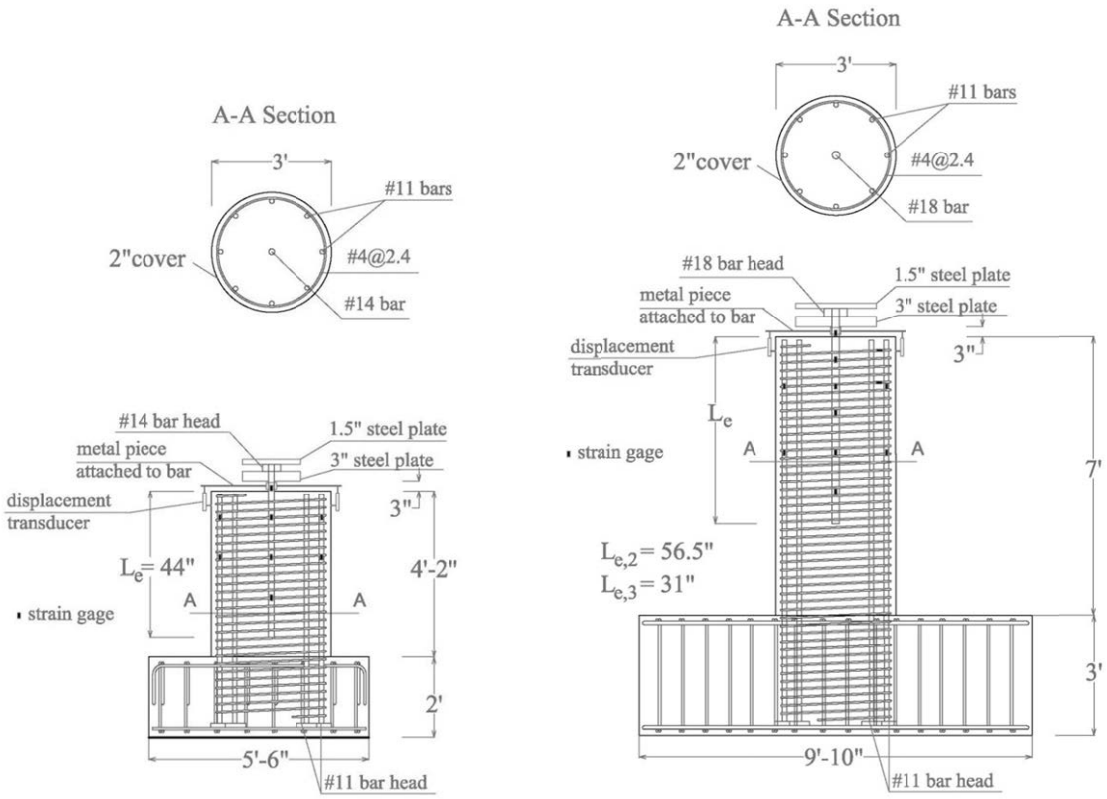

(a) Specimen 1 (b) Specimens 2 and 3

Figure 6.6: Test specimens and instrumentation (1'=305mm, 1"=25.4 mm)

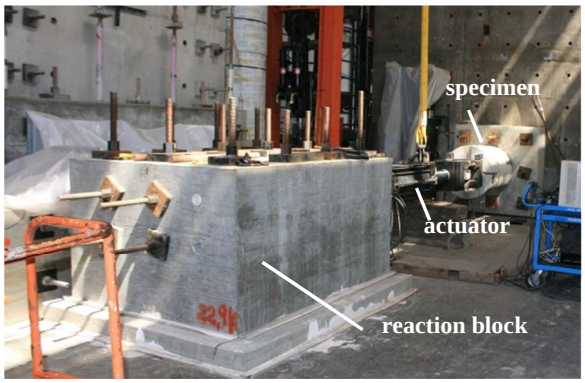

(a) setup for Specimen 1

(b) setup for Specimens 2 and 3

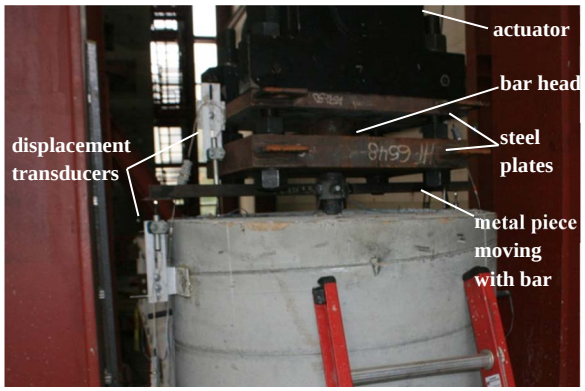

(c) close-up view of test setup at pulled end

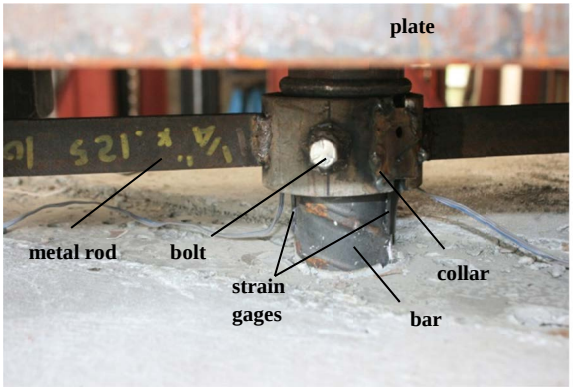

(d) metal piece used to measure bar slip

Figure 6.7: Test setup

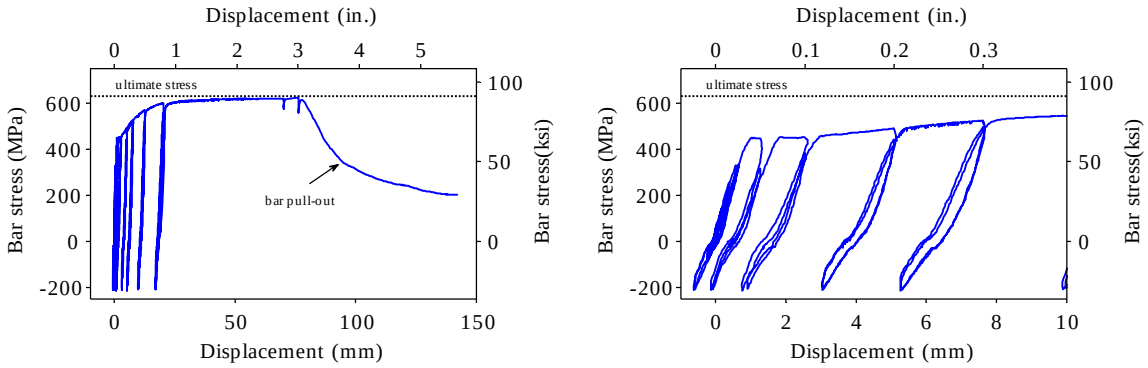

(a) bar stress vs. displacement at loaded end

(b) close-up view of curve in (a)

Figure 6.8: Experimental results for Test 1

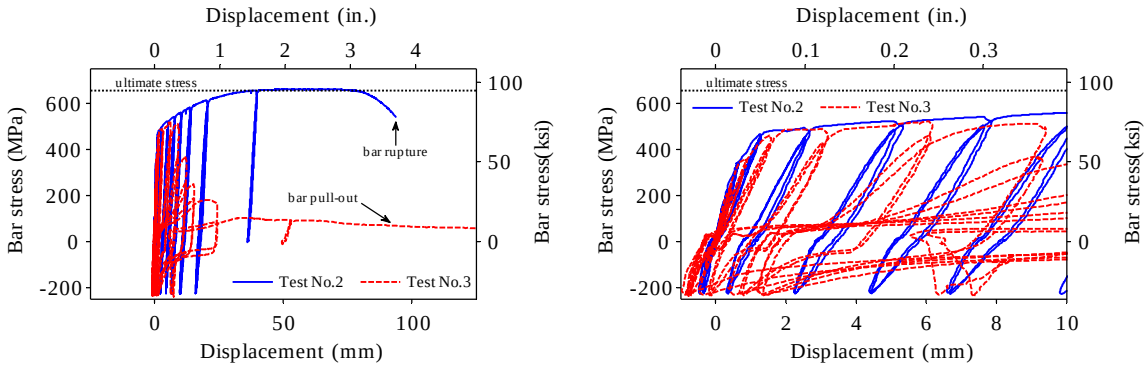

(a) bar stress vs. displacement at loaded end

(b) close-up view of curve in (a)

Figure 6.9: Experimental results for Tests 2 and 3

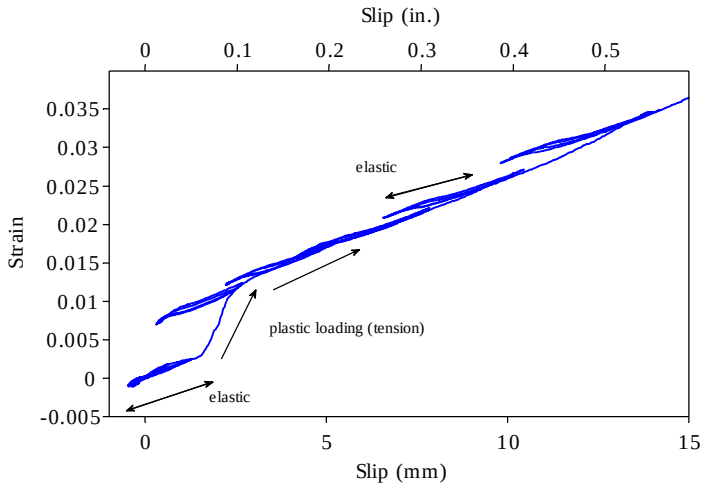

Figure 6.10: Bar strain vs. slip at the top of the anchorage in Test 2

(a) pull-out and cone failure (b) concrete powder between ribs

Figure 6.11: Bar pull-out in Test No. 1

(a) splitting and circular cracks in the concrete cylinder

(b) bar fracture and damage atop of the concrete cylinder

(c) cone-shaped surface

Figure 6.12: Bar fracture and damage in concrete cylinder in Test No. 2

(a) splitting and circular cracks in the concrete cylinder

(b) bar pull-out and damage atop of the concrete cylinder

(c) cone-shaped surface

Figure 6.13: Bar pull-out and damage in concrete cylinder in Test No. 3

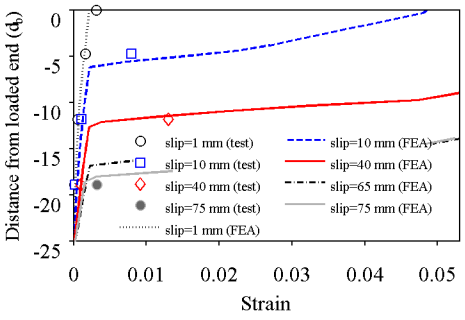

(a) Test No. 1

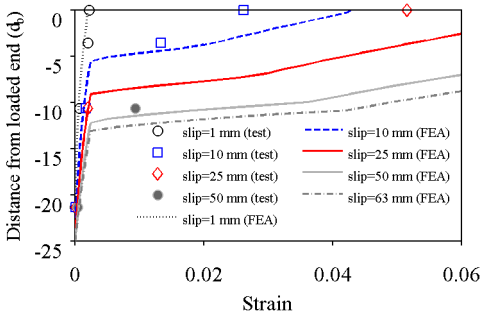

(b) Test No. 2

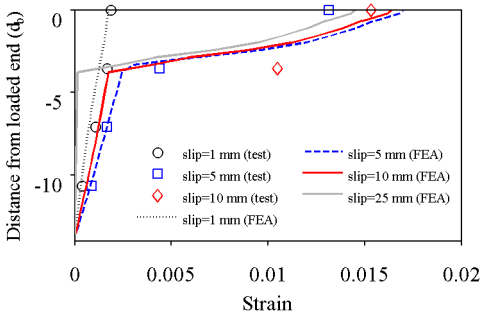

(c) Test No. 3

Figure 6.14: Strain penetration in tests and FE analysis

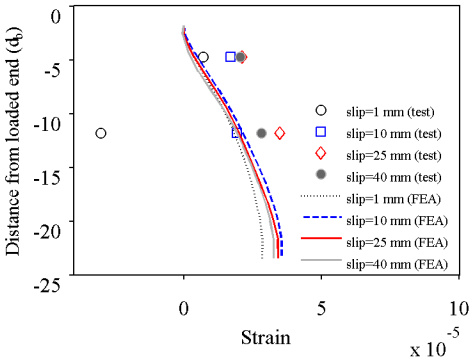

(a) Test No. 1

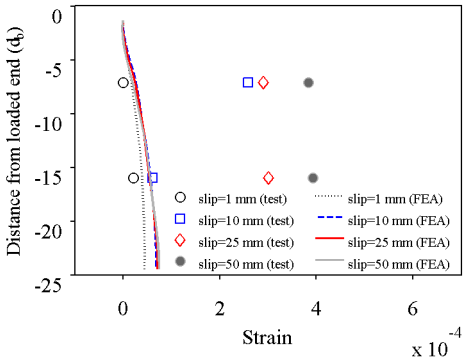

(b) Test No. 2

Figure 6.15: Strain in perimeter bars in tests and FE analysis

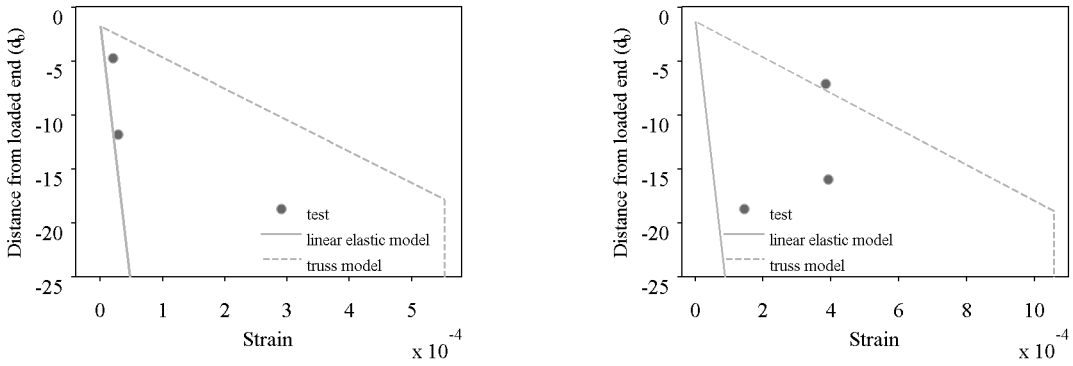

(a) Test No. 1 (slip=40mm) (b) Test No. 2 (slip=50mm)

Figure 6.16: Strains in perimeter bars from tests and simple analytical models

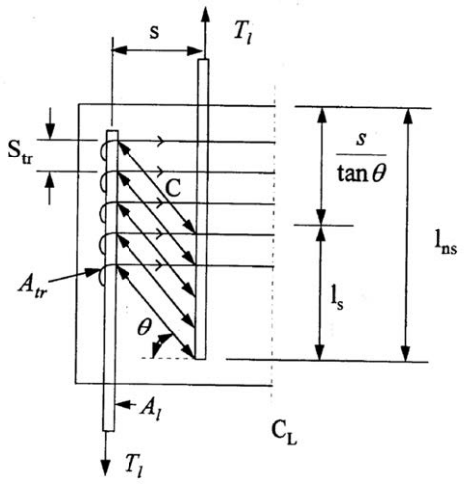

Figure 6.17: Truss analogy used by McLean and Smith (1997) for non-contact lap splices

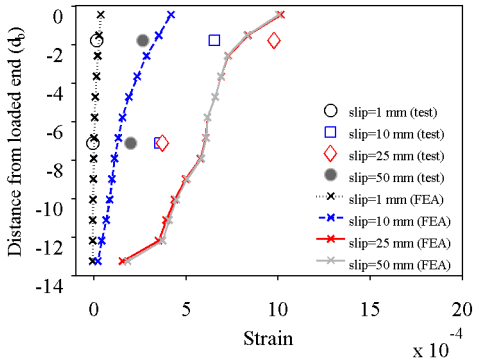

Figure 6.18: Strains in hoops in Test No. 3 and FE analysis

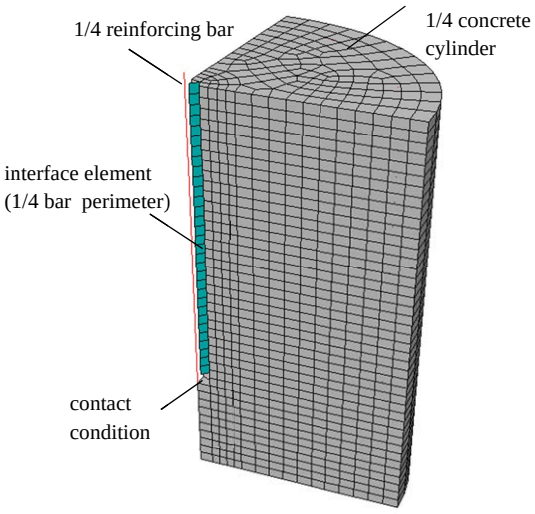

Figure 6.19: FE model for Test No. 3

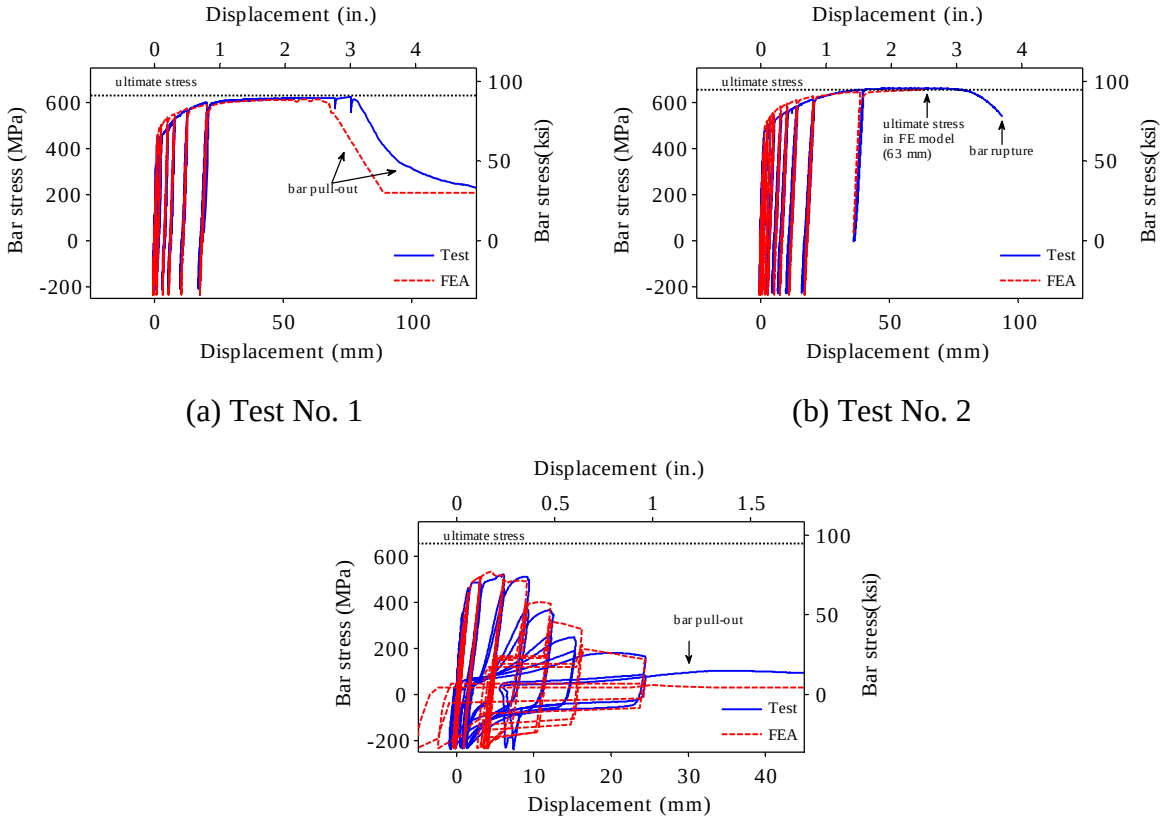

(a) Test No. 1

(b) Test No. 2

(c) Test No. 3

Figure 6.20: Bar stress – bar displacement curves from FE analyses and tests

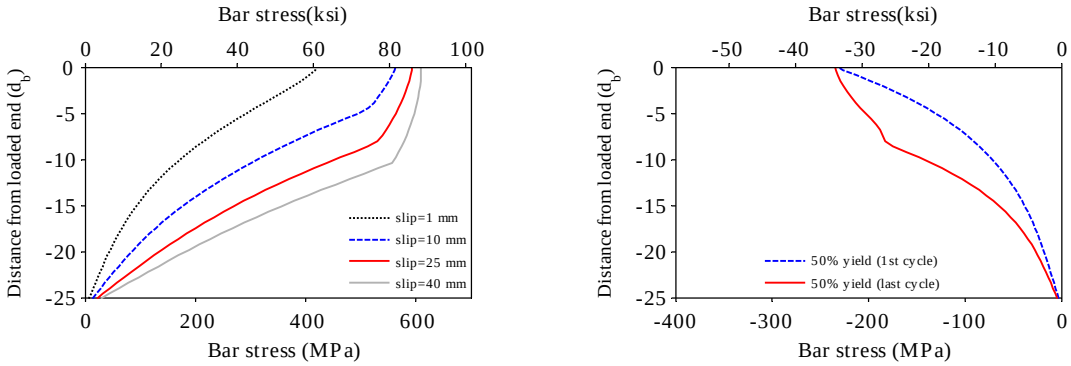

(a) tension (b) compression

Figure 6.21: Bar axial stress distributions from FE analysis for Test No. 1

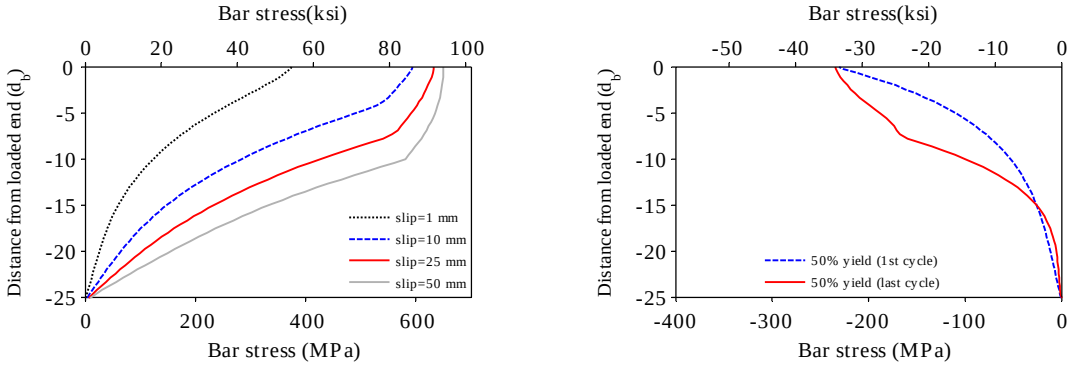

(a) tension (b) compression

Figure 6.22: Bar axial stress distributions from FE analysis for Test No. 2

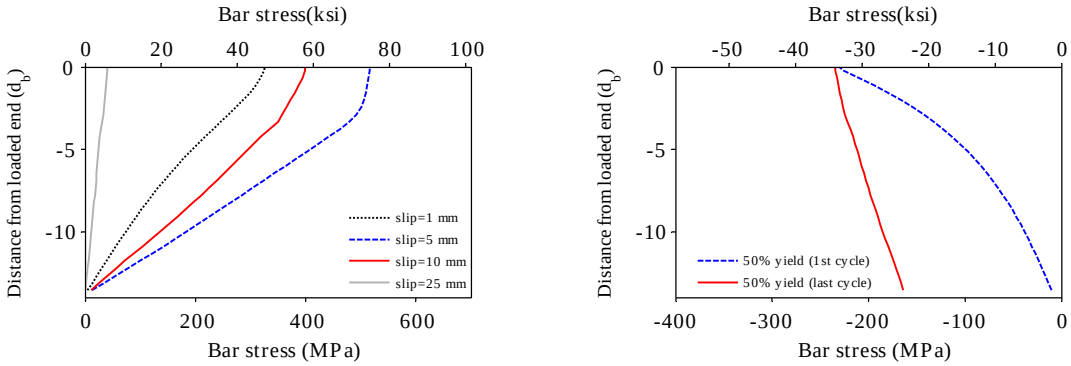

(a) tension (b) compression

Figure 6.23: Bar axial stress distributions from FE analysis for Test No. 3

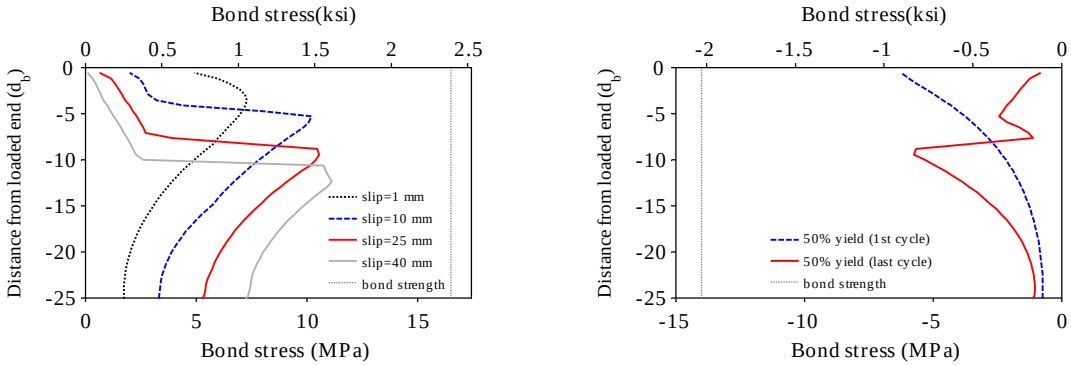

(a) tension (b) compression

Figure 6.24: Bond stress distributions from FE analysis for Test No. 1

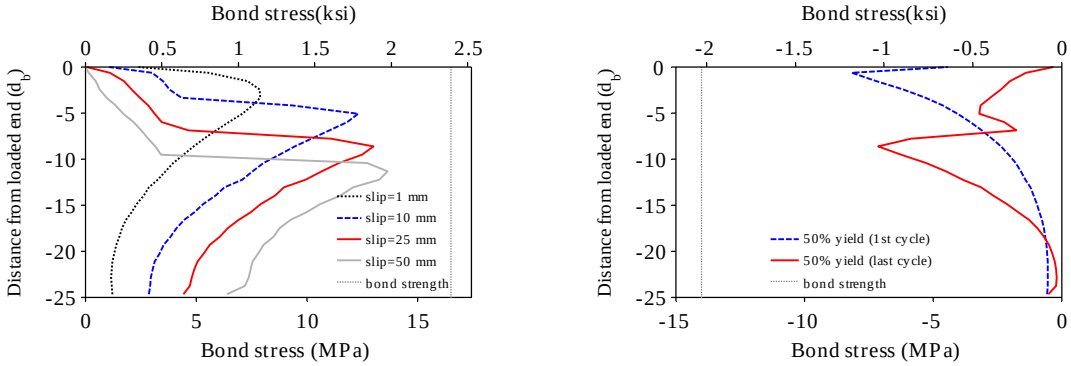

(a) tension (b) compression

Figure 6.25: Bond stress distributions from FE analysis for Test No. 2

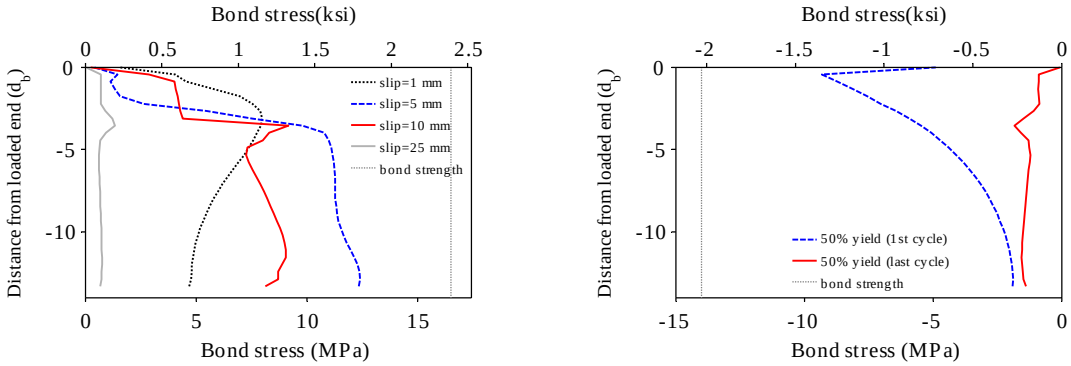

(a) tension (b) compression

Figure 6.26: Bond stress distributions from FE analysis for Test No. 3

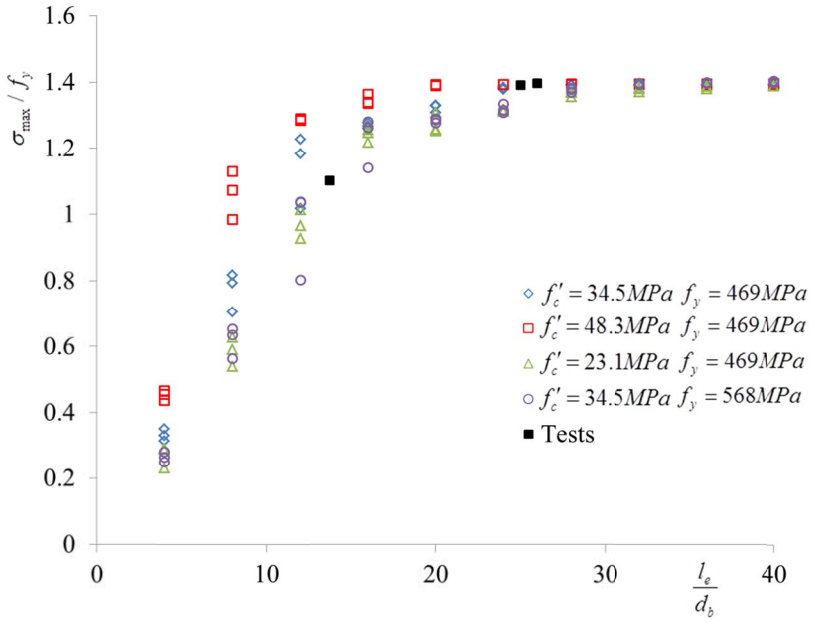

Figure 6.27: Tensile capacity vs. development length

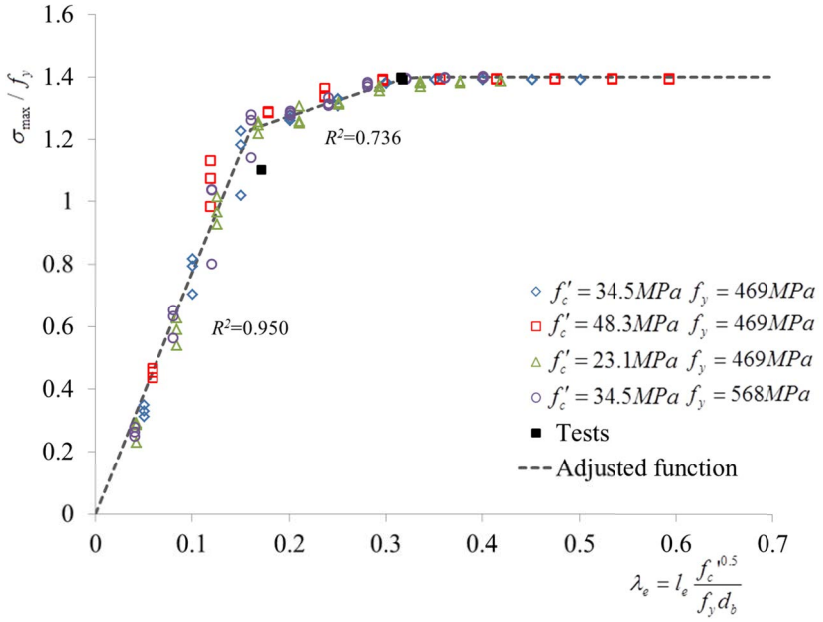

Figure 6.28: Tensile capacity vs. normalized development length for $\kappa = 0.5$

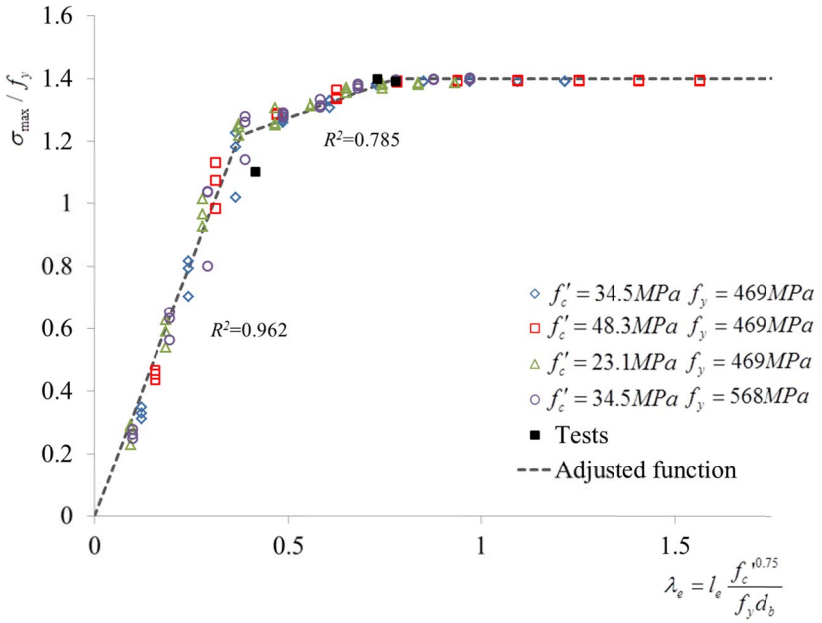

Figure 6.29: Tensile capacity vs. normalized development length for $\kappa = 0.75$

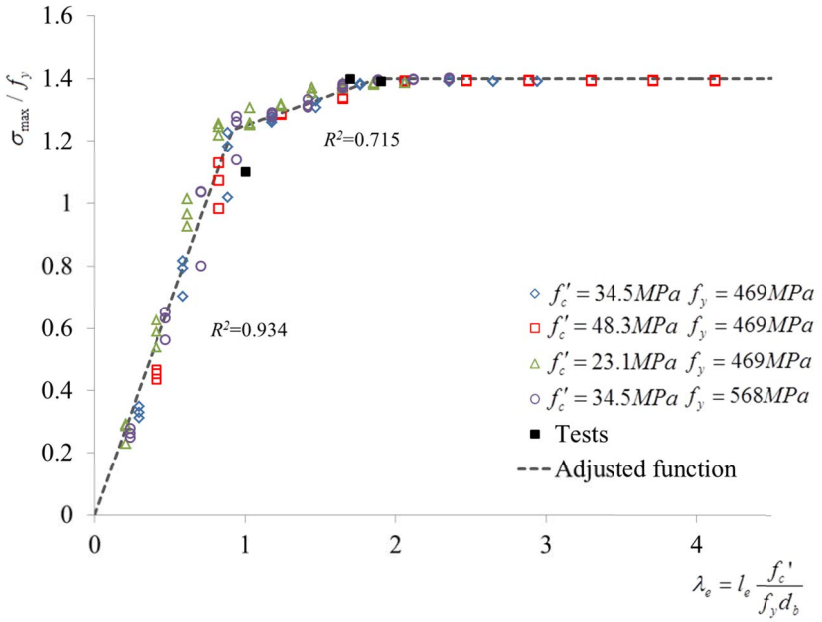

Figure 6.30: Tensile capacity vs. normalized development length for $\kappa = 1$

CHAPTER 7

LARGE-SCALE LABORATORY TESTING OF COLUMN – ENLARGED PILE SHAFT ASSEMBLIES

Pile shafts that are continuous with columns are used frequently in RC bridges because of the convenience in construction. Two types of pile shafts are typically used in California: pile shafts that have the same diameter as the column, and pile shafts with an enlarged section with respect to the column diameter. The California Department of Transportation (Caltrans) classifies them as Type I and Type II shafts, respectively. For Type II shafts, it is not possible to have a continuous reinforcing cage for the column and the shaft, and the column longitudinal reinforcement extended into the shaft is terminated at a certain distance forming a non-contact lap splice with the longitudinal shaft reinforcement.

Prior to 2010, Section 8.2.4 of Caltrans Seismic Design Criteria, SDC (Caltrans 2010) required that column longitudinal reinforcement extended into enlarged (Type II) shafts be terminated in a staggered manner with the minimum embedment lengths of $2D_{c,\max}$ and $3D_{c,\max}$, where $D_{c,\max}$ is the larger cross-sectional dimension of the column.

This was to ensure adequate anchorage of the reinforcement when a plastic hinge forms at the bottom of the column. With this specification, the longitudinal reinforcement in columns with dimensions more than 2.14 m (7 ft) required embedment lengths over 6.4 m (21 ft). For such construction, stringent Cal/OSHA safety standards for construction workers working in a confined space more than 6.1 m (20 ft) below the ground surface would apply. That embedment length requirement was recognized by Caltrans engineers to be over-conservative, and a new requirement was introduced in 2010, which specifies that the minimum embedment lengths for the staggered bars be $D_{c,\max} + l_d$ and $D_{c,\max} + 2l_d$, respectively, where l_d is the required development length for a straight bar in tension. Caltrans SDC specifies this development length as the basic tension development length l_{db} specified in AASHTO LRFD Bridge Design Specifications (AASHTO 2010) multiplied by the compounded modification factors of 0.9 and 0.6 for epoxy-coated and non epoxy-coated reinforcement, respectively. Expected values of 469 MPa (68 ksi) and 34.5 MPa (5 ksi) for the yield strength of steel and compressive strength of concrete, respectively, shall be used in calculating l_{db}. This new requirement is still considered conservative according to an analytical study conducted by Chang and Dameron (2009), and it reduces the required embedment lengths to be within the desired distance of 6.1 m (20 ft) for column cross-sectional dimensions as large as 3.05 m (10 ft) and bars as large as No. 14 (43-mm).

In both the old and current Caltrans specifications, the required embedment length depends on the column dimension $D_{c,\max}$ to account for the damage penetration into the embedment zone, which could shorten the effective development length. However, there

is no evidence to support this large safety cushion. Moreover, a study by McLean and Smith (1997) has shown that non-contact lap splices in enlarged shafts can perform in a satisfactory manner with splice lengths equal to $l_s + s$, where l_s is the splice length required for a contact splice, and is assumed to be $1.7l_d$, which is for Class C lap splices according to AASHTO (2010), and s is the bar spacing in the non-contact splice. The rationale for this recommendation is based on a truss model for force transfer between bars, as represented in Figure 7.1. Assuming that force transfer is through 45-degree struts, the lap splice length has to be increased by s to account for the ineffective transfer region. However, the study of McLean and Smith (1997) considered only No. 4 and 8 (12-mm and 25-mm) bars in reduced-scale specimens; hence, it is not certain that their conclusion is valid for lap splices of larger bars. Based on their model, the transverse steel in the shaft has to be designed to resist the horizontal component of the struts, and they have proposed that

$$s_{tr,\max} = \frac{2\pi A_{tr} f_{y,tr} l_s}{A_l f_u} \tag{7.1}$$

in which $s_{tr,\max}$, A_{tr}, and $f_{y,tr}$ are the maximum spacing, cross-sectional area, and yield strength of the transverse reinforcement, respectively; and A_l and f_u are the total cross-sectional area and ultimate strength of the longitudinal reinforcement, respectively.

Results from McLean and Smith (1997) indicate that the minimum embedment length required by Caltrans SDC for column reinforcement extending into Type II shafts is conservative. Nevertheless, there was no large-scale test data to support a revision. For this reason, large-scale testing and finite element analyses of column-shaft assemblies

were carried out. This chapter focuses on two of the column-shaft tests conducted. The finite element modeling and the development of new design recommendations are presented in Chapter 8.

As part of this study, four full-scale reinforced concrete bridge column - enlarged shaft assemblies were tested under quasi-static cyclic lateral loading in the Powell Structural Engineering Laboratories at UCSD. However, only two of these tests are reported here. The main difference between these two tests was the embedment length of the column cage inside the shaft. In Specimen 1, an embedment length of $D_{c,\max} + l_d$ was used, which is very similar to the current Caltrans requirement, but the specimen had all the column longitudinal bars terminated at the shorter of the two distances specified by Caltrans SDC. This was proven to be safe with preliminary finite element analysis results. With the tests results from the first specimen, the finite element model was validated and refined, and it was decided that the embedment length could be further reduced in the second specimen.

7.1 Description of test specimens

Each test specimen consisted of a bridge column and the upper part of a pile shaft, and was subjected to fully-reversed cyclic lateral loading at the top of the column. The height of each shaft was determined based on the results of an analytical study carried out by Liu (2012) on the lateral load-displacement behavior of column-shaft assemblies with soil-pile interaction. In her study, nonlinear pushover analyses of column-pile-soil systems were performed for different system configurations and soil conditions. In the

analyses, the column and the shaft were modeled using fiber-section beam-column elements with distributed plasticity and the soil was modeled with p-y springs using the software platform OpenSees (PEER 2012). Results of these analyses show that inelastic deformation will concentrate at the base of the column, and that the maximum bending moment will occur in the shaft at a depth no larger than two times the column diameter. Hence, it was decided to limit the height of the shaft in the test specimen to approximately two times the column diameter. As shown in Figure 7.2, the bending moment distribution induced in the upper part of the shaft, where the column cage is embedded, by a point load at the top of the column during a test is a good approximation of that in a pile shaft embedded in soil. Moreover, this test design is conservative in the sense that the moment and shear demands in the lap splice area would be slightly higher than those in a shaft embedded in soil.

7.1.1 Design of specimens

The column and shaft in Specimen 1 were designed to represent existing bridges in California and it complied with the Caltrans Bridge Design Specifications (Caltrans 2008) and Caltrans SDC (Caltrans 2010). The only exception was the embedment length of the column cage inside the shaft in that all the reinforcement was terminated at $D_{c,\max} + l_d$, in which l_d is determined in accordance with AASHTO (2010). The current requirement to terminate half of the bars at $D_{c,\max} + 2l_d$ was not followed. As a result, the total embedment of the column cage was 2286 mm (7 ft - 6 in.), 762 mm (2 ft - 4 in.) shorter than what would be required per Caltrans SDC. This reduction in the embedment length was considered safe based on a preliminary three-dimensional finite element

analysis of the column-shaft assembly. In this analysis, the extent of damage into the shaft when the plastic hinge formed at the base of the column was significantly less than $D_{c,\max}$, which was consistent with the observations from the analyses done by Chang and Dameron (2009). Beyond this point, the bars extending from the column would be away from the severely stressed region, and, therefore, the use of a staggered termination of the bars was unwarranted.

Specimen 2 was designed to represent current practice of Caltrans, which follows AASHTO LRFD Bridge Design Specifications (AASHTO 2010) and Caltrans SDC (Caltrans 2010), with the exception of the embedment length of the column cage inside the shaft and the transverse reinforcement for the shaft in the lap splice area. As shown in Chapter 6, without the consideration of uncertainties in material properties and construction quality, the development lengths specified in AASHTO (2010) for large-diameter bars are appropriate to develop the tensile capacity of a bar. Hence, it was determined to reduce the embedment length for Specimen 2 to $l_d + s + c$, in which s is the spacing between the longitudinal bars extending from the column and those of the shaft (i.e., the lap bars spacing), and c is the concrete cover at the top of the shaft. The additional length $s + c$ is to account for the ineffective transfer region due to the bar offset in the non-contact lap splice, as recommended by McLean and Smith (1997). However, this embedment length is significantly less than that recommended by McLean and Smith (1997), who had l_d in the above expression substituted by $1.7l_d$, which is the development length specified by the AASHTO LRFD Bridge Design Specifications for Class C lap splices. The factor of 1.7 is deemed unnecessary based on the development

tests data shown in Chapter 6, the test results for Specimen 1, and the finite element analysis of the columns-shaft assembly using a model validated by the test. Based on this, the embedment length of the column cage was determined to be 1829 mm (6 ft), which was half of what would be required per Caltrans SDC.

For Specimen 2, the amount of transverse reinforcement in the lap splice region of the shaft was determined with Equation 7.1, but with l_s replaced by l_d to be consistent with the embedment length used.

7.1.2 Specimen geometry and reinforcement

The geometry of Specimen 1 is shown in Figure 7.3. It consisted of a 1219-mm (4-ft) diameter column with a height of 4877 mm (16 ft) to the point of application of the horizontal load, resulting in an aspect ratio (H/D) of 4. The pile shaft was 1829 mm (6 ft) in diameter and 2743-mm (9-ft) high. As mentioned before, the column cage was embedded 2286 mm (7ft - 6in.) inside the shaft. The column longitudinal reinforcement consisted of 18 No. 11 (36-mm) bars (with a reinforcement ratio of 1.55%), and the transverse reinforcement consisted of double No. 5 (16-mm) hoops spaced at 165 mm (6.5 in.) on center (with a volumetric reinforcement ratio of 0.87%). The transverse reinforcement of the column cage embedded in the shaft consisted of single No. 5 hoops spaced at 165 mm (6.5 in.) on center. The shaft longitudinal reinforcement consisted of 28 No. 14 (43-mm) bars (with a reinforcement ratio of 1.55%), and the transverse reinforcement consisted of double No. 6 (19-mm) hoops spaced at 165 mm (6.5 in.) on center (with a volumetric reinforcement ratio of 0.82%).

Specimen 2 consisted of a 1219-mm (4-ft) diameter and 6486-mm (18-ft) tall column (with an aspect ratio = 4.5), and a 1829-mm (6-ft) diameter and 2337-mm (8-ft) tall pile shaft, as shown in Figure 7.4. The column longitudinal reinforcement consisted of 18 No. 14 bars (with a reinforcement ratio of 2.25%), and the transverse reinforcement consisted of double No. 5 hoops spaced at 102 mm (4 in.) on center in the plastic hinge region (with a volumetric reinforcement ratio of 1.41%), and single No. 5 hoops spaced at 152 mm (6 in.) on center in the rest of the column (with volumetric reinforcement ratio of 0.94%). The column cage was embedded 1829 mm (6 ft) in the pile shaft. The transverse reinforcement for the plastic hinge region of the column was extended 610 mm (2 ft) in the shaft, and for the rest of the embedment length single No. 5 hoops spaced at 152 mm (6 in.) on center were used. The shaft longitudinal reinforcement consisted of 26 No. 18 (57-mm) bars (with a reinforcement ratio of 2.55%), and the transverse reinforcement consisted of double No. 7 (22-mm) hoops spaced at 178 mm (7 in.) on center (with a volumetric reinforcement ratio of 1.01%).

Concrete with a specified compressive strength of 31 MPa (4500 psi) at 28 days, a slump of 178 mm (7 in.), and a maximum aggregate size of 9.5 mm (3/8 in.) was used in the shaft for both specimens. Concrete with a specified compressive strength of 31 MPa (4500 psi) at 28 days, a slump of 102 mm (4 in.), and a maximum aggregate size of 25 mm (1 in.) was used in the columns. The specimens were to be tested after the concrete strength in the column and the shaft had reached 34.5 MPa (5.0 ksi). The results of the actual strength of concrete on the days of the test are presented in Table 7.1. All the reinforcement was Grade 60 complying with the ASTM 706 standards. Results from material test on steel reinforcement are presented in Table 7.2.

Both specimens had a 4267-mm x 2438-mm x 1219-mm (14-ft x 8-ft x 4-ft) footing to anchor the shaft to the strong floor. On top of the column, a 2438-mm x 2438-mm x 610-mm (8-ft x 8-ft x 2-ft) load stub was constructed for the application of the vertical and horizontal loads. The reinforcement in the footing and load stub were designed to sustain the maximum loads expected during the test with an acceptable margin of safety.

7.2 Construction

The specimens were casted in five stages: footing, lower portion of the shaft, upper portion of the shaft, column, and load stub. After each pour, some roughness was applied to the cold joint with chisels. Before the following pour, steel brushing of the joint was applied to partially expose the aggregate. The joint was cleaned from debris and dust, and wetted immediately before receiving the fresh concrete. Pictures of the construction of the specimen are presented in Appendix B.

7.3 Instrumentation

The specimens were internally and externally instrumented to characterize the deformations during testing. Internal instrumentation consisted of electrical resistance strain gages attached to longitudinal and transverse reinforcement in the shaft and the column. A total of 152 strain gages were used in Specimen 1 and 145 in Specimen 2. External instrumentation consisted of displacement transducers attached externally to the specimens to measure its lateral displacement and quantify different deformation modes:

flexure deformation, shear deformation, base rotation, and sliding at the interfaces. Pictures of the instrumentation are shown in Appendix B.

Strain gages were placed at different heights in selected column and shaft longitudinal bars near the north and south faces (the specimen was loaded in the north-south direction) to study the strain distributions along these bars, including the lap splice region inside the shaft. The strain gages were placed on the longitudinal rib of the longitudinal bars to avoid having to disturb transverse ribs, which would have affected the bond characteristics. In addition, strain gages were attached on selected column and shaft hoops, with special attention to the anchorage region in the shaft to study the dilatation caused by bar slip. Drawings with the exact locations of the strain gages are shown in Appendix C.

The curvature distribution along the height of the column and the pile was measured using vertical displacement transducers mounted along two parallel lines on the east and west faces of each specimen. These transducers measured the vertical elongation between two rods embedded in the column and shaft concrete at different heights. The same rods were used as reference points to measure the horizontal and diagonal elongation on one side of the specimen to estimate the shear deformation of the column. Vertical displacement transducers were mounted at the base of the column to measure the base rotation with respect to the top of the shaft. Similar measurements were made on the base rotation of the shaft with respect to the footing. In addition, transducers were mounted to measure potential sliding between the different components of the specimen (i.e., the footing, shaft, column, and load stub), and potential sliding and uplift at the

footing with respect to the strong floor. Drawings with the exact locations of the displacement transducers are shown in Appendix C.

7.4 Test setup and loading protocol

The test setup is shown in Figure 7.5. The specimens were secured to the strong floor using 16 rods post-tensioned to a force of 1334 kN (300 kips) each. This force was determined to avoid sliding and decompression at any point in the floor-footing interface during a test. In a test, the top column was subjected to a constant vertical load of 3559 kN (800 kips). Added to the self-weight of the specimen, this load subjected the base of the column to an axial stress equal to 9.4% of the targeted compressive strength of the concrete. The vertical load was applied on top of the specimen using four post-tensioned rods placed symmetrically around the column. Anchored at the top of the load stub, these rods passed through holes in the load stub and the footing and were subjected to a constant force using four center-hole hydraulic jacks located under the strong floor. The hole in the footing was cone-shaped to allow the rotation of the rod as it moved at its top end together with the load stub. Pictures of the test setup are presented in Appendix B.

The specimens were subjected to cyclic lateral displacement in the north-south direction using two 979-kN (220-kip) capacity, 1219-mm (48-in.) stroke actuators placed at the mid-height of the load stub on the north side of the specimen. The actuators were attached to a strong wall at a height of 8.84 m (29 ft) for Specimen 1, and 9.1 m (30 ft) for Specimen 2. The loading protocol used for both tests is plotted in Figure 7.6a. It consisted of four fully-reversed force-controlled cycles up to 25, 50, 75, and 100% of the

lateral load, F'_y, which corresponded to the first yield of the longitudinal reinforcement at the base of the column, and then fully-reversed displacement-controlled cycles with increasing system ductility demands of 1, 2, 3, 4, and so forth until the lateral load resistance dropped significantly due to the fracture of the longitudinal bars in the column. The system ductility demand is defined as $\mu = \Delta / \Delta_y$, in which Δ is the lateral displacement of the specimen at the level of the horizontal actuators, and Δ_y the equivalent yield displacement. As shown in Figure 7.6b, Δ_y is defined as the intersection between the secant line passing through the point (Δ'_y, F'_y) that corresponds to first yield of the column longitudinal bars and the horizontal line passing through the theoretical ultimate load (F_y). Hence,

$$\Delta_y = \frac{F_y}{F'_y} \Delta'_y \tag{7.2}$$

To define the loading protocol, F'_y and F_y were estimated from finite element analysis, and Δ'_y was taken as the average of the maximum displacements in each direction measured in Cycle 4 of the test, in which the theoretical F'_y was reached.

7.5 Global test results

7.5.1 Load-displacement response

The lateral load-vs.-top drift relation obtained for Specimen 1 is plotted in Figure 7.7a. For the plots and the following discussion of the results, the positive direction of

loading is defined to be towards the south, and the negative to be towards the north. The maximum lateral load attained was 1112 kN (250 kip). The drop of the lateral resistance with drift was caused by the P-delta effect of the vertical force. The test was stopped after the system displacement ductility had reached a value of 5.5 when the lateral load capacity started to decrease significantly due to the buckling and subsequent fracture of several longitudinal bars at the base of the column. The ductility values presented in this section do not correspond to the nominal values used for the loading protocol, but those calculated afterwards using the actual value of Δ_y, which is defined in the same way but considering the actual maximum load and the actual displacement at the first yield instead of the theoretical values. The displacement ductility of the column itself reached a maximum value of 6.8, according to the study conducted by Liu (2012) on the behavior of these columns.

The lateral load-vs.-top drift relation obtained for Specimen 2 is plotted in Figure 7.7b. The maximum lateral load reached 1223 kN (275 kips), and the test was stopped after the specimen had reached a system displacement ductility of 7, when one of the longitudinal bars fractured at the base of the column. The maximum displacement ductility of the column itself reached a value of 8, according to the study conducted by Liu (2012). The lateral loads normalized by the respective peak loads are plotted against the system ductility obtained for Specimens 1 and 2 in Figure 7.7c. The difference in the embedment length does not seem to affect the global behavior of the columns. Moreover, Specimen 2 shows a higher ductility than Specimen 1 because bar buckling and fracture were delayed due to the more closely spaced hoops at the base of the column.

7.5.2 Test observations for Specimen 1

Flexural cracks in the column started to be visible in the lower 1 m (3 ft) of the column at Cycle 2, i.e., at a force equal to 50% of that corresponding to the theoretical first yield. At Cycle 4, the theoretical first yield, flexural cracking increased significantly in the column. The cracks developed in Cycle 2 propagated, and more flexural cracks appeared with a more or less uniform spacing of 250 mm (10 in.). However, the crack spacing increased slightly as they appeared farther away from the column base. Cracks were observed as far as 3 m (10 ft) from the base of the column or over 60% of the column height, as shown in Figure 7.8a. Some flexural cracks also appeared on both sides of the shaft (with about 600-mm [2-ft] spacing), as shown in Figure 7.8b and Figure 7.8c. In addition, several radial cracks extended from the column base to the edge of the shaft and continued vertically 300 mm (1 ft) to 600 mm (2 ft) down the surface of the shaft, as shown in Figure 7.8d and Figure 7.8e. These cracks were the result of the splitting forces generated by bar slip.

From Cycles 5 through 9, no new cracks were observed but the existing ones further propagated and opened. These cracks did not propagate further after Cycle 9. At Cycle 7, which was the first cycle at a system ductility of 2.2, the concrete at the base of the column started to be crushed on the north and south faces, as shown in Figure 7.9a. At Cycle 9, which was the first cycle at a ductility of 3.3, spalling of the concrete cover at the base of the column started (see Figure 7.9b), and cracks with significant residual opening were observed. At Cycle 11, which was the first cycle at a ductility of 4.4, spalling occurred in the lower 600 mm (2 ft) of the column with the hoop reinforcement

exposed, as shown in Figure 7.9c. At Cycle 13, which was the first cycle at a ductility of 5.5, spalling became more severe and exposed some of the longitudinal bars on both sides of the column (see Figure 7.9d). On the north side, bars started to buckle at about 1 ft above the base of the column, as shown in Figure 7.9e. Upon load reversal in Cycle 14, which was the second cycle at a ductility of 5.5, these bars were placed in tension, and two of them fractured, as shown in Figure 7.9f. At the same time, two of the bars exposed on the south side started to buckle, and they fractured once the load was reversed. At this moment, the lateral load resistance had dropped significantly and the test was stopped. Finally, when bringing the column back to a zero residual drift, a third bar that had buckled on the north side fractured. The buckling and subsequent fracture of longitudinal reinforcement were also observed in previous tests on well-confined bridge columns, e.g., Lehman and Moehle (2000), Restrepo et al. (2006), and Carrea (2010). This type of fracture is the result of stress concentration in the extreme compression fiber of a buckled bar, which creates micro-cracks that will propagate when the bar is straightened up in tension again (Carrea 2010).

At the end of the test, after the rubbles caused by the crushing of the concrete at the column base had been removed, a circular crack was observed on the top of the shaft, as shown in Figure 7.10a and Figure 7.10b. This crack was the result of a cone shaped failure at the top of the embedment length of the column longitudinal reinforcement. Radial cracks due to the splitting forces introduced by bar slip at the top of the shaft are also visible in Figure 7.10a and Figure 7.10b. The maximum residual width measured in one of these cracks at the end of the test was 3 mm (1/8 in.). The splitting cracks

extended vertically on the lateral surface of the shaft with lengths between 600 mm (2 ft) and 1200mm (4 ft), as shown in Figure 7.10c.

The shape of the lateral displacement of the column, plotted in Figure 7.11 at the peak displacements of different cycles, reveals that the lateral deformation of the shaft was very small, and that most of the displacement in the column was due to the rotation occurring in the plastic hinge and at the column base due to bar slip. The flexural and shear deformations, as well as the base rotation due to bar slip were calculated based on the displacement transducers readings. Information on how these deformations were computed can be found in the study carried out by Liu (2012). The shear deformation was found negligible as compared to the flexural deformation and the base rotation due to bar slip. According to Liu (2012), between 50% and 75% of the total column deformation was due to flexural deformation; the base rotation contributed about 20% to 50% and shear deformation contributed less than 2.5% to the total displacement. The curvature distribution of the column at the peak displacements of different cycles, as plotted in Figure 7.12, shows that most of the flexural deformation occurred at the base of the column. The curvature measurements are compared to the yield curvature calculated by the approximate equation $2.25\frac{\varepsilon_y}{D_c}$, as suggested by Priestley (2003), where D_c is the diameter of the column and ε_y is the yield strain of the longitudinal reinforcement. At Cycle 13, the curvature was higher than the estimated yield curvature in the lower 1.5 m (5 ft) of the column (30% of the column height), where most of the damage occurred. The maximum curvature occurred in the lower 300 mm (1 ft) of the column, and at the last

cycle, it reached a value equal to 12 times the estimated yield curvature. The curvature in the shaft was smaller than the estimated yield curvature.

7.5.3 Test Observations for Specimen 2

The behavior of Specimen 2 during the early cycles was very similar to that of Specimen 1. Flexural cracks appeared in the column and the shaft as early as in Cycle 2, i.e., at a force equal to 50% of that corresponding to the theoretical first yield. Figure 7.13 shows the distribution of flexural cracks in the column and shaft at Cycle 4, at which the theoretical first yield occurred. Radial cracks at the top of the shaft appeared as early as Cycle 3, i.e., at a force equal to 75% of that corresponding to the theoretical first yield, as shown in Figure 7.14. Similarly to Specimen 1, the number of flexural and radial cracks did not increase after Cycle 5.

The evolution of damage in the north and south faces near the base of the column is shown in Figure 7.15 and Figure 7.16, respectively. At Cycle 7, which was the first cycle at a system ductility of 2, the concrete at the base of the column started to be crushed on both sides of the column (see Figure 7.15a and Figure 7.16a). At Cycle 8, which was the second cycle at a ductility of 2, spalling of the concrete cover started in the south side (see Figure 7.16b), while for the north side spalling did not occur until Cycle 11, which was the first cycle at a ductility of 3 (see Figure 7.15c). At Cycle 13, which was the first cycle at a ductility of 5, the lower 600 mm (2 ft) to 900 mm (3 ft) of the concrete cover spalled on both sides of the column and exposed the hoop reinforcement, as shown in Figure 7.15d and Figure 7.16d. At this stage, the damage at the top of the shaft was significant with a circular crack (cone failure) and radial (splitting) cracks

opening widely, as shown in Figure 7.17a. The maximum crack opening measured at this stage was 6 mm (1/4 in.), twice as much as that measured in Specimen 1 at the same system ductility level. Subsequent cycles induced further spalling of the concrete at the base of the column exposing partially some of the longitudinal bars. The damage at the top of the shaft increased, with the cone and splitting cracks opening to such an extent that pieces of concrete started to be detached (see Figure 7.17b). At the beginning of Cycle 18, which was the second cycle at a ductility of 7, one of the column longitudinal bars on the north side fractured at the column-shaft interface (see Figure 7.15f). A drop on the load carrying capacity of the column was observed, and the test was stopped.

Posterior inspection of the column indicated that some of the bars had started to buckle at the location where the bar fractured, as shown in Figure 7.15f. Buckling was not as severe as in Specimen 1 due to the better confinement provided by the hoops. The detached pieces of concrete at the top of the shaft caused by the cone formation and splitting cracks were removed by hand after the test. Figure 7.17c and Figure 7.17d show the aspect of the shaft once these pieces were removed. A cone shaped surface with an average inclination of 25 degrees had formed between the column and the shaft cages, and splitting cracks connecting radially the longitudinal bars in the column and the shaft were visible, as shown in Figure 7.17c. More splitting cracks were observed than for Specimen 1, and they extended vertically with lengths between 900 mm (3 ft) to 1200mm (4 ft) on the lateral surface of the shaft, as shown in Figure 7.17e. The increment of the damage atop of the shaft with respect to Specimen 1 can be explained by the larger splitting forces generated by the larger diameter bars and by the higher ductility demand

attained in the test. It is also possible that this was influenced by a larger slip experienced by the bars.

The shape of the lateral displacement of the column is plotted in Figure 7.18 at the peak displacements of different cycles. Similarly to Specimen 1, this distribution reveals that most of the displacement in the column was due to the rotation occurring in the plastic hinge and at the column base due to bar slip. The displacement measurement at the top of the shaft is not provided after Cycle 9. At this stage, the rod attached to the displacement transducer started to be detached from the shaft due to the widely opened cracks at the top of the shaft. The curvature measurements at the top portion of the shaft have been removed from Figure 7.19 for the same reason. According to Liu (2012), between 50% and 80% of the total column deformation was due to flexural deformation; base rotation contributed between 15% to 50%, and shear deformation contributed less than 3% to the total displacement. As shown in Figure 7.19, the curvature distribution at the peak displacements of different cycles is not perfectly symmetrical: the maximum curvature in the positive direction is higher than that obtained in the negative direction. This difference can be related to the unsymmetrical damage observed at the base of the column. The higher curvature in the positive direction, i.e., when the north face of the specimen was subjected to compression, is consistent with the fact that there was more concrete spalling in the north side. Figure 7.19 also shows that the extent of plastic curvature practically reached 2.1 m (7 ft), i.e., 40% of the effective height of the column, and that the maximum curvature ductility of 20 was reached 305 mm (1 ft) above the column-shaft interface. Like in Specimen 1, the curvature in the shaft was smaller than the theoretical yield curvature.

7.6 Strains in steel reinforcement

7.6.1 Specimen 1

The strain distributions along the column longitudinal bars at the peak displacements of different cycles are plotted in Figure 7.20 and Figure 7.21 for two bars located at the north face and two at the south face of the specimen, respectively. The strain was measured in these bars at different heights in the lower half of the column and inside the embedment length in the shaft, l_e. Only one of the longitudinal bar (northwest bar) yielded at the base of the column before the peak load of Cycle 4 had been reached, as it had been predicted. After yielding, the maximum tensile strains along the bar were measured in the lower 610 mm (2 ft) of the column. Even though the maximum tensile strains occurred at a height of 610 mm (2 ft), this does not necessarily mean that the maximum tensile stresses were developed in this area because the strain gages below experienced significantly higher residual compressive strains. Figure 7.20 and Figure 7.21 also show consistent trends in the strain penetration in the embedment length. The maximum plastic strain penetration developed in all bars, measured at ductility 5.5, was 610 mm (2ft), which is equivalent to 17 times the bar diameter, d_b, or 27% of the total embedment length. The bond stresses in these bars are analyzed in Chapter 8 with a finite element model.

The strain distributions along two of the longitudinal perimeter bars in the shaft at the peak displacements of different cycles are plotted in Figure 7.22. The bars were located at the extreme north and south faces of the shaft. All these bars remained elastic. The strain varied practically linearly along the splice length. From the strain

measurement, the bar axial stress has been calculated, and from the difference in the stresses of two adjacent gages, the average bond stress has been calculated. The bond stresses in this region are small, less than 15% of the maximum bond strength obtained from the tests presented in Chapter 3.

The strains in the column cage hoops located at different heights of the column and inside the embedment length at the peak displacements of different cycles are plotted in Figure 7.23. These strains were measured near the north and south faces of the specimen. All the hoops except those located in the plastic hinge area remained elastic. The hoop located approximately 1 ft above the column base yielded at a system ductility of 4.4. This corresponds to the onset of buckling of some of the longitudinal bars in this region. Before ductility 5.5 was reached, these strain gages were damaged. The hoop located at a depth of 203 mm (8 in.) inside the embedment length area also experienced significant strains on the north side and yielded before the strain gages were damage when the system reached a ductility of 5.5. The rest of the column hoops inside the shaft remained elastic with strains significantly smaller than the yield strain.

Figure 7.24 presents the strains in the shaft hoops at the peak displacements of different cycles. These strains were measured near the north and south faces of the specimen. The strain is higher for the hoops in the upper portion of the lap splice. The hoop located at 305 mm (1 ft) from the top of the shaft reached its yield strain in Cycle 13. The hoops located in the lower half of the embedment length experienced practically no strain.

7.6.2 Specimen 2

The strain gage distributions along the column longitudinal bars at the peak displacements of different cycles are plotted in Figure 7.25 and Figure 7.26 for two bars located at the north face and two at the south face of the specimen, respectively. The observations are similar to those for Specimen 1. The maximum strains are obtained in the lower 610mm (2ft) of the column. For most of the bars, the maximum plastic strain penetration inside the embedment length is 610 mm (2 ft) at ductility 5, which corresponds to $14 d_b$. In two of the bars monitored, the plastic strain penetration reached 915 mm (3 ft), or $21 d_b$. Hence, even though the embedment length was reduced significantly with respect to Specimen 1, the plastic strain penetration was very similar for the same ductility demand. However, given the shorter embedment length of the column reinforcement in Specimen 2, the plastic penetration represents 33 and 50% of the embedment length, respectively. For higher ductility levels, strain gages in the entire embedment length were practically all damaged in all the bars. This indicates that bar slips started to be significant at this stage. The strain and bond stress distributions along these bars are further analyzed with a finite element model in Chapter 8.

The strain distributions along the longitudinal perimeter bars in the shaft at the peak displacements of different cycles are plotted in Figure 7.27. All the bars remained elastic, and the average bond stresses along the lap splice length calculated from the strain readings in this region varied between 5 and 30% of the maximum bond strength obtained from the tests presented in Chapter 3.

The strains in the column cage hoops located at different heights of the column and inside the embedment length at the peak displacements of different cycles are plotted in Figure 7.28. The strains were measured near the north and south faces of the specimen. For two of the hoops located near the base of the column, strains were also measured near the west side of the specimen. Like in Specimen 1, only the hoops located near the column base yielded on the north and south sides of the specimen. These hoops reached the nominal yield strain at ductility 5. Their location corresponds to the region where severe concrete crushing and bar buckling occurred. However, the strains on the west side of these same hoops did not even reach 50% the yield strain. All the column hoops inside the shaft remained elastic and experienced little strains.

Figure 7.29 presents the strains in the shaft hoops at the peak displacements of different cycles. These strains were measured near the north and south faces of the specimen. For three of the upper hoops, strains were also measured near the west side of the specimen. Like in Specimen 1, strain is higher for the hoops in the upper portion of the lap splice. The uppermost hoop, located at 75 mm (3 in.) below the top of the shaft, reached its yield strain in Cycle 13. The strains varied almost linearly along the height, and the hoop located at the bottom of the lap splice area experienced practically no strain. The strains on the west side of the uppermost hoop are very close to those obtained on the north and south sides.

7.7 Summary and conclusions

The behavior of two full-scale column-shaft assemblies subjected to quasi-static cyclic loading has been studied. These tests were intended to study the minimum required

embedment length of column longitudinal reinforcement in enlarged (Type II) shafts. In Specimen 1, an embedment length equal to $D_{c,\max} + l_d$, which is similar to the minimum requirement in current Caltrans SDC (Caltrans 2010), was evaluated. In Specimen 2, the embedment length was reduced to $l_d + s + c$. Despite the difference in the embedment lengths, the two specimens showed a very similar behavior during the tests. Both columns developed a plastic hinge at the base and failed by bar buckling and subsequent fracture of longitudinal bars in the plastic hinge region. Damage on the shafts was limited to cone failure and splitting cracks near the base of the column. This damage was more severe in Specimen 2 owing to the larger splitting forces generated by the larger diameter bars, the larger slip of the bars, and the higher ductility demand attained in the test.

Similar strains were measured in the upper part of the anchorage zone of the column longitudinal bars in the shafts of both specimens. The maximum tensile plastic strain penetration in the column longitudinal bars inside the shaft was $17d_b$ for Specimen 1 and $21d_b$ for Specimen 2. The shaft longitudinal reinforcement remained elastic for both specimens. The strains in the transverse reinforcement of the shafts of both specimens varied almost linearly along the height. The maximum strains occurred in the uppermost hoops, which started to yield in the last few cycles of the tests.

The comparison between the test results obtained from Specimens 1 and 2 indicate that the embedment length can be reduced from $D_{c,\max} + l_d$ to $l_d + s + c$ without affecting the behavior of the column-shaft assembly. The bond-slip and development of the column longitudinal bars in the shaft are further studied in Chapter 8 with finite element analyses. The numerical results are used to supplement the experimental

observations to establish new design recommendations for the minimum embedment length of column reinforcement inside an enlarged shaft, and the minimum transverse reinforcement required in the anchorage region.

Table 7.1: Compressive strength of concrete on the day of test

Specimen No.	Region	Compressive strength of concrete, MPa (ksi)
Specimen 1	Shaft in lap splice region	34.5 (5.0)
	Shaft below lap splice region	42.8 (6.2)
	Column in lower 2.8 m (9 ft)	34.0 (4.9)
	Column in upper 2.1 m (7 ft)	38.6 (5.6)
Specimen 2	Shaft in lap splice region	37.0 (5.4)
	Shaft below lap splice region	39.7 (5.8)
	Column in lower 2.8 m (9 ft)	38.6 (5.6)
	Column in upper 2.4 m (8 ft)	40.7 (5.9)

Table 7.2: Yield and ultimate tensile strengths of longitudinal reinforcement

Specimen No.	Bar	Yield strength, MPa (ksi)	Ultimate strength, MPa (ksi)
Specimen 1	No. 11	448 (65.0)	629 (91.2)
	No. 14	484 (70.1)	672 (97.4)
Specimen 2	No..14	462 (67.0)	638 (92.5)
	No. 18	462 (67.0)	641 (93.0)

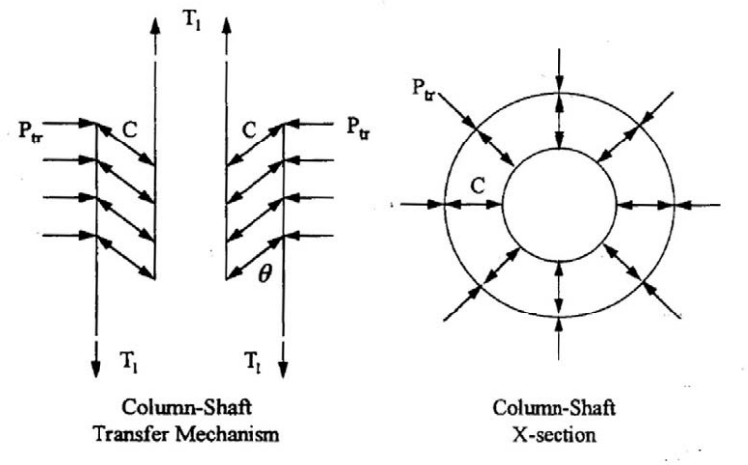

Figure 7.1: Truss analogy proposed by McLean and Smith (1997)

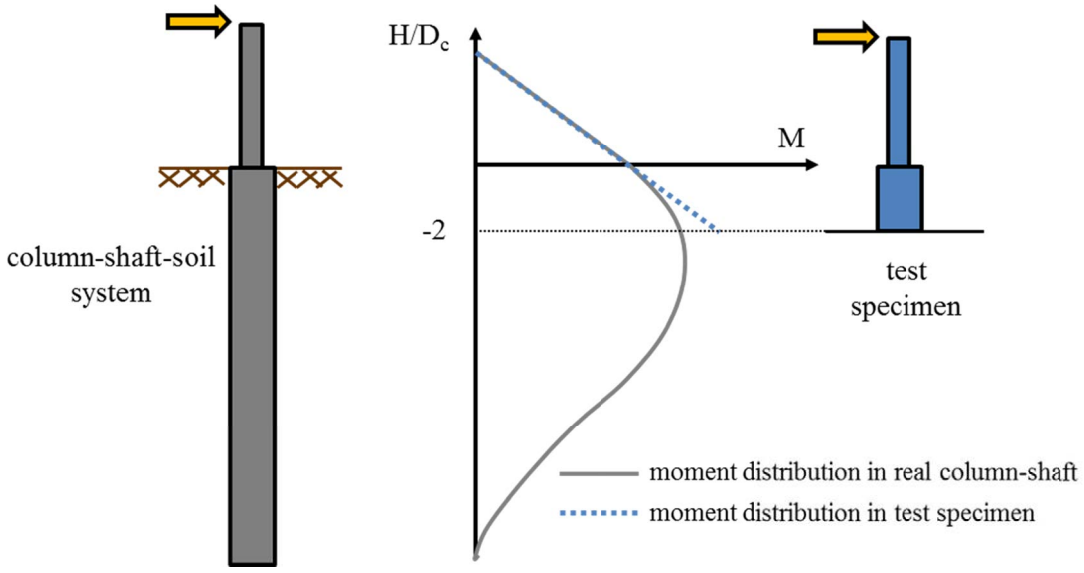

Figure 7.2: Bending moment distributions in a real column-shaft and a test specimen

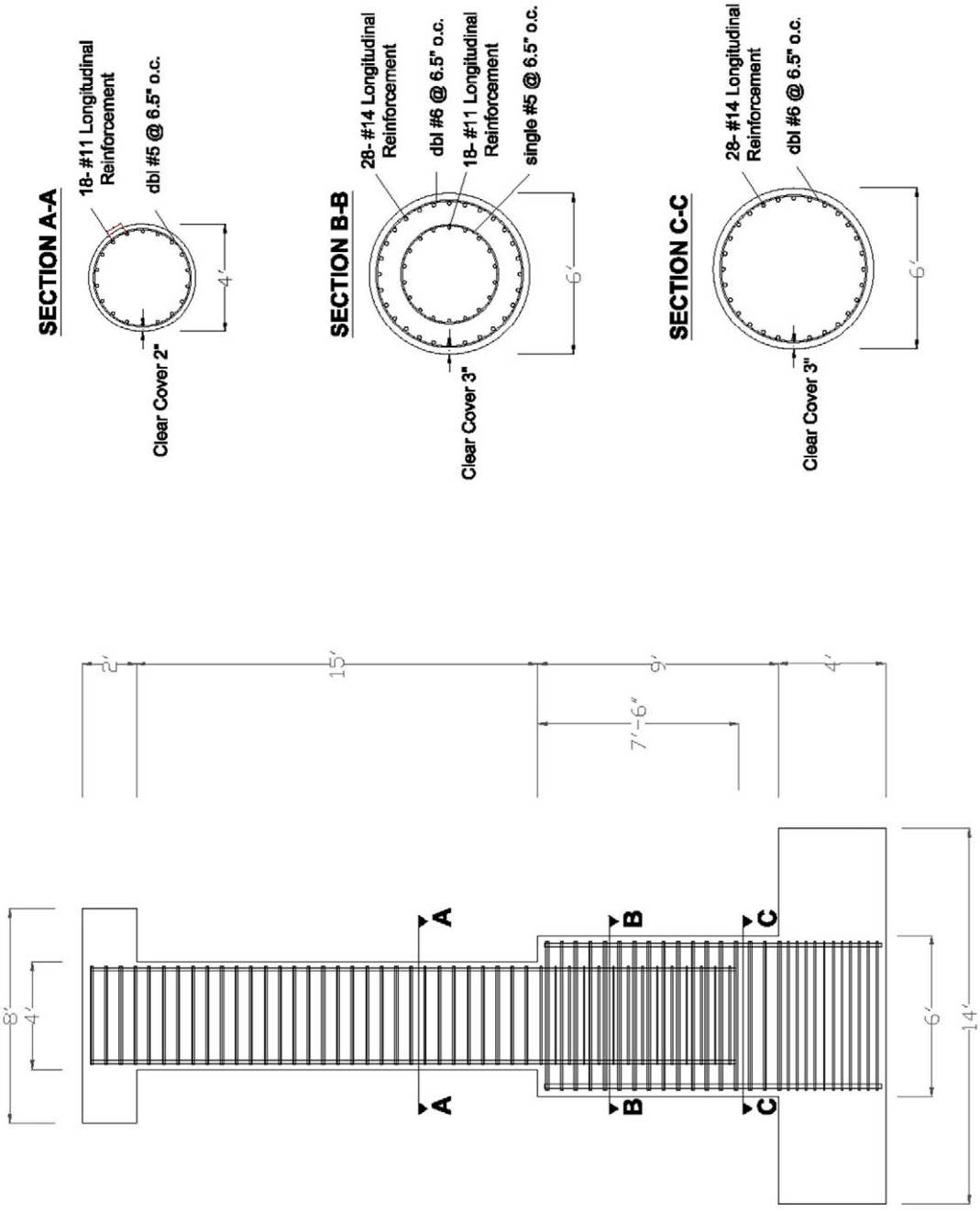

Figure 7.3: Geometry and reinforcement of Specimen 1
(1'=304.8 mm, 1"=25.4 mm)

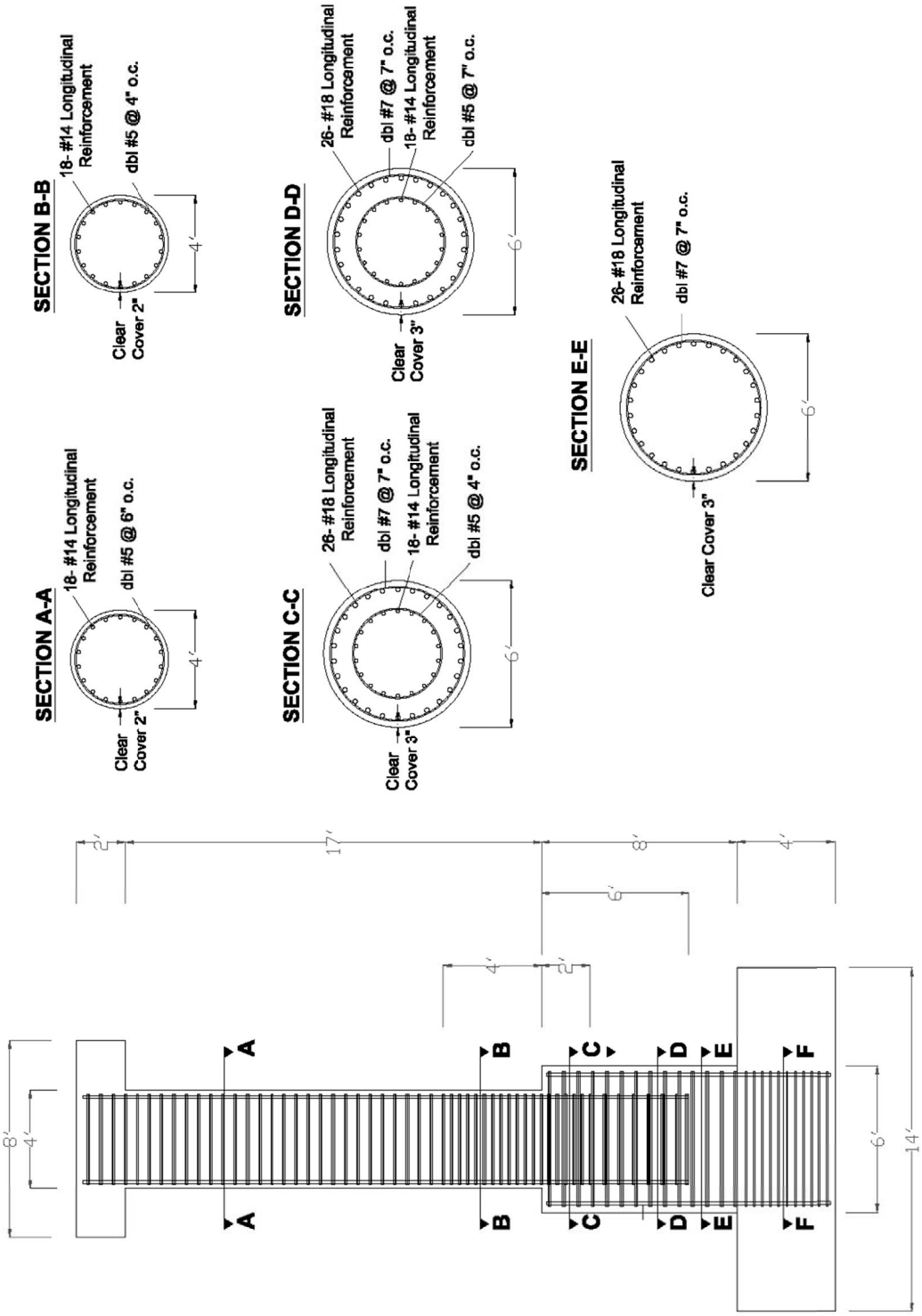

Figure 7.4: Geometry and reinforcement of Specimen 2 (1'=304.8 mm, 1"=25.4 mm)

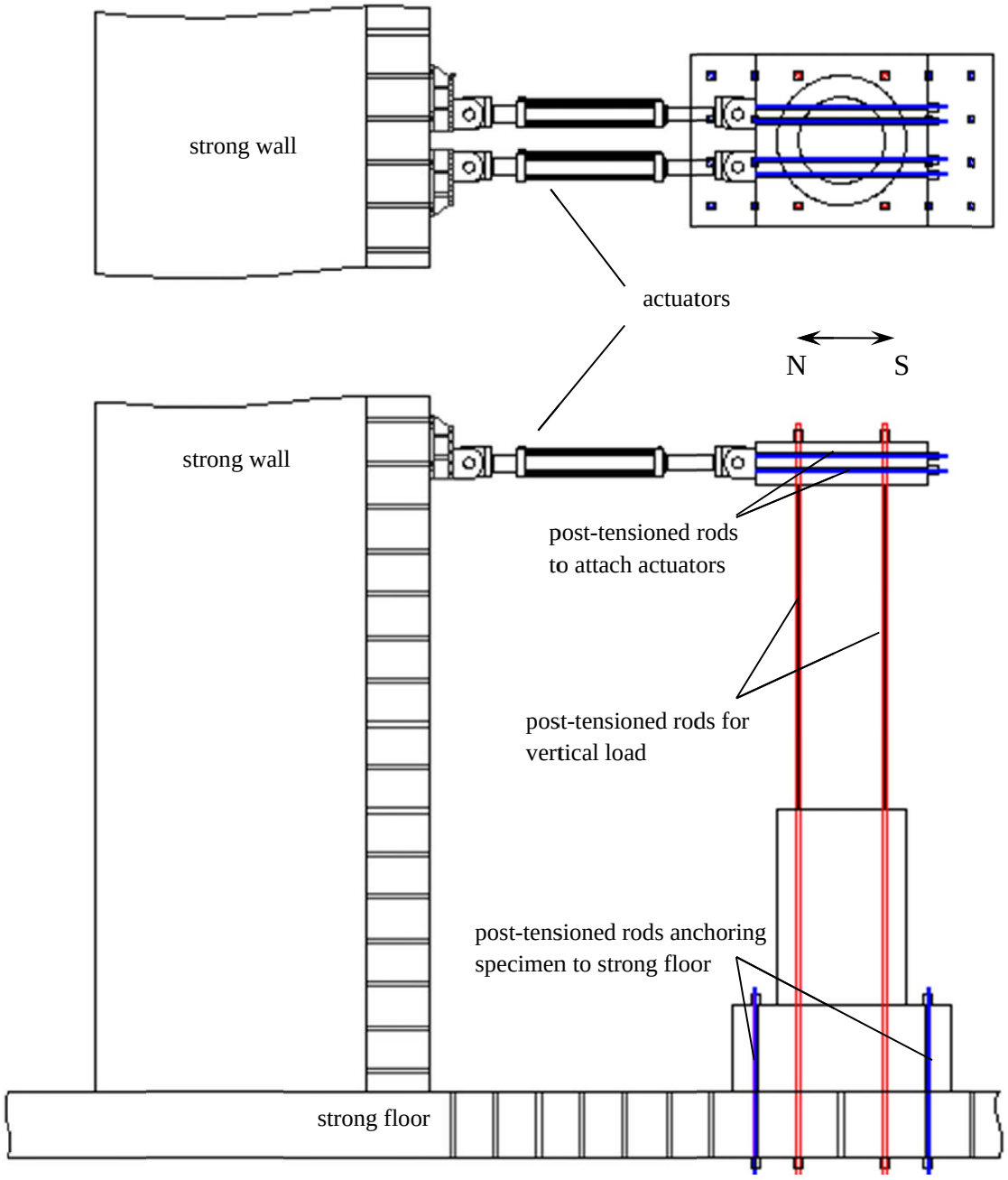

Figure 7.5: Test setup

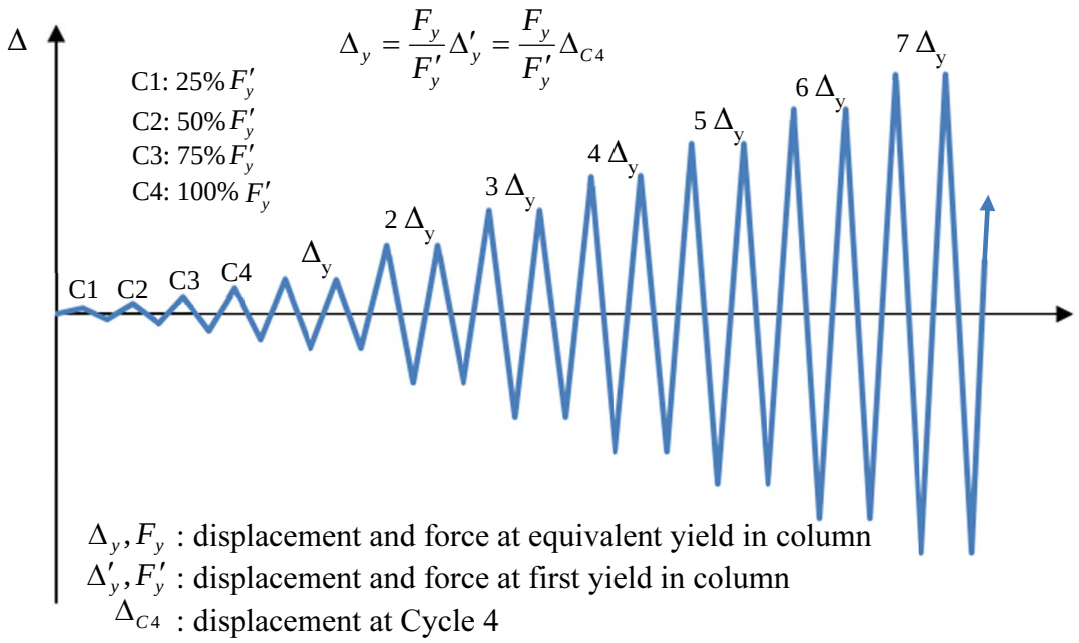

(a) Loading history

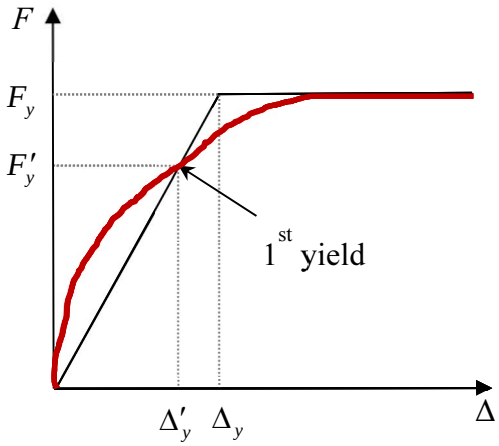

(b) First yield and equivalent yield

Figure 7.6: Loading protocol

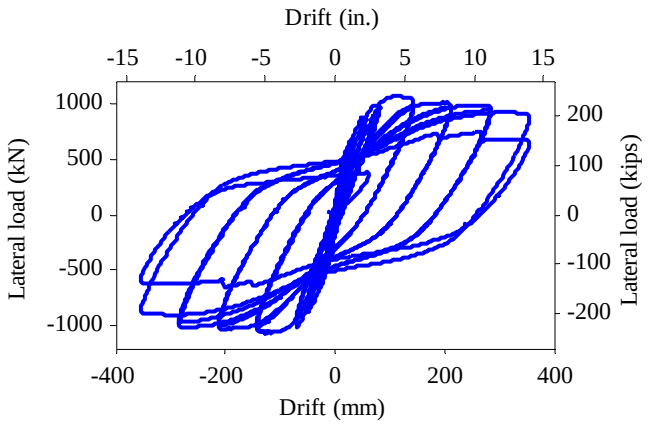

(a) Specimen 1

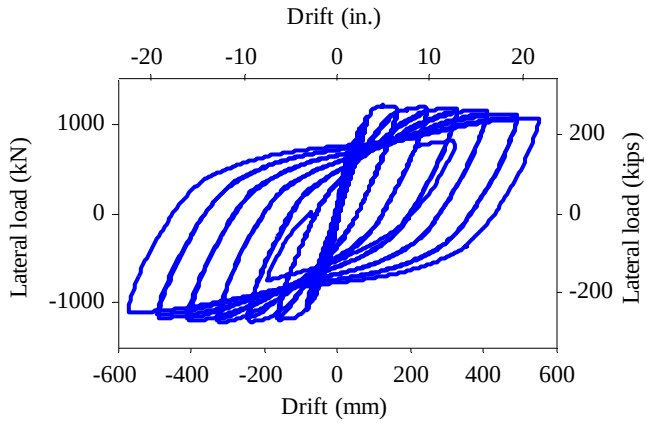

(b) Specimen 2

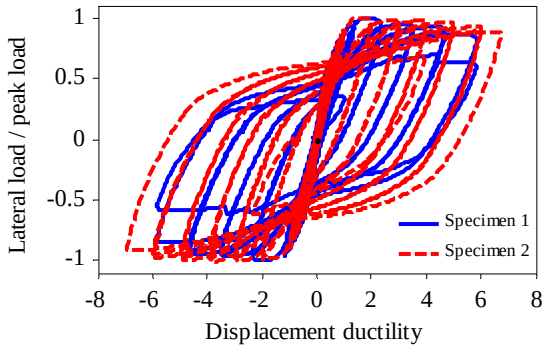

(c) Lateral load / capacity vs. system ductility for both specimens

Figure 7.7: Lateral force vs. drift for Specimens 1 and 2

(a) Column (west view)

(b) Shaft (north face)

(c) Shaft (south face)

(d) Column-shaft interface (north face)

(f) Column-shaft interface (south face)

Figure 7.8: Cracks in Specimen 1 at Cycle 4 (1st yield)

(a) Cycle 7

(b) Cycle 9

(c) Cycle 11

(d) Cycle 13

(e) Cycle 13

(f) Cycle 14

Figure 7.9: Evolution of damage at the column base in Specimen 1 (north face)

(c) Top of the shaft (north side)

(d) Top of the shaft (south side)

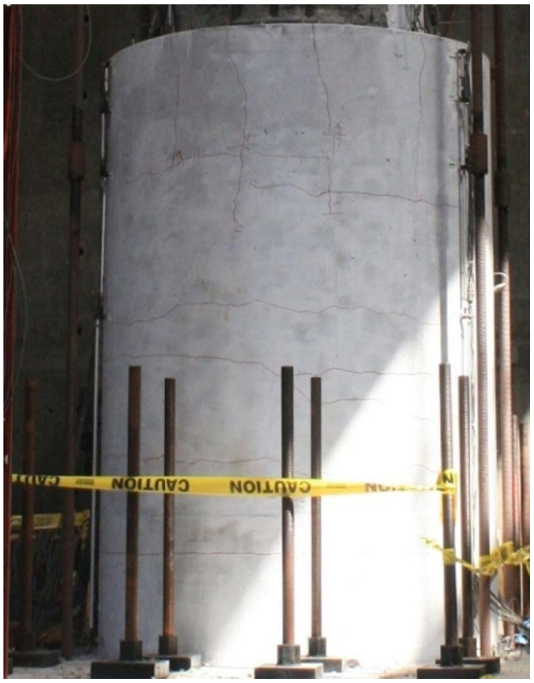

(d) Lateral view of the shaft (south face)

Figure 7.10: Damage at the end of the test in the shaft of Specimen 1

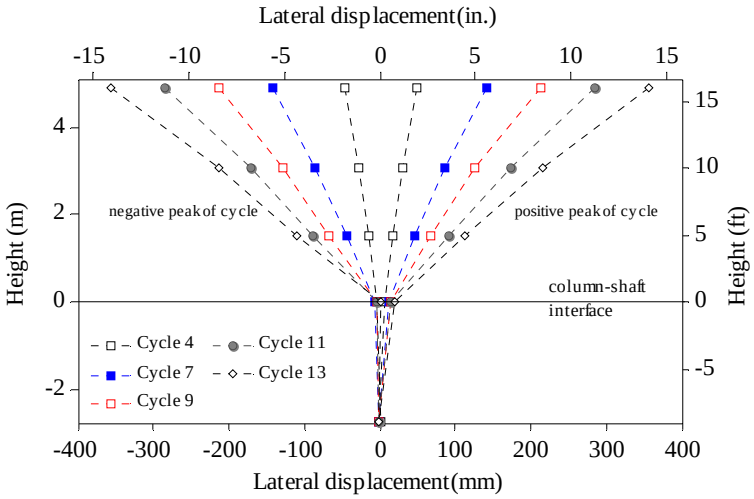

Figure 7.11: Lateral displacement of Specimen 1

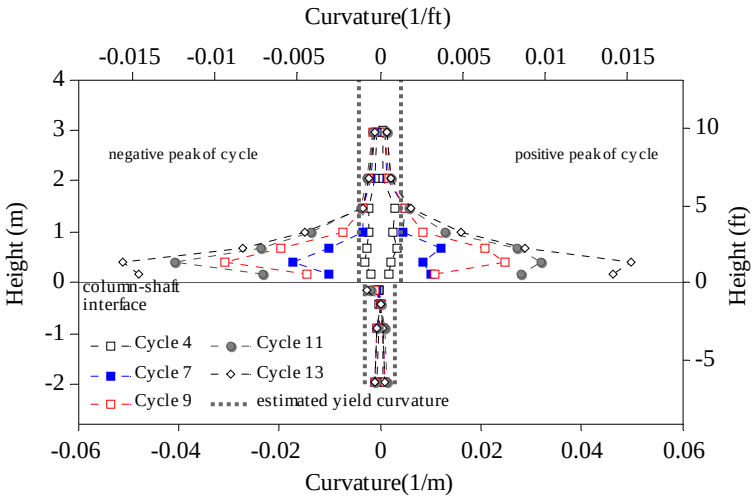

Figure 7.12: Curvature envelopes of Specimen 1

(a) Column (southeast view)

(b) Shaft (north face)

(c) Shaft (south face)

Figure 7.13: Flexural cracks in Specimen 2 at Cycle 4 (1st yield)

(a) Cycle 3 (north face)

(b) Cycle 3 (south face)

Figure 7.14: Splitting cracks at the top of the shaft in Specimen 2 at Cycle 3

(a) Cycle 7 (b) Cycle 9 (c) Cycle 11

(d) Cycle 13 (e) Cycle 15 (f) Cycle 18 (end)

Figure 7.15: Evolution of damage at the column base in Specimen 2 (north face)

(a) Cycle 7 (b) Cycle 8 (c) Cycle 11

(d) Cycle 13 (e) Cycle 15 (f) Cycle 18 (end)

Figure 7.16: Evolution of damage at the column base in Specimen 2 (south face)

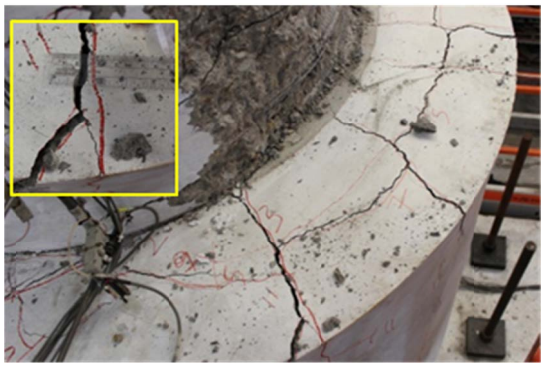

(a) Cycle 13 (south face)

(b) End of the test (south face)

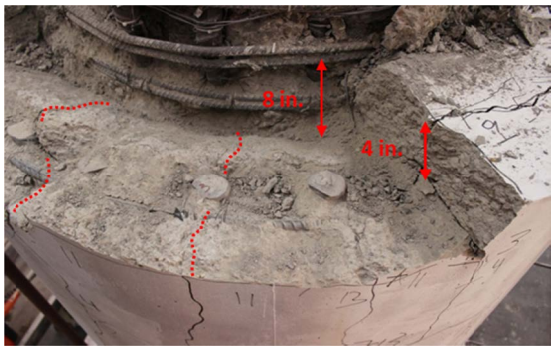

(c) Post-test inspection (Top of north face)

(d) Post-test inspection (Top of south face)

(e) Post-test inspection (north face)

Figure 7.17: Damage in the shaft of Specimen 2

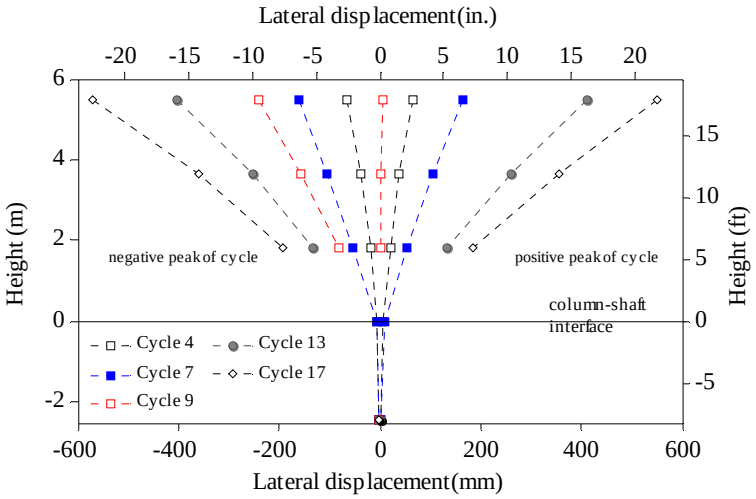

Figure 7.18: Displacement of Specimen 2

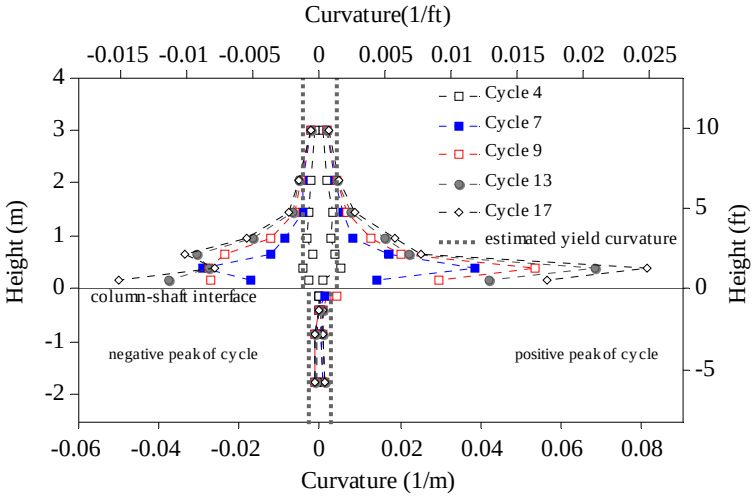

Figure 7.19: Curvature of Specimen 2

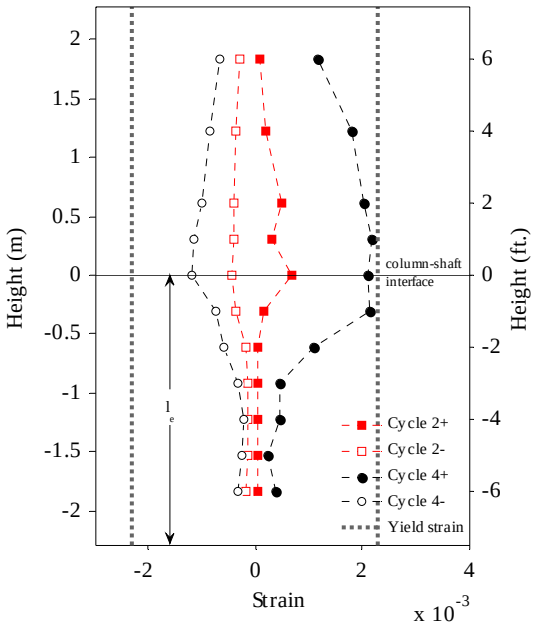

(a) north bar (early cycles)

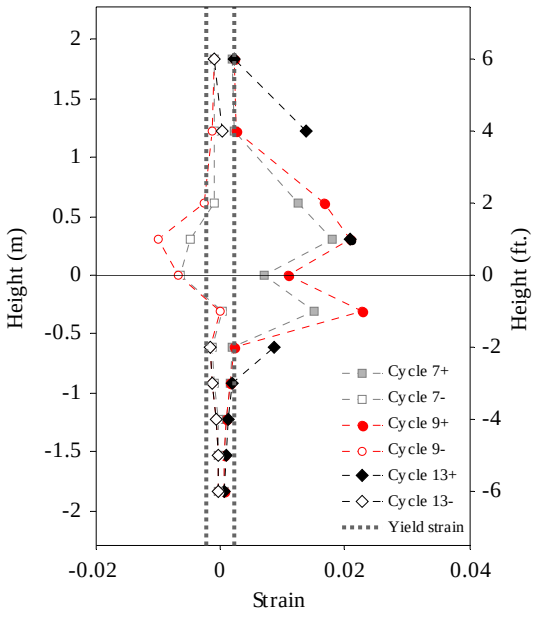

(b) north bar (final cycles)

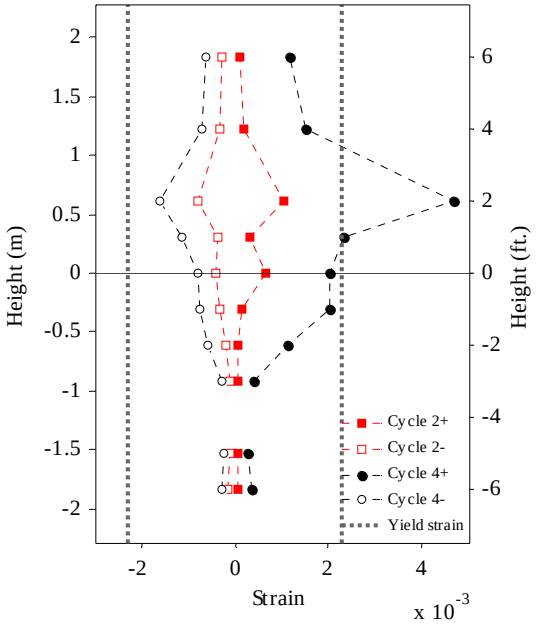

(c) northwest bar (early cycles)

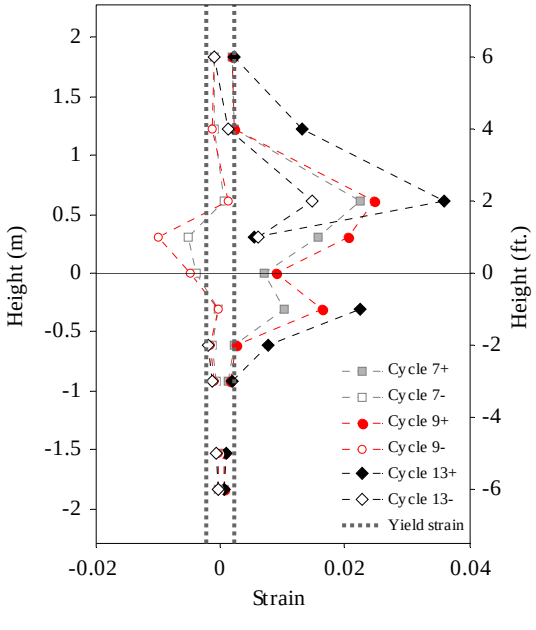

(d) northwest bar (final cycles)

Figure 7.20: Strains in column longitudinal bars in Specimen 1 (north face)

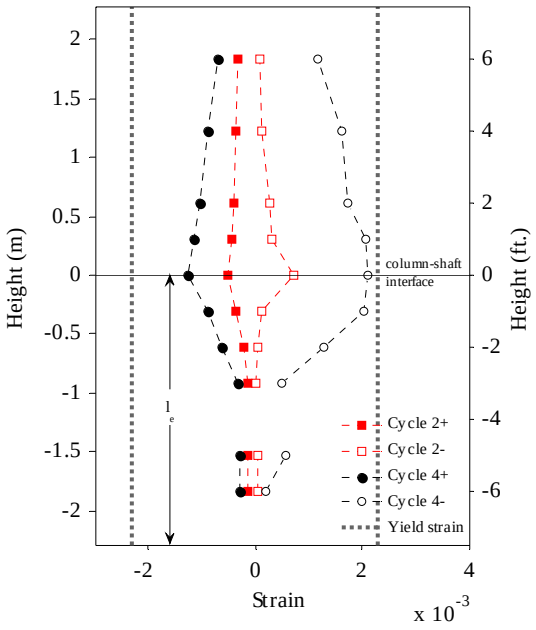

(a) south bar (early cycles)

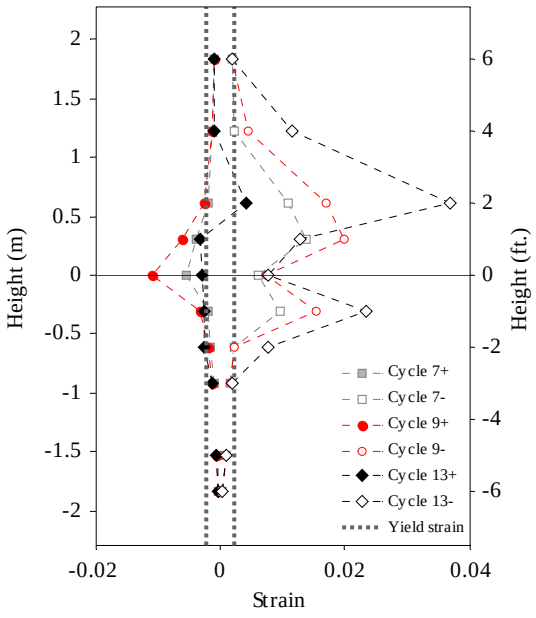

(b) south bar (final cycles)

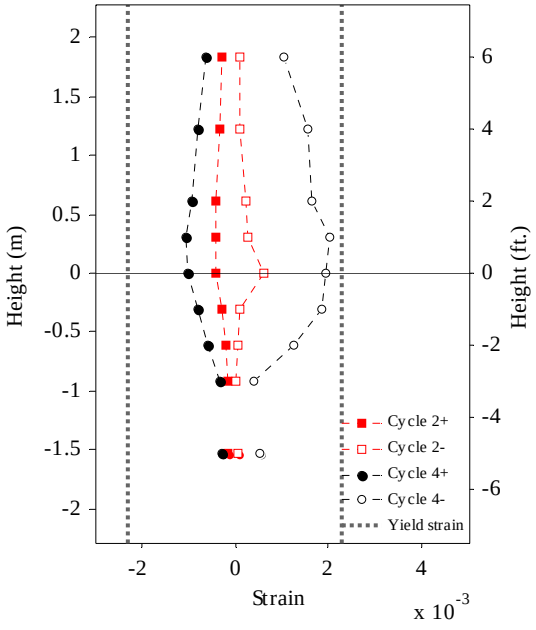

(c) southwest bar (early cycles)

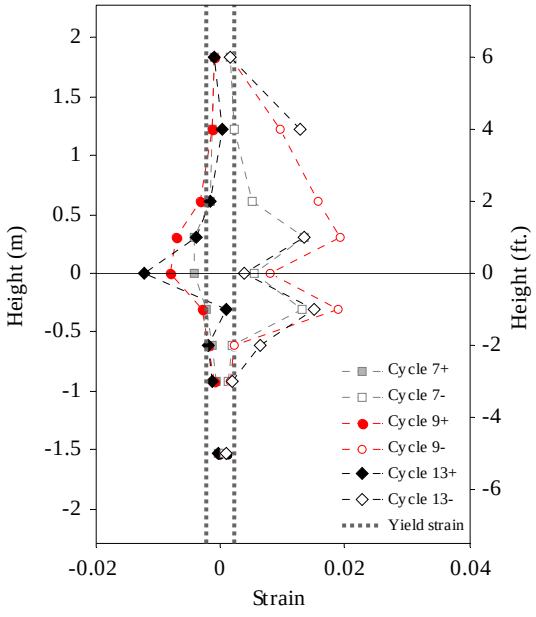

(d) southwest bar (final cycles)

Figure 7.21: Strains in column longitudinal bars in Specimen 1 (south side)

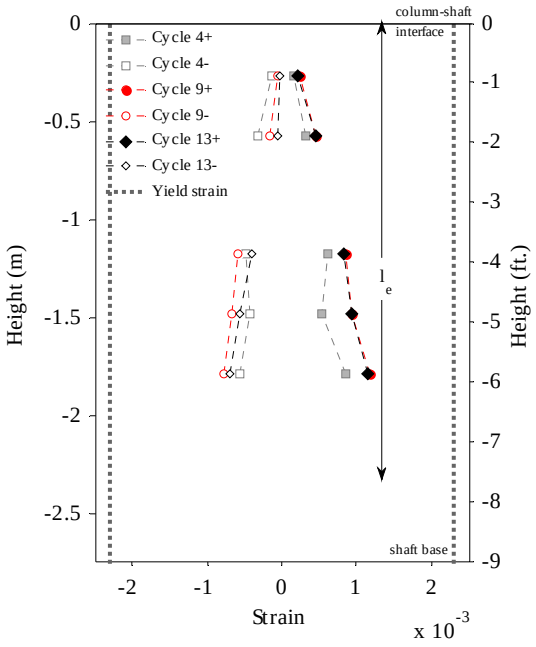

(a) north bar

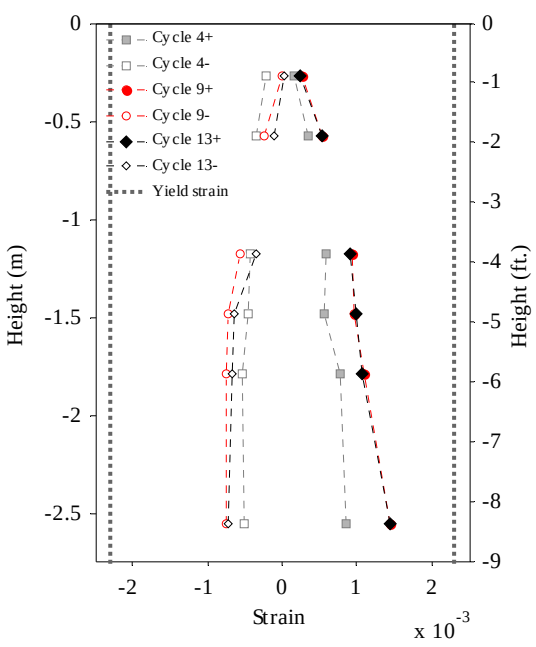

(b) northwest bar

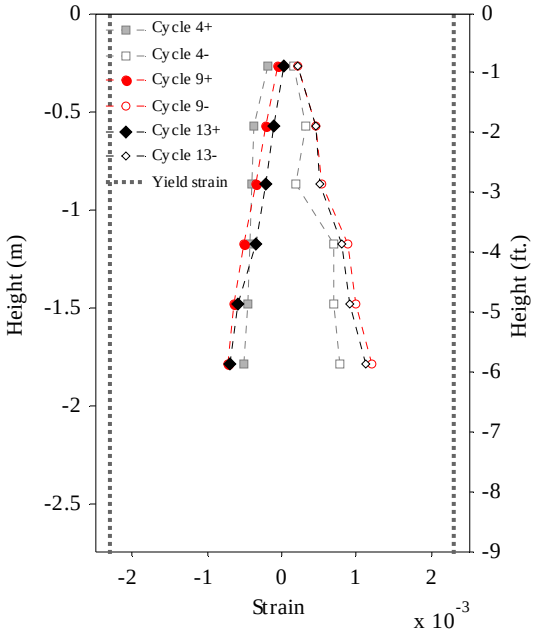

(c) south bar

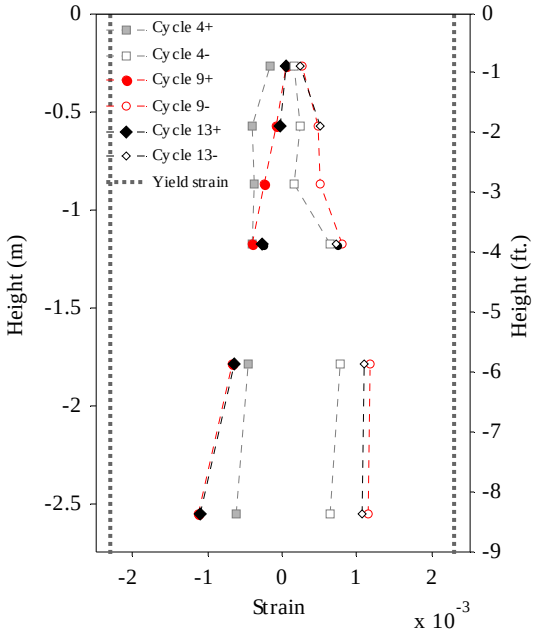

(d) southwest bar

Figure 7.22: Strains in shaft longitudinal bars in Specimen 1

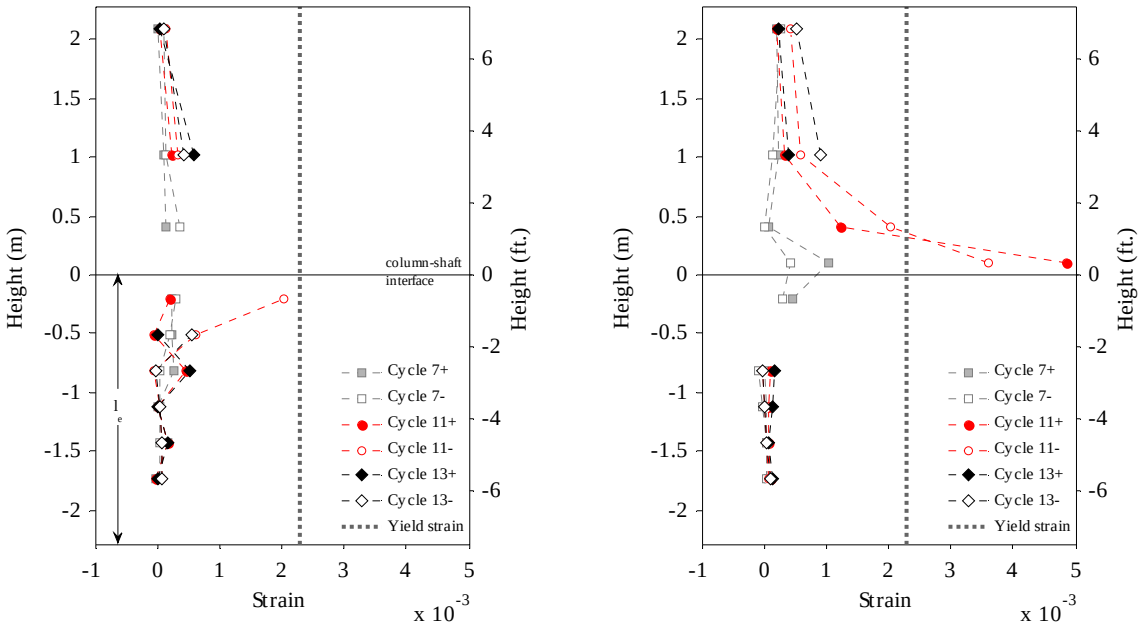

(a) north face (b) south face

Figure 7.23: Strains in column hoops in Specimen 1

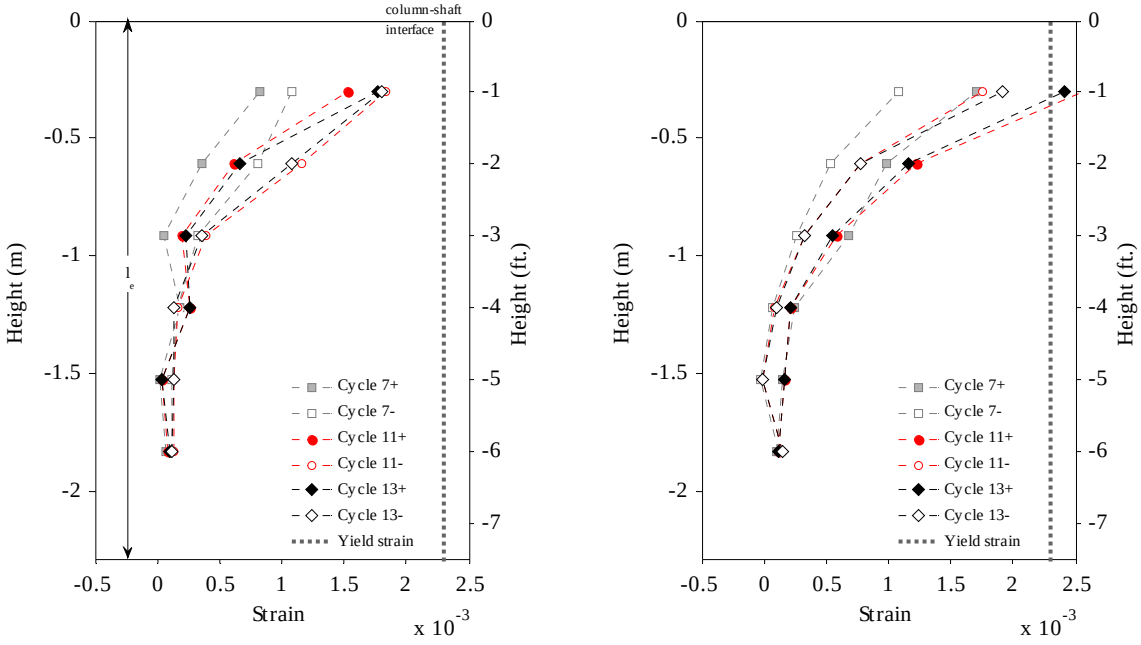

(a) north face (b) south face

Figure 7.24: Strains in shaft hoops in Specimen 1

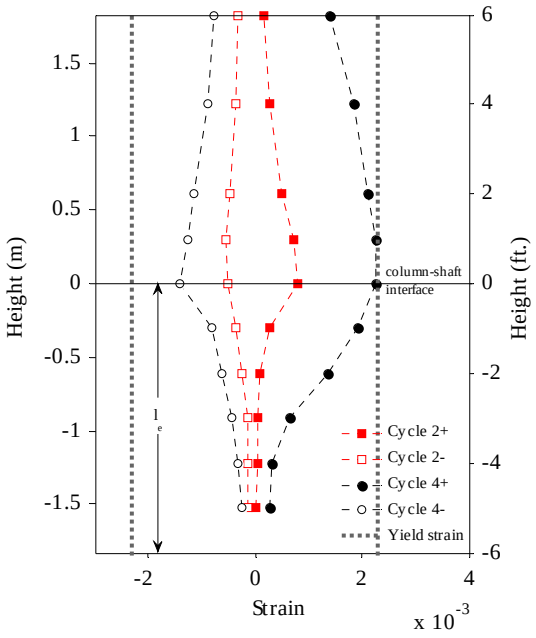

(a) north bar (early cycles)

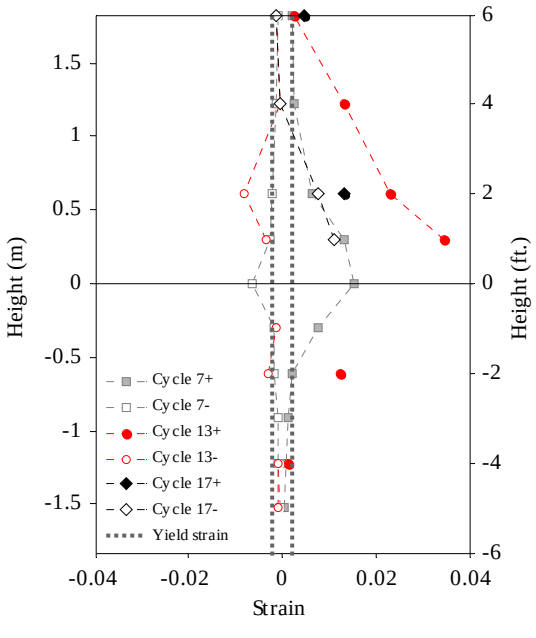

(b) north bar (final cycles)

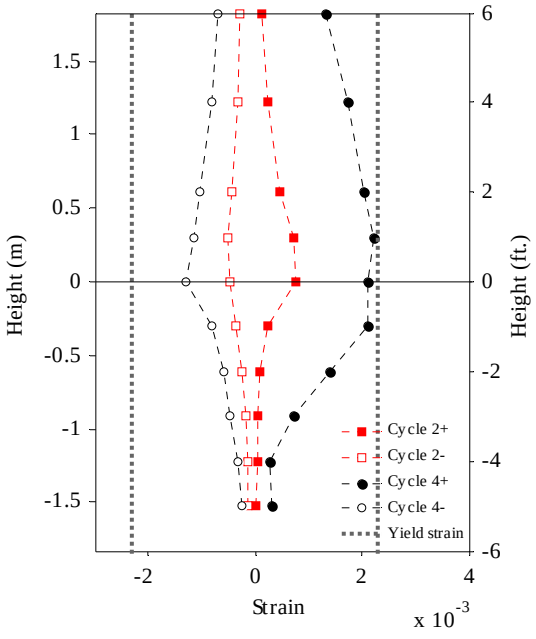

(c) northwest bar (early cycles)

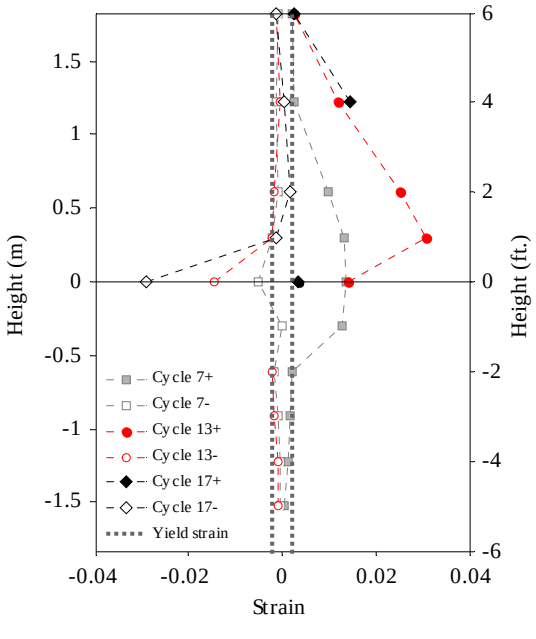

(d) northwest bar (final cycles)

Figure 7.25: Strains in column longitudinal bars in Specimen 2 (north face)

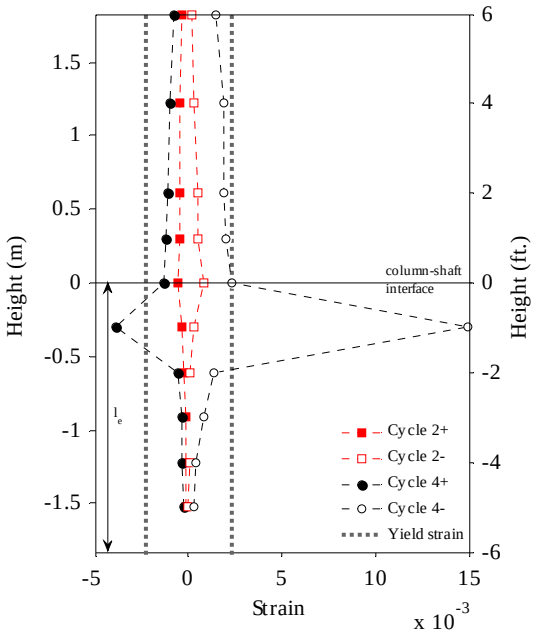

(a) south bar (early cycles)

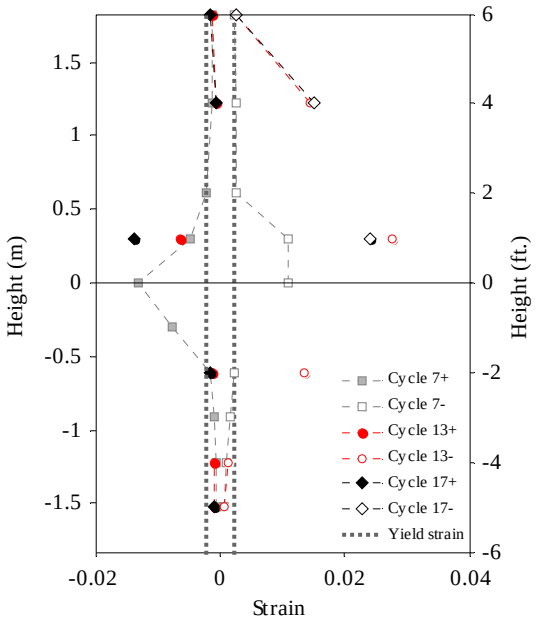

(b) south bar (final cycles)

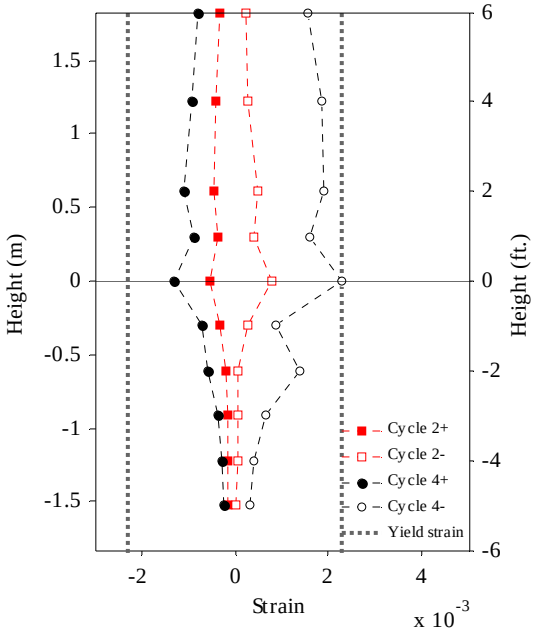

(c) southwest bar (early cycles)

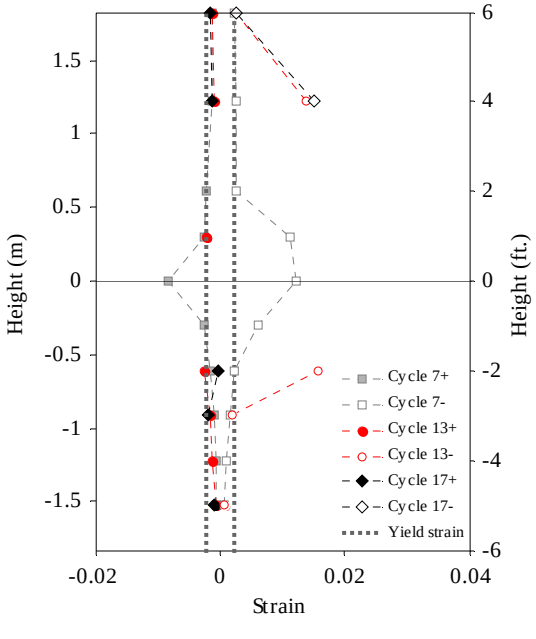

(d) southwest bar (final cycles)

Figure 7.26: Strains in column longitudinal bars in Specimen 2 (south face)

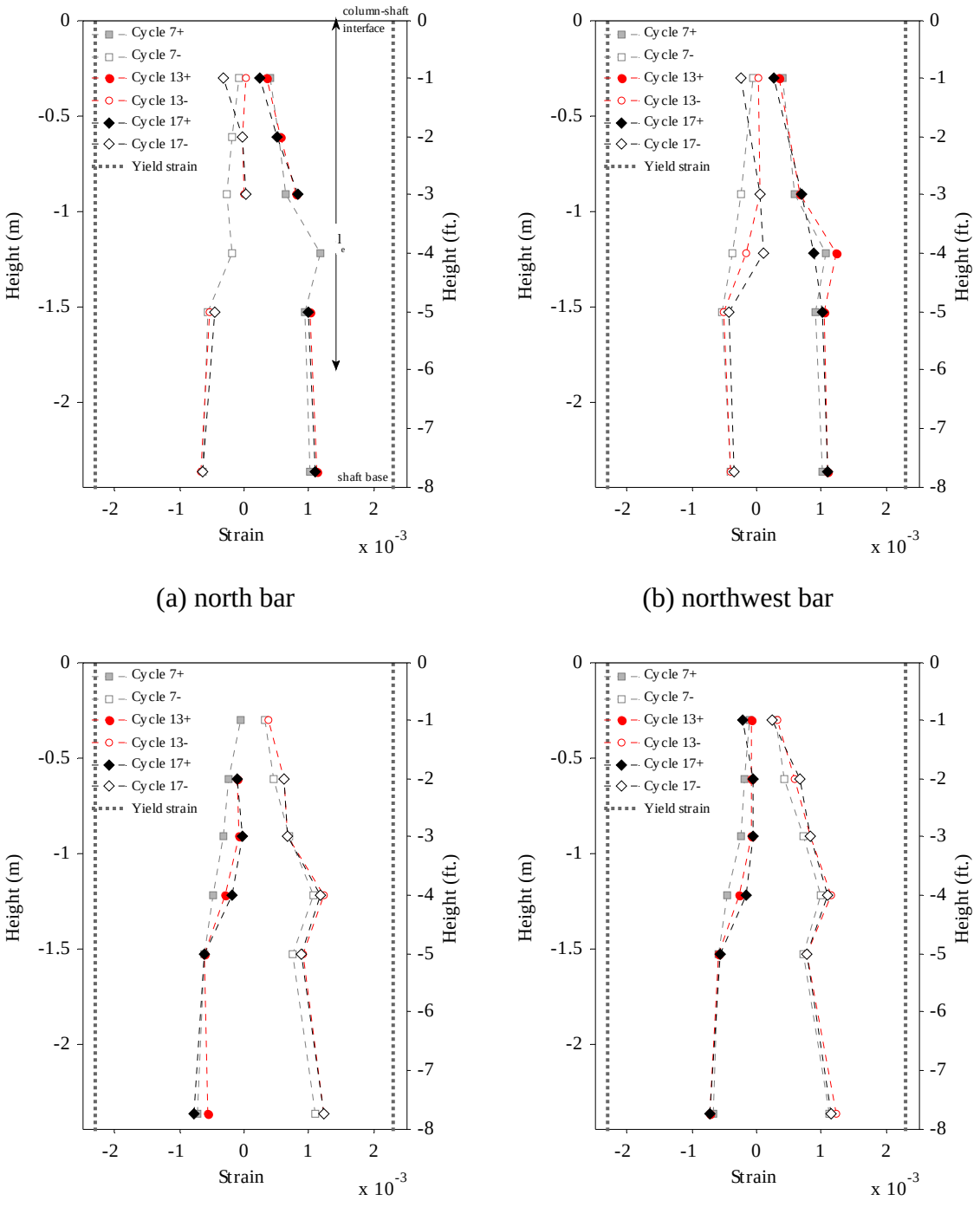

(a) north bar

(b) northwest bar

(c) south bar

(d) southwest bar

Figure 7.27: Strains in shaft longitudinal bars in Specimen 2

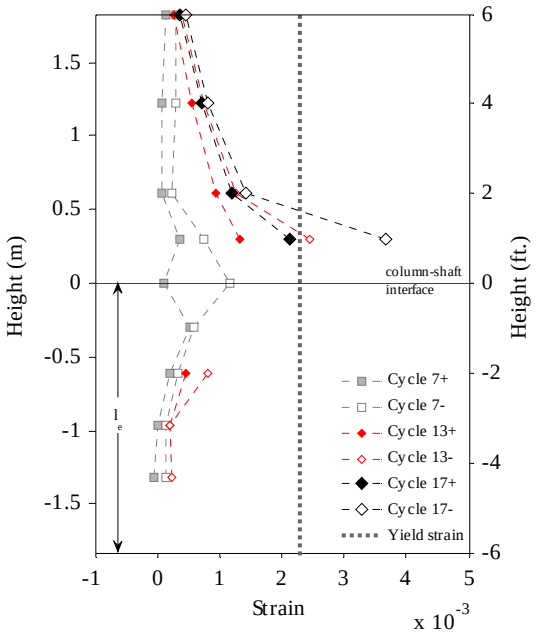

(a) north face

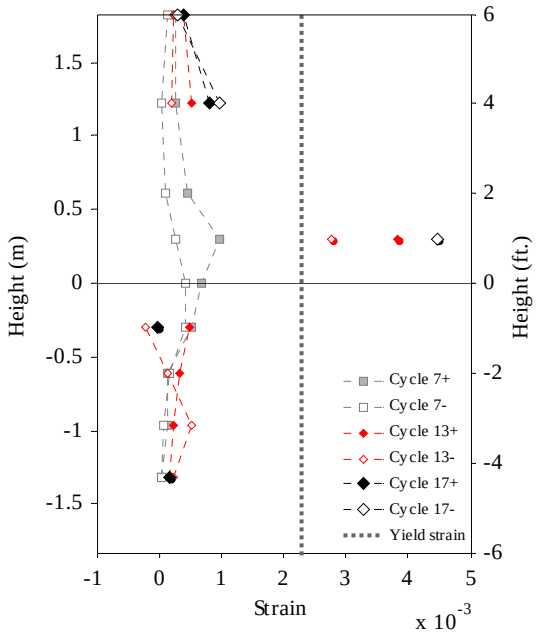

(b) south face

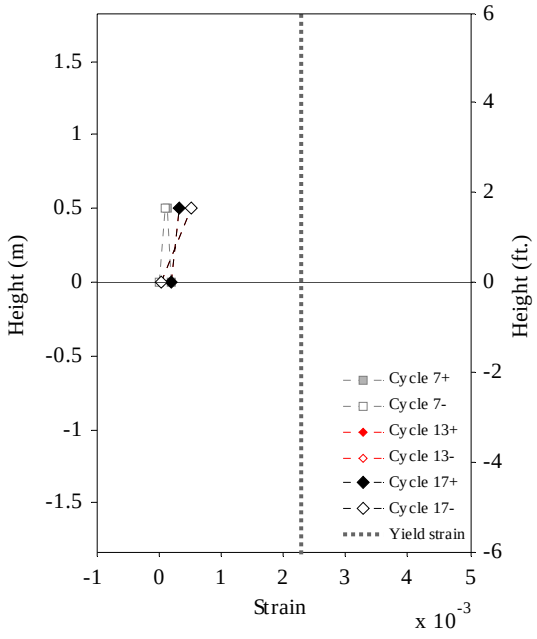

(c) west face

Figure 7.28: Strains in column hoops in Specimen 2

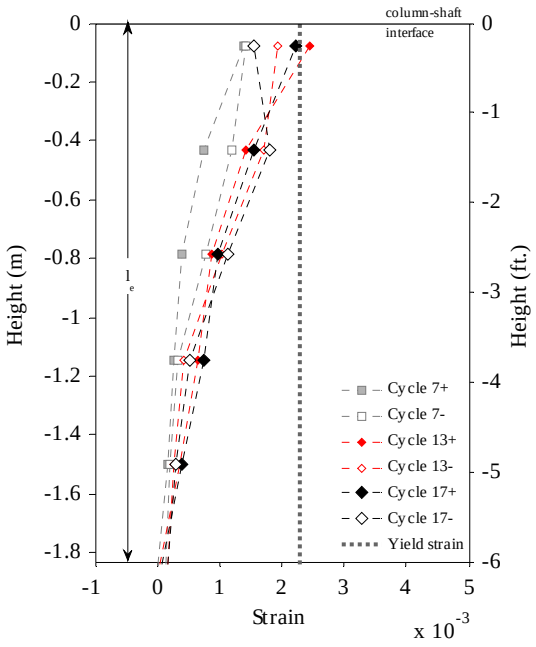

(a) north face

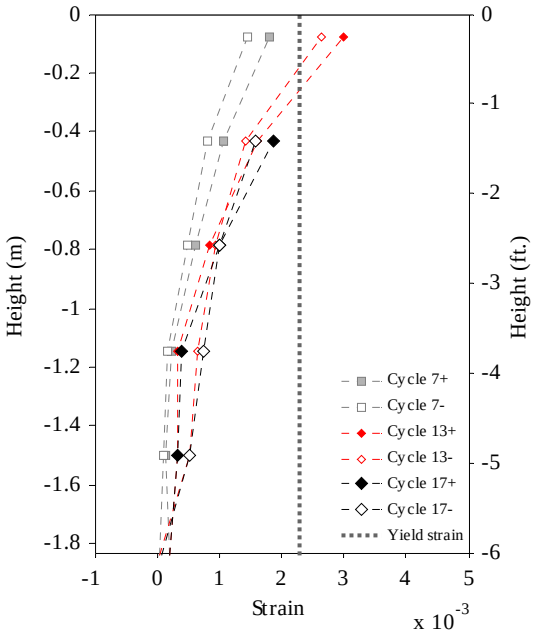

(b) south face

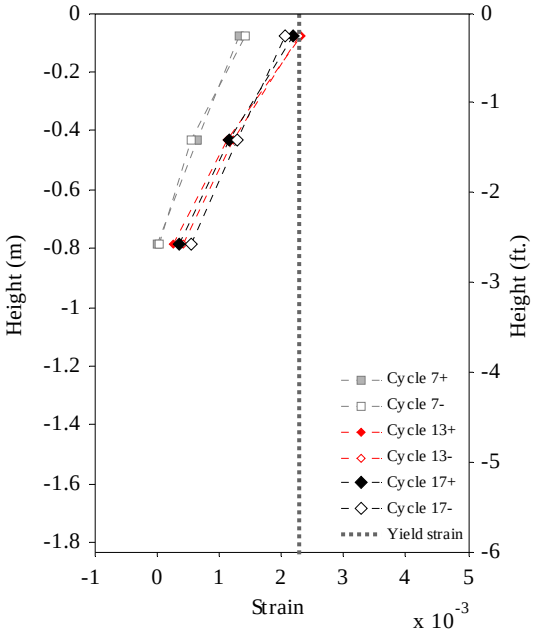

(c) west face

Figure 7.29: Strains in shaft hoops in Specimen 2

CHAPTER 8

FINITE ELEMENT ANALYSIS OF COLUMN – ENLARGED PILE SHAFT ASSEMBLIES AND NEW DESIGN RECOMMENDATIONS

Finite element (FE) analyses have been used together with the large-scale tests presented in Chapter 7 to determine the minimum embedment length required for column longitudinal reinforcement extending into enlarged pile shafts. Initially, FE models were used for the pre-test assessment of the performance of the column-shaft assemblies and to assist the development of the loading protocols for the tests presented in Chapter 7. In particular, the analyses confirmed that the reduced embedment length used in Specimen 2 was close to the minimum required to develop the column longitudinal reinforcement. Once validated by the test results and further refined, the FE models have been used to obtain detailed information, such as the bar stress and bond stress distribution along the longitudinal reinforcement, which is not obtainable from the tests but is crucial for gaining a good understanding the bond-slip behavior of the column reinforcement in the shaft and for determining the adequacy of the embedment length.

Based on the experimental and FE analysis results, new design recommendations have been developed for the minimum embedment length of column longitudinal bars extending into an enlarged shaft and the transverse reinforcement required in the shaft anchorage zone. Finally, the FE models have been used in a parametric study to further verify these new recommendations considering column-shaft assemblies of different dimensions and with different longitudinal reinforcement ratios and bar sizes.

The post-test numerical studies and new design recommendations are presented in this chapter.

8.1 Finite element modeling of the column-shaft tests

A FE model of a column-shaft assembly like those tested in the laboratory is shown in Figure 8.1. Only half of the specimen is represented in the model by taking advantage of the symmetry plane along the north-south (loading) direction. The constitutive models for concrete and steel, which are available in ABAQUS and have been calibrated as discussed in Chapter 4, are used. Bond-slip in the column and shaft longitudinal bars is considered. The bars are modeled with beam elements, and bond-slip is modeled with the phenomenological bond-slip law presented in Chapter 4. Perfect bond is considered for the transverse reinforcement, which is modeled with truss elements embedded in the concrete elements. The properties of the concrete and steel are calibrated with the material test data presented in Chapter 7, while the bond-slip model is calibrated with the method described in Chapter 4 based on the compressive strength of the concrete and the geometry of the reinforcing bars. Contact conditions are imposed at the interface between the column and the shaft, which are meshed independently, and

also at the interface between the shaft and the footing. This is to improve the simulation of the opening and closing of large flexural cracks possible at these locations, which cannot be well represented by the concrete model, as discussed and explained in Chapter 4.

The FE models are subjected to the same vertical load and displacement demands at the top of the column as the test specimens. Geometric nonlinearity is considered in the analyses. The lateral load-vs.-drift relations obtained from the tests and the analyses for Specimens 1 and 2 are shown in Figure 8.2 and Figure 8.3, respectively. The FE models provide a good match with the experimental load-displacement curves, except for the last cycle of the tests. The maximum load carrying capacities are overestimated by 7 and 10% for Specimens 1 and 2, respectively. The gradual drop of the load carrying capacity caused by the P-delta effect is well predicted analytically. The models reproduce the inelastic mechanisms developed in the columns and shafts, such as the concrete crushing at the base of the columns, flexural cracking, bar yielding, and bond-slip. However, they cannot simulate bar buckling and subsequent bar fracture observed near the base of the columns towards the end of the tests. For this reason, the sudden load drop observed in the last cycle of the tests cannot be reproduced, as shown in Figure 8.2 and Figure 8.3. Unloading and reloading behaviors are fairly well represented because of the contact condition introduced at the column-shaft interface. However, the numerical results still show a smaller deterioration of the stiffness in the unloading branches due to the limitation of the concrete model to simulate accurately the closing of cracks in locations other than the column-shaft and shaft-footing interfaces.

Figure 8.4 and Figure 8.5 plot the numerical and experimental strain values for the column longitudinal bar at the north face of Specimens 1 and 2, respectively. A good correlation can be seen between the numerical and experimental results along the column and inside the embedment length in the shaft. As shown in Figure 8.4b, according to the FE analysis, tension yielding of the column longitudinal bars in Specimen 1 penetrates 0.5 m (1.63 ft) into the shaft at the peak displacement of Cycle 13 (the first cycle at ductility 5.5 and the last cycle before bar fracture occurred in the test). This plastic strain penetration is 14 times the bar diameter, d_b. In the test, the plastic strain penetration was measured to be 0.61m (2 ft) at this same cycle. Thus, the model underestimates the plastic strain penetration of this bar by 18%. This difference can be explained by the fact that the adverse effect of the splitting and cone-shaped cracks atop of the shaft on the bond resistance is less severe in the model because a tensile residual resistance is assumed for concrete to overcome convergence problems. In Specimen 2, strain gages were damaged in the last few cycles, so the final plastic strain penetration could not be obtained. According to the FE analysis, the plastic penetration in Cycle 17 (the first cycle at ductility 7 and the last cycle before bar fracture occurred in the test) for Specimen 2 is 0.72 m (2.4 ft), as shown in Figure 8.5b, which is $17d_b$.

Figure 8.6 plots the axial stress distributions along the column longitudinal bars for Specimens 1 and 2 at the peak displacements of different cycles, as predicted by the FE analysis. As shown in Figure 8.6a, the maximum bar stresses developed at the base of the column in Specimen 1 are 550 MPa (80 ksi) in tension and 485 MPa (70 ksi) in compression, while the yield strength and tensile strength of the bar are 448 MPa (65 ksi) and 629 MPa (91.2 ksi), respectively, as obtained from material testing. For Specimen 2,

the maximum bar stresses are 585 MPa (85 ksi) in tension and 470 MPa (68 ksi) in compression (see Figure 8.6b), while the yield strength and tensile strength of the bar are 462 MPa (67 ksi) and 638 MPa (92.5 ksi), respectively. These values indicate that the ultimate strength of the steel was not reached during the tests. As mentioned in Chapter 7, the fracture of these bars during the tests was not caused by exhaustion of the tensile capacity but by the propagation of micro-cracks created when the bar buckled, which is a feature that the FE model cannot capture. In Specimen 2, the bars reached tensile stresses higher than those in Specimen 1 because the bars in Specimen 2 buckled in a later cycle where a higher ductility demand was imposed.

The bond stresses in the column longitudinal bars obtained from the FE analyses provide valuable information to understand the bond-slip behavior of these bars along their anchorage. The bond stress distributions along the embedment length of the column bars located at the north face of Specimen 1 and Specimen 2 are plotted in Figure 8.7 and Figure 8.8, respectively. It is possible to calculate the experimental average bond stresses based on the readings from two adjacent strain gages as long as the bar had not yielded. As shown in Figure 8.7 and Figure 8.8, the numerically obtained bond stresses compare relatively well to the average bond stresses obtained from the experimental data.

For Specimen 1, the bond stress distribution is highly nonlinear when the bar is subjected to tension and compression, as shown in Figure 8.7. The peak bond stress occurs near the top of the embedment length, and it moves downward as the ductility demand is increased. Even though the bar slip is maximum at the top of the embedment length, the peak bond resistance occurs at a lower section. This is mainly due to the severe bond deterioration caused by bar yielding occurring in the upper region of the

embedment length. This behavior is similar to that observed in the development length tests presented in Chapter 6. As shown in Figure 8.7b, the peak bond resistance in Cycle 13 is located 0.53 m (1.75 ft) below the column base, practically at the same location where the plastic strain penetration ends as shown in Figure 8.4. This peak resistance is 6.9 MPa (1 ksi) or 40% of the maximum bond strength. At the peak displacement of Cycle 13, most of the bond resistance is provided in a region located approximately between 0.3 m (1 ft) and 1 m (3.3 ft) from the base of the column. In the remaining 2.3 m (4.2 ft) below this region, little bond resistance is activated, with the bond stress less than 2.5 MPa (0.35 ksi) (i.e., 15% of the bond strength), because the bar has not slipped much. This indicates that there is a significant portion of the embedment length that is not needed to develop the stress in the bar when the maximum ductility capacity of the column is reached.

Figure 8.8 plots the bond stress distributions along the embedment length of the longitudinal bar located at the north face of Specimen 2. The distribution is highly nonlinear when the bar is subjected to compression. However, the bond resistance is more uniform when the bar is subjected to tension. At the peak displacement of Cycle 17, the bond resistance along the upper 0.6 m (2ft) of the embedment length has deteriorated significantly. For the rest of the anchorage length, the bond resistance, when the bar is in tension, is more uniformly distributed than that for Specimen 1, with the bond stresses varying from 2.8 MPa (0.4 ksi) to 6.4 MPa (0.93 ksi), i.e., from 17% to 39% of the maximum bond strength. Hence, the bar has experienced more uniform slip along the anchorage. These results show that the embedment length for Specimen 2 is close to the minimum required with little reserve capacity against pull-out failure.

The numerical and experimental strain values for the shaft longitudinal reinforcement are plotted in Figure 8.9 and Figure 8.10 for Specimens 1 and 2, respectively. The FE models underestimate the strain levels in these bars. The discrepancies in the tensile strains could be attributed to the possibility that the concrete in the model is able to carry higher tensile stresses than that in the test, for which flexural cracks were observed in the shaft. As shown in Figure 8.10, the bar strains at the base of the shaft show a better correlation. This is because the contact interface at the shaft base does not have the concrete to carry tensile stresses, and the tensile stresses are transferred to the footing through the bars.

Figure 8.11 compares the numerical and experimental strain values for the column hoops at the south face of the specimens. The models predict correctly the yielding of the hoops at the base of the column in the latest cycles. However, they overestimate the hoop strains along the height of the column. This could be attributed to an overestimation of the plastic dilatation in the concrete model.

The numerical and experimental strain values for the shaft hoops in Specimens 1 and 2 are compared in Figure 8.12 and Figure 8.13, respectively. For Specimen 1, the model provides a fairly good representation of the peak strains for the north side of the shaft, but overestimates these strains near the top of the embedment length region, as shown in Figure 8.12a. The strain history for the north side of the hoop located at 1 ft below the column base is plotted in Figure 8.12b. During the test, the hoop strain increased when the column was pushed and pulled laterally, i.e., when the column longitudinal bar located near the hoop was pulled and pushed, and decreased when the column was unloaded. The strain increase was largely caused by the radial expansion

induced by the bar slip as it was pulled or pushed. When a bar is pushed, additional dilatation can be introduced by the lateral elastic and plastic expansion of the concrete under axial compression. However, as shown in Figure 8.12b, the FE model shows a different hysteretic behavior in hoop strains. In the FE model, the strain at the north face increases only when the column is pulled (i.e., subjected to a negative load). That is when the longitudinal bar located near the hoop is pushed into the shaft. When the column is unloaded and pushed, the strain remains practically constant. For the shaft hoop located at 3 ft from the base of the column, the strain increases when the column is pushed and decreases when it is pulled.

The problems to replicate the hoop strains in the shaft, as shown in Figure 8.12, could be attributed to the problems in the concrete model to simulate accurately plastic dilatation and closing of tensile splitting cracks, and in the bond-slip model to simulate accurately the radial dilatation caused by bar slip. As explained in Chapter 4, the bond-slip model was developed for well-confined situations and does not accurately account for the wedging action of the ribs. Similar trends have been observed for Specimen 2 in Figure 8.13. The magnitude of the strains for the north side of the hoops correlates well with the experimental results, as shown in Figure 8.13a, but the strain histories for the north side of the uppermost hoop, as plotted in Figure 8.13b, show the same discrepancies between the numerical and experimental results as in Specimen 1. For the west face of this hoop, the numerical strain values plotted in Figure 8.13c increase both when the column is pushed and pulled laterally. However, it is unclear if this is caused by the radial stress introduced by the slip of the column bars when the column is either

pushed and pulled laterally, or by the concrete expansion in the north and south faces of the column when they are subjected to compression.

The FE analysis results presented have shown good correlation with the experimental results in terms of the global lateral load-displacement behavior of the column-shaft assemblies and strain variations in the column longitudinal bars within the columns and embedment regions. However, some modeling limitations have also been identified. One is that the failure of the column caused by the buckling and the subsequent fracture of the bars is not simulated. Also, the concrete model has shown excessive plastic dilatation in concrete, and has a problem to represent the closing of tensile cracks in an accurate manner. While these problems are undesirable, they do not significantly influence the bond-slip behavior of bars, which is the focus of this study. Moreover, the finite element models are not able to capture the strains in the shaft hoops in a very accurate manner. Hence, these models may not have the desired resolution to determine the minimum quantity of transverse reinforcement required for the anchorage region of a shaft.

8.2 Design recommendations

8.2.1 Minimum embedment length of column reinforcement

The FE analyses presented in this chapter and the large-scale tests presented in Chapter 7 show that an embedment length equal to $D_{c,\max} + l_d$ provides a very conservative design. For Specimen 1, which had the above embedment length, the maximum plastic strain penetration of the column longitudinal reinforcement inside the

shaft reached only 27% of the total embedment length. This is small compared to the 44% measured in the development length test of a bar that developed its ultimate strength, as presented in Chapter 6. The low bond stresses activated in the lower half of the embedment length, as shown in the FE analysis, have indicated that a significant portion of the embedment length was not required to develop the maximum bar stress reached in Specimen 1. In addition, during the column-shaft tests, there was no indication of severe damage atop of the shaft, except for the circular and radial cracks caused by the cone-shaped failure and splitting forces, respectively. The low curvature measured in the shaft confirmed this observation. Hence, it does not seem necessary to add $D_{c,\max}$ to the required embedment length. In conclusion, the embedment length of $D_{c,\max}+l_d$ can be considerably reduced without jeopardizing the development of the column reinforcement.

The FE analysis and test results obtained for Specimen 2 indicate that reducing the embedment length to l_d+s+c does not affect the performance of the column. Adding $s+c$ to the development length l_d required by the AASHTO LRFD specifications is reasonable with the consideration of the ineffective bond resistance in the region where a cone failure is expected. Based on the post-test observations, it is conservative to assume that this cone has an inclination of 45 degrees. For Specimen 2, the maximum plastic strain penetration reached 50% of the total embedment length. In addition, the strain gages along the embedment length were damaged in the latest cycles of the test, which indicate that the slip of the bars was significant in these cycles. The FE analysis results show that this specimen had a more uniform bond resistance activated along the entire embedment length as compared to Specimen 1. These observations

indicate that $l_d + s + c$ can be considered as the minimum embedment length required for column longitudinal bars in Type II shafts.

8.2.2 Transverse reinforcement in the shaft

Recommendations for the transverse reinforcement required in the lap splice region to counteract the splitting action of bar slip have been developed based on a simple analytical model. In spite of some radial splitting cracks that were observed, the transverse reinforcement in both Specimens 1 and 2 seemed to provide sufficient confinement to develop the tensile capacity of the column reinforcement. The strains measured in the shaft hoops indicate that only the uppermost hoop in the shaft barely reached the yield strain at the end of the test. However, Specimen 1 had more embedment length than what that was needed. For Specimen 2, the transverse reinforcement in the lap splice region was determined according to the recommendation of McLean and Smith (1997), which is based on a truss analogy that assumes a uniform demand of confining forces along the lap splice region. However, the experimental results have shown that the confining action of the hoops along the embedment length was not uniform. Here, a different analytical model that directly considers splitting forces introduced by bar slip is proposed to determine the minimum transverse reinforcement.

Splitting and confining forces in the lap splice region

The transverse steel in the lap splice region has to counteract the splitting forces caused by the slip of the longitudinal bars. A bar that is being developed exerts a uniform pressure, σ, on the surrounding concrete due to the wedging action of the bar deformations, as shown in Figure 8.14a. The uniform radial stress for a unit length of the

bar can be represented by a set of four splitting forces, as suggested by Cairns and Jones (1996) and shown in Figure 8.14b. Each force is calculated as $f = \sigma d_b$.

The confining pressure (hoop stress) required to develop the bond resistance after the occurrence of tensile splitting in concrete can be determined with the following equilibrium considerations. Figure 8.15 presents a typical cross-section of a pile shaft and the splitting forces induced by the longitudinal bars. It has two sets of bars. One consists of the longitudinal bars close to the perimeter of the shaft and the other consists of bars extending from the column. For simplicity, it is assumed that all the column bars are subjected to uniform tension. In reality, some could be in compression, and compression bars could also induce splitting forces as they slip. It is assumed that both sets of bars can slip and generate splitting forces.

Assuming that the magnitude of the radial stress σ is equal to the bond stress τ, as suggested by Tepfers (1973), one can express the splitting force per unit length of the bar as $f = |\tau_{col}| d_{b,col}$ in the column bars and $f' = |\tau_{sh}| d_{b,sh}$ in the shaft bars. Since the forces from the column longitudinal bars have to be transferred to the shaft longitudinal bars, the total bond force per unit length of the column bars and that of the shaft bars have to be equal over the lap splice region. Hence,

$$N_{col} |\tau_{col}| \pi d_{b,col} = N_{sh} |\tau_{sh}| \pi d_{b,sh} \tag{8.1}$$

which results in

$$f' = \frac{N_{col}}{N_{sh}} |\tau_{col}| d_{b,col} \tag{8.2}$$

Equilibrium is considered for the free bodies represented by the ABCD and CDEF portions of the pile shaft section shown in Figure 8.15. The free body diagrams of these portions are presented in Figure 8.16. The forces acting on the two free bodies are the splitting forces of the bars being spliced (f and f') and the tensile forces in the shaft and column hoop reinforcement (t_{ext} and t_{int}). The line AB is a free surface with no loads applied, and the concrete is assumed to be splitted along the lines AD, DC, CB, DE, EF, and FC (marked as dashed lines in Figure 8.15). Therefore, the concrete cannot transfer any forces along these lines.

For body ABCD, the splitting forces in the tangential direction can be ignored because these forces from two adjacent bars practically cancel each other since they have the same magnitude and the same direction with opposite signs. The splitting forces pointing in the radial direction result in an equivalent pressure, p_{ext}, which is given by Equation 8.3.

$$p_{ext} = \frac{N_{sh} f'}{\pi D_{ext}} = \frac{N_{col} |\tau_{col}| d_{b,col}}{\pi D_{ext}} \tag{8.3}$$

in which D_{ext} is the diameter of the outer reinforcing hoops. Based on the equilibrium of the free body ABCD, the tensile force, t_{ext}, to be provided by the hoops per unit length of the shaft to balance p_{ext} is

$$t_{ext} = p_{ext} \frac{D_{ext}}{2} = \frac{N_{col} |\tau_{col}| d_{b,col}}{2\pi} \tag{8.4}$$

In body CDEF, the splitting forces in the tangential direction can be ignored based on the same argument presented for ABCD. Based on the equilibrium of the free body CDEF,

the tensile force, t_{int}, to be provided by the hoops to compensate for the difference in pressures, p_{ext} and p_{int}, generated by the splitting radial forces of the inner bars and outer bars, respectively, is

$$t_{\text{int}} = p_{\text{int}} \frac{D_{\text{int}}}{2} - p_{ext} \frac{D_{ext}}{2} \tag{8.5}$$

in which D_{int} is the diameter of the inner reinforcing hoops. Similarly to Equation 8.3, the internal pressure, p_{int}, is given by

$$p_{\text{int}} = \frac{N_{col} f'}{\pi D_{\text{int}}} = \frac{N_{col} |\tau_{col}| d_{b,col}}{\pi D_{ext}} \tag{8.6}$$

Substituting Equations 8.3 and 8.6 in Equation 8.5, we have

$$t_{\text{int}} = \frac{N_{col} |\tau_{col}| d_{b,col}}{\pi D_{\text{int}}} \frac{D_{\text{int}}}{2} - \frac{N_{col} |\tau_{col}| d_{b,col}}{\pi D_{ext}} \frac{D_{ext}}{2} = 0 \tag{8.7}$$

Hence, the inner hoops will not develop tension, and can be considered ineffective for confining the lap splices. For this reason, they will be ignored here.

Minimum transverse reinforcement in a pile shaft

The transverse steel in the lap splice region of the shaft should provide the tensile hoop force as given in Equation 8.4 for a unit length of the shaft. As shown by the FE analysis results, the bond stress distribution along the development length of a bar is not uniform and the location of the peak stress depends on the plastic strain penetration. However, the maximum bond stress cannot exceed the bond strength τ_u obtained from monotonic bond-slip tests. Hence, to determine the transverse steel, it is conservative to assume that the peak bond stress be τ_u. This is conservative because the actual bond stress will be much lower due to the tensile yielding of the bars. With the above-

mentioned assumption, the following equation can be obtained from Equation 8.4 to determine the quantity of transverse reinforcement required to balance the splitting force and, thereby, maintain the bond resistance.

$$A_{tr} = \frac{1}{2\pi} \frac{N_{col} \tau_u d_{b,col} s_{tr}}{f_{y,tr}} \tag{8.8}$$

in which A_{tr} is the cross-sectional area of a transverse reinforcing bar, s_{tr} is the spacing of the transverse reinforcement, τ_u is the ultimate bond strength of the column longitudinal reinforcement, which can be assumed to be 16.5 MPa (2.4 ksi) for a 34.5-MPa (5-ksi) concrete, $f_{y,tr}$ is the nominal yield stress of the transverse reinforcement, $d_{b,col}$ is the diameter of the longitudinal bars in the column, and N_{col} is the number of longitudinal bars in the column. For concrete strengths other than 34.5 MPa (5 ksi), τ_u can be scaled with the assumption that it is proportional to $f_c'^{3/4}$, as suggested in Chapter 4.

Given the uncertainty in the location of the peak bond stress, it is suggested that the transverse steel calculated with Equation 8.8 be distributed along the entire lap splice length. This equation remains valid when bundled bars are used. With this new recommendation, the volumetric ratios of the transverse reinforcement in the shafts would have been slightly increased for the test specimens presented in Chapter 7. For Specimen 1, the volumetric ratio would have been increased from 0.82% to at least 0.98%, and for Specimen 2, from 1.04% to at least 1.17%. Given the good performance of these two specimens, as presented in Chapter 7, this recommendation is conservative.

Transverse reinforcement to limit crack opening

The design recommendation according to Equation 8.8 is to prevent the degradation of the bond strength after the development of tensile splitting cracks and, thereby, prevent bar pull-out failure. However, it does not control the opening of a splitting crack, which can be significant as observed in the tests. An additional criterion is derived here to control the opening of the splitting cracks that develop in the lap splice region of the pile shaft. To this end, it is assumed that radial splitting cracks develop at every shaft longitudinal bar. This assumption is consistent with the splitting crack pattern observed in Specimens 1 and 2, as presented in Chapter 7. The transverse reinforcement controls the opening of this crack, and the relation between the strain in the transverse reinforcement and the opening of a radial crack, u_{cr}, can be established based on the diagram shown in Figure 8.17. Assuming that the strain in the transverse reinforcement is uniform, we have:

$$u_{cr} = \frac{\pi D_{ext}}{N_{sh}} \varepsilon_s \tag{8.9}$$

The maximum allowable strain, $\varepsilon_{s,\max}$, in the hoop reinforcement is then related to the maximum allowable crack opening as follows:

$$\varepsilon_{s,\max} = \frac{u_{cr,\max} N_{sh}}{\pi D_{ext}} \tag{8.10}$$

The required transverse reinforcement can then be established with Equation 8.8 by replacing $f_{y,tr}$ with $\varepsilon_{s,\max} f_{y,tr} / \varepsilon_y \le f_{y,tr}$ as follows.

$$A_{tr} = \frac{1}{2\pi} \frac{N_{col} \tau_u d_{b,col} s_{tr}}{\alpha f_{y,tr}} \tag{8.11a}$$

in which

$$\alpha = \frac{\varepsilon_{s,\max}}{\varepsilon_y} = \frac{u_{cr,\max} N_{sh}}{\pi D_{ext} \varepsilon_y} \leq 1 \qquad (8.11b)$$

Here, the maximum crack opening is assumed to be 0.3 mm (0.012 in.), which is based on a recommendation from ACI (2001) for members in contact with soils under service conditions. Hence, for crack width control, the volumetric ratio of the transverse reinforcement in the shaft would have been significantly increased for the test specimens presented in Chapter 7. In Specimen 1, the volumetric ratio would have been increased from 0.82% to at least 1.32%, and in Specimen 2, from 1.04% to at least 1.70%.

8.3 Parametric study to verify the minimum embedment length of column reinforcement in enlarged pile shafts

Finite element analyses of 12 column-shaft models have been carried out with cyclic loading to verify the minimum embedment length of column reinforcement in enlarged pile shafts. The column-shaft configurations analyzed including their main geometric and reinforcement characteristics are presented in Table 8.1.The nomenclature for the models is based on a set of four numbers. The first two numbers correspond to the column diameter (D_c) and shaft diameter (D_s), respectively, in feet. The third number corresponds to the size of the column longitudinal bars. Wherever needed, a forth number is added to distinguish models with the same dimensions and reinforcement, but with different embedment lengths of the column cages in the shafts and/or different transverse reinforcements in the shafts. Based on the first three numbers in the nomenclature, the models are divided into five groups. Two of these models, Models *4-6-11-1* and *4-16-14-*

1, correspond to the column-shaft assemblies tested in the laboratory. The results of these two models have been discussed in detail in Section 8.1. Ten more analyses have been carried out on column-shaft models with different embedment lengths of the column cages in the shafts, column and shaft diameters, longitudinal reinforcements, and transverse reinforcements in the shafts. The concrete, steel, and bond-slip properties used in these models are the same as those for the analyses presented in Section 8.1. The same loading protocol was used, except that an extra half cycle was added at the end to subject the system to a maximum ductility demand of 10.

The design recommendation proposed for the minimum embedment length of column longitudinal reinforcement in enlarged pile shafts, $l_d + s + c$, has been verified for columns and shafts with different cross-sectional dimensions and longitudinal bar sizes. Five models have been analyzed for this purpose. They represent small-size (D_c =1219 mm [4 ft]) and large-size (D_c= 2438 mm [8 ft]) columns, and include bar sizes between No. 11 and 18. In all these models, the transverse steel in the lap splice region is determined based on Equation 8.8. These are Models *4-6-11-2*, *4-6-14-2*, *8-10-14-1*, *8-12-14*, and *8-12-18* shown in Table 8.1.

The columns and shafts in Models *4-6-11-2* and *4-6-14-2*, have the same dimensions, with D_c =1219 mm (4 ft) and D_s =1829 mm (6 ft), and longitudinal reinforcement as Specimens 1 and 2, respectively. Model *8-10-14-1* corresponds to an assembly with D_c= 2438 mm (8 ft) and D_s= 3048 mm (10 ft), and with No. 14 (43-mm) and 18 (57-mm) longitudinal bars in the column and shaft, respectively. In Models *4-6-11-2*, *4-6-14-2*, *8-10-14-1*, the shaft diameter is 610 mm (2 ft) larger than the column

diameter, which is the minimum enlargement required in Caltrans SDC (Caltrans 2010). As a result, the separation between the column and shaft cages is slightly less than 305 mm (1 ft). Two models have been analyzed with D_c= 2438 mm (8 ft) and D_s= 3658 mm (12 ft), to verify the embedment length requirement when a larger separation between the column and shaft cages is provided. In one of the models, Model *8-12-14*, No. 14 and 18 longitudinal bars were used in the column and shaft, respectively. In the other, Model *8-12-18*, both the column and the shaft had No. 18 longitudinal bars.

The analysis results show that the minimum required embedment length recommended here is sufficient to develop the full capacity of the columns. More details about the FE analysis results obtained for these models are provided in the following sections.

8.3.1 Small-size column-shaft assemblies

Model *4-6-11-2* has the same column and shaft dimensions and reinforcement as Specimen 1 but with $l_e = l_d + s + c$. Figure 8.18 shows that it has identical force-displacement curves as the model for Specimen 1 (Model *4-6-11-1*), in which $l_e = D_{c,\max} + l_d$. Hence, the reduction of the embedment length has no influence in the system response. Model *4-6-11-3* has an even shorter embedment length of $0.7l_d$. For this model, several column longitudinal bars are pulled out from the shaft when the maximum drift reached for Specimen 1 has been achieved. Pull-out of the bars causes a drop of the load-carrying capacity with respect to the other two models, as shown in Figure 8.18. For embedment lengths longer than $0.7l_d$, pull-out failures will not occur,

based on finite element analysis. These results indicate that the new recommendation for the minimum embedment length has some margin of safety.

The strain distributions of the column bars located at the north face of Models *4-6-11-1*, *4-6-11-2*, and *4-6-11-3* at the peak displacement of Cycle 13 are plotted in Figure 8.19a. The maximum plastic strain penetration is about 0.5 m (1.63 ft) or $14d_b$ in all the models. The distance between the bottom of the bar to the point where the bar has yielded is $50d_b$, $26d_b$, and $7d_b$ for Models *4-6-11-1*, *4-6-11-2*, and, *4-6-11-3*, respectively. With only $7d_b$ to develop the yield capacity of the bar in the last case, the pull-out failure occurring in the last model is not unexpected. Differences are observed in the bond stress distributions of the same bars at the peak displacement of Cycle 13, as shown in Figure 8.19b. For a shorter embedment length, the bar slips more and the bond stress becomes higher and more uniformly distributed along the anchorage.

In Specimen 2, the new minimum embedment length, $l_d + s + c$, was tested, but the transverse reinforcement in the shaft was determined according to McLean and Smith (1997). A model with the same embedment length but transverse reinforcement in the shaft determined based on Equation 8.8 has been analyzed (*4-6-14-2*) and compared to the model of Specimen 2 (*4-6-14-1*). With the new recommendation, the volumetric ratio of the hoops in the lap splice region is 1.19% as compared to 1.04% provided in Specimen 2. In addition, two more models with the same embedment length but different transverse reinforcements have been analyzed. In Model *4-6-14-3*, no specific recommendation has been followed for the transverse reinforcement in the lap splice area. This reinforcement has been determined following the general specifications for

compression members in AASHTO (2010), resulting in a volumetric ratio of 0.74%. In Model *4-6-14-4*, the more stringent condition proposed in Equation 8.11 to control splitting cracks in the shaft has been followed. In this model, the size and spacing of hoops has been identical as in Model *4-6-14-3*, and the remaining confinement required by Equation 8.11 has been provided with a 6.3-mm (0.25-in.) thick steel casing made of A36 steel (with a nominal yield strength equal to 248 MPa [36 ksi]).

The force-displacement curves plotted in Figure 8.20 show no difference between the models. The strain and bond stress distributions in the column bar located at the north face of the specimen at the maximum drift reached for Specimen 2 are plotted in Figure 8.21. The plastic strain penetration increases as the transverse steel decreases, as shown in Figure 8.21a. However, the differences are very small, with the maximum plastic penetration ranging between 0.64 m (2.1 ft) and 0.72 m (2.4 ft). Similarly, the peak bond resistance increases and the bond stress distribution becomes less uniform with the increase of the transverse steel, as shown in Figure 8.21b. The hoop strains in the transverse reinforcement and in the steel casing at the peak displacement of Cycle 17 are plotted against the height of the shaft in Figure 8.22. The analysis results confirm that the strains needed to provide the required confining force increase with the decrease of the transverse reinforcement. In the case with the lowest confinement, the three upper hoops located in the upper 0.4 m (1.3 ft) of the shaft yield, while only the uppermost hoop is close to yielding when the recommendations proposed here and by McLean and Smith (1997) are used. No yielding of the hoop reinforcement and steel casing happens for the case with the highest confinement. These results show that the increase of the transverse reinforcement improves slightly the anchorage of the column longitudinal bars.

Model *4-6-14-5* replicates Specimen 2 but employs a reduced embedment length $l_e = 0.65 l_d$ in order to obtain a pull-out failure during the last few loading cycles. This failure is shown in Figure 8.20 with a drop in the load-carrying capacity of the column. The bond stress distribution in the north bar as plotted in Figure 8.21b shows that as the bar is pulled out from the shaft, the bond resistance has practically disappeared at the peak displacement of Cycle 17. The results plotted in Figure 8.22 show that the pull-out of the bar causes a significant increase in the strain of the transverse reinforcement in the lap splice region, and, therefore, wider splitting cracks should be expected. The upper hoops yield, with the top hoop experiencing a strain four times larger than that experienced in Model *4-6-14-2,* which has the same amount of transverse steel.

8.3.2 Large-size column-shaft assemblies

Two models of a column-shaft assembly with D_c = 2438 mm (8 ft) and D_s= 3048 mm (10 ft) have been analyzed. The proposed recommendations for the embedment length and transverse reinforcement in the shaft are used in Model *8-10-14-1*. The response of this model is compared to that of Model *8-10-14-2,* in which the embedment length is reduced to $l_e = 0.75 l_d$ to obtain a pull-out failure. The force-displacement curves plotted in Figure 8.23 show a drop in the load-carrying capacity in Model *8-10-14-2* caused by bar pull-out. At a system ductility equal to 7, reached at the peak displacement of Cycle 17, the plastic strain penetration in *8-10-14-1* is equal to 0.95 m (3.1 ft) or $22 d_b$, as shown in Figure 8.24a. According to the numerical results, plastic strains penetrate deeper in this case than in the case with D_c= 1219 mm (4 ft) and D_s=

1829 mm (6 ft), which has a plastic strain penetration of $17d_b$. This is caused by the more severe damage induced in the top of the shaft due to the smaller ratio of the shaft diameter to the column diameter. This increase in damage also is reflected in the bond stress distribution, which shows that the peak resistance moves towards the bottom of the embedment length, as shown in Figure 8.24b. Despite the increase in damage, the embedment length in *8-10-14-1* is clearly sufficient to avoid the failure of the anchorage.

Finally, two models of a column-shaft assembly with D_c= 2438 mm (8 ft) and D_s= 3658mm (12 ft) have been analyzed with the minimum recommended embedment length and transverse steel proposed here. Model *8-12-14* and *8-12-18* use No. 14 and 18 bars for column longitudinal reinforcement, respectively. Their force-displacement curves as plotted in Figure 8.25 and Figure 8.26 do not show any sign of load drop other than the P-delta effect. The strain distribution in the north column bar of Model *8-12-14* at the peak displacement of Cycle 17 (ductility 7) as plotted in Figure 8.27a indicates a plastic strain penetration of 0.95 m (3.1 ft) or $22d_b$. The plastic strain penetration is the same as that in Model *8-10-14,* but in this case, more embedment length is provided to account for the larger separation between the reinforcing cages. The bond stress distribution shows a peak located far from the end of the bar, as shown in Figure 8.27b. For the model with larger bars, the plastic strain penetration at the same ductility level is $18d_b$ (1.03 m [3.4 ft]), as shown in Figure 8.28a. The bond stress distribution as plotted in Figure 8.28b also shows a clear peak located far from the end of the bar. Hence, these two models seem to have a higher margin of safety against bond failure as compared to the models with D_s= 3048 mm (10 ft).

8.4 Conclusions

The ability of the FE models of column-shaft assemblies to simulate the bond-slip behavior has been validated by the results of the large-scale column-shaft tests. They have been used to study the development of column longitudinal bars in enlarged pile shafts, including the bond stress distributions along the anchorage of these bars in the two tests presented in Chapter 7. The analytical and experimental observations indicate that $l_e = D_{c,\max} + l_d$ as used in Specimen 1 was an over-conservative design. Based on the analytical and experimental results for Specimen 2, it is recommended that the minimum embedment length of column bars in enlarged shafts be $l_d + s + c$.

Through FE simulations, this new length has been verified for larger column-shaft assemblies, with different separations between the column and shaft reinforcing cages, and different column longitudinal reinforcements. Simulation results from a limited number of models have also indicated that pull-out failures should be expected when the embedment length is equal to or shorter than $0.75l_d$. This implies that there is a margin of safety when $l_d + s + c$ is used.

FE models have shown limitations to reproduce accurately the splitting action of bar slip in the pile shaft. For this reason, the transverse steel required in the bar anchorage region of a shaft has been studied with a simple analytical model of the splitting forces caused by bar slip. Based on this study, a recommendation has been established for the minimum transverse reinforcement required in the shaft to avoid the pull-out failure of the column longitudinal bars. A more stringent design recommendation has also been provided if one also wants to limit the width of the splitting cracks in the shaft.

Table 8.1: FE models of column-shaft assemblies for parametric study

Model ID	D_c mm (ft)	D_s mm (ft)	Column / shaft longitudinal reinforcement	$\rho_{v,shaft}$ [1]	l_e mm (ft)
4-6-11-1 (Test Specimen 1)	1219 (4)	1829 (6)	18 No. 11/ 28 No. 14	0.82%	2286 (7.5)
4-6-11-2				**1.07%**	**1422 (4.67)**
4-6-11-3				1.07%	762 (2.5)
4-6-14-1 (Test Specimen 2)	1219 (4)	1829 (6)	18 No. 14/ 26 No. 18	1.04%	1829 (6)
4-6-14-2				**1.19%**	**1829 (6)**
4-6-14-3				0.74%	1829 (6)
4-6-14-4				1.87%	1829 (6)
4-6-14-5				1.19%	1092 (3.6)
8-10-14-1	2438 (8)	3048 (10)	38 No. 14/ 48 No. 18	**1.58%**	**1829 (6)**
8-10-14-2				1.58%	1092 (3.6)
8-12-14	2438 (8)	3658(12)	40 No. 14/ 56 No. 18	**1.31%**	**2134 (7)**
8-12-18	2438 (8)	3658(12)	34 No. 18/ 56 No. 18	**1.53%**	**2565 (8.4)**

[1]: volumetric ratio of shaft transverse reinforcement

Note: models employing the new design recommendations are highlighted in bold.

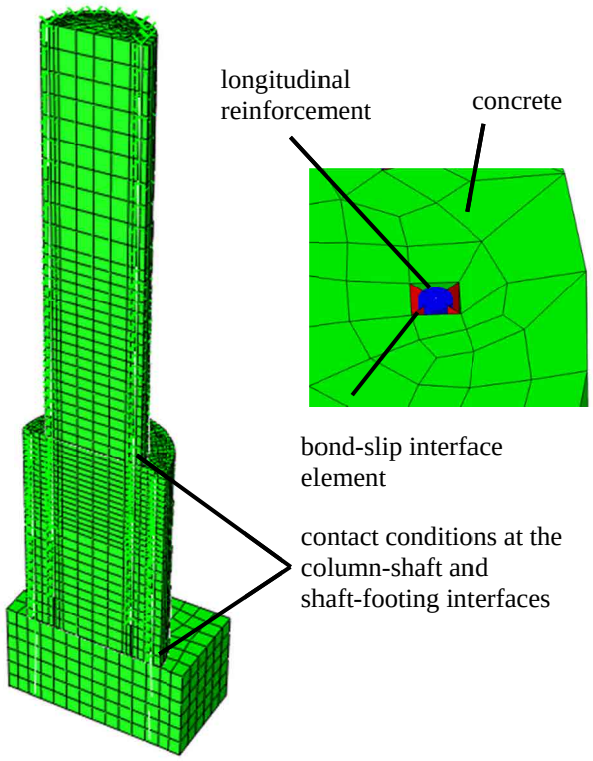

Figure 8.1: FE model of column-shaft assembly

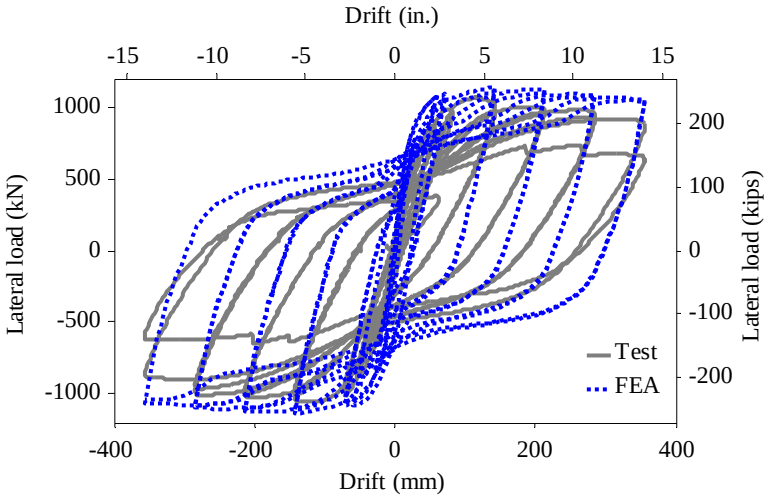

Figure 8.2: Lateral load vs. drift curves for Specimen 1

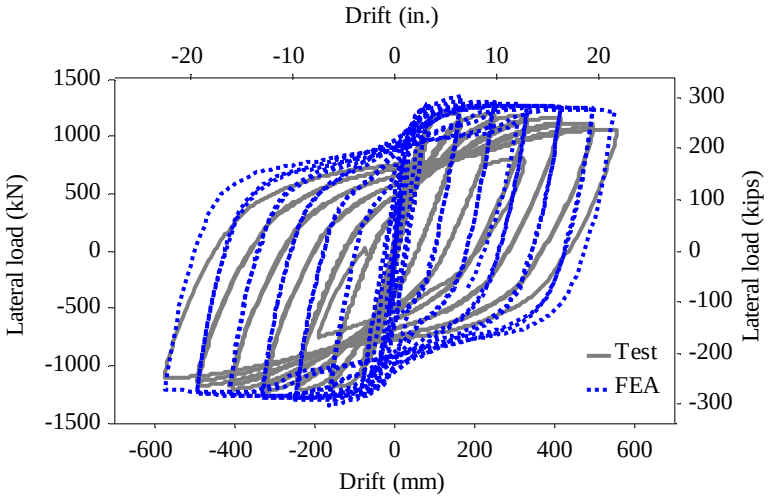

Figure 8.3: Lateral load vs. drift curves for Specimen 2

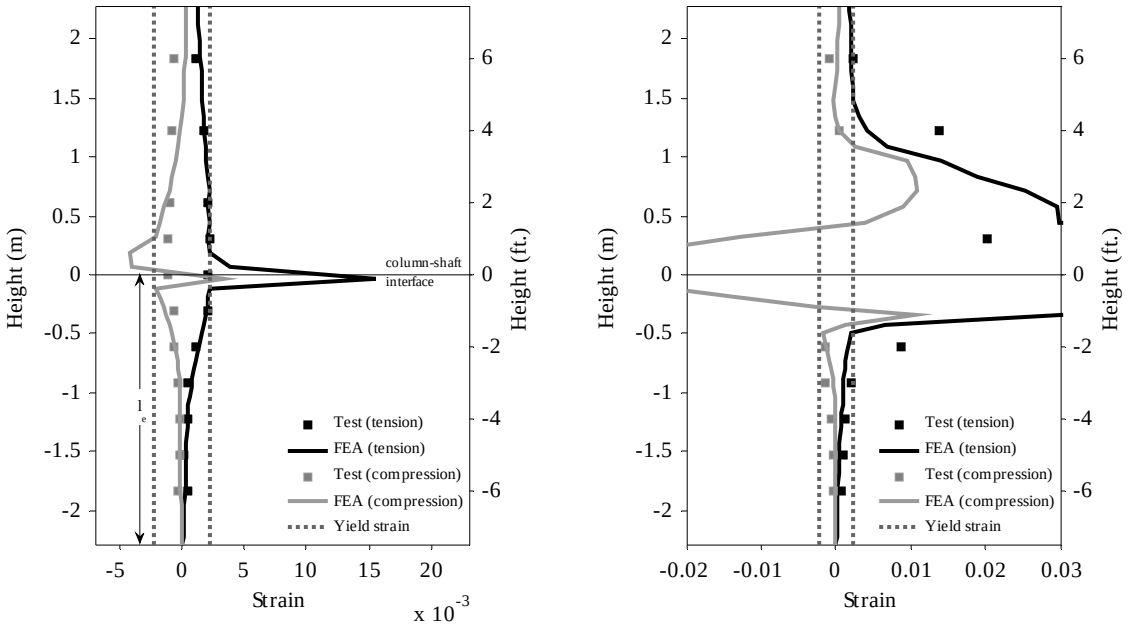

(a) Peak displacements of Cycle 4 (b) Peak displacements of Cycle 13

Figure 8.4: Strains in the column longitudinal bar at the north face of Specimen 1

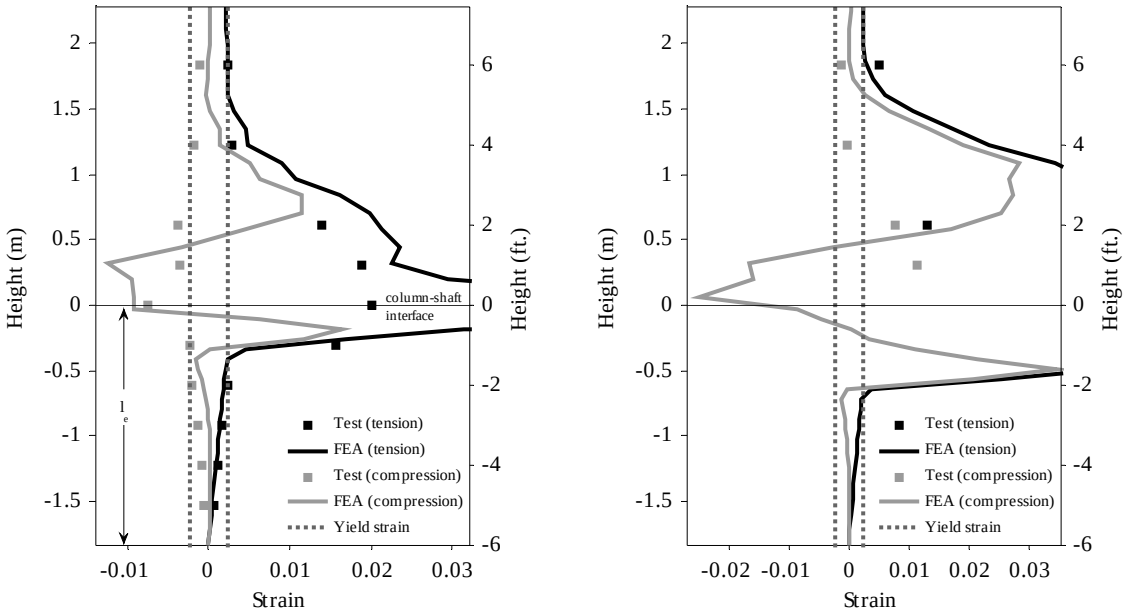

(a) Peak displacements of Cycle 9 (b) Peak displacements of Cycle 17

Figure 8.5 Strains in the column longitudinal bar at the north face of Specimen 2

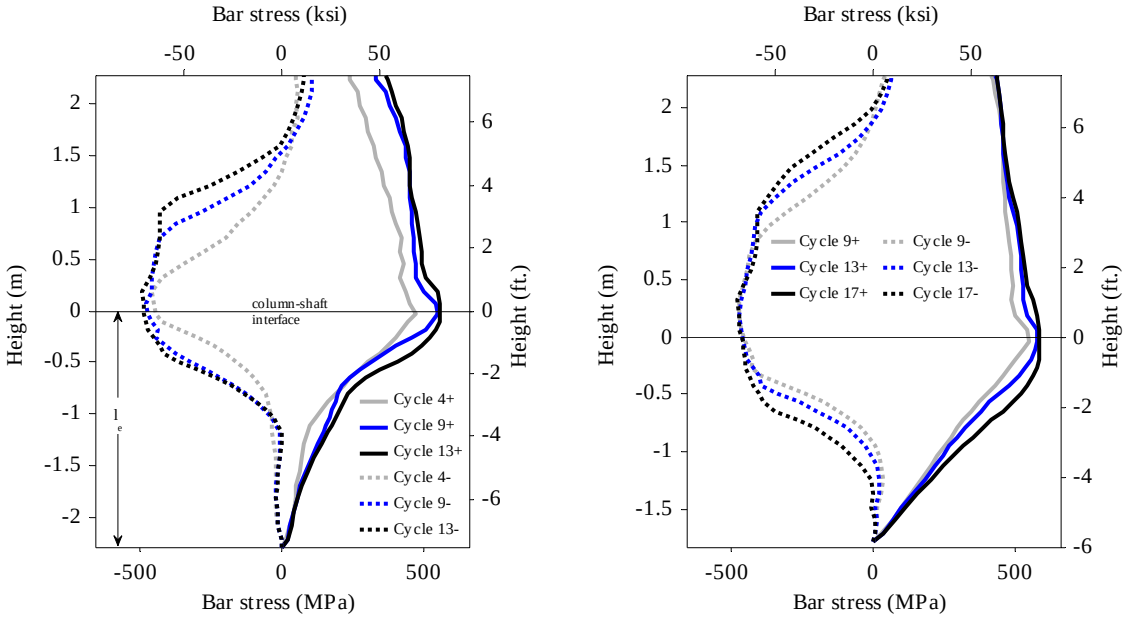

(a) Specimen 1 (b) Specimen 2

Figure 8.6: Axial stress variation in the column longitudinal bars at the north face of the specimens

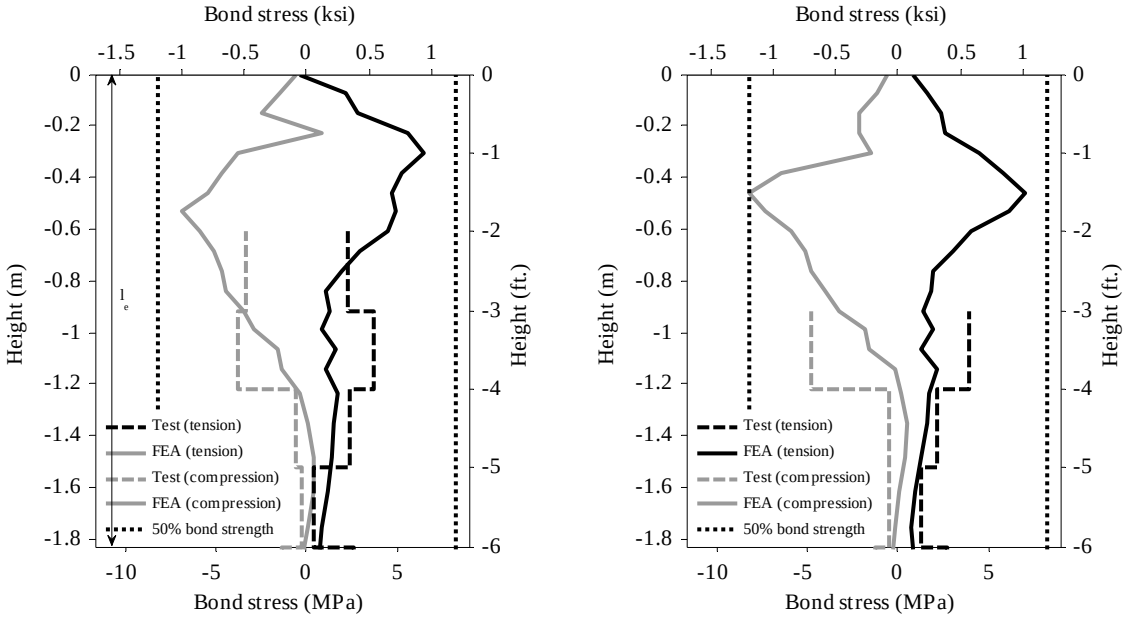

(a) Peak displacements of Cycle 9 (b) Peak displacements of Cycle 13

Figure 8.7: Bond stresses along the column longitudinal bar at the north face of Specimen 1

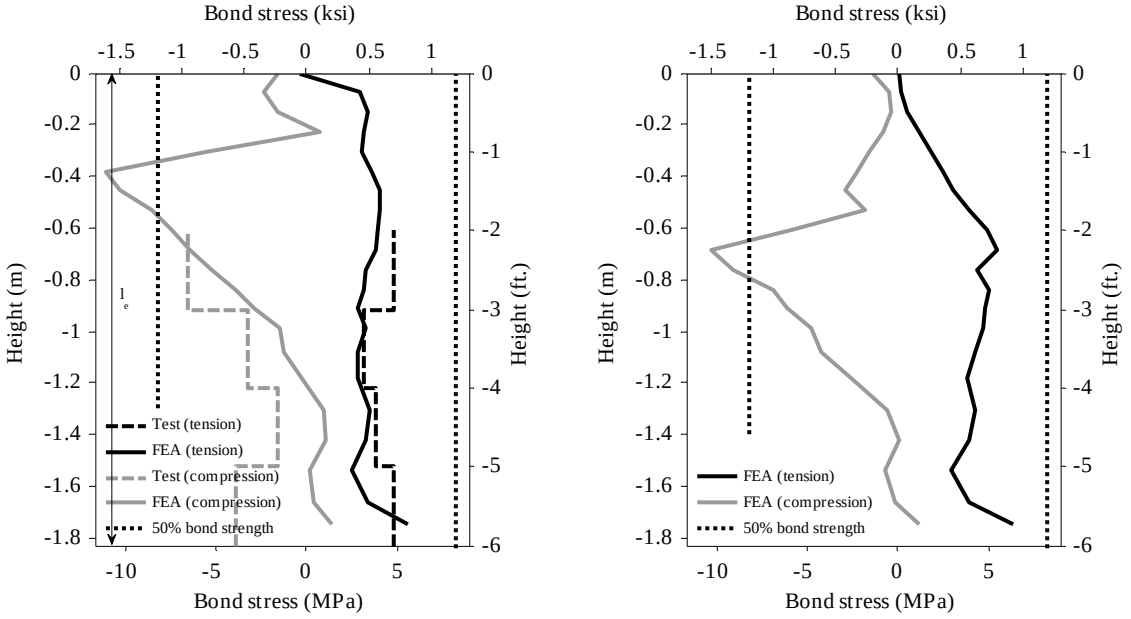

(a) Peak displacements of Cycle 9 (b) Peak displacements of Cycle 17

Figure 8.8: Bond stresses along the column longitudinal bar at the north face of Specimen 2

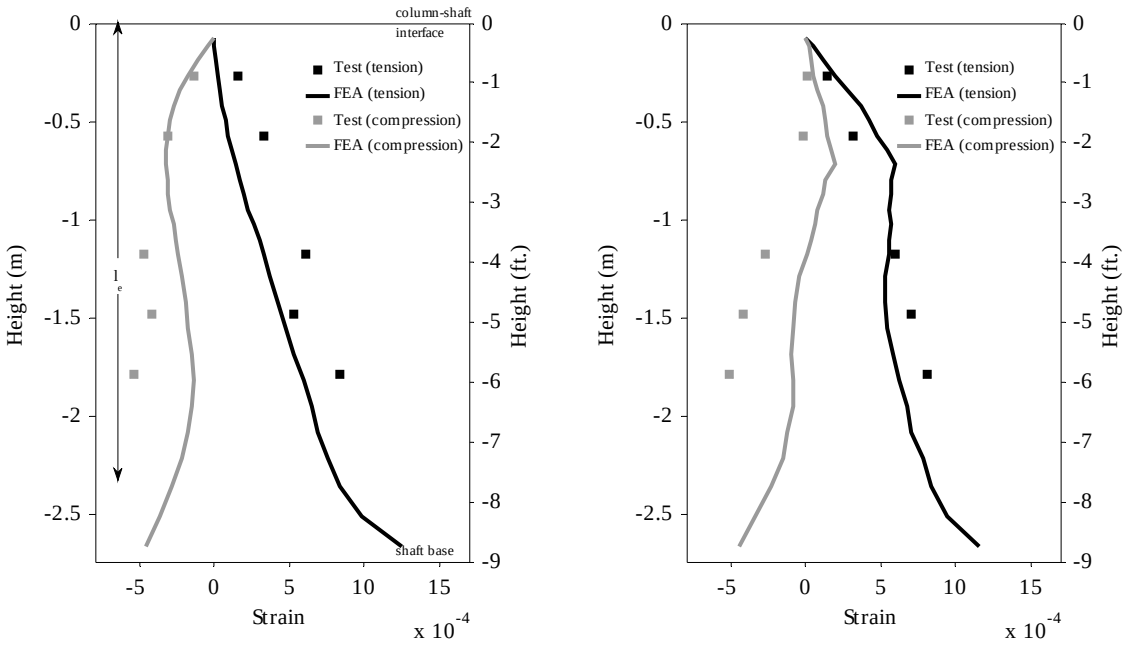

(a) Peak displacements of Cycle 4 (b) Peak displacements of Cycle 13

Figure 8.9: Strains in the longitudinal shaft bar at the north face of Specimen 1

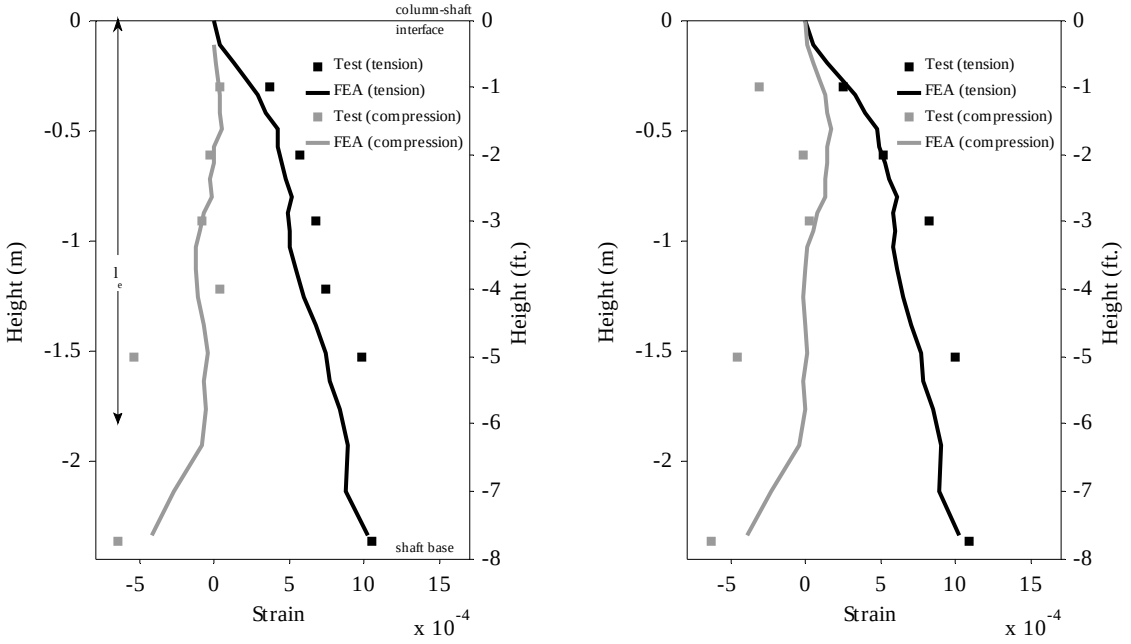

(a) Peak displacements of Cycle 9 (b) Peak displacements of Cycle 17

Figure 8.10: Strains in the longitudinal shaft bar at the north face of Specimen 2

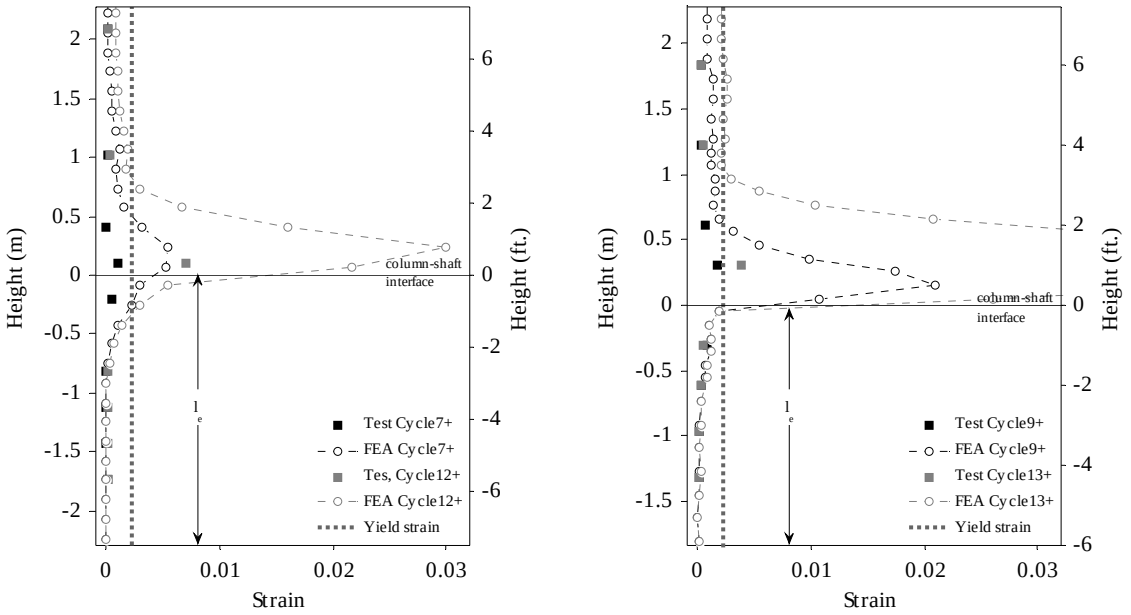

(a) South face of Specimen 1 (b) South face of Specimen 2

Figure 8.11: Strains in the column hoops

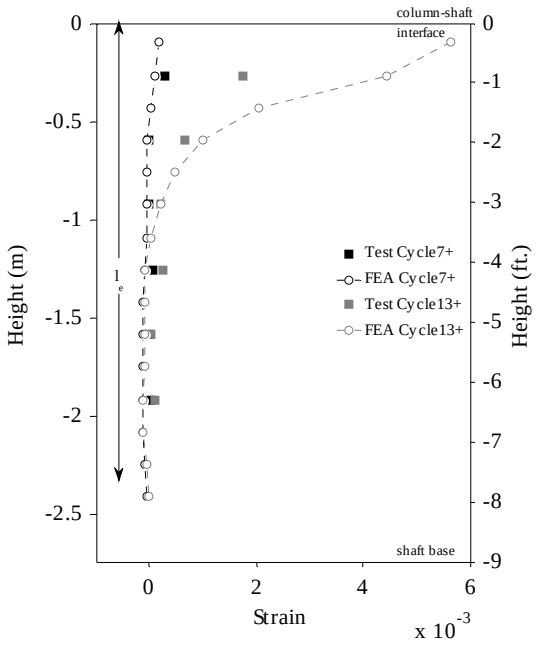

(a) Shaft hoops

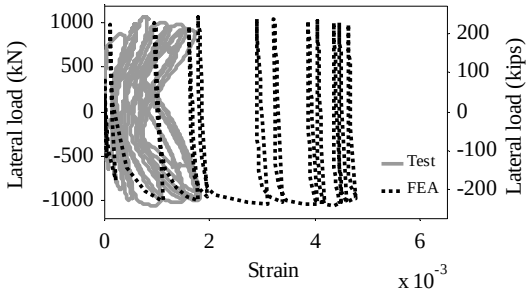

(b) Hoop at -1 ft

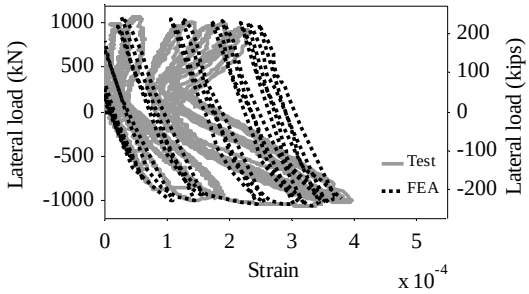

(c) Hoop at -3 ft

Figure 8.12: Strains in shaft hoops at the north face of Specimen 1

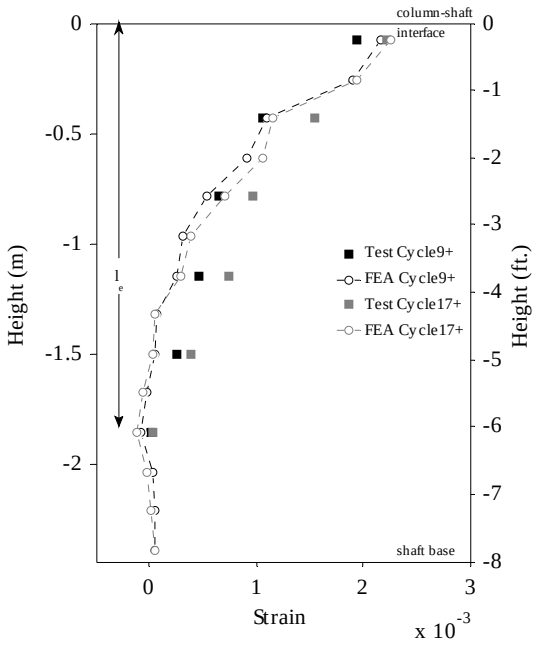

(a) Shaft hoops (north face)

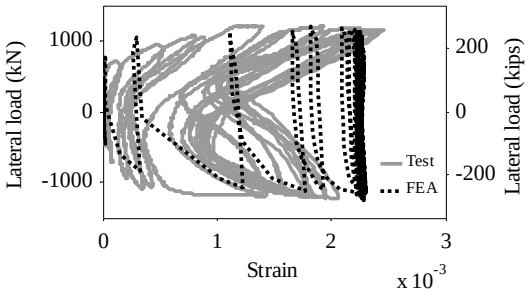

(b) Hoop at -3 in. (north face)

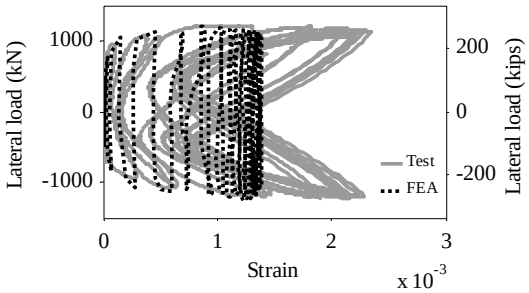

(c) Hoop at -3 in. (west face)

Figure 8.13: Strains in shaft hoops in Specimen 2

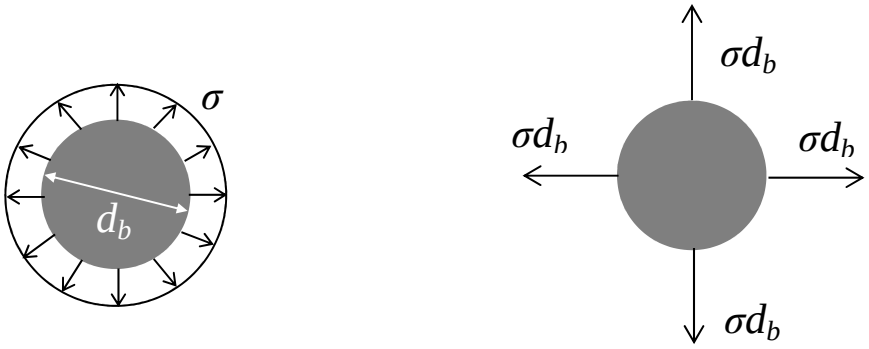

(a) Radial stress (b) Splitting forces per unit length of bar

Figure 8.14: Splitting stress and forces in developed bar

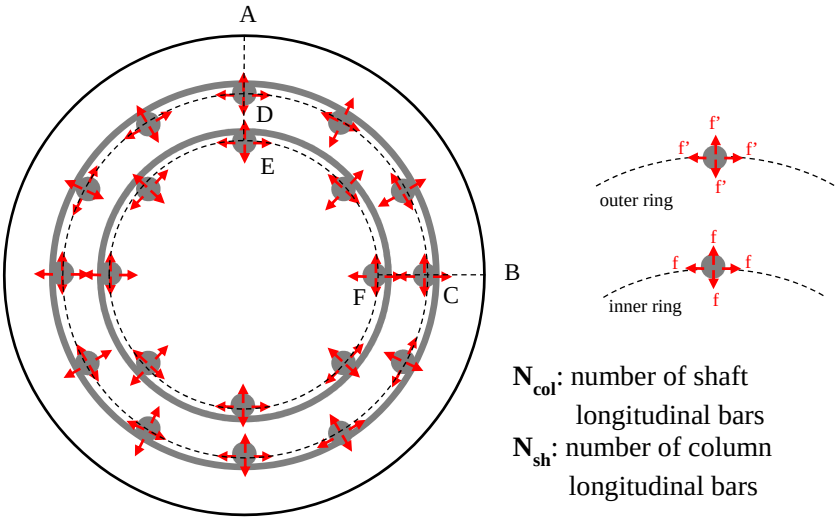

Figure 8.15: Cross-section of pile shaft and splitting forces

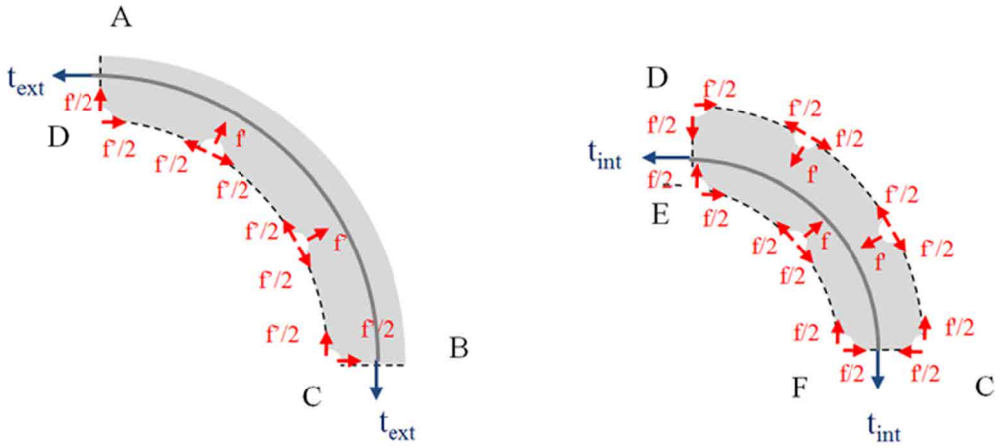

Figure 8.16: ABCD and CDEF free body diagrams

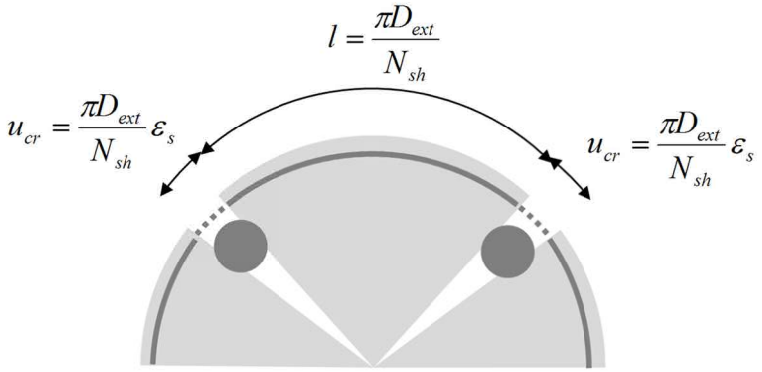

Figure 8.17: Splitting crack opening and strain in hoop reinforcement

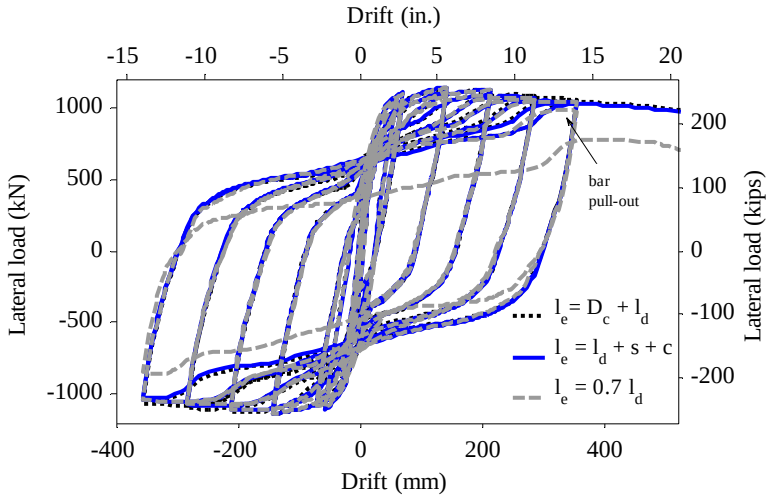

Figure 8.18: Lateral load vs. drift curves for Models *4-6-11-x*

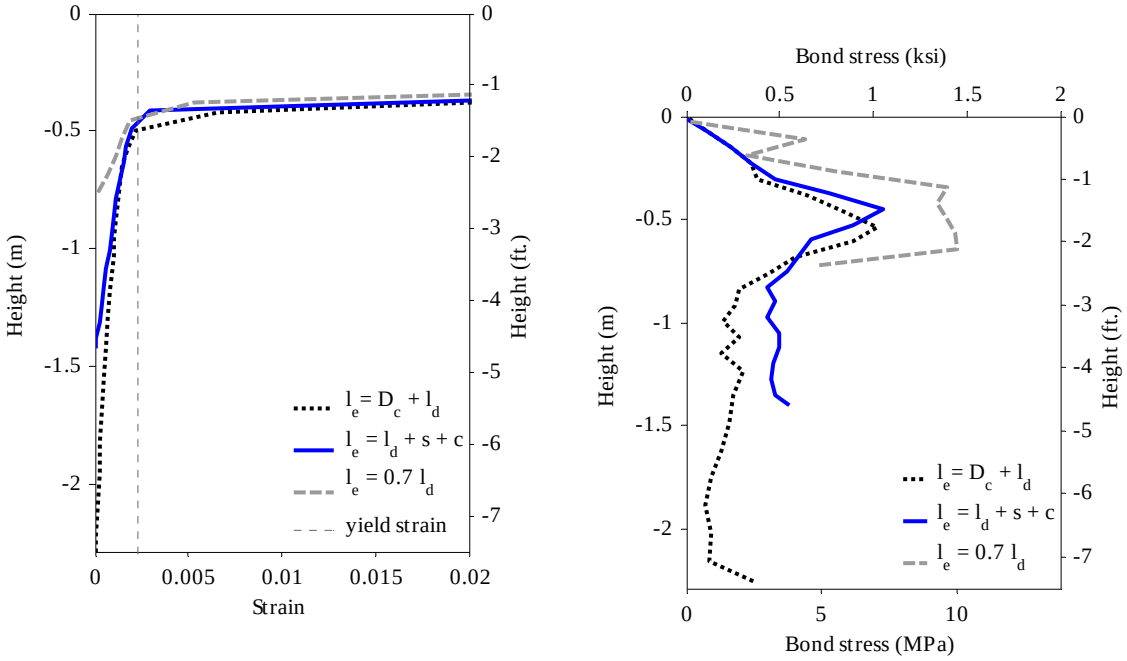

(a) Axial strain (b) Bond stress

Figure 8.19: Results for north column longitudinal bar in Models *4-6-11-x* at the peak displacement of Cycle 13

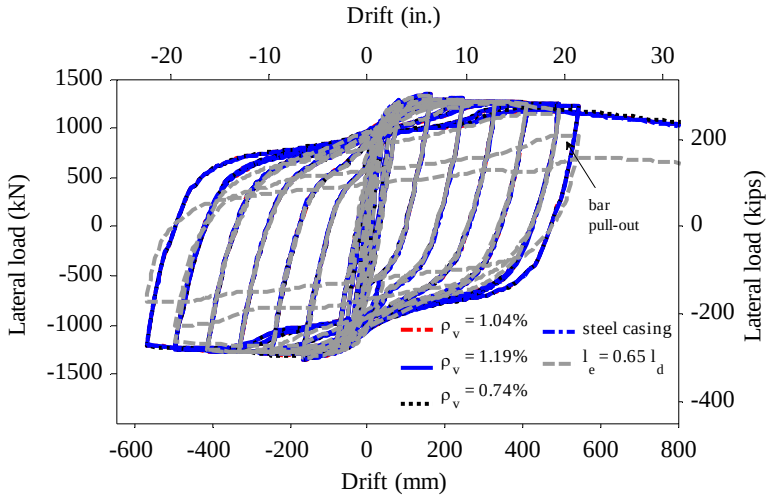

Figure 8.20: Lateral load vs. drift curves for Models *4-6-14-x*

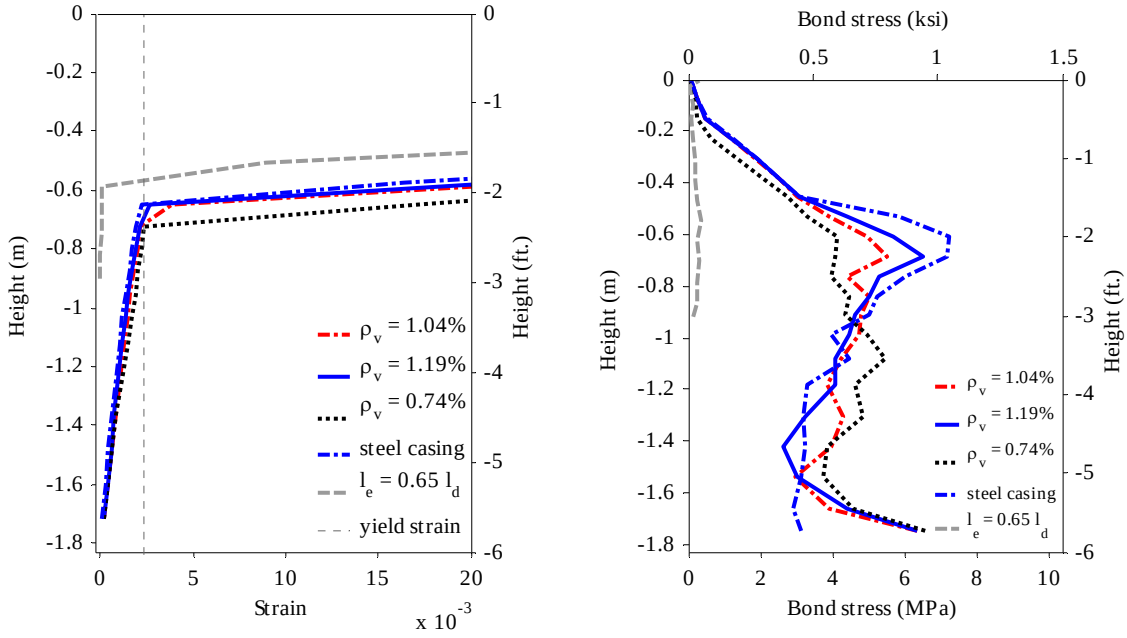

(a) Axial strain (b) Bond stress

Figure 8.21: Results for north column longitudinal bar in Models *4-6-14-x* at the peak displacement of Cycle 17

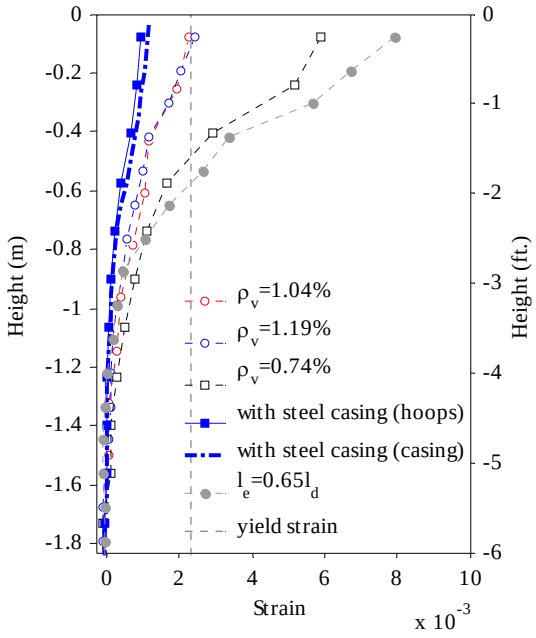

Figure 8.22: Strains in shaft hoop in Models *4-6-14-x* at the peak displacement of Cycle 17

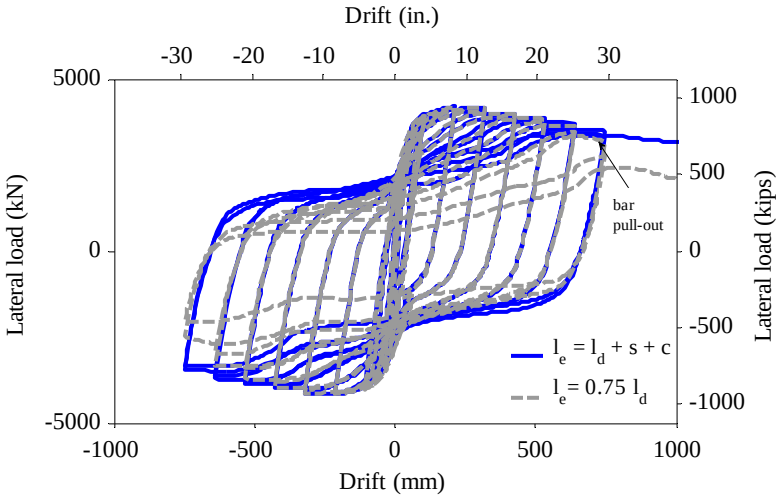

Figure 8.23: Lateral load vs. drift curves for Models *8-10-14-x*

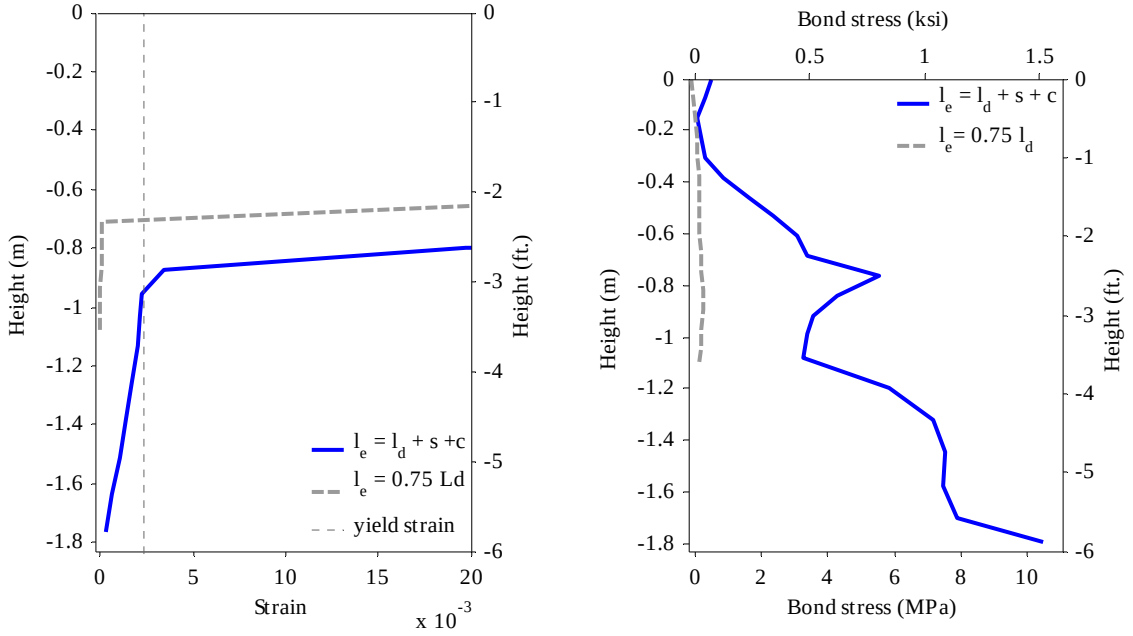

(a) Axial strain (b) Bond stress

Figure 8.24: Results for north column longitudinal bar in Models *8-10-14-x* at the peak displacement of Cycle 17

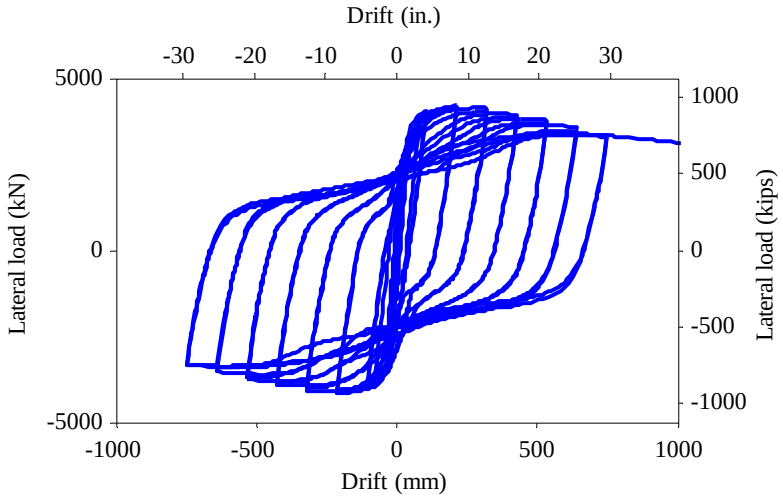

Figure 8.25: Lateral load vs. drift curve for Model *8-12-14*

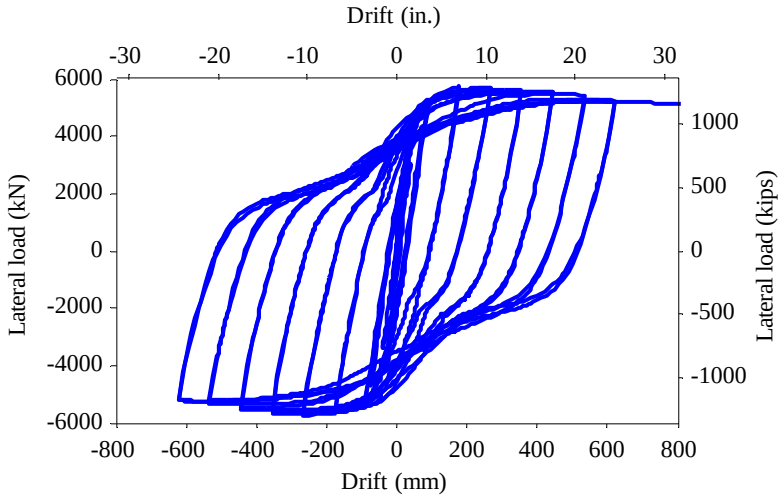

Figure 8.26: Lateral load vs. drift curve for Model *8-12-18*

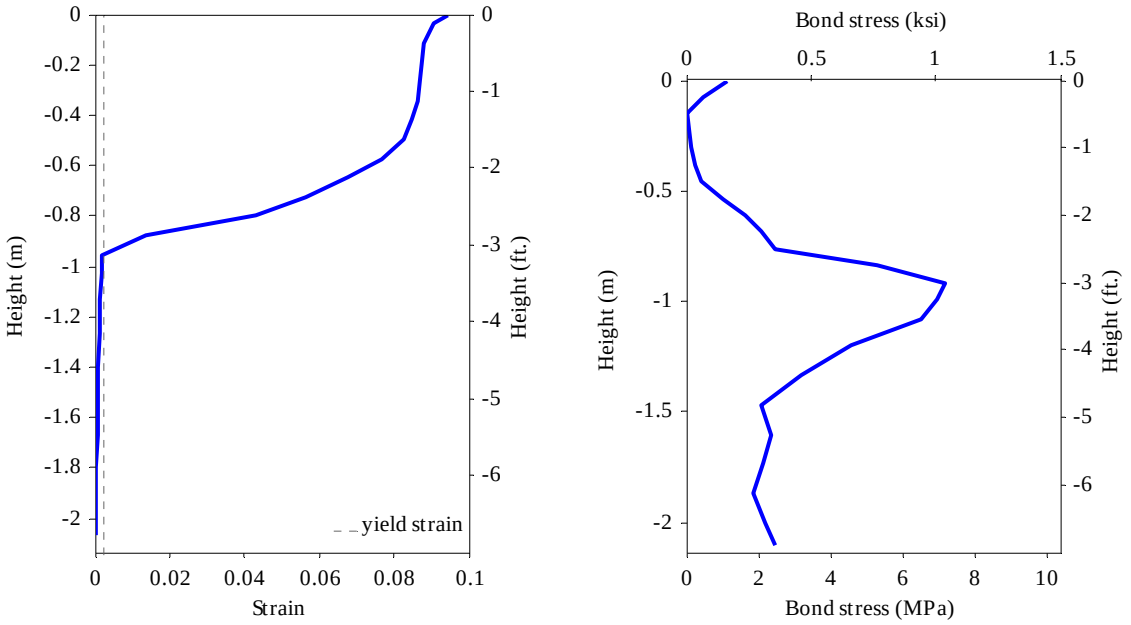

(a) Axial strain (b) Bond stress

Figure 8.27: Results for north column longitudinal bar in Model *8-12-14* at the peak displacement of Cycle 17

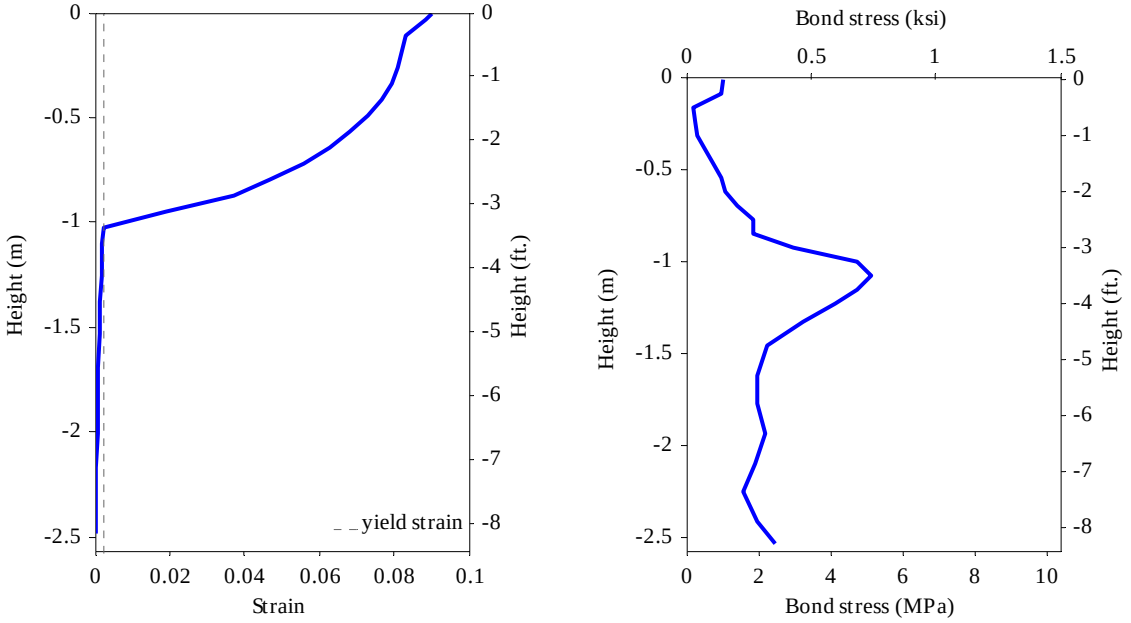

(a) Axial strain (b) Bond stress

Figure 8.28: Results for north column longitudinal bar in in Model *8-12-18* at the peak displacement of Cycle 17

CHAPTER 9

SUMMARY AND CONCLUSIONS

9.1 Summary

An investigation on the bond-slip behavior and development of longitudinal column reinforcing bars in enlarged pile shaft foundations has been presented in this dissertation. This investigation consisted of experimental and computational studies to provide insight into the fundamental bond-slip behavior of bars, and resulted in analytical tools to predict this behavior as well as a new design recommendation for the minimum embedment length required for column longitudinal reinforcement in enlarged (Type II) pile shafts.

An experimental study was carried out to generate much-needed data on the bond strength and cyclic bond deterioration of large-diameter bars, No. 11 and larger, which are typically used in large bridge columns and piles. A total of 22 pull-out and pull-pull tests were performed on No. 11, 14, and 18 bars embedded in concrete cylinders representing the confinement condition of an enlarged pile shaft. Basic bond stress-vs.-slip relations for monotonic and cyclic loading were obtained, as well as data on the effect of the compressive strength of concrete and bar size on the bond strength.

A new phenomenological bond stress-vs.-slip law for bars embedded in well-confined concrete has been proposed for monotonic and cyclic loading. This law has been developed based on the basic bond-slip data generated in this study and has extended concepts proposed in previous models. The relation between the bond stress and slip is described by a set of polynomial functions for monotonic loading. For cyclic loading, a similar bond stress-slip relation is used, but the bond strength is reduced at each slip reversal using two damage parameters, whose values are based on the slip history, to account for cyclic bond deterioration. The law also takes into account the reduction of the bond resistance due to the tensile yielding of a bar. It has been calibrated with the basic bond-slip data obtained for large-diameter bars, but can be used for any bar size. This law has been implemented in an interface element in the commercial finite element (FE) program ABAQUS as a user-defined subroutine. The interface element incorporates the wedging action of the ribs by defining the normal stress as a fraction of the bond stress along the interface. The new element has been used in three-dimensional FE analyses of well-confined reinforced concrete members. A plastic-damage constitutive model for concrete and an elasto-plastic model with kinematic hardening for steel available in ABAQUS have been used for the analyses.

A second interface model has been proposed to simulate the bond-slip behavior of bars under a wide range of confinement levels. This model is physics-based and adopts a multi-surface plasticity formulation with a non-associated flow rule to control the shear dilatation of the interface. The constitutive equations are integrated numerically using an elastic prediction - plastic correction algorithm using a generalized mid-point rule. The

model has been implemented as an interface element in ABAQUS to be used to investigate the influence of confinement on the bond-slip behavior of bars.

The development in tension of large-diameter bars embedded in well-confined concrete, such as that in a bridge foundation, was studied with experimental testing and computational analyses. The bond-slip demands of column longitudinal bars during an earthquake were characterized with data from a full-scale bridge column tested on the NEES-UCSD Outdoor Shake-Table (Restrepo et al. 2010). The bond-slip and development of large-diameter bars with long embedment lengths was evaluated in more detail with quasi-static pull-push tests. The test specimens consisted of No. 14 and 18 bars embedded in a concrete cylinder with the same confinement characteristics as the basic bond-slip tests. These tests were conducted to evaluate the current AASHTO LRFD Bridge Design Specifications (2010) for the development length of straight bars in tension. Two tests, one for each bar size, were performed with an embedment length equal to the development length required by this specification. A third test with an embedment length 40% shorter was carried out for a No.18 bar. This test was done to confirm that this reduced length was sufficient to develop bar yielding, as predicted by FE analysis with the phenomenological bond-slip model. The FE models were validated with the experimental data, and were used to study analytically the tension development capacity of bars embedded in well-confined concrete. Based on results of the FE analyses, an empirical equation has been proposed to calculate the tension capacity of well-confined bars as a function of the embedment length, compressive strength of concrete, and yield strength of steel. This equation has been used in Monte Carlo

simulations to study the reliability of the current AASHTO specifications on the development length of large-diameter bars.

The minimum embedment length required for column longitudinal reinforcement in Type II shafts was studied with large-scale tests of column-shaft assemblies and FE analysis. Two full-scale 1219-mm (4-ft) diameter column and 1829-mm (6-ft) diameter shafts assemblies were tested under lateral cyclic loading at the UCSD Powell Laboratories. The first specimen was to assess the level of conservatism of the current Caltrans design recommendations. The embedment length was taken as $D_c + l_d$, in which D_c is the column diameter and l_d is the minimum development length required in the AASHTO LRFD Bridge Design Specifications (2010). During this test, a plastic hinge formed at the base of the column, and the specimen failed by buckling and subsequent tensile rupture of several longitudinal bars in the plastic hinge. No significant damage was observed in the upper region of the shaft where the column reinforcement was anchored. FE analysis of this test was performed using the phenomenological bond-slip model to complement the experimental data. Based on the experimental and analytical results, it was determined that the minimum embedment length could be reduced to $l_d + s + c$, in which s is the spacing of the column and shaft reinforcing cages and c the vertical cover of the shaft. A second specimen was tested with this minimum embedment length. The transverse reinforcement in the lap splice area of the shaft was calculated with the formula proposed by McLean and Smith (1997). This specimen behaved in a similar manner as the first one, with no indication of anchorage failure. Finally, FE analysis has been used to verify that $l_d + s + c$ can be taken as the minimum embedment

length for column-shaft assemblies with different sizes and different reinforcement characteristics.

9.2 Conclusions

The basic bond-slip tests presented in this investigation have shown that the monotonic and cyclic bond stress-vs.-slip behavior of large size bars, No.11 and larger, embedded in well-confined concrete is very similar to that of No. 8 bars, as observed by Eligehausen et al. (1983). These tests have also shown a slight increase of the bond strength when increasing the bar size, and that the compressive strength of concrete, f_c', has a notable effect on the bond strength. The bond strength observed here is proportional to $f_c'^{3/4}$. Results from this and other studies have indicated that the influence of the concrete strength and bar size on the bond strength depends on the level of confinement in the concrete specimen. However, data supporting this conclusion is limited.

The phenomenological bond-slip model proposed in this dissertation is distinct from others in that it has only three parameters to calibrate and can be applied to any bar size and concrete strength. The model successfully reproduces the bond-slip behavior of the large-diameter bars tested in this study as well as that of smaller bars tested by others, including the decay in bond strength under different load histories. Implemented in an interface element in ABAQUS, it provides a versatile tool to simulate the effect of bond-slip of reinforcement in reinforced concrete members. Comparison with experimental data from pull-out tests from different studies and tests on RC columns have shown the accuracy of the model to simulate the bond-slip behavior of bars in well-confined

concrete members. Also, through a simple representation of the wedging action of the ribs, this model can simulate in an approximate manner splitting failures and bond decay due to lack of confinement. For these reasons, and given the computational efficiency of this model, it has been used for the numerical studies on the development of large-diameter bars and required embedment length of column longitudinal bars in enlarged pile shafts.

The new plasticity-based dilatant interface model reproduces in a satisfactory way the monotonic and cyclic bond-slip behavior, and pull-out and splitting failures observed in tests carried out by different researchers. The existence of multiple yield surfaces and plastic flow rules poses a challenge in the numerical implementation, which is based on an elastic prediction – plastic correction method. This has been addressed with a stress return algorithm that assures a smooth transition from one yield surface to another. The plasticity-based dilatant interface model is more general than the phenomenological model in that it can simulate bond-slip under a wide range of confinement conditions due to a more precise representation of the wedging action of the ribs. However, this is achieved at a higher computational cost because the iterative stress-update algorithm. For this reason, the plasticity-based bond-slip model is more for detailed studies on the effects of the concrete cover, bar spacing, and transverse reinforcement on the bond strength and bond-slip behavior of bars than for finite element analysis of structural assemblies.

The experimental and analytical investigations carried out in this study have confirmed that the AASHTO LRFD Bridge Design Specifications (2010) for the tension development length of large-diameter bars in well-confined concrete are appropriate.

These specifications are intended to ensure that the tensile yield strength of steel can be reached. Tests presented in this investigation have shown that these lengths are sufficient not only to develop tensile yielding of the bar, but to sustain large inelastic deformations up to the ultimate strain of the steel. Considering several sources of uncertainties, a reliability analysis has been conducted to confirm that the AASHTO specifications for large-diameter bars in well-confined concrete are sufficient for these bars to develop their yield strength with an acceptable reliability level. However, the analysis has also indicated that if one wants to preclude bond failures in longitudinal reinforcement before reaching the flexural failure limit state in a hinging column with an appropriate reliability level, the development lengths need to be increased.

Large-scale testing and FE analysis of column-shaft assemblies have confirmed that the minimum embedment length required by Caltrans Seismic Design Criteria (Caltrans 2010) for column longitudinal bars in an enlarged pile shaft is over-conservative. The experimental and analytical results have also shown that the minimum embedment length, l_e, can be taken as

$$l_e = l_d + s + c \tag{9.1}$$

In Equation 9.1, l_d is the tension development length determined with AASHTO LRFD Bridge Design Specifications (2010). This length ensures that the column bar will sustain large inelastic deformations, as mentioned above. The second term in Equation 9.1, $s+c$, accounts for the ineffective development region at the top of the shaft caused by the formation of the cone failure, assuming that this cone has a 45 degree angle.

A minimum transverse reinforcement for the shaft in the lap splice region is also recommended to provide sufficient confinement to ensure the development of the column bars. Based on an analytical study of the splitting stresses in the lap splice region, the transverse reinforcement required to resist the splitting stresses caused by bar slip should be taken as

$$A_{tr} = \frac{1}{2\pi} \frac{N_{col} \tau_u d_{b,col} s_{tr}}{f_{y,tr}} \tag{9.2}$$

in which A_{tr} is the cross-sectional area of a transverse reinforcing bar, s_{tr} is the spacing of the transverse reinforcement, τ_u is the ultimate bond strength of the column longitudinal reinforcement, which can be assumed to be 16.5 MPa (2.4 ksi) for a 34.5-MPa (5-ksi) concrete, $f_{y,tr}$ is the nominal yield stress of the transverse reinforcement, $d_{b,col}$ is the diameter of the longitudinal bars in the column, and N_{col} is the number of longitudinal bars in the column. For concrete strengths other than 34.5 MPa (5 ksi), τ_u can be scaled with the assumption that it is proportional to $f_c'^{3/4}$. A more stringent confinement condition is also provided in Chapter 7 if one wants also to limit the width of the splitting cracks in the shaft.

The new recommendation on the minimum embedment length has been validated with FE analysis for column-shafts of different sizes, different separation between the column and shaft cages, and different longitudinal reinforcement. The design of the transverse steel has not been sustained on simulation results, but rather on simpler analytical models and experimental results, because the FE models have shown limitations to reproduce accurately the splitting action of bar slip in the pile shaft.

Finally, a third and fourth column-shaft tests have been conducted at UCSD to further validate the new recommendations. The results of these tests have not been included in this dissertation. These results will be published in a separate report.

9.3 Recommendations for future research

The comparison between experimental results obtained in this investigation and those in studies by others has highlighted the need for a comprehensive study on how the bond strength varies with the bar size and compressive strength of concrete, including the level of confinement as a variable. As indicated in the conclusions, the influence of the concrete strength and bar size on the bond strength seems to depend on the level of confinement in the concrete, but there is not sufficient data to accurately quantify the influence.

Column longitudinal reinforcement always experiences slip with respect to the concrete in the foundation even if good anchorage is provided due to the strain penetration along the anchorage. This slip produces a rotation of the base of the column leading to extra flexibility in the system. Several empirical formulas have been proposed to account for this source of deformation, e.g., see Priestley et al. (1996). The newly available experimental data from the column-shaft tests and the shake table test on the bridge column together with the FE models developed in this investigation could be used to examine and develop better formulas to account for the effect of strain penetration.

The plasticity-based interface model has shown a very good potential to study the effect of confinement on the bond-slip behavior of bars. However, the validation and use

of this model has been restricted to pull-out tests. Further validation is required to assure the reliability of the model and evaluate its capabilities for larger scale simulations.

Some shortcomings have been identified regarding the computational models used in this investigation for the concrete and reinforcing bars. The plastic-damage constitutive model available in ABAQUS for concrete has shown limitations to represent the opening and closing of cracks in tension, and to predict the increase of ductility in compression with increasing confinement. For this reason, the development of a new three-dimensional model for concrete is recommended. New models capable of predicting the buckling and subsequent fracture of bars are also desirable.

The new design recommendation for the transverse steel in the region of the shaft in which the longitudinal column reinforcement is embedded has been developed with a simple analytical model and conservative assumptions. Further analyses and experimental tests could provide a better estimation of the minimum transverse steel required in this region.

APPENDIX A: CONSTRUCTION OF PULL-PUSH TEST SPECIMENS

The construction sequence of the pull-push specimens presented in Chapter 6 is shown in Figure A.1 through Figure A.6. These pictures correspond to the construction of Specimen 2.

Figure A.5 shows how the strain gages were attached to the central bar and the gage wires routed. The gages were installed on the longitudinal rib of the bar to minimize the disturbance on the bond characteristics. The gage wires were not routed along the central bar to avoid damage in the wires due to bar slip. Instead, they were routed laterally inside plastic tubes placed horizontally.

Figure A.1: Footing and cylinder cages and footing form

Figure A.2: Concrete pour of the footing

Figure A.3: Cylinder form

Figure A.4: Installation of the central bar

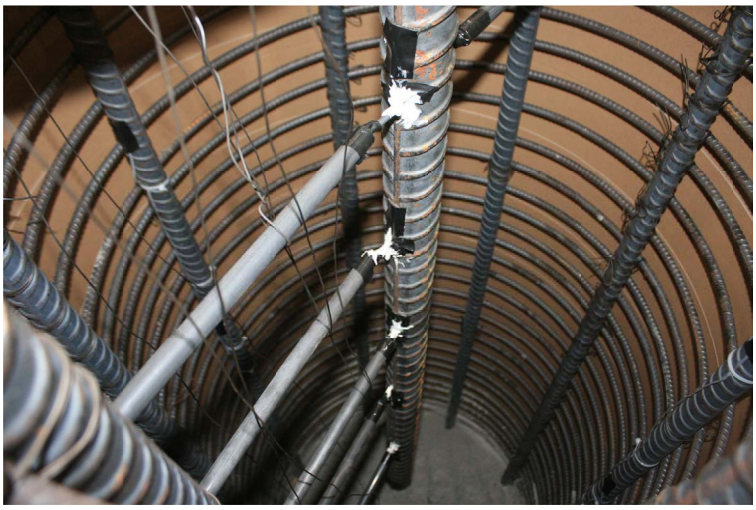

Figure A.5: Close-view of the strain gages attached to the central bar

Figure A.6: Concrete pour of the cylinder

APPENDIX B: CONSTRUCTION OF THE COLUMN-SHAFT ASSEMBLIES

This appendix contains pictures of the construction and instrumentation sequence of the column-shaft assemblies presented in Chapter 7. These pictures correspond to Specimen 1. The same sequence applies to Specimen 2.

Figure B.1: Strain gages on longitudinal reinforcing bars

Figure B.2: Strain gage on longitudinal rib of bar

Figure B.3: Shaft cage instrumented with strain gages

Figure B.4: Column cage instrumented with strain gages

Figure B.5: Footing and shaft cages

Figure B.6: Concrete pour of the footing (Pour 1)

Figure B.7: Steel form for the shaft

Figure B.8: Construction joint at footing-shaft interface after steel brushing (same preparation for all construction joints)

Figure B.9: Concrete pour of the lower portion of the shaft (Pour 2)

Figure B.10: Pour 2 completed at the level to which the column cage will be embedded

Figure B.11: Installation of the column cage

Figure B.12: Concrete pour of the upper portion of the shaft where the column cage is embedded (Pour 3)

Figure B.13: Removal of the shaft form

Figure B.14: Column form and falsework for load stub

Figure B.15: Concrete pour of the column (Pour 4)

Figure B.16: End of Pour 4

Figure B.17: Load stub reinforcing cage

Figure B.18: Concrete pour of the load stub (Pour 5)

Figure B.19: Column-shaft after removal of the form and falsework

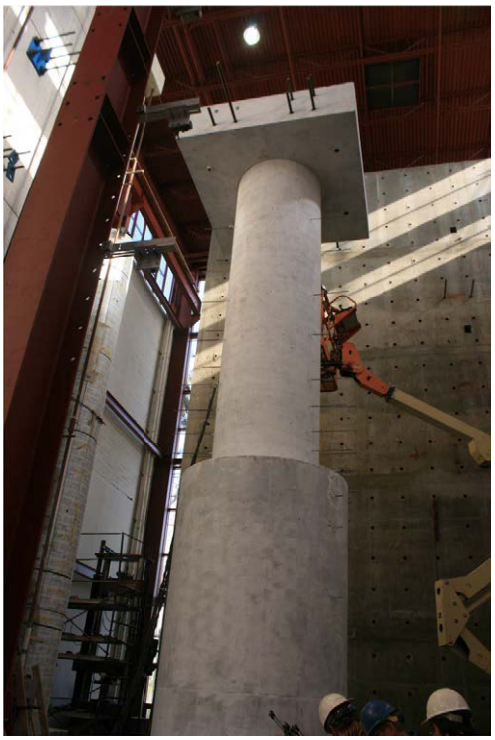

Figure B.20: Column-shaft painted white for easier crack identification during the test

Figure B.21: Column-shaft assembly instrumented (east side)

Figure B.22: Displacement transducers at the base of the column (east side)

Figure B.23: Column-shaft assembly instrumented (west side)

Figure B.24: Post-tensioning rod to apply vertical load and cone-shaped hole in the footing

Figure B.25: Setup of hydraulic jacks under the strong floor to control the load of the vertical rods

APPENDIX C: INSTRUMENTATION PLANS FOR THE COLUMN-SHAFT ASSEMBLIES

This appendix contains drawings of the instrumentation plans for the column-shaft assemblies presented in Chapter 7. The instrumentation plans include the following:

Instruments	Specimen 1	Specimen 2
Strain gages on column longitudinal bars	Figure C.1	Figure C.9
Strain gages on shaft longitudinal bars	Figure C.2	Figure C.10
Strain gages on column hoops	Figure C.3	Figure C.11
Strain gages on shaft hoops	Figure C.3	Figure C.12
Displacement transducers (linear potentiometers) to compute the curvature and shear deformations in the column and shaft	Figure C.4 through Figure C.6	Figure C.13 through Figure C.15
Displacement transducers (linear potentiometers) to compute the base rotation and slip at the interfaces	Figure C.7	Figure C.16
Displacement transducers (string potentiometers) to measure the lateral deflection of the specimen	Figure C.8	Figure C.17

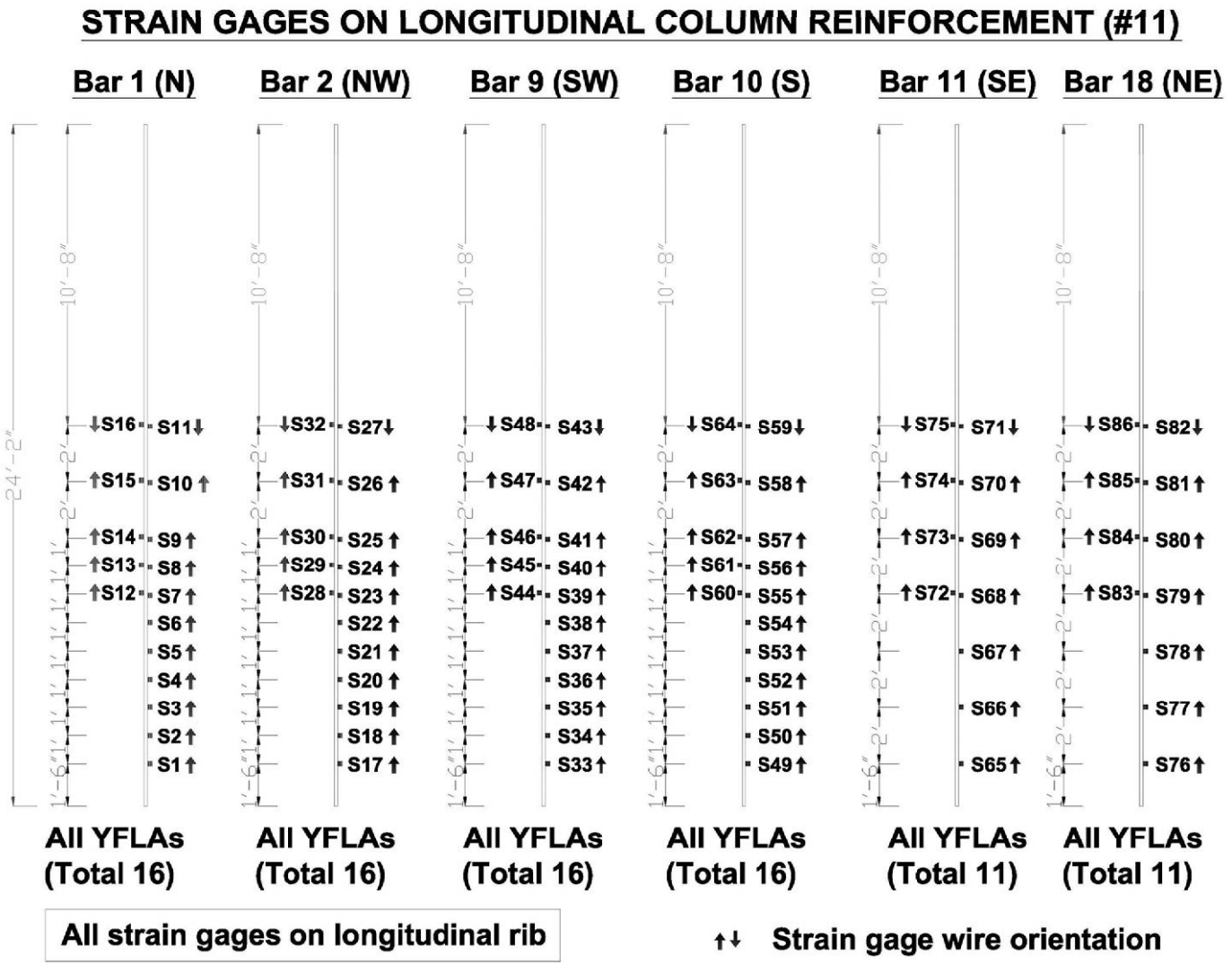

Figure C.1: Strain gages on column longitudinal bars in Specimen 1

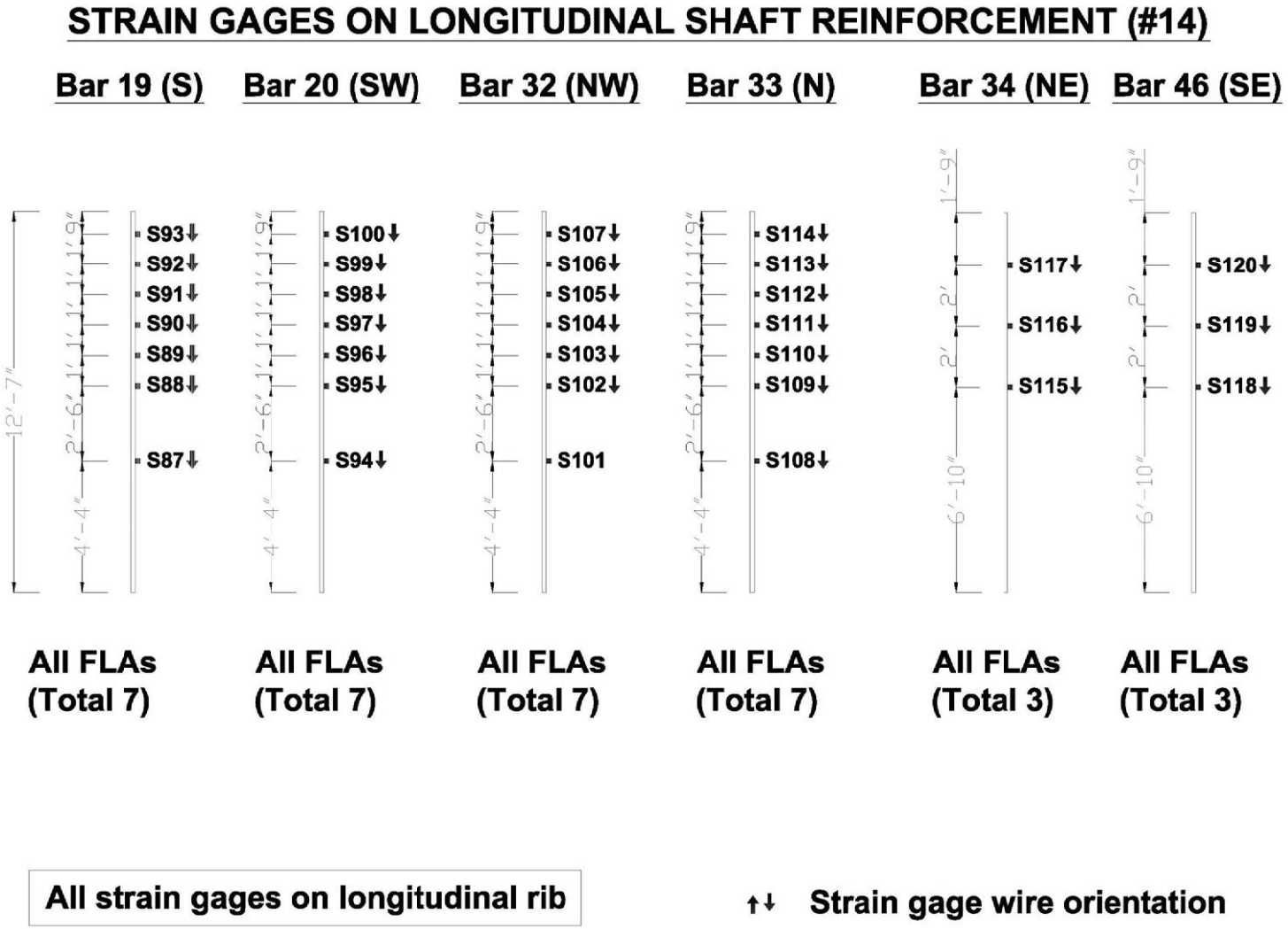

Figure C.2: Strain gages on shaft longitudinal bars in Specimen 1

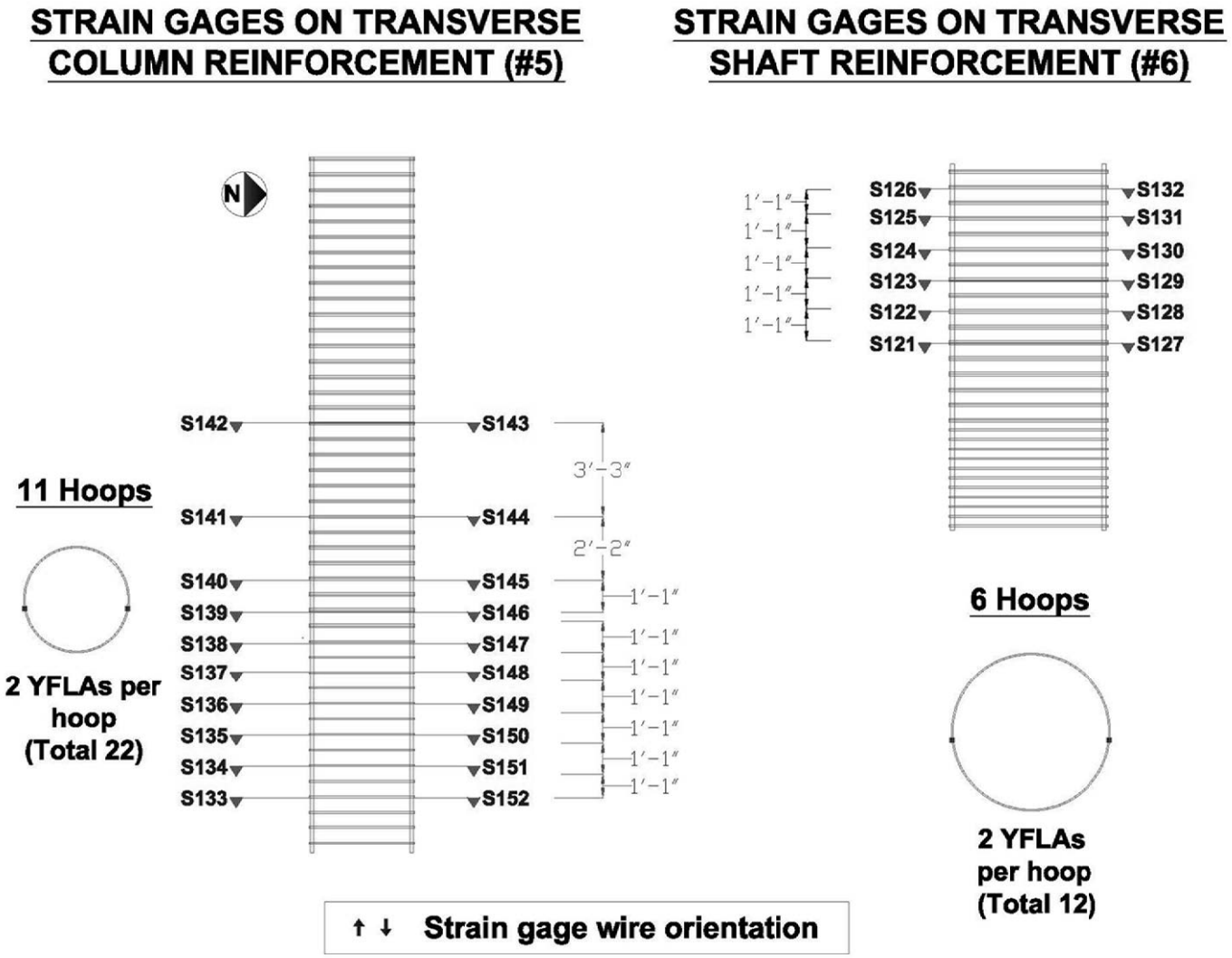

Figure C.3: Strain gages on transverse reinforcement in Specimen 1

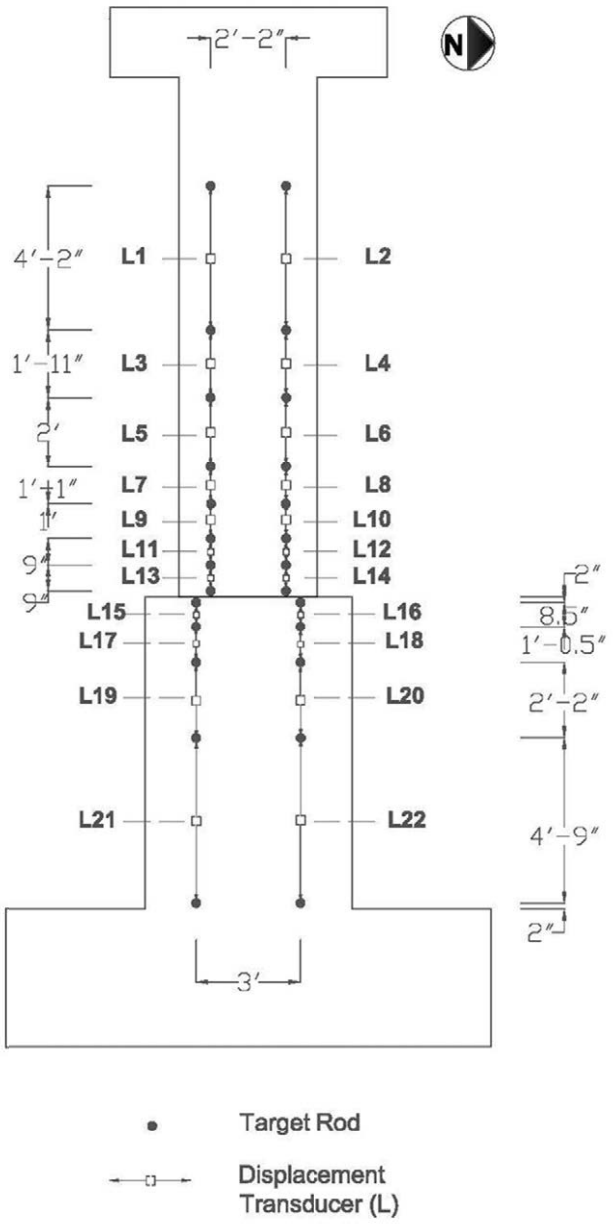

#	CENTER-TO-CENTER DISTANCE	STROKE
L1	4'-2"	2" (+1.5", -0.5")
L2	4'-2"	2" (+1.5", -0.5")
L3	1'-11"	2" (+1.5", -0.5")
L4	1'-11"	2" (+1.5", -0.5")
L5	2'	2" (+1.5", -0.5")
L6	2'	2" (+1.5", -0.5")
L7	1'-1"	2" (+1.5", -0.5")
L8	1'-1"	2" (+1.5", -0.5")
L9	1'	2" (+1.5", -0.5")
L10	1'	2" (+1.5", -0.5")
L11	9"	2" (+1.5", -0.5")
L12	9"	2" (+1.5", -0.5")
L13	9"	2" (+1.5", -0.5")
L14	9"	2" (+1.5", -0.5")
L15	~ 8 1/2"	2" (+1.5", -0.5")
L16	~ 8 1/2"	2" (+1.5", -0.5")
L17	~ 1 1/2"	2" (+1.5", -0.5")
L18	~ 1 1/2"	2" (+1.5", -0.5")
L19	~ 2'-2"	2" (+1.5", -0.5")
L20	~ 2'-2"	2" (+1.5", -0.5")
L21	~ 4'-9"	2" (+1.5", -0.5")
L22	~ 4'-9"	2" (+1.5", -0.5")

Figure C.4: Vertical displacement transducers on the east face of Specimen 1

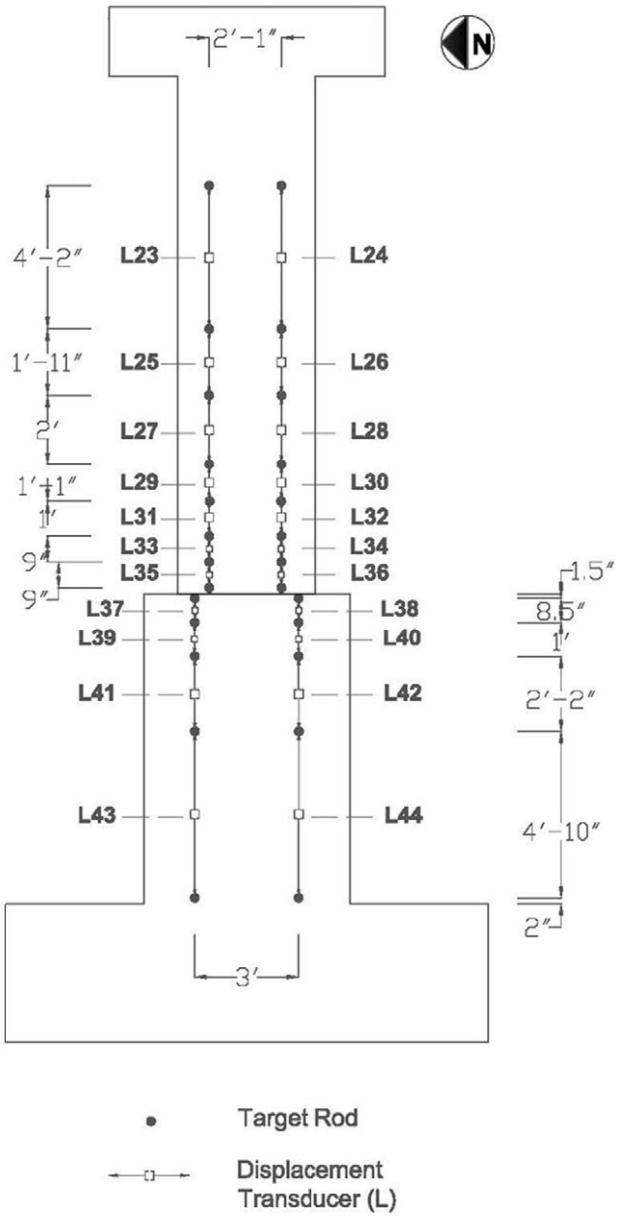

#	CENTER-TO-CENTER DISTANCE	STROKE
L23	4'-2"	2" (+1.5", -0.5")
L24	4'-2"	2" (+1.5", -0.5")
L25	1'-11"	2" (+1.5", -0.5")
L26	1'-11"	2" (+1.5", -0.5")
L27	2'	2" (+1.5", -0.5")
L28	2'	2" (+1.5", -0.5")
L29	1'-1"	2" (+1.5", -0.5")
L30	1'-1"	2" (+1.5", -0.5")
L31	1'	2" (+1.5", -0.5")
L32	1'	2" (+1.5", -0.5")
L33	9"	2" (+1.5", -0.5")
L34	9"	2" (+1.5", -0.5")
L35	9"	2" (+1.5", -0.5")
L36	9"	2" (+1.5", -0.5")
L37	~ 8.5"	2" (+1.5", -0.5")
L38	~ 8.5"	2" (+1.5", -0.5")
L39	~ 1'	2" (+1.5", -0.5")
L40	~ 1'	2" (+1.5", -0.5")
L41	~ 2'-2"	2" (+1.5", -0.5")
L42	~ 2'-2"	2" (+1.5", -0.5")
L43	~ 4'-10"	2" (+1.5", -0.5")
L44	~ 4'-10"	2" (+1.5", -0.5")

Figure C.5: Vertical displacement transducers on the west face of Specimen 1

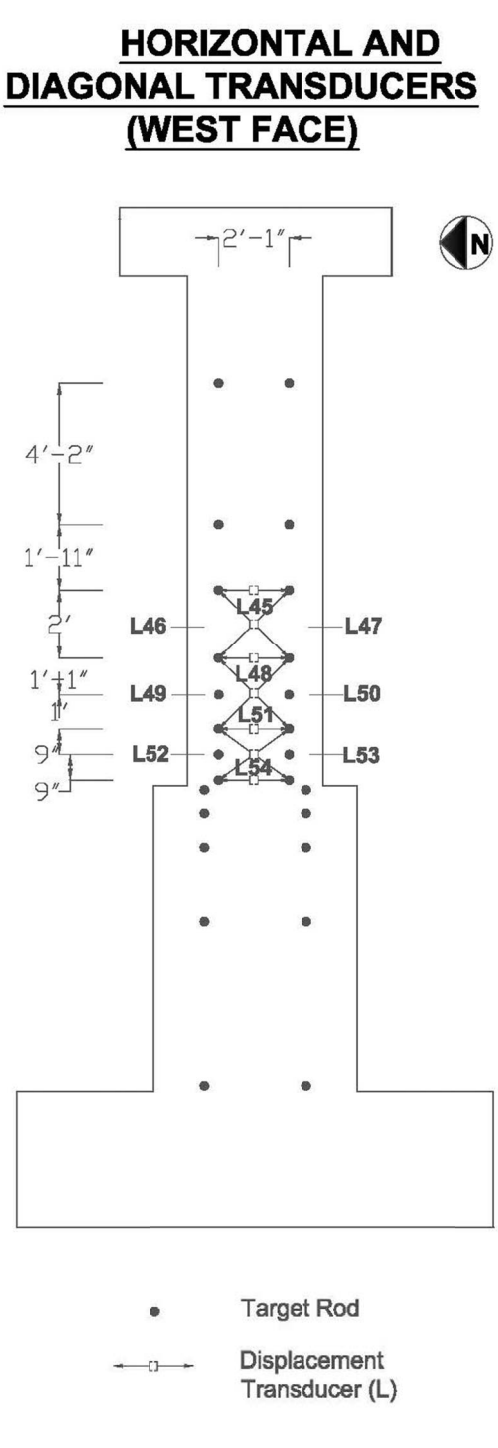

#	CENTER-TO-CENTER DISTANCE	STROKE
L45	~2'-1"	2" (+1.5", -0.5")
L46	~2'-10 1/2"	2" (+1.5", -0.5")
L47	~2'-10 1/2"	2" (+1.5", -0.5")
L48	~2'-1"	2" (+1.5", -0.5")
L49	~2'-11 1/4"	2" (+1.5", -0.5")
L50	~2'-11 1/4"	2" (+1.5", -0.5")
L51	~2'-1"	2" (+1.5", -0.5")
L52	~2'-6 3/4"	4" (+2.5", -1.5")
L53	~2'-6 3/4"	4" (+2.5", -1.5")
L54	~2'-1"	2" (+1.5", -0.5")

Figure C.6: Horizontal and diagonal displacement transducers on the west face of Specimen 1

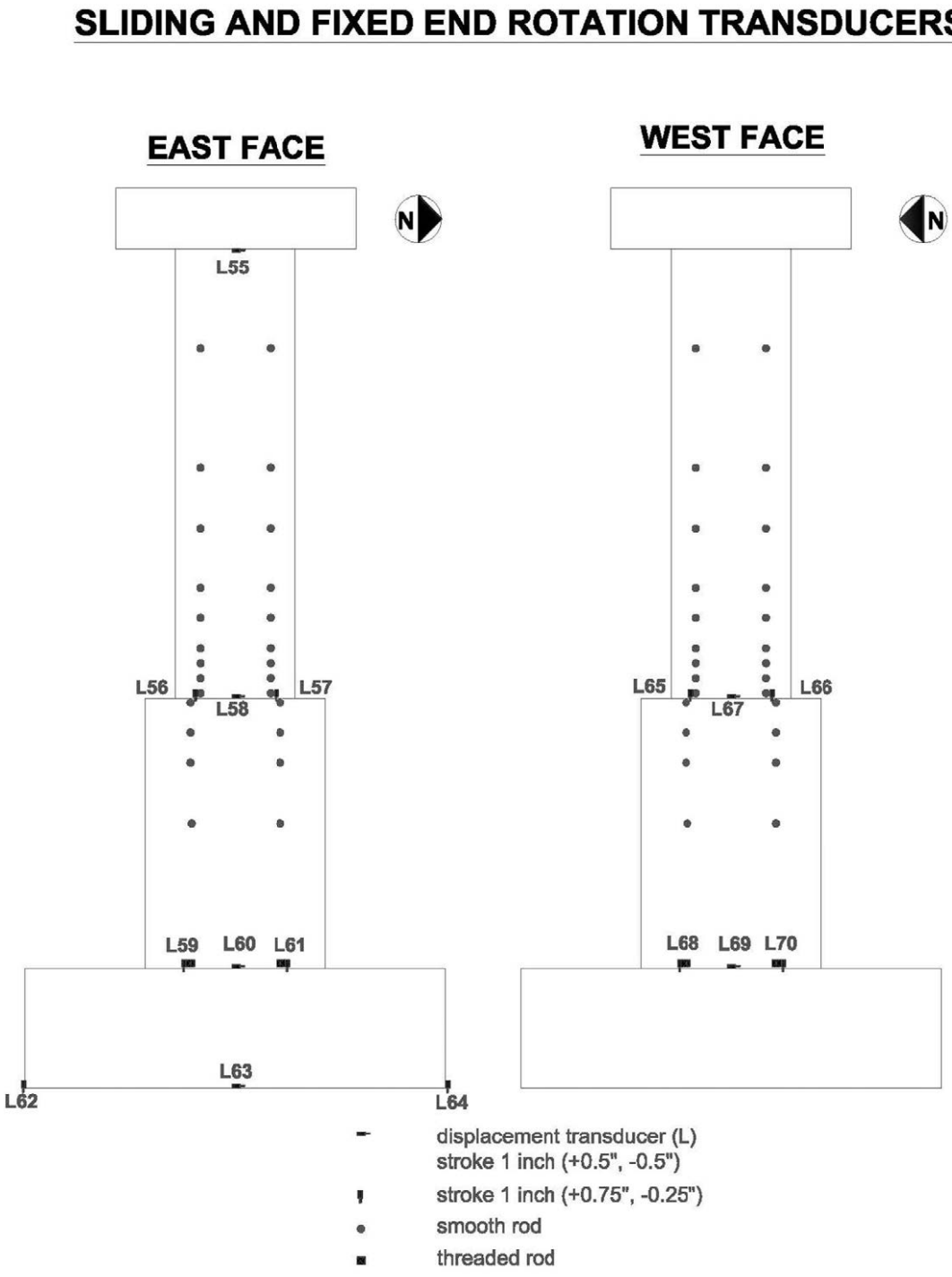

Figure C.7: Displacement transducers to measure slip and base rotation in Specimen 1

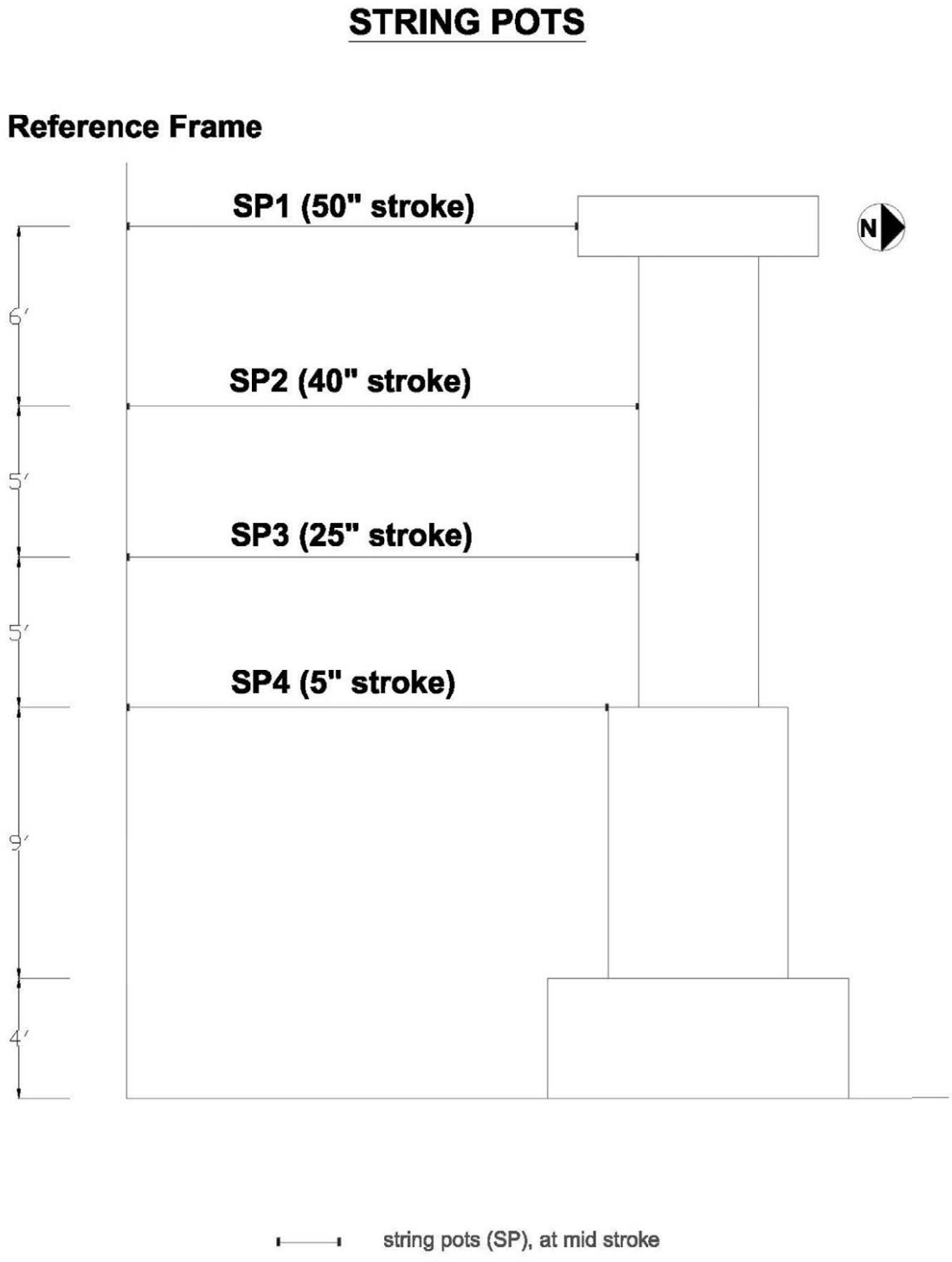

Figure C.8: String potentiometer to measure the lateral deflection of Specimen 1

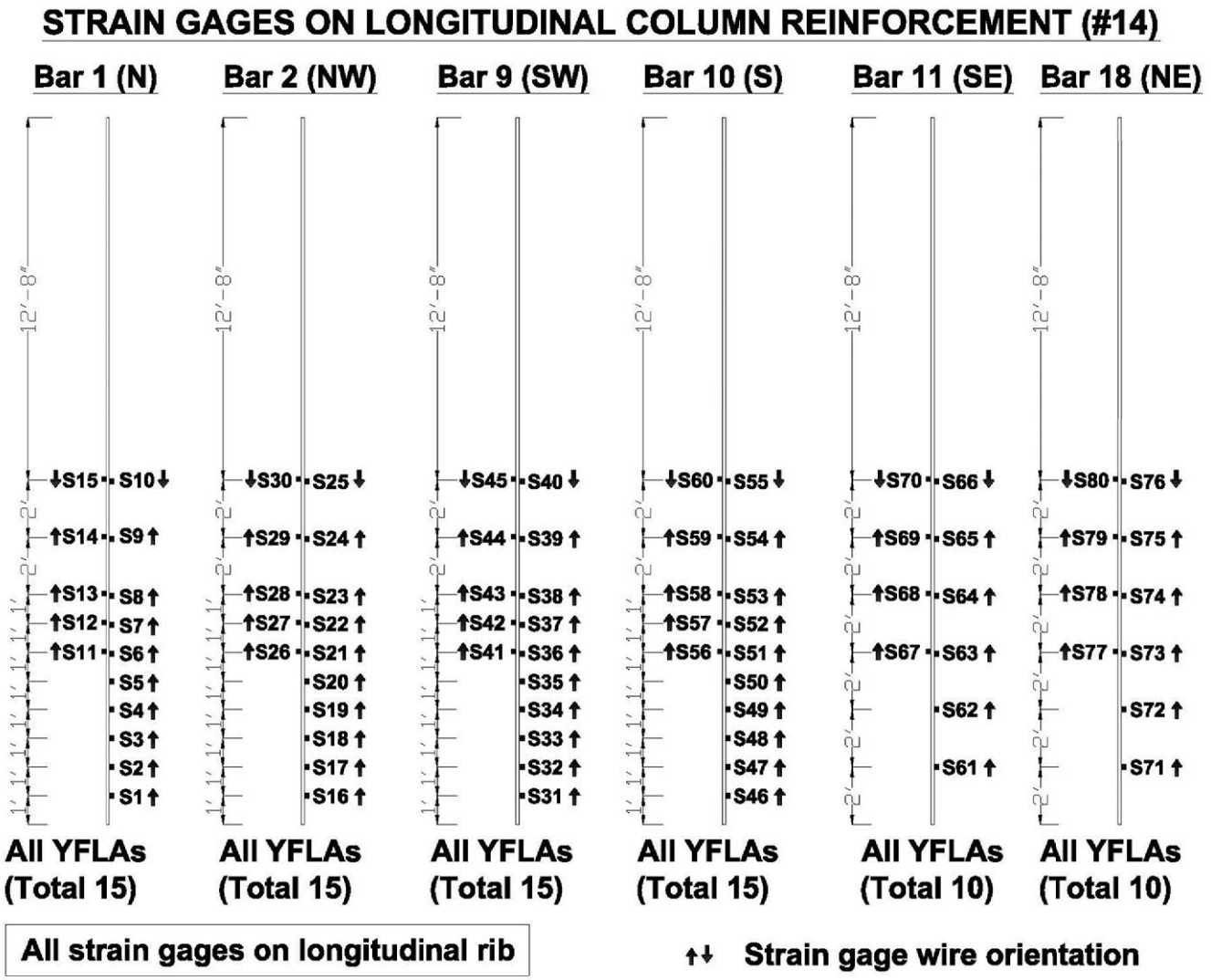

Figure C.9: Strain gages on column longitudinal bars in Specimen 2

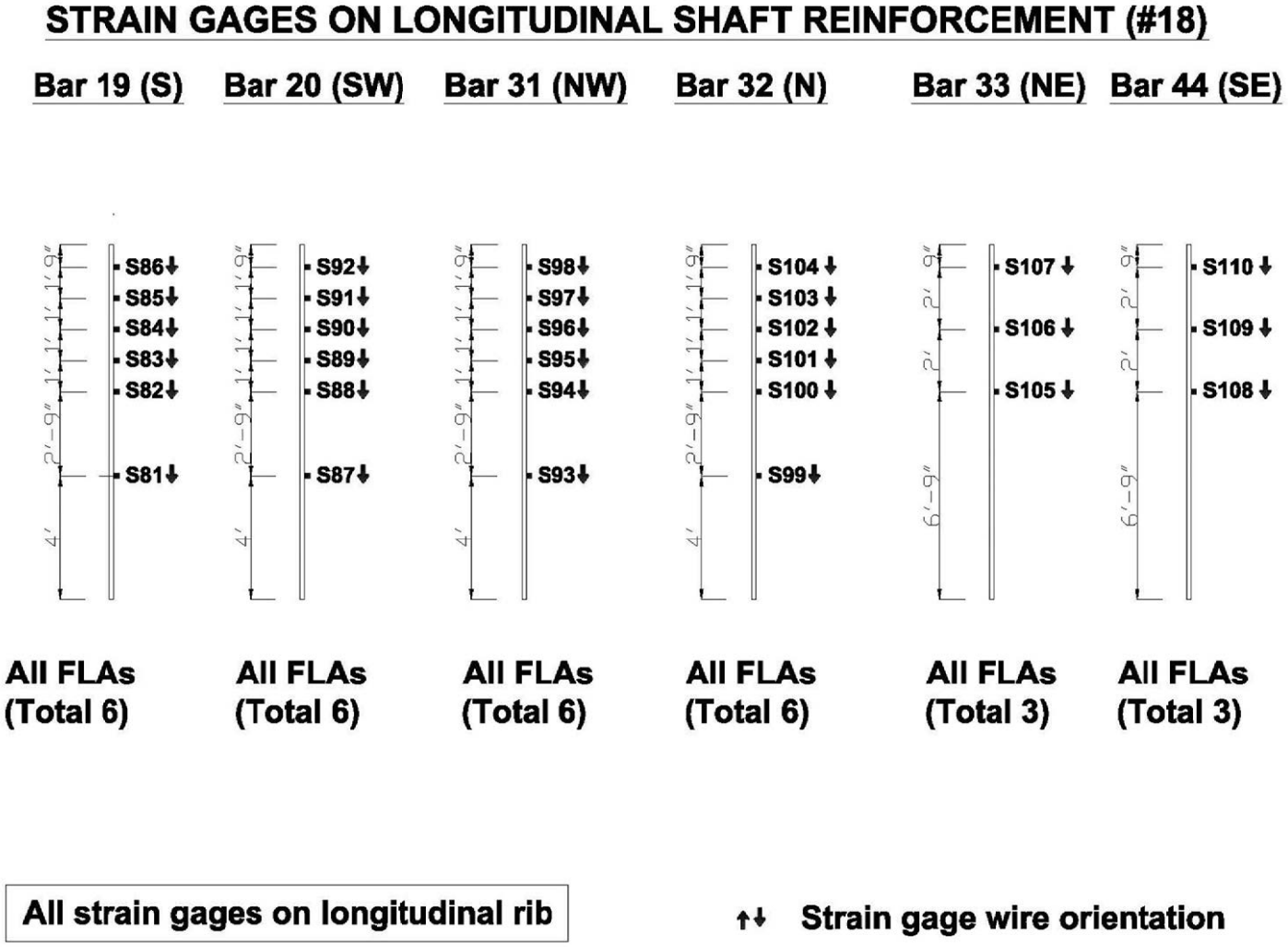

Figure C.10: Strain gages on shaft longitudinal bars in Specimen 2

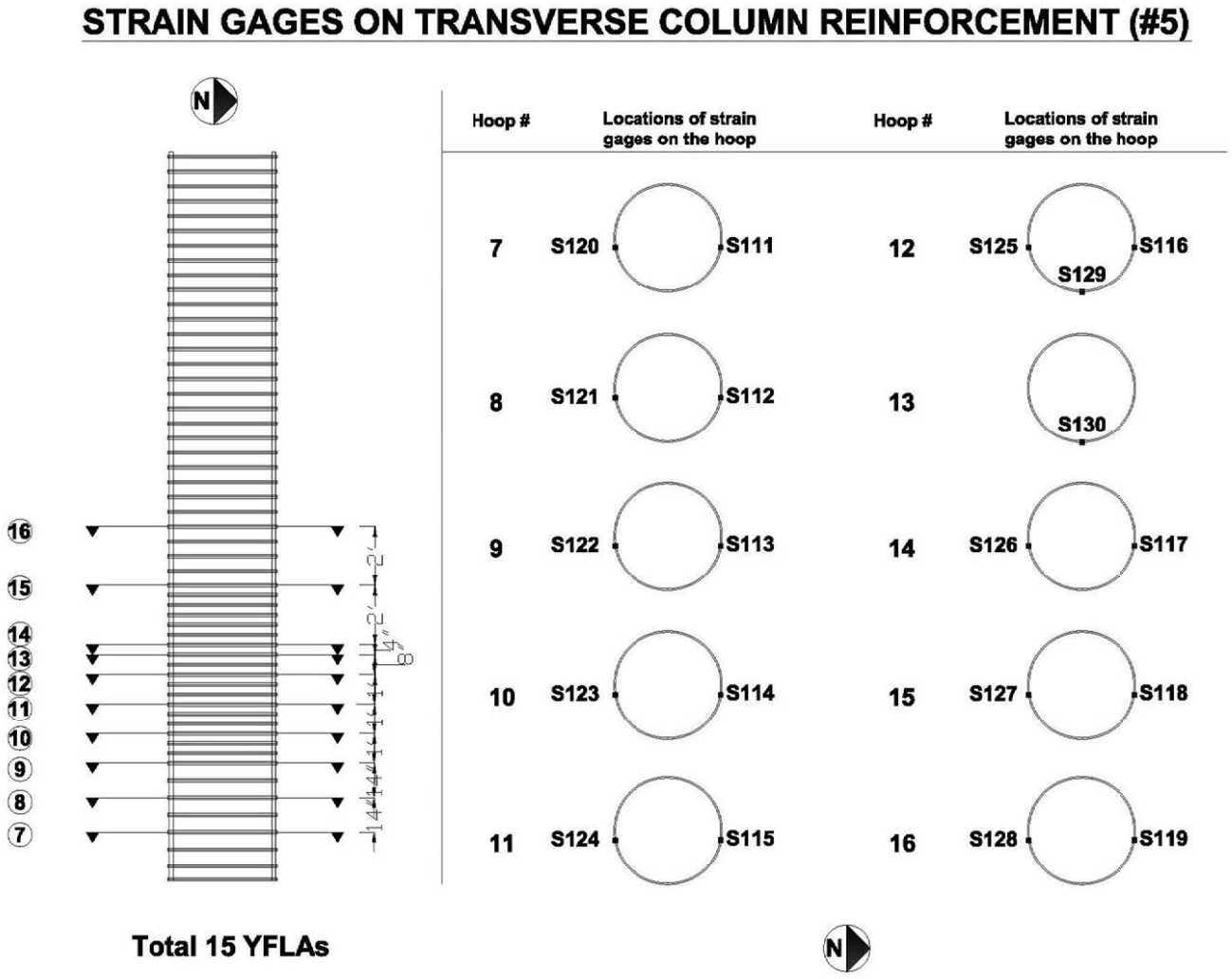

Figure C.11: Strain gages on column transverse reinforcement in Specimen 2

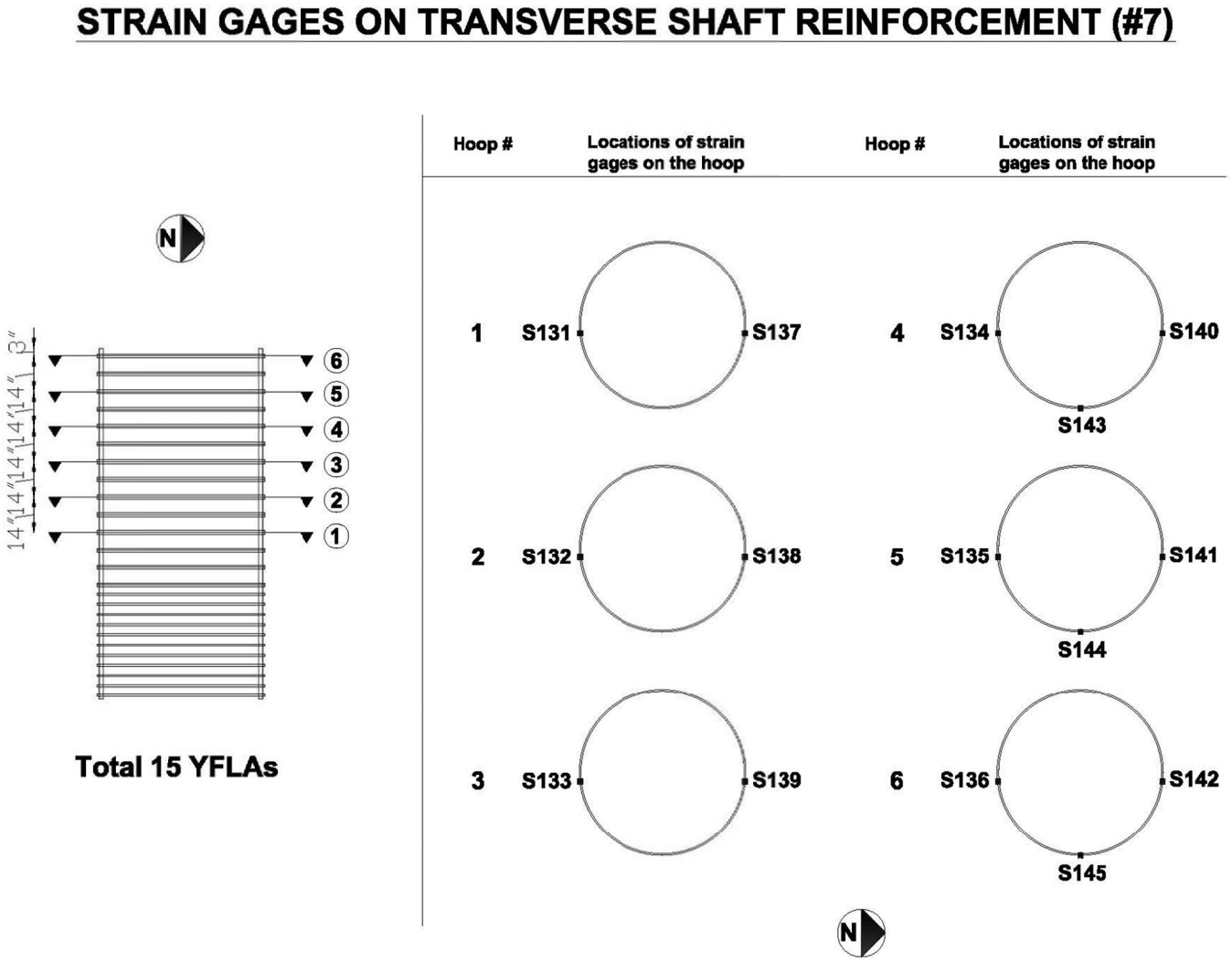

Figure C.12: Strain gages on shaft transverse reinforcement in Specimen 2

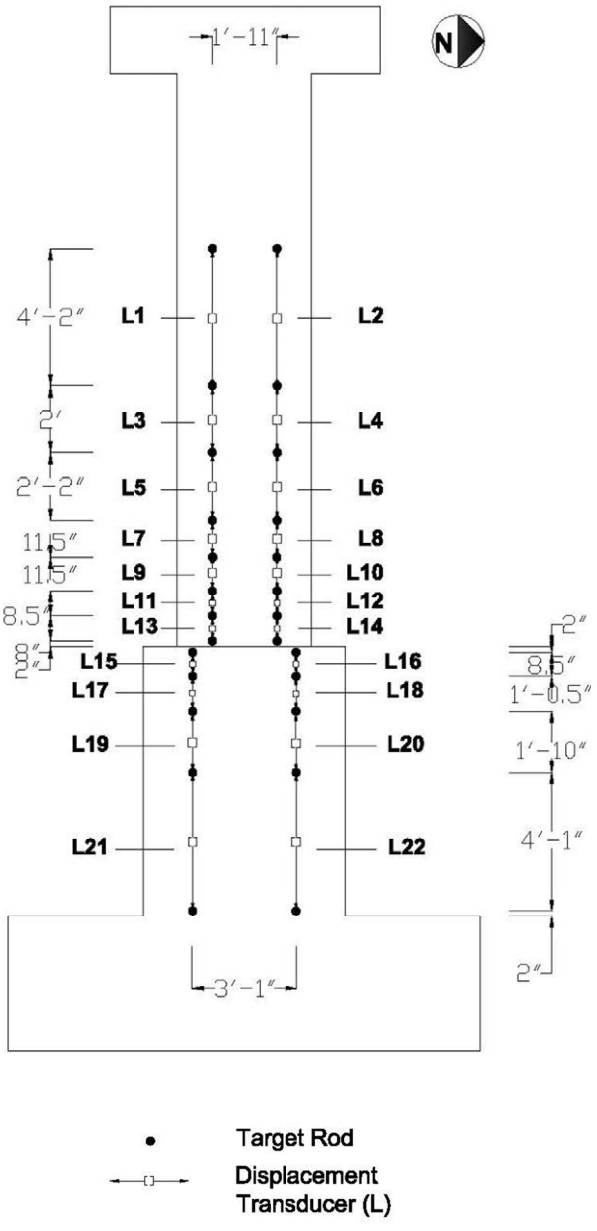

#	CENTER-TO-CENTER DISTANCE	STROKE
L1	~ 4'-2"	2" (+1.5", -0.5")
L2	~ 4'-2"	2" (+1.5", -0.5")
L3	~ 2'	2" (+1.5", -0.5")
L4	~ 2'	2" (+1.5", -0.5")
L5	~ 2'-2"	2" (+1.5", -0.5")
L6	~ 2'-2"	2" (+1.5", -0.5")
L7	~ 11 1/2"	2" (+1.5", -0.5")
L8	~ 11 1/2"	2" (+1.5", -0.5")
L9	~ 11 1/2"	2" (+1.5", -0.5")
L10	~ 11 1/2"	2" (+1.5", -0.5")
L11	~ 8 1/2"	2" (+1.5", -0.5")
L12	~ 8 1/2"	2" (+1.5", -0.5")
L13	~ 8"	2" (+1.5", -0.5")
L14	~ 8"	2" (+1.5", -0.5")
L15	~ 8 1/2"	2" (+1.5", -0.5")
L16	~ 8 1/2"	2" (+1.5", -0.5")
L17	~ 1'-1/2"	2" (+1.5", -0.5")
L18	~ 1'-1/2"	2" (+1.5", -0.5")
L19	~ 1'-10"	2" (+1.5", -0.5")
L20	~ 1'-10"	2" (+1.5", -0.5")
L21	~ 4'-1"	2" (+1.5", -0.5")
L22	~ 4'-1"	2" (+1.5", -0.5")

Figure C.13: Vertical displacement transducers on the east face of Specimen 2

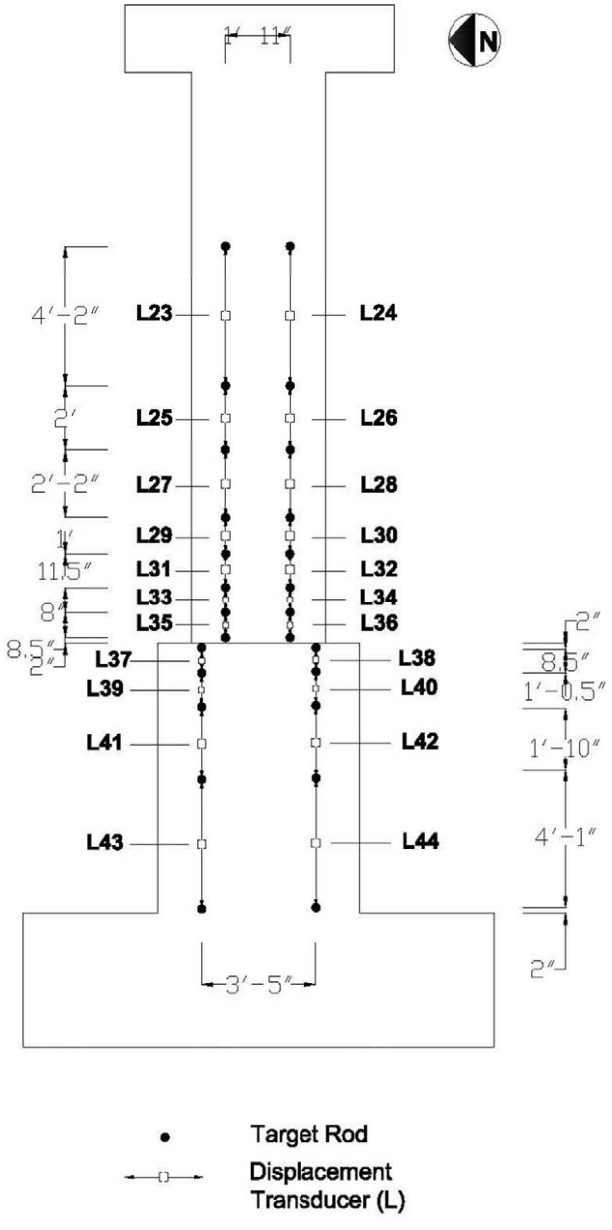

#	CENTER-TO-CENTER DISTANCE	STROKE
L23	~ 4'-2"	2" (+1.5", -0.5")
L24	~ 4'-2"	2" (+1.5", -0.5")
L25	~ 2'	2" (+1.5", -0.5")
L26	~ 2'	2" (+1.5", -0.5")
L27	~ 2'-2"	2" (+1.5", -0.5")
L28	~ 2'-2"	2" (+1.5", -0.5")
L29	~ 1'	2" (+1.5", -0.5")
L30	~ 1'	2" (+1.5", -0.5")
L31	~ 11 1/2"	2" (+1.5", -0.5")
L32	~ 11 1/2"	2" (+1.5", -0.5")
L33	~ 8"	2" (+1.5", -0.5")
L34	~ 8"	2" (+1.5", -0.5")
L35	~ 8 1/2"	2" (+1.5", -0.5")
L36	~ 8 1/2"	2" (+1.5", -0.5")
L37	~ 8 1/2"	2" (+1.5", -0.5")
L38	~ 8 1/2"	2" (+1.5", -0.5")
L39	~ 1'-1/2"	2" (+1.5", -0.5")
L40	~ 1'-1/2"	2" (+1.5", -0.5")
L41	~ 1'-10"	2" (+1.5", -0.5")
L42	~ 1'-10"	2" (+1.5", -0.5")
L43	~ 4'-1"	2" (+1.5", -0.5")
L44	~ 4'-1"	2" (+1.5", -0.5")

Figure C.14: Vertical displacement transducers on the west face of Specimen 2

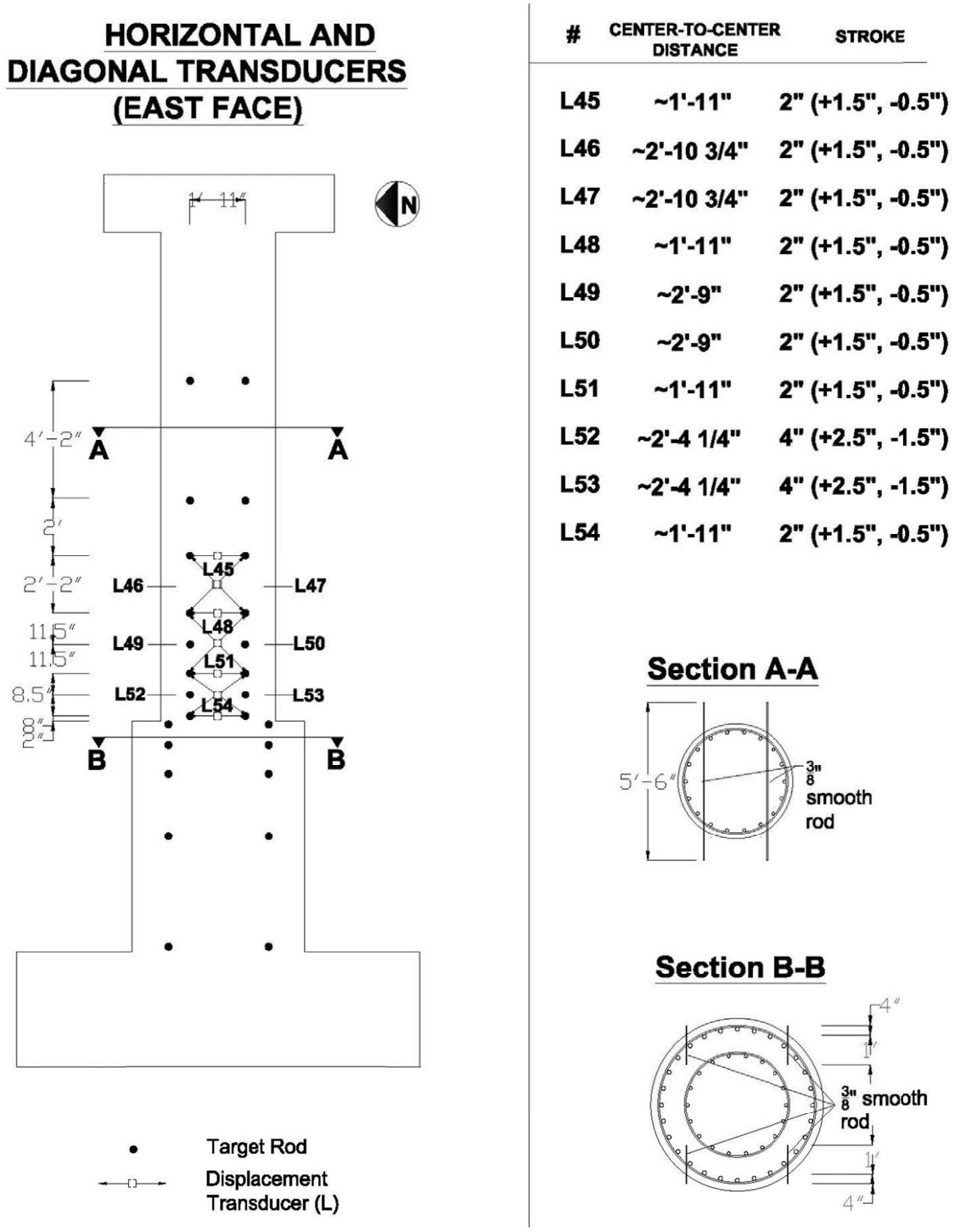

Figure C.15: Horizontal and diagonal displacement transducers on the east face of Specimen 2

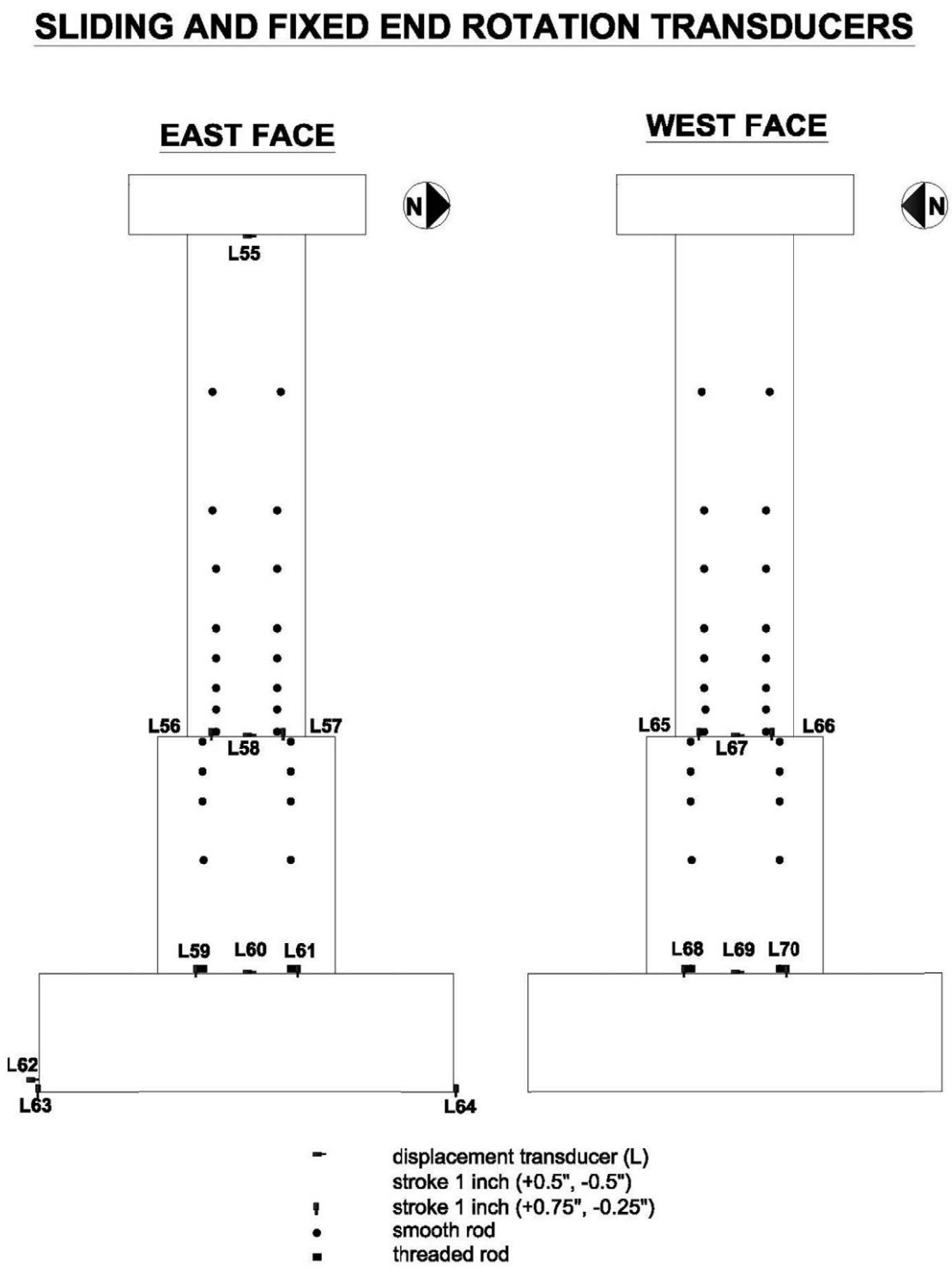

Figure C.16: Displacement transducers to measure slip and base rotation in Specimen 2

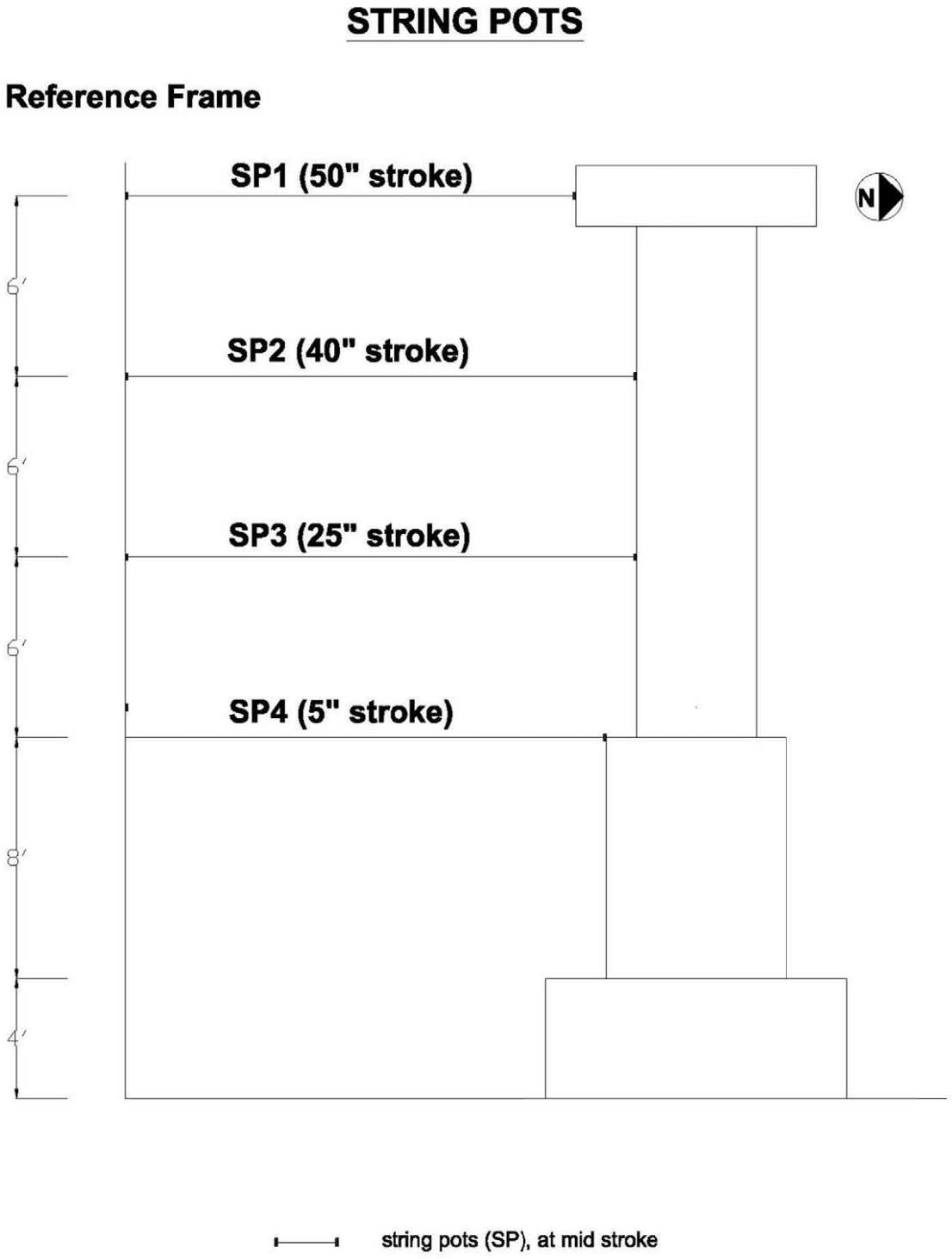

Figure C.17: String potentiometer to measure the lateral deflection of Specimen 2

REFERENCES

Abrams, D.A., "Tests on bond between concrete and steel," *University of Illinois Bulletin*, Vol. XI, No.5, 1913.

American Association of State Highway and Transportation Officials (AASHTO), *LRFD Bridge Design Specifications,* 5th Edition, Washington DC, 2010.

American Concrete Institute (ACI), *Control of Cracking of Concrete Structure (ACI 224R-01),* ACI Committee 224, Farmington Hills, MI, 2001.

American Concrete Institute (ACI), *Bond and Development of Straight Reinforcing Bars in Tension (ACI-408R-03),* ACI Committee 408, Farmington Hills, MI, 2003.

American Concrete Institute (ACI), *Building Code Requirements for Structural Concrete (ACI-318-08) and Commentary*, ACI Committee 318, Farmington Hills, MI, 2008.

American Concrete Institute (ACI), *Report on Bond of Steel Reinforcing Bars Under Cyclic Loads (ACI-408R-12),* ACI Committee 408, Farmington Hills, MI, 2012.

ASTM International, *A706/A706M-09b Standard Specification for Low-Alloy Steel Deformed and Plain Bars for Concrete Reinforcement*, West Conshohocken, PA, 2009.

Ayoub, A., "Nonlinear Analysis of Reinforced Concrete Beam–Columns with Bond-Slip Inelastic," *Journal of Engineering Mechanics*, Vol. 132, No. 11, November 2006, pp. 1177-1186.

Berry, M.P., Eberhard, M.O., *Performance Modeling Strategies for Modern Reinforced Concrete Bridge Columns*, PEER Report 2007/07, Pacific Earthquake Engineering Research Center, University of California, Berkeley, CA, 2008.

Budek, A.M., Priestley, M.J.N., Benzoni, G., "Inelastic seismic response of bridge drilled-shaft RC pile/columns," *Journal of Structural Engineering*, Vol. 24, No. 4, April 2000, pp. 510-517.

Cairns, J., Jones, K., "An evaluation of the bond-splitting action of ribbed bars," *ACI Materials Journal*, Vol. 93, No.1, January-February 1996, pp. 10-19.

California Department of Transportation (Caltrans), *Bridge Design Specifications*, Sacramento, CA, 2008.

California Department of Transportation (Caltrans), *Caltrans Seismic Design Criteria, Version 1.6*, Sacramento, CA, 2010.

Carol, I., Prat, P.C., Lopez, C.M., "Normal/shear cracking model: application to discrete crack analysis," *ASCE Journal of Engineering Mechanics*, Vol. 123, No. 8, August 1997, pp. 765-773.

Carrea, F., *Shake-Table Test on a Full-Scale Bridge Reinforced Concrete Column*, MS Thesis, Faculty of Engineering, University of Bologna, Italy, 2010.

Chai, Y.H., "Flexural strength and ductility of extended pile-shafts I: Analytical model," *Journal of Structural Engineering*, Vol. 128, No. 5, May 2002, 586-594.

Chai, Y.H., Hutchinson, T., "Flexural strength and ductility of extended pile-shafts II: Experimental study," *Journal of Structural Engineering*, Vol. 128, No. 5, May 2002, pp. 595-602.

Chang, P., Dameron, R., *Finite element analysis of main column bars in column-shaft foundation connections and analysis of rebar bond*, David Evans and Associates Project No. CALT00590201.ANA, 2009.

Choi, O.C., Hadje-Ghaffari, H., Darwin, D., McCabe, S. L., *Bond of Epoxy-Coated Reinforcement to Concrete: Bar Parameters*, SM Report No. 25, University of Kansas Center for Research, Lawrence, KS, July 1990.

Choi, E., Chung, Y., Kim, Y., Kim., J., "Monotonic and cyclic bond behavior of confined concrete using NiTiNb SMA wires," *Smart Materials and Structures*, Vol. 20, No. 7, July 2011.

Ciampi, V., Eligehausen, R., Bertero, V.V., Popov, E.P., *Analytical Model for Concrete Anchorages of Reinforcing Bars under Generalized Excitations*, Report No. UCB/EERC-82/23, Earthquake Engineering Research Center, University of California, Berkeley, CA, 1982.

Clark, A.P., "Comparative Bond Efficiency of Deformed Concrete Reinforcing Bars," *ACI Journal*, Vol. 43, No. 4, December 1946, pp. 381-400.

Clark, A. P., "Bond of Concrete Reinforcing Bars," *ACI Journal*, Vol. 46, No. 3, November 1950, pp. 161-184.

Cox, J.V., Herrmann., L.R., "Development of a plasticity bond model for steel reinforcement," *Mechanics of Cohesive-Frictional Materials*, Vol. 3, No. 2, April 1998, pp. 155-180.

Cox, J.V., Herrmann., L.R., "Validation of a plasticity bond model for steel reinforcement," *Mechanics of Cohesive-Frictional Materials*, Vol. 4, No. 4, July 1999, pp. 361–389.

Daoud, A., Maurel, O., Laborderie, C., "Mesoscopic modeling of the interaction between steel reinforcement and the early-age cracking during cement hydration," *Bond in Concrete 2012*, Brescia, Italy, June 2012.

Darwin, D., Graham, E.K., "Effect of Deformation Height and Spacing on Bond Strength of Reinforcing Bars," *ACI Structural Journal*, Vol. 90, No. 6, November-December 1993, pp. 646-657.

Darwin, D., Idun, E.K., Zuo, J., Tholen, M.L.., "Reliability-based strength reduction factor for bond," *ACI Structural Journal*, Vol. 95, No. 4, July-August 1998, pp. 434-442.

Eligehausen, R., Popov, E.P., Bertero, V.V.," Local Bond Stress - Slip Relationships of Deformed Bars under Generalized Excitations," UCB/EERC- 83/23, Earthquake Engineering Research Center, University of California, Berkeley, CA, 1983.

Fédération Internationale du Béton (fib), *Bond of Reinforcement in Concrete,* fib bulletin 10, Lausanne, Switzerland, 2000.

Fédération Internationale du Béton (fib), *Model Code 2010 - Final draft, Volume 1*, fib bulletin 65, Lausanne, Switzerland, 2012.

Fernandez Ruiz, M., Muttoni, A., Gambarova, P.G., "Analytical Modeling of the Pre- and Postyield Behavior of Bond in Reinforced Concrete," *ASCE Journal of Structural Engineering*, Vol. 133, No.10, October 2007, pp. 1364-1372.

Filippou, F.C., Popov, E.G., Bertero, V.V., "Modeling of R/C joints under cyclic excitations," *ASCE Journal of Structural Engineering*, Vol. 109, No.11, November 1983, pp. 2666-2684.

Gambarova, P., Rosati, G.P., Zasso, B., "Steel-to-concrete bond after concrete splitting: test results," *Materials and Structures*, Vol. 22, No. 127, January 1989, pp. 35-47.

Gambarova, P., Rosati, G.P., "Bond and splitting in reinforced concrete: test results on bar pull-out," *Materials and Structures*, Vol. 29, No. 189, June 1996, pp. 267-276.

Goto, Y., "Cracks Formed in Concrete Around Deformed Tension Bars," *ACI Journal*, Vol. 68, No. 4, April 1971, pp. 244-251.

Herrmann, L.R., Cox, J.V., *Development of a plasticity bond model for reinforced concrete*, CR 94-001, Naval Facilities Engineering Service Center, Port Hueneme, CA, 1994.

Hurblut, B.J., *Experimental and computational investigation of strain-softening in concrete*, MS Thesis, University of Colorado, Boulder, CO, 1985.

Ichinose, T., Kanayama, Y., Inoue, Y., Bolander Jr., J.E., "Size Effect on Bond Strength of Deformed Bars," *Construction and Building Materials*, Vol. 18, No. 7, September 2004, pp. 549-558.

Karthik, M.M., Mander, J.B., "Stress-block parameters for unconfined and confined concrete based on a unified stress-strain model," *ASCE Journal of Structural Engineering*, Vol. 137, No.2, February 2011, pp. 270-273.

Koutromanos, I., Shing, P.B., "Cohesive crack model to simulate cyclic response of concrete and masonry structures," *ACI Structural Journal*, Vol. 109, No. 3, May-June 2012, pp. 349-358.

Lee, J., Fenves, G.L., "Plastic-Damage Model for Cyclic Loading of Concrete Structures," *ASCE Journal of Engineering Mechanics*, Vol. 124, No.8, August 1998, pp. 892–900.

Lehman, D.E., Moehle, J.P., *Seismic performance of well-confined concrete bridge columns*, PEER Report 1998/01, Pacific Earthquake Engineering Research Center, University of California, Berkeley, CA, 2000.

Liu, P., Lin, H., Der Kiureghian, A., *CALREL User Manual*, UCB/SEEM-89/18, Department of Civil Engineering, University of California, Berkeley, CA, 1989.

Liu. Y., *Lateral Behavior of Reinforced Concrete Columns Supported on Type II Shafts*, MS Thesis, Department of Structural Engineering, University of California, San Diego, CA, 2012.

Lotfi, H.R., Shing, P.B., "Interface model applied to fracture of masonry structures," *ASCE Journal of Structural Engineering.* Vol. 120, No. 1, January 1994, pp. 63–80.

Lowes, L.N., Moehle, J.P., Govindjee, S., "Concrete-Steel Bond Model for Use in Finite Element Modeling of Reinforced Concrete Structures," *ACI Structural Journal*, Vol. 101, No. 4, July-August 2004, pp. 501-511.

Lubliner, J., Oliver, J., Oller, S., Oñate, E., "A Plastic-Damage Model for Concrete," *International Journal of Solids and Structures*, Vol. 25, No.3, 1989, pp. 229–326.

Lundgren, K., "Pull-out Tests of Steel-encased Specimens Subjected to Reversed Cyclic Loading," *Materials and Structures*, Vol. 33, No. 231, August-September 2000, pp. 450-456.

Lundgren, K., Magnusson, J., "Three-dimensional modeling of anchorage zones in reinforced concrete," *ASCE Journal of Engineering Mechanics*, Vol. 127, No.7, July 2001, pp. 693-699.

Lundgren, K.," Bond between ribbed bars and concrete. Part 1: Modified model," *Magazine of Concrete Research*, Vol. 57, No.7, September 2005, pp. 371-382.

Maekawa, K., Pimanmas, A., Okamura, H., *Nonlinear mechanics of reinforced concrete*, Ed. Spon Press, New York, NY, 2003.

Malvar, J., "Bond of Reinforcement under Controlled Confinement," *ACI Materials Journal*, Vol. 89, No. 6, November-December 1992, pp. 593-601.

Mander, J.B., Priestley, M.J.N., Park, R., "Observed stress-strain behavior of confined concrete," *ASCE Journal of Structural Engineering*, Vol. 114, No.8, August 1989, pp. 1827-1849.

McLean, D.I., Smith, C.L., *Noncontact lap splice in bridge column-shaft connections*, Report No. WA-RD 417.1, Washington State Transportation Center, Washington State University, WA, 1997.

Monti, G., Filippou, F.C., Spacone, E., "Finite element for anchored bars under cyclic load reversals," *ASCE Journal of Structural Engineering*, Vol. 123, No. 5, May 1997, pp. 614-623.

Monti, G., Spacone, E., "Reinforced concrete fiber beam element with bond-slip," *Journal of Structural Engineering*, Vol. 126, No. 6, June 2000, pp. 654-661.

Murcia-Delso, J., Stavridis, A., Shing, P.B., "Bond Strength and Cyclic Bond Deterioration of Large-Diameter Bars," *ACI Structural Journal* (in press).

Nowak, A.S., Szerszen, M.M., "Calibration of Design Code for Buildings (ACI 318): Part 1—Statistical Models for Resistance," *ACI Structural Journal*, Vol. 100, No. 3, May-June 2003, pp. 377-382.

Orangun, C.O., Jirsa, J.O., Breen, J.E., *The Strength of Anchored Bars: A Reevaluation of Test Data on Development Length and Splices*, Research Report No. 154-3F, Center for Highway Research, University of Texas at Austin, TX, January 1975.

Orangun, C.O., Jirsa, J.O., Breen, J.E., "Reevaluation of Test Data on Development Length and Splices," *ACI Journal*, Vol. 74, No. 3, March 1977, pp. 114-122.

Ortiz, M., Popov, E.P., "Accuracy and stability of integration algorithms for elastoplastic constitutive relations," *International Journal for Numerical Methods in Engineering*, Vol. 21, No.10, September 1985, pp. 1561-1576.

Pacific Earthquake Engineering Research Center (PEER), Open System for Earthquake Engineering Simulation (OpenSees), Berkeley, CA, 2012.

Plizzari, G., Mettelli, G., *Experimental Study on the Bond Behavior of Large Bars, Technical Report*, Dept. of Civil Engineering, Architecture and Environment, University of Brescia, Italy, 2009.

Pochanart, S., Harmon, P., "Bond-Slip Model for Generalized Excitations Including Fatigue," *ACI Materials Journal*, Vol. 86, No. 5, September-October 1989, pp. 465-474.

Priestley M.J.N., Seible, F., Calvi, G.M., *Seismic Design and Retrofit of Bridges*, John Wiley &. Sons, New York, NY, 1996.

Priestley M.J.N., *Myths and Fallacies in Earthquake Engineering, Revisited*, IUSS Press, Pavia, Italy, 2003.

Puntel, E., Bolzon, G., Saouma, V.E., "Fracture mechanics based model for joints under cyclic loading," *ASCE Journal of Engineering Mechanics*, Vol. 132, No. 11, November 2006, pp. 1151-1159.

Raynor, D.J., *Bond Assessment of Hybrid Frame Continuity Reinforcement*, MS Thesis, University of Washington, WA, 2000.

Rehm, G., 1961, "Uber die Grunlagen des Verbundes Zwischen Stahl und Beton (On the fundamentals of steel-concrete bond)," *Deutscher Ausschuss fur Stahlbeton*, No. 1381, 1961.

Reinhardt, H.W., Blaauwendraad, J., Vos, E., "Prediction of bond between steel and concrete by numerical analysis", Materials and Structures., Vol. 17, No. 100, July-August 1984, pp. 311-320.

Reinhardt, H.W., "Fracture mechanics of an elastic softening material like concrete," *Heron*, Vol. 29, No.2, 1984.

Restrepo, J.I., Seible, F., Stephan, B., Schoettler, M.J., "Seismic Testing of Bridge Columns Incorporating High-Performance Materials," *ACI Structural Journal*, Vol.103, No.4, July-August 2006, pp. 496-504.

Restrepo, J., Schoettler, M.J., Guerrini, G., Personal Communication, 2010.

Restrepo-Posada, J.I., Park, R., Buchanan, A.H., *Seismic behaviour of connections between precast concrete members*, Research report 93-3, Department of Civil Engineering, University of Canterbury, New Zealand, April 1993.

Santos, J., Henriques, A.A., "FE modelling of bond-slip response including steel strains," *Bond in Concrete 2012*, Brescia, Italy, June 2012.

Serpieri, R., Alfano, G., "Bond-slip analysis via a thermodynamically consistent interface model combining interlocking, damage and friction", *International Journal for Numerical Methods in Engineering*, Vol. 85, No. 2, January 2011, pp. 164-186.

Shima, H., Chou, L., Okamura, H., "Bond-Slip-Strain Relationship of Deformed Bars Embedded in Massive Concrete," *Proceedings of JSCE*, Vol.6, No.387, February 1987, pp. 79-94.

Shima, H., Chou, L., Okamura, H., "Bond Characteristics in Post-Yield Range of Deformed Bars," *Proceedings of JSCE*, Vol.6, No. 387, February 1987, pp. 113-124.

Simo, J.C., Hughes, T.J.R., *Computational Inelasticity*, Springer-Verlag, New York, NY, 1998.

Simulia, ABAQUS V. 6.10, Dassault Systemes Simulia Corp., Providence, RI, 2010.

Spacone, E., Filippou, F. C., Taucer, F. F. ''Fiber beam-column model for nonlinear analysis of R/C frames. Part I: Formulation,'' *Earthquake Engineering and Structural Dynamics*, Vol. 25, No. 7, July 1996, pp. 711–725.

Sritharan, S., Priestley, M.J.N., Seible, F., "Nonlinear Finite element analyses of concrete bridge joint systems subjected to seismic actions," *Finite Elements in Analysis and Design*, Vol. 36, No. 3-4, November 2000, pp. 215-233.

Steuck, K.P., Eberhard, M.O., Stanton, J.F., "Anchorage of Large-Diameter Reinforcing Bars in Ducts," *ACI Structural Journal*, Vol. 106, No. 4, July-August 2009, pp. 506-513.

Tepfers, R., *A Theory of Bond Applied to Overlapped Tensile Reinforcement Splices for Deformed Bar*., Publ. 73:2, Division of Concrete Structures, Chalmers University of Technology, Goteborg, Sweden, May 1973.

Tepfers R., Olsson P., "Ring Test for Evaluation of Bond Properties of Reinforcing Bars. International Conference, " *Bond in Concrete - From Research to Practice*, Riga, Latvia, October 1992.

Unanwa, C., Mahan, M., "Statistical Analysis of Concrete Compressive Strengths for California Highway Bridges," *Journal of performance of Constructed Facilities*, posted ahead of print September 22, 2012.

Viwathanatepa, S, Popov, E.P., Bertero, V.V., *Effects of Generalized Loadings on Bond of Reinforcing Bars Embedded in Confined Concrete Blocks*, Report No. UCB/EERC-79/22, Earthquake Engineering Research Center, University of California, Berkeley, CA, 1979.

Yankelevsky, D.Z., Moshe, A.A., Farhey, D.N., "Mathematical Model for Bond-Slip Behavior under Cyclic Loading," *ACI Structural Journal*, Vol. 89, No. 6, November-December 1992, pp. 692-698.

Yashinsky, M., “Earthquake Damage to Structures”, *Structural Engineering Handbook*, Ed. Lian Duan, Boca Raton: CRC Press LLC, 2001.

Zhao, J., Sritharan, S., “Modeling of Strain Penetration Effects in Fiber-Based Analysis of Reinforced Concrete Structures,” *ACI Structural Journal*, Vol. 104, No. 2, March-April 2007, pp. 133-141.

Zsutty, T., “Empirical Study of Bar Development Behavior,” *ASCE Journal of Structural Engineering*, Vol. 111, No. 1, January 1985, pp. 205-219.

Zuo, J., Darwin, D, “Splice Strength of Conventional and High relative Rib Area Bars in Normal and High-Strength Concrete,” *ACI Structural Journal*, Vol. 97, No. 4, July-August 2000, pp. 630-641.